

A Thesis Submitted for the Degree of PhD at the University of Warwick

**Permanent WRAP URL:** 

http://wrap.warwick.ac.uk/162196

### **Copyright and reuse:**

This thesis is made available online and is protected by original copyright.

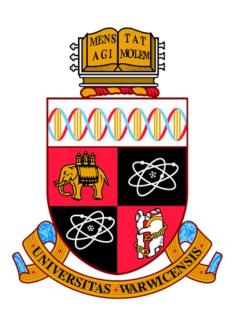
Please scroll down to view the document itself.

Please refer to the repository record for this item for information to help you to cite it.

Our policy information is available from the repository home page.

For more information, please contact the WRAP Team at: wrap@warwick.ac.uk

# Characterisation of A Novel Solution Precursor to Zirconia



## By James Morgan Crosland

A thesis submitted in partial fulfilment of the requirements for the degree of

Doctor of Philosophy in Chemistry

Department of Chemistry, University of Warwick January 2021

### **Contents**

Acknowledgements	V
Declaration	vi
Abstract	vii
Chapter 1: Introduction	
1.1 Industry and Project Background	1
1.2 Early Understanding of the Structure of Zirconium (Solution) Species:	
The Prevalence of the 'Zirconyl' Ion	2
1.3 A Modern Understanding of the Structure of Zirconium Species in Aqueous	
Solution: The Discovery of the Zirconium Tetramer	6
1.4 The Chemistry of Nitrate-Based Aqueous Solutions of Zirconium	10
1.5 The Use of Nitrate-Based Aqueous Solutions of Zirconium in Industry	15
1.6 Project Aims	17
1.7 Bibliography	19
Chapter 2: Synthesis of Poly-Zirconium Nitrate (PZN) Aqueous Solutions of Zirconium	
2.1 Experimental Setup	22
2.2 Synthesis Procedure	25
Chapter 3: Characterisation of Aqueous Zirconium Solutions by Vibrational	
Spectroscopy	28
3.1 Introduction	28
3.2 Literature Overview	29
3.3 Experimental Methods	32
3.3.1 Fourier-Transform Infrared Spectroscopy (FTIR)	32
3.3.2 Raman Spectroscopy	32
3.4 Characterisation by Infrared Spectroscopy	34
3.4.1. Initial Benchmarking	34
3.4.2 Infrared Measurements of PZN Solutions of Varying Composition	43

	3.4.3 Infrared Measurements of PZN Solutions During Synthesis	47		
	3.4.4 Infrared Measurements of PZN Solutions After Aging	51		
	3.5 Characterisation by Raman Spectroscopy	55		
	3.5.1 Initial Benchmarking	55		
	3.5.2 Raman Measurements During PZN Synthesis	61		
	3.5.3 Testing of PZN Solutions of Varying Composition	63		
	3.5.4 Variation of Heat Treatment Temperature During PZN Synthesis	67		
	3.5.4.1. Discussion of Spectra	67		
	3.5.4.2 Quantitative Analysis of Spectra	74		
	3.6 Summary and Conclusions	80		
	3.7 Bibliography	82		
Chapter 4: Characterisation of Aqueous Zirconium Solutions by Small-Angle X-Ray				
Scatt	ering	85		
	4.1 Introduction	85		
	4.2 Explanation of Terms	86		
	4.3 Literature Overview	87		
	4.4 Experimental Methods	92		
	4.4.1 Theory of SAXS	92		
	4.4.2 Experimental Setup	94		
	4.5 Results and Discussion	97		
	4.5.1 Characterisation of PZN Solutions of Varying Composition	97		
	4.5.1.1 Discussion of Results	97		
	4.5.1.2 Determination of Particle Sizes	104		
	4.5.2 SAXS Measurements of PZN Solutions During Synthesis	113		
	4.5.3 SAXS Measurements of Aged PZN Solutions	116		
	4.5.4. Variation of Heat Treatment Temperature During PZN Synthesis	118		
	4.5.5 SAXS Measurements of PZN Solutions with <i>In Situ</i> Heating	122		
	4.6 Summary and Conclusions	127		

4.7 Bibliography	129
Chapter 5: Characterisation of Aqueous Zirconium Solutions by Synchrotron X-Ray	
Techniques: EXAFS and XPDF	131
5.1 Introduction	131
5.2 Experimental Methods	132
5.2.1 Extended X-Ray Absorption Fine Structure (EXAFS)	132
5.2.2 X-Ray Pair Distribution Function (XPDF)	138
5.3 Literature Overview	140
5.4 EXAFS Results	143
5.5 PDF Results	154
5.6 Summary and Conclusions	160
5.7 Bibliography	161
Chapter 6: Synthesis and Characterisation of Zirconium Mandelate: First Structure	
Elucidation via NMR Crystallography	165
6.1 Introduction	165
6.2 The Chemistry of Mandelic Acid	166
6.3 Zirconium Mandelate as a Gravimetric Analysis Reagent	167
6.3.1 Discovery and Development of Knowledge Regarding the Complex	167
6.3.2 Historical Syntheses	170
6.4 Experimental Methods	170
6.4.1 Thermogravimetric Analysis (TGA)	170
6.4.2 Fourier-Transform Infrared Spectroscopy (FTIR)	170
6.4.3 Extended X-Ray Absorption Fine Structure (EXAFS)	171
6.4.4 Powder X-Ray Diffraction (PXRD)	171
6.4.5 Solid-State <sup>1</sup> H and <sup>13</sup> C Nuclear Magnetic Resonance (NMR)	173
6.4.6 Scanning Electron Microscopy (SEM)	174
6.4.7 Helium Pycnometry	174
6.5 Initial Results and Discussion	174

	6.5.1 Testing of (Alternative) Methods of Synthesis of Zirconium Mandelate and		
	Preliminary Results	174	
	6.5.2 An Optimised Synthesis Method	177	
	6.6 Discussion of Results from the Optimised Synthesis Method	181	
	6.6.1 Experimental Results and Structural Solution	181	
	6.6.2 The Crystal Structure of Zirconium Mandelate	191	
	6.7 Summary and Conclusions	194	
	6.8 Bibliography	197	
Chap	ter 7: Conclusions and Further Work	202	
	7.1 Conclusions	202	
	7.2 Further Work	206	
Appe	ppendices		
	A.1 Quantities of Reagents used to make Aqueous Nitrate-Based Zirconium	208	
	Solutions		
	A.2 Fitting to Raman Spectra in Section 3.5.4.2	209	
	A.3 Plots from Determination of Particle Sizes in Section 4.5.2	219	
	A.4 Plots from the Determination of Particle Sizes in Section 4.5.3	223	
	A.5 Plots from the Determination of Particle Sizes in Section 4.5.4	226	
	A.6 Refined Parameters from Zr K-edge EXAFS Analysis of Samples in	234	
	Section 5.4		

### Acknowledgements

I would firstly like to thank Professor Richard Walton for all the help, guidance and support received over the last five years, especially for the reassurance that I was always heading in the right direction. And to thank him, Dave Scapens, Deb Harris and the team at Luxfer MEL Technologies jointly, without whom the opportunity to work on this project would not have been possible.

Thank you to all members of the Walton group who I have encountered over the same five years, especially Dan, Lucy, Tom, Katie and Jasmine for their company in the office and the lab. And thanks should be given to Tom, Ehsan, Lucy, Lu and Aron for help during beamtime and with various experimental techniques that I did not know how to or could not carry out myself.

I would also like to thank Steven Huband for his training and help with all of the SAXS experiments undertaken during this project, and for putting up with all of my questions, and Dave Hammond for help and conversation in the TGA lab. Also Marco Pinto for training on Raman equipment, and the assorted beamline scientists and any others who have helped along the way whom I may have missed out here.

And finally, many thanks and gratitude to my family and other friends for the endless support and encouragement, which has helped a great deal in me getting to the point I am at now.

### **Declaration**

All of the work presented here in this thesis was carried out by the author, unless otherwise stated, at the University of Warwick. This thesis has been composed by myself and has not been submitted at any other academic institution or submitted in any previous application for any degree.

Work leading to part of this thesis has been published, and it is expected that further work from this project may be published in due course.

"Isolated Zirconium Centres Captured from Aqueous Solution: The Structure
of Zirconium Mandelate Revealed from NMR Crystallography"

J. M. Crosland, E. K. Corlett, D. Scapens, N. Guillou, S. P. Brown and R. I.
Walton, *Chem. Commun.*, 2020, 56, 10159-10162.

### **Abstract**

Aqueous nitrate-based solutions of zirconium ('poly-zirconium nitrate') of a range of compositions have been synthesised and then characterised with a number of analytical techniques including Fourier-transform infrared spectroscopy, Raman spectroscopy, small-angle X-ray scattering, extended X-ray absorption fine structure spectroscopy and X-ray pair distribution function analysis. Synthesis was carried out on the laboratory scale with a process mimicking the pilot plant production of analogous solutions as used in industry as precursors to a wide range of solid zirconium-based materials.

Raman spectroscopy has revealed the changes occurring in solution as a direct result of the hydrolysis of zirconium in these solutions due heating and aging and has been demonstrated to provide a useful measure of the extent of this reaction over time during synthesis. Results also suggest the presence of hydrolysed zirconium solution species similar to the zirconium tetramer.

How the sizes of solution species change with time and temperature has been seen *via* small-angle X-ray scattering, and manual extraction of size parameters from scattering data has been done so in a way consistent with the idea of particles growing in solution as if they were cylindrical, or predominantly growing along one axis.

The presence of, and presence of structures based upon, the zirconium tetramer in the specific aqueous zirconium solutions studied, regardless of exact solution composition, has been confirmed by Zr K-edge extended X-ray absorption fine structure measurements at the Diamond Light Source Synchrotron, and the growth of these species as ladder-like chains of connected tetramers has been seen *via* X-ray pair distribution analysis from data also collected at Diamond.

In addition, an optimised synthesis of the reference material and gravimetric analysis reagent zirconium mandelate, and its crystal structure, have been reported for the first time following work utilising NMR crystallography methods.

### Chapter 1:

### Introduction

### 1.1 Industry and Project Background

The work described in this thesis was carried out as part of collaborative project between the University of Warwick and Luxfer MEL Technologies (LMT). LMT are a global manufacturer of engineered magnesium and zirconium materials. Their zirconium-based commercial products are marketed as being relevant to the aerospace, automotive, catalysis, ceramics, coatings and solutions, defence, healthcare and oil and gas industries. These include zirconia (zirconium dioxide, ZrO<sub>2</sub>) both undoped and doped with other metals such as yttrium, zirconium hydroxide-type materials, various modified solutions of zirconium and other specialty zirconium chemicals. Many of these products begin as aqueous solutions of zirconium, from which solid materials may be created in a proprietary synthesis route involving modification of these solutions (heat treatment, variation of composition, addition of organic complexing agents for example), precipitation from solution and subsequent firing or calcination. The properties of the final products (surface area, particle and pore size for example) are believed to be strongly influenced by the nature of the starting solutions themselves. The solutions studied in this project are nitrate-based, with the synthesis involving aqueous nitric acid, and are thus known as 'PZN' or 'poly-zirconium nitrate' in industry. This work aimed to shed new light on these types of solutions specifically, and to elucidate what types of zirconium species are present in these solutions.

### 1.2 Early Understanding of the Structure of Zirconium (Solution) Species: The Prevalence of the 'Zirconyl Ion'

Early studies on the nature of zirconium in aqueous solution were concerned with the 'zirconyl' theory of zirconium structure and bonding. The idea that the main zirconium species present in solution was ZrO<sup>2+</sup> prevailed in the times of the 19<sup>th</sup> and early 20<sup>th</sup> century chemists such as Berzelius, Hermann, Bailey and others. The belief at the time was that the majority of zirconium materials were derived from 'zirconyl,' 'dizirconyl,' and other similar species. It was taken as fact that compounds such as zirconyl chloride, zirconyl sulphate and other products from the hydrolysis of the Zr<sup>4+</sup> ion containing one or maybe two equivalents of acid per Zr atom were sufficiently understood with their formulae well established. The theory however was still disputed in the literature and it soon came to pass that there was no reliable and justifiable proof of this idea.

For the most part, studies of aqueous zirconium have focused on chloride, and to a lesser extent, sulfate solutions. It was seen that when dissolved in water, zirconium tetrachloride gave an extractable compound that always featured approximately two chlorine atoms per zirconium atom. This caught the attention of a number of workers, such as Berzelius, who first reported this phenomenon. He did not give his material, which could be extracted by repeatedly concentrating the solution or treating with concentrated HCl, a definite formula, but saw that this basic chloride had a Zr:Cl ratio in the range of 1:1.6 to 1:1.9. It was also seen to give a ready loss of water and HCl, alluding to its composition. In 1844 Hermann announced the existence of zirconyl chloride, to which he ascribed the possible formulae ZrOCl<sub>2</sub>.9H<sub>2</sub>O and Zr(OH)<sub>2</sub>Cl<sub>2</sub>.8H<sub>2</sub>O, though this was based entirely on the Zr:Cl ratio and not upon the knowledge that the material may release water and HCl. In two following papers Hermann established the use of the zirconyl formula for basic zirconium chloride, based on the same reasoning. Not long after, Endemann isolated a monochloride to which he gave the formula Zr<sub>2</sub>O<sub>3</sub>Cl<sub>2</sub>·xH<sub>2</sub>O. Paykyll<sup>6,7</sup> and Bailey<sup>8,9</sup> also assigned the zirconyl structure to

the basic chlorides, and extended the application to other basic and complex zirconium compounds.

Developments of the zirconyl theory were still forthcoming; in the early 1900's Ruer published a number of papers describing electromigration of the metal in chloride solutions, <sup>10</sup>-<sup>12</sup> noting that zirconium has a preference to migrate to the cathode, indicative of positively charged species and something which had already been noted by Becquerel in 1831.<sup>13</sup> Ruer considered that Zr ions in chloride had the zirconyl ion structure, along with the dizirconyl structure. In measuring the electrical conductivity of a zirconium dichloride solution he found that hydrolysis increases with time and is much more extensive at higher temperatures. 10, 11 This was later repeated by Venable and Jackson who demonstrated the dependence of hydrolysis of on the concentration of the initial solution, specifically that hydrolysis increases with dilution, for both chloride and sulphate solutions. <sup>14</sup> Ruer also tried a repeated evaporation of a dilute aqueous solution of zirconium dichloride and obtained gelatinous precipitates which he described as having the composition (ZrO)<sub>5</sub>(OH)<sub>8</sub>Cl<sub>2</sub>·xH<sub>2</sub>O and Zr<sub>10</sub>O<sub>19</sub>Cl<sub>2</sub>·xH<sub>2</sub>O.<sup>15</sup>, <sup>16</sup> He believed these 'metazirconyl chlorides' to be derived from 'metazirconic acid' or ZrO(OH)<sub>2</sub>, again having the zirconyl structure. These materials were particularly stable but could be converted to normal zirconyl chloride by boiling in concentrated HCl. Over 40 years later Blumenthal still put forward Ruer's ideas as solid evidence for the zirconyl theory of zirconium compounds. 17-19 Ruer's work on sulfate solutions 12, 20 drew a different conclusion, which was that zirconium is seen to migrate to the anode, indicative of negatively charged species. He attributed this to the presence of a [ZrO(SO<sub>4</sub>)<sub>2</sub>]<sup>2-</sup> complex ion. Alongside Ruer, Chauvanet was another who gave great weight to the zirconyl theory. In carrying out conductimetric titrations of aqueous solutions of zirconium salts he produced titration curves that had a degree of curvature, unlike the straight lines seen with acid-base titrations. Drawing tangents at the end of the curve intersected at a point corresponding to around 2 equivalents of alkali, which he considered convincing proof of the existence of the zirconyl ion.<sup>21</sup> He also conducted cryoscopic measurements on neutral and basic nitrate solutions and neutral sulfate solutions that came to the same conclusion.<sup>22-24</sup>

Meanwhile, other workers were beginning to concentrate on the sol or colloid and potentially gelatinous properties exhibited by aqueous zirconium solutions. In 1898 Venable and Baskerville made possibly the earliest reference to this, when they comment on obtaining a gelatinous 'hydrogele' from a zirconium oxybromide solution. This is suggestive of extensive polymerisation of zirconium taking place in aqueous solution. They also noted the propensity for variation in the formulae assigned to such compounds, as the method of preparation is seen to have a great influence on the number of waters of hydration that remain associated with the material.<sup>25</sup> Venable was also a strong proponent of the zirconyl theory and promoted the idea in his 1924 book reviewing zirconium and its compounds. <sup>26</sup> The peptisation of zirconium hydroxide by water was seen by Müller and others to occur readily, resulting in a clear colloid system, <sup>27</sup> building on the previous observation by van Bemmelen that zirconium hydroxide does not form hydrates of any definite composition.<sup>28</sup> This is somewhat suggestive of amorphous material, as noted by Haber who reported detecting no crystalline structure in freshly precipitated zirconium hydroxide.<sup>29</sup> Bohm and Niclassen also came to the same conclusion.<sup>30</sup> Biltz and Hauser reported that peptisation of the hydroxide by nitrate and sulphate solutions produced a particularly stable product, that retains sol-like properties for an extended period of time without conversion to the basic zirconium nitrate or sulfate. 31, 32 It is also seen that these materials are sensitive to the action of electrolyte salts such as KCl and KBr which can effect precipitation of zirconium sols.<sup>33-35</sup> Hydrolysis of zirconium extensive enough to show apparent polymerisation is later studied by Adolf and Pauli, who from freezing point studies see that the extent of hydrolysis of zirconyl chloride with time is irregular, and that after an equilibrium period of around 10 days the degree of hydrolysis reaches 35-50%. They conclude that only polymer species of low molecular weight are formed in strongly acidic media.<sup>36</sup>

Not everyone was so convinced by the zirconyl theory however, firstly Kulka, who argued that zirconium dichloride could be described by a formula that does not include the zirconyl oxygen atom.<sup>37</sup> A study of precipitation of zirconium hydroxides by Britton closed with the idea that zirconium chloride and sulfate solutions are composed of highly dispersed

basic particles and hydrolysed acid. He produced no evidence for the existence of the zirconyl ZrO<sup>2+</sup> species. He repeated Chauvanet's work from 1920<sup>21</sup> and found that his statement about the zirconyl ion was incorrect.<sup>38</sup> According to Britton, the mean composition of zirconium chloride in solution changes during an electrometric titration, due to the basic chlorides not containing zirconyl groups and that the quantity of hydroxyl groups attached to the zirconium increases continuously with pH. Zirconium tetrachloride, on dissolution in water to give a 0.1M solution, undergoes 58% hydrolysis, while the basic chloride with a Zr:Cl ratio of 1:1.737 in 0.01M solution is 54% hydrolysed. One of the hydrolysis products is a chloride of empirical formula Zr(OH)<sub>3.5</sub>Cl<sub>0.5</sub>. Britton claimed that this chloride is responsible for the inflection on Chauvanet's curve, taken to indicate existence of ZrO<sup>2+</sup>. Hence from this and the results of the same experiment with zirconium sulfate, Britton rejected the idea of the zirconyl ion. He did though confirm Chauvanet's observation of a highly hydrolysed sulfate with a Zr:SO<sub>4</sub><sup>2-</sup> ratio of 1:0.5. He focussed some of his work on the colloidal nature of solutions of zirconium salts and showed that the process of precipitation from zirconium solutions involves the formation of a colloid that subsequently coagulates. In the majority of precipitations the colloidal solution stage is so rapidly passed that it is not observed. He also interrogated the work of Adolf and Pauli. He concluded that the degree of hydrolysis appears to be a function of particle size (from relating that to the solution appearances – degree of opalescence) and as such the smaller amounts of hydrolysis in the clear solutions of Adolf and Pauli must have been due to the presence of particles 'which had been rendered small by the solution effect of the free acid.' He noted that the degree of dispersion of colloid basic chloride solutions is dependent on the amount of acid present. Colloidal solutions of basic chloride in which some free acid is present tend to become clear on standing, and he attributed this to the tendency of the particles to 'pass into solution.' With this idea he questioned the observations of Rodd, who reported 'multiple' hydrolyses of zirconyl chloride that forms more complex species such as Zr<sub>5</sub>O<sub>8</sub>Cl<sub>4</sub>.xH<sub>2</sub>O.<sup>39</sup> Rodd saw that when the solution became more acidic due to 'separation' of the basic chloride, crystals of ordinary ZrOCl<sub>2</sub>.H<sub>2</sub>O began to form. Britton however said that he must have obtained his complex salts by using a concentration of hydrochloric acid much less than that required for the crystallisation of the usual ZrOCl<sub>2</sub>·8H<sub>2</sub>O, and thus obtained a substance with nearly twice the concentration of hydroxide as that shown to exist in the solution during the second part of the titration with NaOH, Zr(OH)<sub>3.2</sub>Cl<sub>0.8</sub>. Britton obtained Zr(OH)<sub>3.5</sub>Cl<sub>0.5</sub>.

### 1.3 A Modern Understanding of the Structure of Zirconium Species in Aqueous Solution: The Discovery of the Zirconium Tetramer

In 1956 Abraham Clearfield and Philip Vaughan noted that the complex aqueous chemistry of zirconium was still poorly understood. 40 At the time zirconium(IV) ions in aqueous solution were known to undergo hydrolysis (due to the small, charge dense nature of the Zr<sup>4+</sup> ion), polymerisation and complex formation with anions. They referenced a number of works that show that there was still disagreement over the extent of polymerisation in these solutions. Hoping to shed some light on this problem, they carried out the first crystallographic study of any of the zirconyl oxyhalides, specifically the chloride and bromide octahydrates, ZrOX<sub>2</sub>·8H<sub>2</sub>O (the chloride being arguably the most widely used precursor for zirconium solutions). Their X-ray diffraction experiment allowed them to deduce the atomic positions in ZrOCl<sub>2</sub>·8H<sub>2</sub>O and ZrOBr<sub>2</sub>·8H<sub>2</sub>O and conclude that they both are of tetragonal unit cells and consist of a complex in which four zirconium ions sit at the corners of a slightly distorted square and are linked along each edge by two bridging OH groups, one above and one below the plane of the complex (Fig. 1.1). Each zirconium has a further four bound water molecules giving a distorted square antiprism at each Zr site. Zirconium-halogen bonds are not present in the structure – remaining water molecules and the chloride ions form a matrix holding the complexes together. They posed the question of whether this [Zr<sub>4</sub>(OH)<sub>8</sub>·16H<sub>2</sub>O]<sup>8+</sup> species was present in aqueous solution and thought it favourable. In 1967 Thomas Mak further refined the crystal structure of the chloride octahydrate with new experimental data. 41 He confirmed the existence of the tetranuclear [Zr<sub>4</sub>(OH)<sub>8</sub>(H<sub>2</sub>O)<sub>16</sub>]<sup>8+</sup> complex, however finding that each zirconium site is better described as dodecahedral. He more convincingly explained the argument for bridging OH groups over bridging water molecules on a basis of bond lengths and relative stabilities, and showed that the chloride ions sit in both four and five-coordinate positions, with the O atoms of additional water molecules being three-coordinate – both having much more pronounced thermal motions. For Clearfield and Vaughan's study only the Zr positions were found with any degree of certainty. Mak gave new bond lengths of Zr-OH (bridging) =  $2.142 \pm 0.019$  Å and Zr-OH<sub>2</sub> (terminal) =  $2.272 \pm 0.032$  Å, and cell parameters of  $a = 17.11 \pm 0.02$  Å and  $c = 7.71 \pm 0.01$  Å.

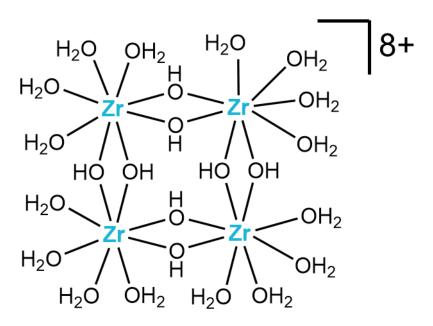


**Figure 1.1** A schematic of the zirconium tetramer, first described by Clearfield and Vaughan. 40

X-ray scattering experiments by Muha and Vaughan in 1960 produced strong evidence that the zirconium tetramer *was* the dominant species in solution across a range of concentrations, for zirconium and hafnium chloride and bromide solutions. They proposed a structure like that found in the crystalline solid studies previously.<sup>42</sup> They noted that their data for the zirconium solutions is not as good as for those of hafnium, and the differences led them to suggest a greater degree of polymerisation for the zirconium solutions. This they said might be seen in the form of additional X-ray scattering at low angles. Bromide was also found to

be more weakly bound to the tetramers compared to chloride, as evidenced by its larger thermal parameter.

In reviewing the preceding literature at the time, and in light of the studies described above, Aberg observed that the predominant species resulting from hydrolysis in aqueous zirconium solutions are polynuclear (of the tetramer type)<sup>43</sup> even in very dilute solutions of high acidity, for complexes where the complexing anions (Cl-, Br-, ClO<sub>4</sub>-) are in excess by 2:1 compared to the zirconium. At other stages of hydrolysis however little was known about the species present, resulting in her study involving a wider range of anion/Zr molar ratios (X/Zr = 1,2 for Cl, Br and  $ClO_4/Zr = 1.7$  to 4.3). At X/Zr = 1, 'higher' complexes than tetramers are suggested to predominate. For the halide solutions, the data suggests that because of the high charge of the Zr<sub>4</sub> complex it is reasonably likely that halide ions are present in a second coordination sphere outside the tetramer, held in place by electrostatic forces; it is unlikely that these ions enter the first coordination sphere in solution. These M-X interactions were seen to be over a longer range for Br than for Cl. Data for the perchlorate solutions supported the same structural models as for the halide solutions. From comparison of radial distribution functions generated from experimental X-ray scattering curves to those produced with a theoretical model, for halide solutions found to be of  $n_{HO} = 3$  ( $n_{HO}$  being the average number of HO groups per M atom) and those of  $n_{HO} = 2$  solutions, a structural change is apparent (when the degree of hydrolysis has increased). Also, the more hydrolysed solutions contain much larger species. It was seen that for these aggregates, the first coordination sphere of O around Zr is unchanged, suggestive of the same tetramer structures, on a local level. Radial distribution peaks were seen to broaden and increase in position; more distinct Zr-Zr distances are measured. In addition there was no clear indication of any coordination of halide to Zr in the second coordination sphere.

Polymerisation via hydrolysis in solutions of zirconium(IV) is known to take place with solution aging, heating or reduction of acidity, leading to formation of an amorphous and gelatinous hydrous oxide. Clearfield proposed a probable mechanism for the hydrolytic polymerisation of the  $[Zr_4(OH)_8(H_2O)_{16}]^{8+}$  species, which proceeds by the formation of double

OH bridges between tetramers.<sup>44</sup> An irregular polymerisation is said to occur upon addition of OH to a solution of such species, but a more ordered structure is produced by refluxing or boiling the zirconium solution. Even with an increase in acidity caused by boiling, some polymerisation of the tetramer in solution still occurs at low pH values. Addition of base results in displacement of some coordinated water by hydroxyl groups. When sufficient groups are present then condensation to form hydoxy bridges occurs between individual tetramers; given the multiplicity of these sites, polymer growth may proceed in different directions simultaneously, which tends to produce a random structure. Two-dimensional sheets may come together to form three-dimensional particles by further olation. X-ray and neutron scattering data supported the existence of the two-dimensional particles, which have a structure closely resembling that of tetragonal zirconia.<sup>45</sup> Returning to Aberg's work,<sup>43</sup> the scattering curves of more hydrolysed halide solutions of n<sub>HO</sub> = 3 for example may be explained by assuming the presence of randomly formed polymers as per Clearfield's mechanism. A possible scheme for this is given in Equation 1.1:

$$4nZr(OH)_4 + nxH_2O + 4nyH_3O^+ \rightleftharpoons [Zr_4O_x(OH)_{16-2x-4y}(H_3O)_{2x+8y}]_n^{4y+}$$
 (Equation 1.1)

The factor x takes into account the possible formation of an -O- bridge and a coordinated water molecule instead of a double -OH- bridge in and or between some tetramers. For the perchlorate solutions however, even the most hydrolysed of these showed no tendency towards polymer formation, despite  $n_{HO} > 2$ ; data analysis showed this to be the same case as for the solutions with a lower degree of hydrolysis.

Compared to chloride, the sulfate anion is a much stronger complexing agent and so the aqueous chemistry of sulfate solutions of zirconium is markedly different. In sulfate solutions SO<sub>4</sub><sup>2</sup>- may readily displace OH<sup>-</sup> groups in a monodentate, bridging and/or chelating fashion. The resulting zirconium sulfates can be categorised as acid salts, neutral and low basicity salts and highly basic salts. Chelation of zirconium by sulfate only occurs in the acid salts; in strongly acidic conditions these form only low molecular weight species due to the acid present and the strong chelation preventing polymerisation.

### 1.4 The Chemistry of Nitrate-Based Aqueous Solutions of Zirconium

The majority of the work in the literature regarding the aqueous chemistry of zirconium focuses on chloride or sulfate solutions of zirconium. However comparably little exists for nitrate solutions. No structure has been explicitly identified in solutions of zirconyl nitrate, Zr(OH)<sub>2</sub>(NO<sub>3</sub>)<sub>2</sub>, though it would seem apt to assume that the tetramer form or a modified version of this predominates. In the solid salt, powder X-ray diffraction identifies linear chains of cations that are held together by hydrogen bonding and free nitrate groups, featuring similar structural motifs to the tetramer – zirconium centres linked by hydroxy bridges (Fig. 1.2).<sup>46</sup> The zirconium atoms are eightfold coordinated by four OH groups, two water molecules and one bidentate nitrate group. Additional water molecules and nitrate groups are found between the chains, which are of the formula [Zr(OH)<sub>2</sub>(NO<sub>3</sub>)]<sub>n</sub><sup>n+</sup>. <sup>14</sup>N NMR measurements on zirconyl nitrate solution suggest that half of the nitrate anions are fully aquated, thus available for fast exchange reactions, whilst the other half remain associated with the Zr cations such that their NMR signal is not detected.<sup>47</sup>

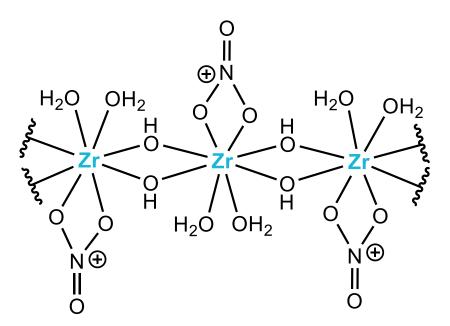


**Figure 1.2** A schematic of a section of the zirconium chains as found in solid zirconium nitrate. <sup>46</sup> Individual chains are held together in the solid state *via* further nitrate and water groups.

Woodhead reported in his US patent a novel zirconium compound with an approximately 1:1 nitrate to zirconia ratio, made by reaction of zirconium hydroxide or carbonate with nitric acid to make a water-based sol.<sup>48</sup> He claimed the creation of a material of empirical formula [Zr<sub>4</sub>(OH)<sub>12</sub>(NO<sub>3</sub>)<sub>2</sub>(H<sub>2</sub>O)<sub>4</sub>](NO<sub>3</sub>)<sub>2</sub>.2H<sub>2</sub>O, containing covalent nitro groups and ionic nitrate groups, consistent with the later NMR study discussed above.<sup>47</sup> His synthesis involved about half of the used zirconium hydroxide being added to the nitric acid and the remainder slurried in water; the two portions were then mixed with stirring over a period of 15 minutes and maintained at 70 °C for 1 hour.

More recently, Southon *et al.* have reported a synthesis of zirconium nitrate solutions and sols, using a similar method. <sup>49-51</sup> Their aqueous zirconium nitrate solutions were made by dissolving zirconium carbonate in concentrated nitric acid, and sols made by adding a further amount of zirconium nitrate, slurried with water, to zirconium nitrate solution. The mixtures were stirred and heated at 70 °C for several hours, forming a nearly transparent sol. Varying the nitrate to zirconium ratio was carried out by adjusting the amount of additional carbonate used. They recalled that increasing the pH of a zirconium salt solution leads to further hydrolysis, and rapid addition of strong base causes zirconium hydroxide to precipitate from solution. This two-step synthesis they noted, like that first reported by Woodhead, results in a more controlled reaction, producing a stable colloidal suspension whereby the added base is substituted by additional zirconium carbonate, which decomposes in the already acidic solution. The decomposition of the added carbonate consumes acid, and promotes hydrolysis and polycondensation to form colloidal particles. This method results in nano-sized particles, and no other anions are added to the system.

In their initial study,<sup>49</sup> Southon *et al.* reported that in the sols, Raman spectroscopy indicated that almost all of the nitrate present was fully aquated, with a small amount of nitrato or bound nitrate groups attached to the particles. Peaks attributed to oxide and hydroxide Zr-O bonds (< 700 cm<sup>-1</sup>) were also found in the spectra, but there was no match with peaks in the spectra of any crystalline structure. In addition, for their organic-route sol, further polymerisation was indicated by the increase in intensity of peaks assigned to Zr-OH-Zr

bridging bonds (445 and 615 cm<sup>-1</sup>) over a period of 3 months. They believed the structure of the material to be a largely amorphous polymeric network of Zr<sub>4</sub> tetrameric units as opposed to dense particles. They note the idea that the particles in the sols are stabilised by ions adsorbed onto the surface, in this case nitrato groups.

In the subsequent study, <sup>50</sup> Southon *et al.* investigated a series of zirconium nitrate solutions with a range of nitrate to zirconium ratios of 1:1 to 2:1. Dynamic light scattering (DLS) and <sup>14</sup>N NMR spectroscopy were used in addition to Raman spectroscopy. For the 2:1 solution, no light-scattering particles were observed by DLS. Although the results were to be treated with caution, for the 1:1 sol some light scattering was seen, with the majority of particles in the size range 3-6 nm. Most of their samples were found to contain a small fraction of 10-20 nm particles, accounting for up to 50% of the scattered light, but these were only less than 5% of the total solids volume. They were able to undertake a comprehensive analysis of the Raman spectra, with the help of computer modelling. Peaks above 650 cm<sup>-1</sup> were assigned to various nitrate groups, and two symmetries were identified; fully-aquated D<sub>3h</sub> nitrate groups unaffected by other nearby molecules, and C<sub>2v</sub> bidentate-coordinated nitrate ligands. In all samples only a small fraction of the nitrate groups were coordinated, and there was very little change in peak position or intensity upon changing the nitrate to zirconium ratio. The spectra clearly showed significant changes occurring in the short-range structure of the zirconium species during particle growth. For example, the peaks assigned to terminal-hydroxy groups (575 and 450 cm<sup>-1</sup>, broad symmetric Zr-OH stretch) become less intense as particles were formed, whilst the peaks assigned to Zr-O hydroxy-bridges (375, 420 and 520 cm<sup>-1</sup>) grew as the particles developed. These were strongly indicative of the condensation processes know to occur during particle growth, though weren't regarded as definitive assignments.

<sup>14</sup>N NMR spectra featured a single broad peak at 6 ppm for the 2:1 solution, whereas no peak was observed for the 1:1 sol. Upon approach of a nitrate anion to zirconium, the <sup>14</sup>N relaxation rate increases and its NMR signal broadens, becoming undetectable. This shows that all unassociated nitrate species in the original solution become associated with the zirconium species as the particles are formed, as they become increasingly invisible to NMR.

The combination of NMR and Raman spectroscopies reveals the behaviour of the nitrate anions in the zirconium solutions. Three states are identifiable; the solvated, unassociated  $D_{3h}$  species giving a strong Raman peak and NMR signal; the weakly associated  $D_{3h}$  species that give rise to a Raman peak but no NMR signal, likely separated by one or two layers of hydration; and the coordinated  $C_{2v}$  species that give a slightly shifted Raman peak and again no NMR signal. Conservation of symmetry for the variably-associated species suggests association is most likely to occur at the surface of particles, not within them. The small fraction of bidentate-coordinated nitrate was seen to remain roughly constant.

The lack of any light-scattering colloidal particles in the initial concentrated zirconium nitrate solution is suggestive of the presence of aquated, cationic species only. As zirconium carbonate is added to the synthesis mixture, this both produces more aquated zirconium species, and consumption of acid by the decomposing carbonate promotes further hydrolysis of existing zirconium species (Equation 1.2):

$$[Zr(OH^b)_2.H_2O]_n^{2n+} + nOH^- \rightleftharpoons [Zr(OH^b)_2(OH^t)]_n^{n+} + nH_2O$$
 (Equation 1.2)

This, Southon proposed, had the initial effect of increasing the number of terminal hydroxy groups (OH' in Equation 1.2), reducing the species charge. The less positively charged species can then interact more readily, with the terminal hydroxy groups condensing to form hydroxy bridges (OH<sup>b</sup> in Equation 1.2); a net conversion of terminal hydroxy groups and coordinated water molecules into hydroxy bridges. Condensation continues and small particles of zirconium hydroxide grow from solution. Incomplete hydrolysis results in some species retaining a degree of positive charge, which by like-charge repulsive effects prevents aggregation, making the sol more stable.

In their final paper on the topic,<sup>51</sup> Southon *et al.* extend their structure characterisation by including Extended X-ray Absorption Fine Structure (EXAFS) and Small-Angle X-ray Scattering (SAXS) measurements. The SAXS experiments revealed that the nitrate solutions scattered X-rays only very weakly, and the scattering curve was consistent with that of spherical particles best described by a radius of gyration of  $0.40 \pm 0.04$  nm and diameter 0.52

nm. These dimensions were seen to be very close to those reported for the zirconium tetramer in chloride solutions from previous SAXS experiments, suggesting that these species predominate in nitrate solutions also, and this is supported by the presence of bands for Zr-O vibrations of bridging hydroxyl groups in Raman spectra. The zirconium sols (following heat treatment of the solutions) were also seen to scatter X-rays weakly, and fitting of the scattering curves suggested simple plate-like particles, of dimensions  $2.8 \pm 0.4$  nm wide by  $0.5 \pm 0.1$  nm thick. Dilution of sol samples to reduce low-Q or low angle distortion arising from interparticle scattering in the relatively concentrated sols gave similar results to the original sol. Differences in the average particle 'size' between SAXS and Raman measurements was attributed to the presence of surface hydroxyl and nitrate groups and a layer of bound water. All of these are incorporated in the hydrodynamic diameter but do not contribute to the X-ray scattering due to minimal contrast between them and the surrounding water matrix.

In an attempt to further elucidate particle structure in the sols, EXAFS measurements were carried out on the corresponding gel material to probe the structure of this across short ranges. These results provided good evidence for the square arrangement of the zirconium atoms, and the presence of a small number of coordinated nitrate groups. Southon *et al.* proposed a short-range structural model in which zirconium atoms, joined by double hydroxyl bridges, are arranged in a two-dimensional square lattice, giving an ideal stoichiometry of Zr(OH)4. However the coordination numbers found were lower than expected, which could be explained by defects in the lattice, the edges of the sheet, and places where oxy bridges have replaced hydroxy bridges. From the size and shape data from the SAXS measurements it appeared that each individual particle is built up from a number of stacked sheets, along with any associated water and nitrate groups. The Raman spectra of sol and gel are seen to be very similar below 650 cm<sup>-1</sup> (above 650 cm<sup>-1</sup> the peaks are attributed to mostly nitrate anions), highlighting further the similarity in structures present.

### 1.5 The Use of Nitrate-Based Aqueous Solutions of Zirconium in Industry

The industry synthesis procedure for zirconium nitrate solutions differs from that employed by Woodhead and Southon yet uses the same basic precursors. Concentrated nitric acid is diluted with deionised water to give 20% HNO3 in solution, into which is added zirconium basic carbonate (ZBC). The amount of concentrated nitric acid initially used dictates the final Zr:NO<sub>3</sub> ratio in the product. Heating of the mixture to 60 °C aids complete dissolution and helps to drive off dissolved CO<sub>2</sub> that arises from decomposition of carbonate groups in the acidic solution. Organic additives (in this case mandelic acid) are then added, and additional deionised water added also, to give the correct percentage solids. The mixture is then heated to the chosen peak temperature followed by a dwell at temperature for the required time. The forcing conditions of this heat treatment period accelerates the growth and development of the particles in solution leading to more sol-like properties. Synthesis is complete after cooling to room temperature, and any water lost through evaporation is replaced. This process is attractive to industry as the basic precursor materials are inorganic and readily commercially available, and the method itself is water-based and straightforward. Thus resulting in simplicity, relative ease of scale-up, low cost and minimal environmental impact.

The interest in the use of nitrate as opposed to chloride-based solutions can be considered as being based upon the differing extent of interaction between these anions and the zirconium species in solution,<sup>47</sup> which is theorised to lead to more control over the rate and extent of particle growth (oligomerisation or hydrolysis) in solution. Despite a small amount of nitrate being able to coordinate directly to the zirconium in the solution species, the interaction of NO<sub>3</sub><sup>-</sup> anions with the growing particles is considered weaker than that for Cl<sup>-</sup>. In contrast, sulfate groups, SO<sub>4</sub><sup>2</sup>-, coordinate strongly to zirconium and may act as bridging ligands, as seen in the solid zirconium sulfates.<sup>52</sup> This weaker interaction of nitrate groups, arising from a more diffuse electron or charge density, should mean that the polymerisation of aqueous zirconium species is able to proceed more readily. The resulting oligomers will

have a degree of positive charge (also dependent on the extent of hydrolysis and number of coordinated nitrate groups) and so counter-anions will accumulate around them in an electric double-layer type arrangement. Thus the counter-ion 'barrier' around the particles in the case of the nitrate solution is more diffuse, allowing further interaction between oligomers to take place more easily leading to more pronounced particle growth. Also contributing to the weaker nature of the nitrate barrier sphere is its slightly larger anion size compared to chloride (0.189 nm versus 0.181 nm), and its non-spherical shape, which could affect the packing around the oligomers. In addition, the hydration energy of Cl<sup>-</sup> is greater than that of NO<sub>3</sub><sup>-</sup>, which would favour a stronger interaction with water and thus a less impenetrable hydration sphere.

Alternatively, considering that a small portion of added nitrate has been seen to end up directly coordinated to zirconium in the solution species, the shielding of zirconium particles (with respect to potential zirconium-zirconium interaction) by counter-anions would be expected to be reduced in the case of the nitrate solutions, as some of the positive charge of the zirconium species is neutralised (that would otherwise attract counter-ions). However, the end result is the same; more readily occurring particle growth. As a result of the ideas discussed, it would seem intuitive to assume then that varying the Zr:NO<sub>3</sub> ratio of the synthesis mixture would alter the extent of double layer formation, and ultimately the degree of particle growth.

The reaction of zirconium species during the hydrolysis process is thought to be further modified by the addition of other complexing agents, whereby the affinity for zirconium of these species 'blocks' more reactive zirconium sites, limiting species/particle growth.<sup>53</sup> The use of  $\alpha$ -hydroxy carboxylic acids, such as mandelic acid for instance (Fig 1.3), has been proposed by LMT as such an agent in a recent patent.<sup>54</sup> This patent describes the use of aqueous zirconium solutions or sols as precursors to zirconium oxides amongst other applications; covering solutions and sols modified by the presence of nitrate, acetate and/or chloride, and organic complexing agents featuring amine, organosulfate, sulfonate, hydroxyl, ether, or carboxylic acid functional groups. Mandelic acid is already known to have a strong affinity for zirconium, and zirconium mandelate finds use in the gravimetric determination of

zirconium and hafnium.<sup>55</sup> It has already been seen to have effects on the crystallinity, surface area, and other properties of the zirconia produced as a result of the decomposition of such zirconium carboxylates.<sup>56</sup>

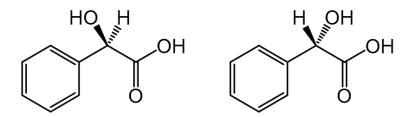


**Figure 1.3** Structures of the two enantiomeric forms of mandelic acid, C<sub>6</sub>H<sub>5</sub>CH(OH)CO<sub>2</sub>H; (R)- left, (S)- right.

### 1.6 Project Aims

Overall, this project is concerned with furthering the understanding of the species present in nitrate-based aqueous solutions of zirconium, both generally and in the specific case of the solutions studied here, synthesised by LMT's method (which is different to that used by Southon *et al.*<sup>49-51</sup> and Woodhead.<sup>48</sup>) It has been noted already that there is relatively little in the literature regarding such solutions, with only the work of Southon *et al.*, and one study utilising EXAFS spectroscopy from around the same time,<sup>57</sup> so far suggesting the presence of the zirconium tetramer in these solutions. Otherwise, solutions of zirconium containing chloride are the main focus of other authors' work, and the solutions studied tend to be relatively dilute; the solutions employed by LMT are much more highly concentrated with respect to zirconium.

More specific goals to be covered by this project, beneficial to both LMT and scientific curiosity, are outlined below:

• <u>Literature Review</u> "An in-depth look at the current understanding of the nature of zirconium species in aqueous solutions from initial investigation of these systems to the present day. To assess what experimental techniques are most relevant and the best sources of data to allow full characterisation of LMT solution precursors and final products."

- <u>Initial Benchmarking</u> "To investigate a set of zirconium solution types (e.g. oxychloride, oxynitrate and hydroxynitrate) with the most promising experimental techniques, and to include a degree of methodology development to tailor measurements to samples."
- Further Investigation "To identify a suitable in-house technique to be used at
  LMT for in-process analysis of solutions. To use the 'best' techniques to
  investigate a greater range of zirconium solutions (including aging effects for
  example)."
- Optimum Zirconium Species "To identify and theorise what the best zirconium solution species would be for continuing LMT's solution manufacturing process."
- Possible Later Goals "To publish pertinent results from the project and to look into patenting ideas of direct benefit to industry. Further study would be focussed on solution reproducibility and aging effects, and an initial investigation of powder properties of materials made from the zirconium solutions. Following this, scale-up of the most promising solutions, and final conclusions."

### 1.7 Bibliography

- 1. J. J. Berzelius, *Pogg. Ann.*, 1825, **4**, 117.
- 2. R. Hermann, J. Prakt. Chem., 1844, 31, 75.
- 3. R. Hermann, *Jahrb. Berz.*, 1866, 189.
- 4. R. Hermann, J. Prakt. Chem., 1866, 97, 321.
- 5. H. Endemann, J. Prakt. Chem., 1875, 11, 219.
- 6. S. Paykyll, *Ber.*, 1879, **12**, 1719.
- 7. S. Paykyll, *Ber.*, 1873, **6**, 1467.
- 8. G. H. Bailey, Chem. News, 1899, **60**, 8.
- 9. G. H. Bailey, *Proc. Ray. Soc.*, 1889, **46**, 74.
- 10. R. Ruer, Z. Anorg. Allg. Chem., 1904, 43, 282.
- 11. R. Ruer, Z. Anorg. Allg. Chem., 1904, 42, 94.
- 12. R. Ruer and M. Levin, Z. Anorg. Allg. Chem., 1904, **46**, 449.
- 13. A. G. Becquerel, Ann. Chim. Phys., 1831, 48, 337.
- 14. F. P. Venable and D. Jackson, J. Am. Chem. Soc., 1920, 42, 2531-2534.
- 15. R. Ruer, Z. Anorg. Allg. Chem., 1904, 43, 87.
- 16. R. Ruer, Z. Anorg. Allg. Chem., 1906, 46, 465.
- 17. W. B. Blumenthal, *J. Chem. Educ.*, 1949, **26**, 472-475.
- 18. W. B. Blumenthal, *Ind. Eng. Chem.*, 1954, **46**, 528-539.
- W. B. Blumenthal, *The Chemical Behaviour of Zirconium*, Van Nostrand, Princeton,
   N.J., 1958.
- 20. R. Ruer, Z. Anorg. Allg. Chem., 1904, 43, 85.
- 21. E. Chauvanet, Ann. Chim. Phys., 1920, 13, 82.
- 22. E. Chauvanet and H. Gueylard, *Compt. Rend.*, 1918, **167**, 201.
- 23. E. Chauvanet and L. Nicolle, *Compt. Rend.*, 1918, **166**, 781.
- 24. E. Chauvanet and L. Nicolle, *Compt. Rend.*, 1918, **166**, 821.
- 25. F. P. Venable and C. Baskerville, *J. Am. Chem. Soc.*, 1898, **20**, 321-329.

- F. P. Venable, *Zirconium and its Compounds*, The Chemical Catalog Company, Inc., New York, 1922.
- 27. A. Muller, Z. Anorg. Allg. Chem., 1907, **52**, 316.
- 28. J. V. Bemmelen, Z. Anorg. Allg. Chem., 1906, **49**, 125.
- 29. F. Haber, *Ber.*, 1922, **55**, 1717.
- 30. J. Bohm and H. Niclassen, Z. Anorg. Chem., 1924, **132**, 1.
- 31. W. Biltz, Ber., 1904, 37, 1095.
- 32. O. Hauser, Z. Anorg. Allg. Chem., 1907, **54**, 208.
- 33. A. Posenheim and T. Hertzmann, *Ber.*, 1907, **40**, 813.
- 34. B. Szilard, J. Chem. Phys., 1908, 5, 488-494.
- 35. B. Szilard, J. Chem. Phys., 1908, 5, 640.
- 36. M. Adolf and W. Pauli, *Kolloid-Z.*, 1921, **29**, 173-184.
- 37. O. Kulka, PhD thesis, University of Bern, 1902.
- 38. H. T. S. Britton, J. Chem. Soc., 1925, 127, 2110-2120.
- 39. E. H. Rodd, J. Chem. Soc., 1917, **111**, 396-407.
- 40. A. Clearfield and P. A. Vaughan, *Acta Cryst.*, 1956, **9**, 555-558.
- 41. T. C. W. Mak, Can. J. Chem., 1968, 46, 3491-3497.
- 42. G. M. Muha and P. A. Vaughan, J. Chem. Phys., 1960, 33, 194-199.
- 43. M. Aberg, Acta Chem. Scand. B, 1977, **31**, 171-181.
- 44. A. Clearfield, G. P. D. Serrette and A. H. Khazi-Syed, *Catal. Today*, 1994, **20**, 295-312.
- 45. J. Livage, K. Doi and C. Mazieres, J. Am. Chem. Soc., 1968, **51**, 349-353.
- 46. P. Benard, M. Louer and D. Louer, *J. Solid State Chem.*, 1991, **94**, 27-35.
- J. Livage, M. Chatry, M. Henry and F. Taulelle, *Mat. Res. Soc. Symp. Proc.*, 1992,
   271, 201-212.
- 48. J. L. Woodhead, US Pat., Aqueous sol and gel of zirconium compounds, No. 3 645 910, 1966.

- 49. P. D. Southon, J. R. Bartlett, J. L. Woolfrey and M. G. Stevens, *Ceram. Trans.*, 1998, 81, 75-80.
- 50. P. D. Southon, J. R. Bartlett, K. S. Finnie, J. L. Woolfrey, B. Ben-Nissan and G. S. K. Kannangara, *J. Aust. Ceram. Soc.*, 1999, **35**, 7-12.
- P. D. Southon, J. R. Bartlett, J. L. Woolfrey and B. Ben-Nissan, *Chem. Mater.*, 2002,
   14, 4313-4319.
- 52. T. E. MacDermott, Coord. Chem. Rev., 1973, 11, 1-20.
- 53. D. A. Scapens, personal communication, LMT internal technical document on new manufacturing process.
- 54. D. A. Scapens, US Pat., Structured zirconium solutions, No. 10 501 332, 2019.
- J. M. Crosland, E. K. Corlett, D. Scapens, N. Guillou, S. P. Brown and R. I. Walton,
   Chem. Commun., 2020, 56, 10159-10162.
- 56. M. H. Al-Hazmi, Y. Choi and A. W. Apblett, *Adv. Phys. Chem.*, 2014, **2014**, 1-8.
- 57. V. V. Kanazhevskii, B. N. Novgorodov, V. P. Shmachkova, N. S. Kotsarenko, V. V. Kriventsov and D. I. Kochubey, *Mendeleev Commun.*, 2001, **11**, 211-212.

### Chapter 2:

### Synthesis of Poly-Zirconium Nitrate (PZN) Aqueous Solutions of Zirconium

#### 2.1 Experimental Setup

In order to make an effective study of the zirconium solutions as employed by industry, an experimental setup mimicking the industrial synthesis route as closely as possible is essential. On site, production of commercial solutions starts at the research and development level and is gradually scaled up *via* the use of pilot plant facilities until final decisions are made regarding process parameters such as level of heating, stirring, exact quantities and ratios of solid and liquid reagents, at which point production of solutions can take place in large quantities on plant.

It is straightforward to attempt to replicate these solutions on the laboratory scale using a conventional hotplate and glass beaker setup with magnetic stirring. However, uniform heating and stirring of the solution mixture is not guaranteed when the application of heat is only towards one surface of the beaker and stirring is managed by a magnetic flea. Heat losses from an open beaker and loss of water vapour also would otherwise result in energy inefficiency and a change in the composition (relative concentrations of solution components) of the solutions. This could be overcome to some extent by the use of a round-bottomed flask and reflux condenser, but stirring would still be limited to magnetic methods which have limited power. Powerful constant stirring of solutions was deemed essential as this would help to negate any issues arising from gelation of the zirconium solutions *via* hydrolysis, exacerbated by non-uniform heating of the solution.

After an assessment of other commercially available alternatives, the Reactor-Ready<sup>TM</sup> product made by Radleys was deemed the most suitable. This takes the form of a double-walled glass reaction vessel through which hot oil may be circulated, ensuring that heat may be applied totally surrounding the entire volume of the solution. Oil heating is

achieved with a Huber Ministat cooling and heating oil bath circulator with a Pilot ONE controller enabling programming of fully automated heating and cooling profiles. Stirring is realised by a mains-powered overhead stirrer with an anchor-shaped stirring paddle reaching to the bottom of the vessel. The Teflon®-coated temperature probe that measured the temperature of the solution was inserted as far as possible into the vessel without clashing with the stirrer paddle. As a result the synthesis method had to be modified slightly from the original industry procedure to ensure that the tip of the temperature probe was always submerged. The internal volume of the glass vessel was nominally 250 cm<sup>3</sup>, however no issues were found when total solution volumes of ~300 cm<sup>3</sup> were used. Despite the top level of the solution being raised due to the vortex induced by stirring, the entire volume of solution was still completely surrounded by the hot circulating oil. Addition of liquid and solid reagents to the reactor was via the 'B'-type screw-stoppered opening in the top cover of the vessel, with one of the further openings used to mount a water-cooled condenser to minimise loss of water vapour. Extraction of solution after synthesis was via the tap opening in the bottom of the vessel. Following synthesis zirconium solutions were stored in polypropylene plastic bottles once the solution had completely cooled to room temperature. Sampling of small volumes of solution from the reactor during synthesis could be carried out through the same opening as used to add the reagents. A plastic syringe extended with the shaft of a standard disposable plastic pipette was found to effectively draw the solution out. A picture of the setup, located in a standard laboratory fume cupboard, can be seen in Figure 2.1.



**Figure 2.1** The Radleys Reactor-Ready<sup>TM</sup> used to produce the aqueous zirconium solutions studied in this project. Not pictured is the water-cooled condenser. The oil heating and circulating equipment is positioned sideways behind the reactor vessel stand, connected to the vessel via two pairs of insulated hoses. The top of the temperature probe is just visible behind the upper rotating parts of the overhead stirrer.

### 2.2 Synthesis Procedure

All of the PZN syntheses carried out in this project were via the same experimental method as described below. The only changes between synthesis runs were the relative amounts of nitric acid, zirconium basic carbonate, mandelic acid and deionised water where applicable, and the maximum heat treatment temperature applied. 30 wt% aqueous nitric acid, zirconium basic carbonate and mandelic acid were supplied by LMT. The deionised water used was provided by a Purite<sup>TM</sup> water purification system outputting water of resistivity up to 18 M $\Omega$ ·cm. All reagents were measured out by mass on a 4 decimal point balance. The total time taken for the entire synthesis procedure, including portioning and addition of reagents to the reactor, and the running of the temperature control program was up to 5 – 6 hours. A typical temperature profile as seen during synthesis is displayed in Figure 2.2. The different amounts of each of the reagents used for the solutions studied in this project may be found in the Appendices (Table A.1). This procedure resulted in solutions of concentration ~1.35 M with respect to zirconium. The general procedure was as follows:

- 1. To the reactor was added the appropriate amount of nitric acid which was diluted with deionised water to give a nitric acid concentration of up to 20 wt%. The amount of nitric acid used was varied to give the desired final Zr:NO<sub>3</sub> molar ratio.
  Depending on the amount of nitric acid used, additional deionised water was sometimes required to ensure that the tip of the temperature probe was always submerged. Stirring of the solution mix was started from the beginning of this step onwards and the oil heater was set manually to a temperature of 25 °C.
- 2. The temperature program controlling the Huber oil heater was started, and the oil was heated to the first temperature set-point of 60 °C to ensure complete dissolution of the zirconium basic carbonate. Upon reaching 60 °C, the temperature was constant for up to 20 minutes. From the start of heating up to 60 °C, the zirconium basic carbonate was added to the reactor in small portions to avoid excessive

- effervescence. Upon dissolution the acidic conditions result in the generation of carbon dioxide gas.
- Once all of the zirconium basic carbonate was fully dissolved and by the end of the
  first temperature dwell, the mandelic acid organic complexing agent was added in
  the required amount to give the desired final mol% of solution mandelic acid
  relative to zirconium.
- 4. The remaining deionised water was gradually added to the reactor vessel to result in the correct final volume and solution solids content. Until this water was added, it was heated on a hotplate at 60 °C to avoid a sudden drop in temperature of the reactor contents when the water was added. The aim was a zirconium content equivalent to 14% ZrO<sub>2</sub> by mass. In practice, some of this water (up to ~40g) was added early according to Step 1.
- 5. The temperature control program was allowed to run to completion. This involved a further ramp in temperature up to the maximum heat treatment temperature, a dwell at this temperature for 2 hours, and a ramp down in temperature to cool the zirconium solution down to room temperature. In order to heat the reactor contents to the highest temperature used of 94 °C, the oil circulating through the walls of the glass vessel was heated to up to ~110 °C.

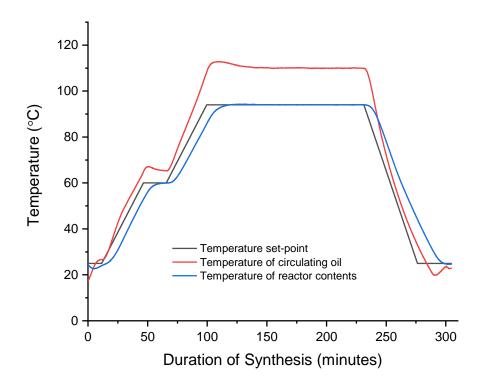


**Figure 2.2** An example temperature profile from a PZN synthesis reaching a maximum solution heat treatment temperature of 94 °C. The duration of synthesis refers to the elapsed time since the start of the temperature control program. The temperature of the reactor contents is that as measured by the probe submerged into the solution; the oil temperature is that as it exits the heating and circulating equipment.

# **Chapter 3:**

# Characterisation of Aqueous Zirconium Solutions by Vibrational Spectroscopy

#### 3.1 Introduction

This chapter describes work carried out to investigate the properties of aqueous nitrate-based solutions of zirconium (PZN – polymerised zirconium nitrate) as made by LMT via two vibrational spectroscopy methods: Raman spectroscopy and (Fourier-transform) infrared spectroscopy. These methods can give an insight into the types of chemical bonds or functional groups present in a given sample, with measured spectra acting like a chemical 'fingerprint' of a material.<sup>1</sup> Both techniques are suitable for solid and aqueous samples alike, and so were quickly identified as being relevant characterisation techniques for this project. Results from infrared spectroscopy are presented here from an initial benchmarking of solutions, and from later measurements upon a wider range of solution compositions. Raman results from the same initial benchmarking are included and from a more in-depth study of zirconium solutions including variation of solution composition, and temperature of heat treatment during synthesis. The results of the Raman measurements in particular were found to be extremely informative, with the benefit of spectra being able to be both easily measured and interpreted. An additional objective of this project was to identify any characterisation methods that might be suitable for in-house testing in industry, during the manufacturing process or for product development, so this work also aimed to fulfil this.

#### 3.2 Literature Overview

In the course of searching and reviewing the literature regarding the aqueous solution chemistry of zirconium in various forms, a modest number of papers were found that employed Raman spectroscopy as the main or complementary characterisation technique. Reports of the use of infrared spectroscopy in characterising such aqueous solutions of zirconium however are particularly sparse.

In general, the majority of studies carried out have investigated zirconium species in so-called 'non-coordinating media' such as nitrate, perchlorate and chloride solutions. One of the earliest papers found, produced by Baglin and Breger in the 1970s, presented a study of aqueous zirconium species in perchlorate and sulfate solution, and reported for the first time direct spectroscopic evidence *via* Raman for the structure of a strongly coordinated sulfate species in aqueous solution.<sup>2</sup> The authors made useful assignments for bands arising from Zr-O vibrations, partly based on previous work.<sup>3</sup> They note finding no evidence to suggest that there is a single preferred species based upon Zr(SO<sub>4</sub>)<sub>2</sub> present in sulfate solutions that is stable across a range of conditions, as previously observed by Clearfield.<sup>4</sup> They also could not find any evidence for the elusive ZrO<sup>2+</sup> zirconyl ion<sup>5</sup> nor that any complexation between zirconium and perchlorate (ClO<sub>4</sub>) takes place in solution.

Tosan *et al.* reported investigations into aqueous zirconium solutions submitted to a reflux at 105 °C for various amounts of time, 6 a method not too dissimilar to that used to make the PZN solutions studied in this project. Also added to the solutions studied were amounts of NaOH and HCl. They reported the presence of bands in Raman spectra thought to be characteristic of the zirconium tetramer, and that these spectra do not change even after 120 hours of reflux. For other solutions, hydrolysed to different extents by differing amounts of NaOH present, the evolution and disappearance of a number of bands were followed over time with further reflux. Although band positions were reported, the authors do not make explicit assignments to the origins of each. A further paper by Tosan *et al.* introduced carboxylic acids into similar solutions aged to varying extents, 7 and discussed the evolution of Raman bands

with time of solution species in the presence of acetic and formic acids. They noted the disappearance of an initial band indicative of the zirconium tetramer, and the formation of new bands characteristic of zirconium carboxylate complexes. In experimenting with deuteration of the studied solutions, isotopic shifts in peak positions by 10-15 cm<sup>-1</sup> for the Raman bands seen signified that they were seeing connectivity via double hydroxy groups (-(OH)<sub>2</sub>-) between zirconium, not oxy (-O-) or water (-(OH<sub>2</sub>)-) groups (the latter of which would have seen a bigger shift of ~25 cm<sup>-1</sup>). The same effect is seen when deuterating the free zirconium tetramer.<sup>8, 9</sup> Based on their observations from both Raman and infrared measurements (the discussion of infrared spectra was only concerned with bands of the carboxylate ligands themselves, not Zr-O features) they concluded that the coordination of carboxylates to zirconium as bidentate ligands results in starting species that are subject to a progressive structural rearrangement, and that the species generally present in such zirconium solutions are likely distorted tetramers with chelating bidentate carboxylate ions.

At a similar time Aberg and Glaser reported an <sup>17</sup>O and <sup>1</sup>H NMR study of solutions of zirconium perchlorate that included characterisation of solutions with Raman spectroscopy. <sup>10</sup> They reported on a number of Raman bands for a perchlorate solution and compared these to those seen for a chloride solution and solid zirconium oxychloride, though did not make specific band assignments.

The only papers found that report Raman spectroscopy measurements on aqueous solutions of zirconium *that also contained nitrate* were produced by Southon *et al.*<sup>11-13</sup> The first of these covered the synthesis of a zirconium nitrate sol from zirconium carbonate and nitric acid; the main difference compared to the synthesis route used in this project being that their method introduced the carbonate precursor in two steps, without, and then with, heating. It was found that almost all of the nitrate present in the solutions was fully aquated, with a small amount of nitrato (bound nitrate) groups attached to the hydrolysed zirconium species. Raman bands at wavenumbers of 700 cm<sup>-1</sup> and below were assigned to various (hydr)oxide Zr-O or Zr-OH bonds, with the overall structure of particles likely to be a largely amorphous,

polymeric network of zirconium tetramers, stabilised by adsorbed nitrato groups. The second of these papers covered in more detail the origins of the Raman band assignments, which were done with the aid of computational modelling. The overall conclusion in terms of the Raman results is that the spectra of the solutions/sols change noticeably as the particles are formed, with the shift in position of characteristic peaks indicative of the condensation of terminal hydroxy groups to form bridging hydroxy groups. The peaks observed and assigned are summarised in Table 3.1.

**Table 3.1** Assignment of Raman bands seen for aqueous nitrate-based solutions of zirconium made by Southon *et al.*<sup>12</sup> Superscript 't' and 'b' labels denote terminal and bridging hydroxy groups respectively.

Peak Position (cm <sup>-1</sup> )	Assignment	
1046	$v_1$ aquated nitrate (D <sub>3h</sub> )	
1028	$v_2$ bidentate nitrate ligand ( $C_{2v}$ )	
760	$v_5$ bidentate nitrate ligand ( $C_{2v}$ )	
715	$v_4$ aquated nitrate (D <sub>3h</sub> )	
625	Unassigned	
575	ν(Zr-OH <sup>t</sup> ), symmetric	
540	ν(Zr-OH <sup>b</sup> ), symmetric (tentative assignment)	
450	ν(Zr-OH <sup>t</sup> ), symmetric	
420	v(Zr-OH <sup>b</sup> ), 'vertical stretch', symmetric	
375	ν(Zr-OH <sup>b</sup> ), 'horizontal stretch', non-symmetric	

The two most recent papers concerning Raman results from zirconium solutions report results in line with those already described in the literature.<sup>6,7</sup> Ambrosi *et al.* also saw the effects of solution aging and addition of NaOH in their Raman spectra,<sup>14</sup> and described the transformation of zirconium tetramer-like species into more condensed species through the disappearance and appearance of specific bands. They assigned that at 540 cm<sup>-1</sup> as being indicative of Zr-O-Zr bonding reported to connect tetramers in polymeric species, which Southon *et al.* were uncertain about.<sup>12</sup> Gossard *et al.* only made brief comments on their Raman results,<sup>15</sup> noting that during the transformation from sol to gel, the formation of new Zr-O bonds (presumably from bridging hydroxy groups) is evidenced by the increase in intensity of a band at 420 cm<sup>-1</sup>, also in agreement with results previously discussed.

## 3.3 Experimental Methods

# 3.3.1 Fourier-Transform Infrared Spectroscopy (FTIR)

Infrared spectra of solutions were taken using a Bruker ALPHA Platinum ATR spectrometer across a spectral range of 400 – 4000 cm<sup>-1</sup> with a resolution of 2 cm<sup>-1</sup> under ambient conditions. Each spectrum was generated as an average of 16 scans combined for noise reduction purposes. 2-3 drops of solution was added to the top surface of the diamond ATR (attenuated total reflectance) cell, with the instrument anvil (usually used to compress solid material against the cell) unused. Pre-sample-measurement background measurements (instrument backgrounds and water backgrounds) were performed under the same conditions. Baseline correction of spectra was carried out using the software supplied with the instrument.

#### 3.3.2 Raman Spectroscopy

When monochromatic electromagnetic radiation (*e.g.* laser light) hits a sample, it can be scattered in all directions, as well as being reflected or absorbed. When scattering occurs, a small portion of the light (approximately 1 in  $10^7$  photons) emerges with a frequency or wavelength different to that of the incident radiation. This scattering is said to be *inelastic*, and the resulting change in frequency or wavelength of the scattered photons, due to changes in polarizability of chemical bonds within a sample, is a source of structural information about the sample. The changes in polarizability – a measure of the deformation of a chemical bond within an electric field – arise from the interaction of the electric field of the incident radiation with electrons forming the bond between the atoms.<sup>1</sup>

Collection of Raman spectra was performed on a ThermoFisher Scientific DXR2 instrument. Sample excitation was by means of a 633 nm laser in backscattering geometry. Measurements, carried out under ambient conditions, consisted of up to eight 30-second exposures through a 50  $\mu$ m slit, which were combined to improve signal-to-noise (Fig. 3.1), across a spectral range of 3500 – 50 cm<sup>-1</sup> (Raman shift). Fluorescence effects (which serve to

distort the baseline and 'swamp' actual spectral peaks) were mitigated by reducing the exposure time and laser power where necessary. Solutions were contained within a 1 cm quartz cuvette which was positioned in the vicinity of the focal point of the objective lens from which the laser emanates, held in a Teflon® sample holder supported by an adjustable x-y-z stage. The approximate position of the front wall of the cuvette (that which faces the laser) relative to the focal point was checked by maximising the intensity of the peaks of the spectra of SiO<sub>2</sub>. The cuvette was then moved slightly toward the lens so that the focal point was then in the bulk of the solution. As such mostly only sample material was detected; there was minimal contribution to the spectra seen from the walls of the cuvette and none from the Teflon® sample holder. The latter was eliminated by placing a matt black coated foil around the rear and sides of the cuvette to absorb any laser light that strayed beyond these walls of the cuvette. Any additional fluorescence and baseline correction of spectra was carried out with the software supplied with the instrument, and OriginPro software. This was achieved in both cases by the creation and subtraction of a polynomial spline function from sample spectra. Fitting of peaks in Raman spectra was also carried out with OriginPro software.

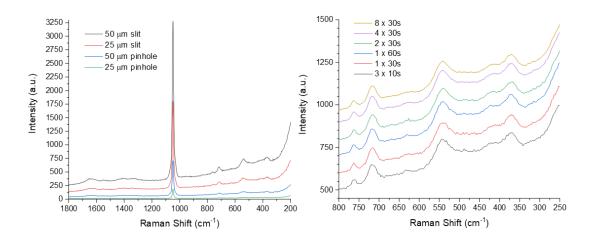


**Figure 3.1:** Plots of Raman spectra of a PZN sample showing the effects of choice of instrument aperture (left) and measurement collection time (right) on peak intensity and quality of spectra. Spectra are not baseline corrected. Only the spectra on the right have been manually offset.

## 3.4 Characterisation by Infrared Spectroscopy

# 3.4.1 Initial Benchmarking

A number of bands are present in infrared spectra of the benchmarking solutions, arising due to water, nitrate species and Zr-O groups, though not all of them could be confidently assigned according to comparison with the literature. In general, the spectra are dominated by the bands from the water that makes up the bulk of the solutions (Fig. 3.2). Three spectral regions are attributable to water; arising from O-H stretches (~3290 cm<sup>-1</sup>), a H-O-H scissor vibrational bending mode (~1633 cm<sup>-1</sup>), and a combination of both modes (~2090 cm<sup>-1</sup>).<sup>16</sup> By comparison of the spectra of the zirconium solutions to that of nitric acid and the nitric acid/mandelic acid mix, it is clear that the bands in the 1500 – 1200 cm<sup>-1</sup> region are of nitrate or nitric acid. The more prominent of the two appears in the spectrum for nitric acid at ~1320 cm<sup>-1</sup> with the associated shoulder at ~1380 cm<sup>-1</sup>. These are attributable to symmetric <sup>17</sup>, <sup>18</sup> and asymmetric <sup>19, 20</sup> nitrate stretches, respectively. There is a slight shift in position for these features to ~1339 cm<sup>-1</sup> for the main peak and to up to ~1385 cm<sup>-1</sup> for the shoulder in the spectra of the nitric acid/mandelic acid mix and the zirconium solutions containing nitric acid. These bands do not feature in the spectra for the chloride-based analogues. Four further features are distinguishable in the spectra for nitric acid, a shoulder at ~1735 cm<sup>-1</sup>; and peaks at ~1038, ~953 and ~824 cm<sup>-1</sup>, the first of which appears also in the spectra of the nitric acid based zirconium solutions at ~1045 cm<sup>-1</sup>. No suitable assignment could be found in the literature for that at ~1735 cm<sup>-1</sup>; the latter three bands are most likely a nitrate N-O stretch, <sup>20, 21</sup> a nitrate N-O-H stretch<sup>22, 23</sup> and a nitrate NO<sub>2</sub> deformation, <sup>19</sup> respectively. Looking closer still, two broad bands at 2695 cm<sup>-1</sup> and 2328 cm<sup>-1</sup> are also present in the spectra for the nitric acid solution that do not appear in the other spectra. In the spectra of the zirconium solutions, specifically those containing nitric acid, a small feature is present at ~1545 cm<sup>-1</sup>, which could be attributable to nitrate coordinated to zirconium species, given that it does not feature in the spectra of nitric acid itself nor that of the nitric acid/mandelic acid mix. Otherwise, the closest match found in the literature was for a nitrate vibration overtone.<sup>23</sup> There is no sign in these

spectra of any contributions from mandelic acid, or zirconium mandelate<sup>24</sup> (Fig. 3.2). A summary of assignments for the features described is given in Table 3.2.

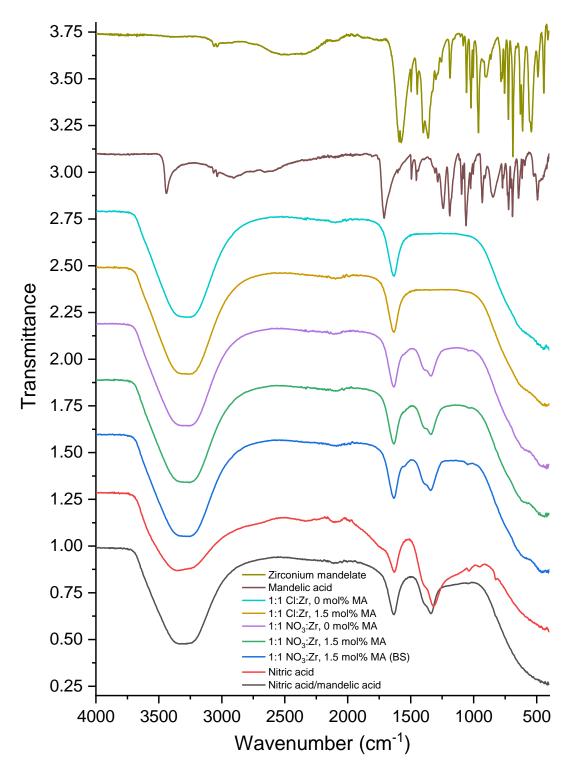


**Figure 3.2** Infrared spectra of the PZN and PZC solutions used for the initial benchmarking study, with relevant reference materials (the mandelate and mandelic acid spectra are from dry solid samples). Spectra are vertically offset for clarity.

**Table 3.2** Assignment of bands seen in the infrared spectra (Figures 3.2 and 3.3) of zirconium solutions characterised in the initial benchmarking work. Assignments denoted 'by comparison' are of bands that could not be matched to those in the literature, but were assumed to be of nitrate/nitric acid due to their presence only in spectra containing nitrate/nitric acid.

Peak Position (cm <sup>-1</sup> )	Assignment	Ref.
3540	HNO <sub>3</sub> ⋅H <sub>2</sub> O species	22
	HNO <sub>3</sub> O-H stretch	17, 25
3290	Water O-H stretch	1
3040	HNO <sub>3</sub> ⋅H <sub>2</sub> O species	22
2695	Nitrate (by comparison)	
2328	Nitrate (by comparison)	
2090	Water combination mode	1
1755	Nitrate (by comparison)	
1735	Nitrate (by comparison)	
1620, 1633	Water H-O-H scissor	1
1545	NO <sub>3</sub> vibration overtone	23
	Coordinated nitrate?	
1380, 1385	NO <sub>2</sub> asymmetric stretch of NO <sub>3</sub>	19, 20
1320, 1339	A <sub>1</sub> NO <sub>2</sub> symmetric stretch of NO <sub>3</sub>	17, 18, 26
1038, 1045	N-O stretch of NO <sub>3</sub>	20, 21
953	A <sub>1</sub> N-OH stretch	22, 23, 26
824	NO <sub>2</sub> deformation of NO <sub>3</sub>	19
620	Zr-O or further nitrate	
435	Zr-O or further nitrate	

Using a background measurement of water, subsequently subtracted from the sample spectra, reveals more features in the spectra of the various zirconium solutions (Fig. 3.3). Removal of the band for the bulk O-H stretch leaves two broad bands at ~3540 cm<sup>-1</sup> and ~3040 cm<sup>-1</sup> for the zirconium solutions containing nitric acid, the latter of which also being present for the chloride-based zirconium solutions. All spectra in Figure 3.3 feature a weakly intense band at ~1620 cm<sup>-1</sup> which given its position may be the remnants of the band for the water H-O-H scissor vibrational mode. The spectra for the solutions containing nitric acid contain two further bands visible at ~1755 cm<sup>-1</sup> and ~1545 cm<sup>-1</sup>; the latter of which was just visible in the spectra in Figure 3.2. That at ~1045 cm<sup>-1</sup> remains. Also now visible following water background subtraction are two broad (and noisy) bands at ~620 cm<sup>-1</sup> and 435 cm<sup>-1</sup>. Given that they feature in all five spectra displayed in Figure 3.2, and are located at lower wavenumbers (indicative of chemical bonds between atoms of greater mass), these are likely due to Zr-O bonding within the zirconium solution species themselves. Further discussion of these is made later in this section. The band at ~620 cm<sup>-1</sup> also appears more intense for the

solutions containing nitric acid, which could be indicative of greater growth of zirconium species in these solutions, or due to a contribution from further bands of nitrate. It is useful to note that although transmittance is not linearly proportional to the concentration of a particular chemical bond, absorbance is, and the two are related by  $A = -\log_{10}(T)$  (or  $A = 2-\log_{10}(\%T)$ ). Once again, there is nothing to suggest in these spectra that mandelic acid is (or is not) present in the solutions studied – though the amount used was only 1.5 mol% relative to zirconium.

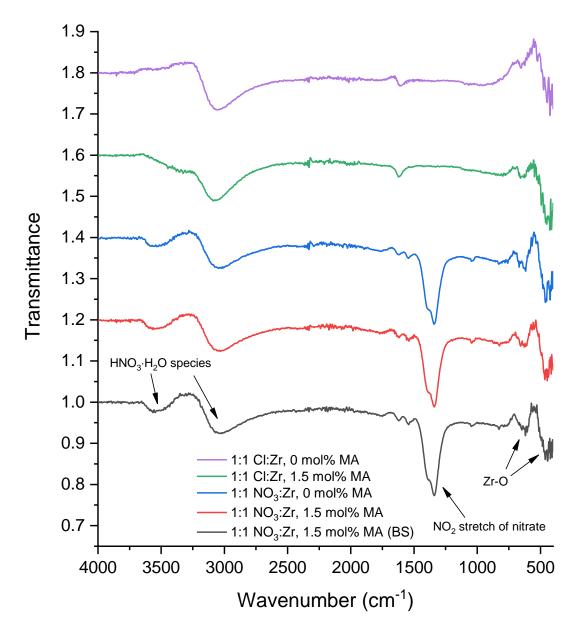


**Figure 3.3** Infrared spectra of the solutions used for the initial benchmarking study, with a water background subtracted. Spectra are vertically offset for clarity, and some key bands highlighted.

To gather more information about the zirconium solution species by infrared spectroscopy, measurements of benchmarking solutions that had reduced to a glassy gel by oven drying were also carried out (Fig. 3.4). Again, clear differences are seen between the spectra depending on whether the solution was nitrate or chloride based. Firstly, common to all five spectra is a broad band from the O-H stretching mode of water remaining in the gel. However the position of maximum intensity is different for the chloride and nitrate gels, at ~3125 cm<sup>-1</sup> and ~3290 cm<sup>-1</sup> respectively. This may be due to a contribution, in the case of the nitrate gels, from hydrogen bonded HNO<sub>3</sub> species. It could also reflect how strongly associated water molecules are to the zirconium species in the two types of gel. The band for the water H-O-H scissor mode also remains, appearing at ~1605 cm<sup>-1</sup> for the chloride gels and as a shoulder at ~1599 cm<sup>-1</sup> for the three gels containing nitrate. The remaining features for the chloride gels at ~780, ~635, and ~445 cm<sup>-1</sup> are, by a process of deduction, most likely from Zr-O(H) bonding. These also appear in the spectra of the nitrate gels, superimposed by additional peaks from nitrate, given the difference in composition. Discussion regarding these and the remaining bands in the spectra for the nitrate gels is centred around Figure 3.5, which shows a comparison between a nitrate gel and its parent solution.

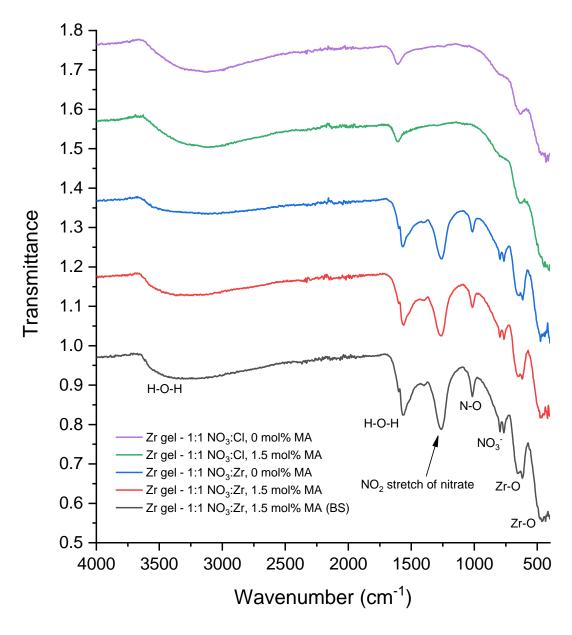


**Figure 3.4** Infrared spectra of the solutions used for the initial benchmarking study, following drying to a solid gel. Spectra are vertically offset for clarity, and some key bands highlighted.

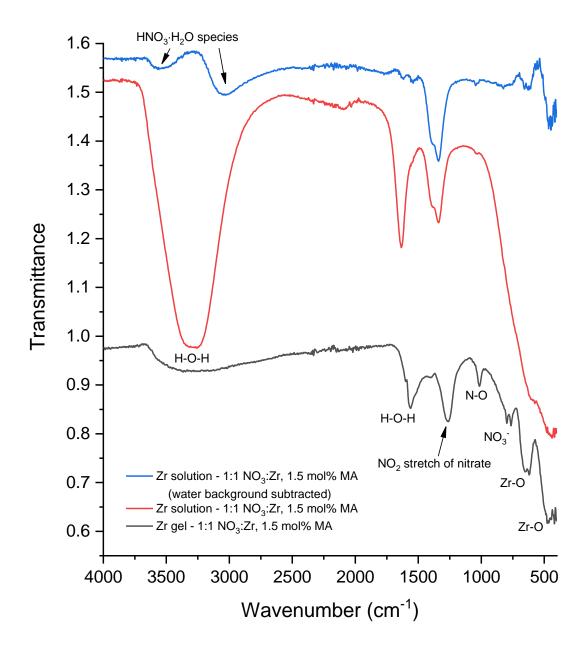


**Figure 3.5** A comparison of infrared spectra of a nitrate-based zirconium solution and the gel formed by drying the same solution. Spectra are vertically offset for clarity, and some key bands highlighted.

In the case of the spectrum of the nitrate gel, the band at ~1012 cm<sup>-1</sup> is ascribed to the nitrate N-O stretch, seen previously in the solution spectra at ~1038 cm<sup>-1</sup>. The band at ~1265 cm<sup>-1</sup> in the spectrum for the gel is relatively intense, and shifted to lower wavenumbers compared to the similar feature in the solution spectra, so is likely a symmetric NO<sub>2</sub> stretch, of possibly coordinated nitrate. The band at ~1561 cm<sup>-1</sup> is also likely due to coordinated nitrate (Zr-ONO<sub>2</sub>) as a band at this position is known in the literature for zirconium nitrate<sup>27, 28</sup> (and

is possibly the asymmetric stretch this time). A sample of 'zirconium oxynitrate hydrate' was also characterised by infrared spectroscopy and found to have intense bands in the same spectral region as the two bands just discussed (Fig. 3.6). In general, bands in this region are ascribed to NO<sub>2</sub> stretches of nitrate species.<sup>29</sup> There are no bands of higher wavenumbers that might otherwise be used to determine if the mode of nitrate coordination is mono- or bidentate.<sup>30</sup>

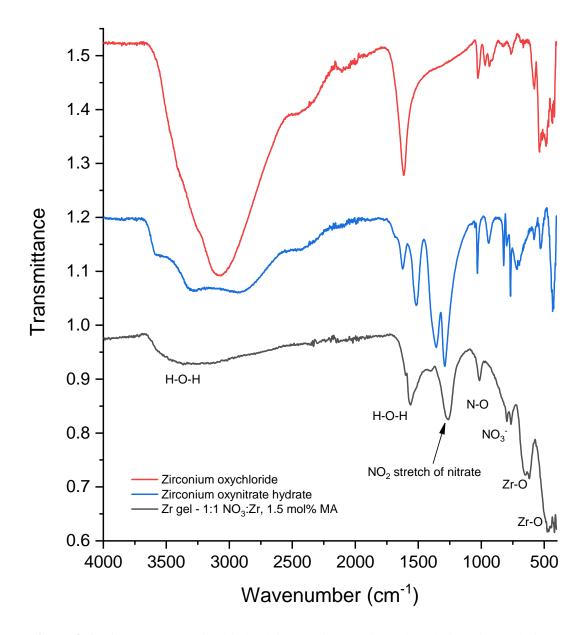


**Figure 3.6** Infrared spectra of a dried gel formed from a nitrate-based zirconium solution, zirconium oxynitrate hydrate and zirconium oxychloride. Spectra are vertically offset for clarity, and some key bands highlighted.

Ascertaining the specific assignment of gel bands at lower wavenumbers of <1000 cm<sup>-1</sup> is more complex, as a number of modes are known in this region for both nitrate groups<sup>27</sup> and Zr-O/Zr-OH groups.<sup>31</sup> The broad band at <500 cm<sup>-1</sup> in the nitrate (and chloride) gel spectra is attributable to Zr-O-Zr vibrations;<sup>32</sup> it also features in the measured infrared spectrum of zirconium oxychloride which has a structure based upon the zirconium tetramer (Fig. 3.6). The band with a peak at ~650 cm<sup>-1</sup> is likely due to Zr-O vibrations of Zr-OH groups.<sup>32</sup> Vibrations of Zr-O-Zr-O four membered rings (*cf.* two Zr centres joined by two bridging OH groups) are also expected in this region.<sup>33</sup> The sharp peak ~767 cm<sup>-1</sup> however is possibly an additional NO<sub>3</sub><sup>-</sup> vibration;<sup>27</sup> a band for a different vibrational mode of the same group is also expected at ~670 cm<sup>-1</sup>,<sup>27</sup> which may be overlapping with that at ~650 cm<sup>-1</sup> previously mentioned. Table 3 summarises the assignments made to the gel sample measurements.

**Table 3.3** Assignment of bands seen in the infrared spectra of zirconium gels as characterised in the initial benchmarking work.

Peak Position (cm <sup>-1</sup> )	Assignment	Ref.
3290	O-H stretch of residual water and	
	HNO <sub>3</sub> ·H <sub>2</sub> O species	
3125	O-H stretch of residual water	
1599, 1605	Water H-O-H scissor	
1561	Asymmetric(?) NO <sub>2</sub> stretch of	27, 28
	coordinated NO <sub>3</sub>	
1265	Symmetric NO <sub>2</sub> stretch of	17, 18
	coordinated NO <sub>3</sub> -	
1012	N-O stretch of NO <sub>3</sub>	18, 20
767	$NO_3^-$	27
670	$NO_3^-$	27
650	Zr-O vibrations of Zr-OH	32
< 500	Zr-O-Zr vibrations	32

## 3.4.2 Infrared Measurements of PZN Solutions of Varying Composition

Infrared spectroscopy measurements of PZN solutions of varying nitric acid and mandelic acid composition are presented here in Figures 3.7 and 3.8, without and with water background subtraction, respectively. The same bands are seen for these solutions as previously discussed in section 3.4.1. The main point of note is that the intensity of bands associated with nitrate species can be seen to increase with increasing solution nitric acid content. This is the case for the NO<sub>3</sub><sup>-</sup> vibrations at 1345 and 1385 cm<sup>-1</sup>, the nitrate band at ~1755 cm<sup>-1</sup> and the band at ~2990 cm<sup>-1</sup>, previously ascribed to O-H stretches of hydrogen bonded HNO<sub>3</sub>·H<sub>2</sub>O species. The low wavenumber bands of Zr-O do not follow an obvious trend in the same way, however. These changes are highlighted in Figures 3.9 and 3.10. For fuller discussion of assignment of bands in these spectra, the reader is referred to the previous section.

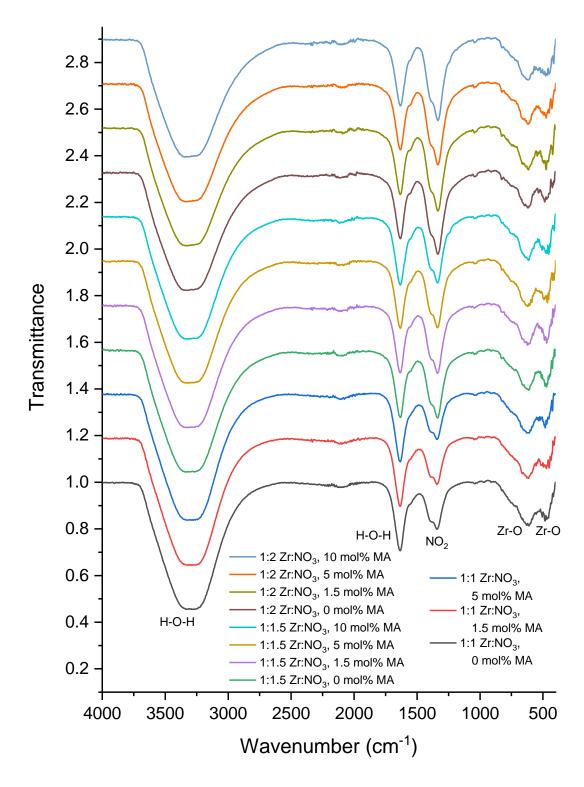


**Figure 3.7** Baseline corrected infrared spectra of PZN solutions of a range of nitric acid and mandelic acid (MA) composition. Spectra are vertically offset for clarity. The groups that give rise to key bands are highlighted.

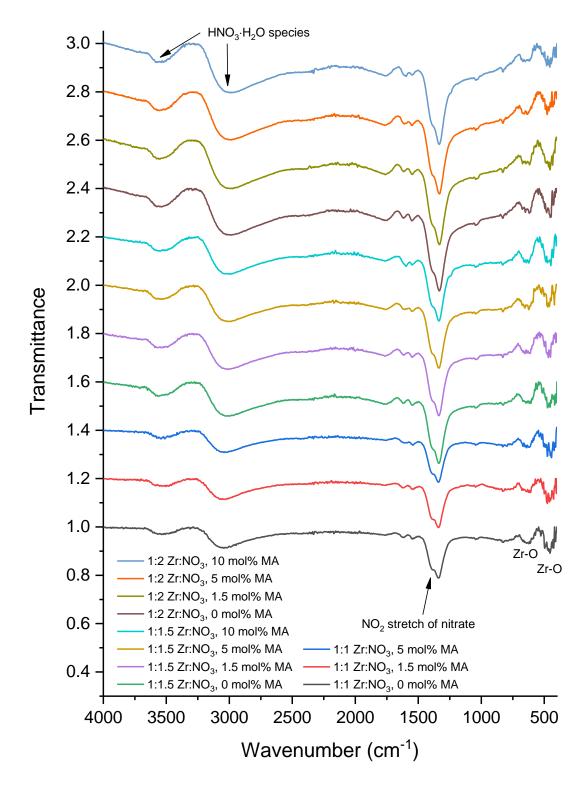


**Figure 3.8** Baseline corrected infrared spectra of PZN solutions of a range of nitric acid and mandelic acid (MA) composition, with a water background subtracted. Spectra are vertically offset for clarity. The groups that give rise to key bands are highlighted.

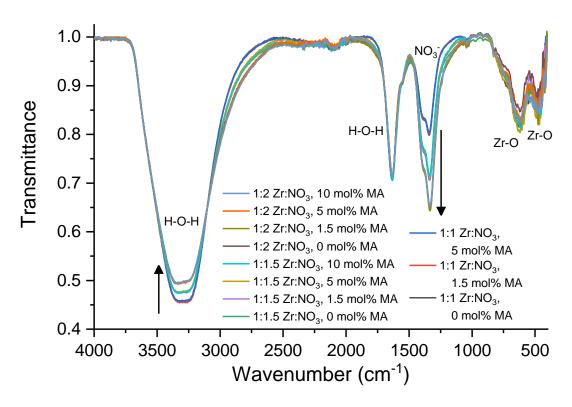


**Figure 3.9** Non-offset baseline corrected infrared spectra of PZN solutions of a range of nitric acid and mandelic acid (MA) compositions. Black arrows highlight the changes in the bands discussed in the main text, with arrow direction signifying increasing nitrate content. The groups that give rise to key bands are highlighted.

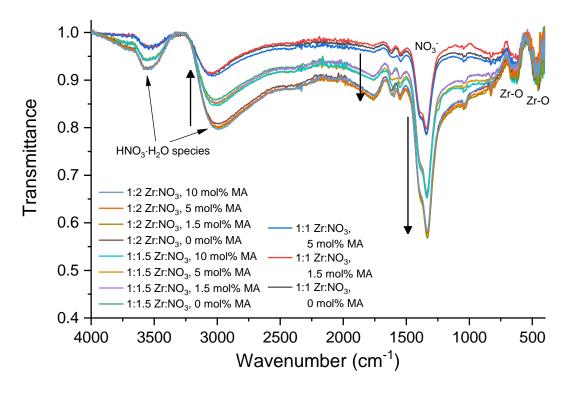


**Figure 3.10** Non-offset baseline corrected infrared spectra of PZN solutions of a range of nitric acid and mandelic acid (MA) compositions, with water backgrounds subtracted. Black arrows highlight the changes in the bands discussed in the main text, with arrow direction signifying increasing nitrate content. The groups that give rise to key bands are highlighted.

## 3.4.3 Infrared Measurements of PZN Solutions During Synthesis

Infrared measurements of samples taken from the reactor during the synthesis of a PZN solution of composition 1:1 Zr:NO<sub>3</sub> and 1.5 mol% mandelic acid are presented here in Figures 3.11 and 3.12, without and with water background subtraction, respectively. The purposes of this were to ascertain the usefulness of this technique in following any changes during synthesis, i.e. the development of zirconium solution species due to the applied heat treatment. Figures 3.13 and 3.14 show the same data, without the vertical offset. For fuller (discussion of) assignment of bands in these spectra, the reader is referred to Section 3.4.1.

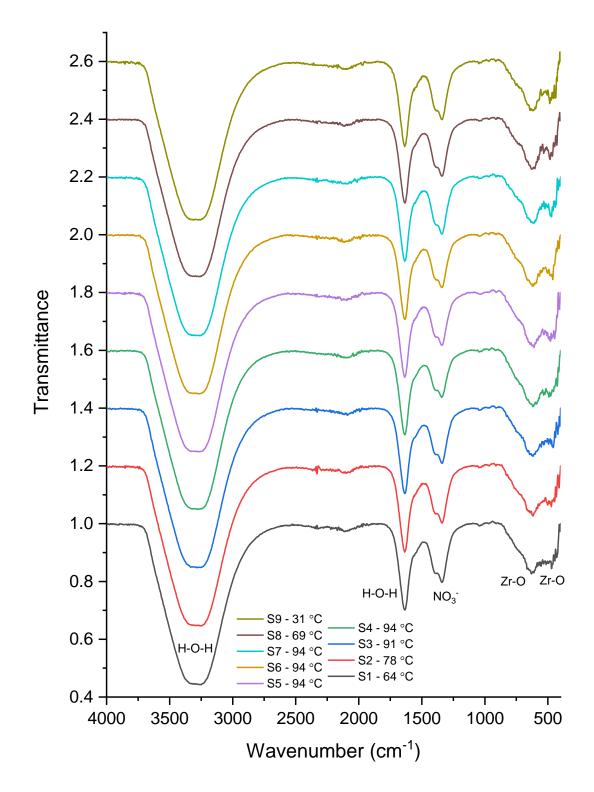


**Figure 3.11** Baseline corrected infrared spectra of samples of PZN solution taken from the reactor during synthesis. Order of sampling (progress of reaction) is bottom-to-top (S1 to S9; S = 'sample'). The temperature of the reactor contents at the time of sampling is given. Spectra are vertically offset for clarity. The groups that give rise to key bands are highlighted.

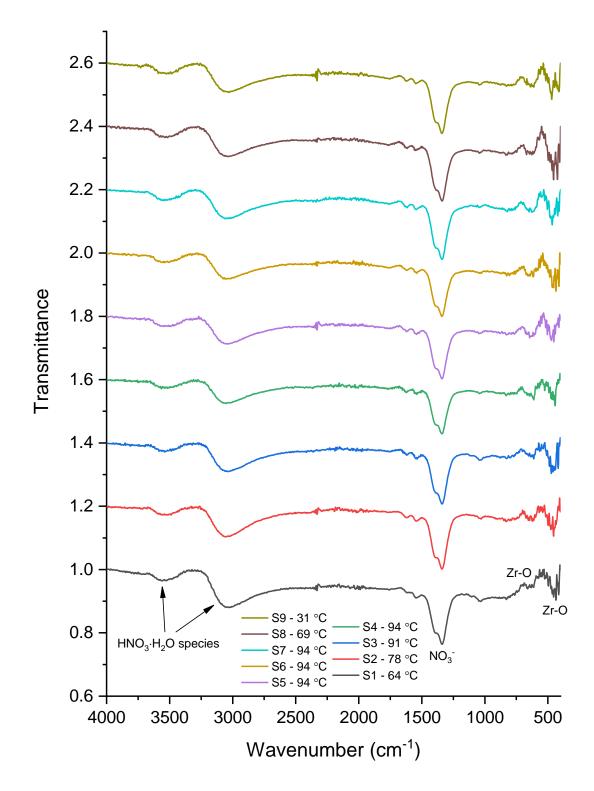


**Figure 3.12** Baseline corrected infrared spectra of samples of PZN solution taken from the reactor during synthesis, with a water background subtracted. Order of sampling (progress of reaction) is bottom-to-top (S1 to S9; S = 'sample'). The temperature of the reactor contents at the time of sampling is given. Spectra are vertically offset for clarity. The groups that give rise to key bands are highlighted.

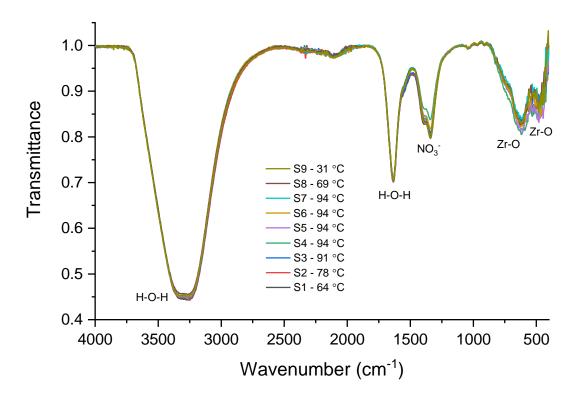


**Figure 3.13** Non-offset baseline corrected infrared spectra of samples of PZN solution taken from the reactor during synthesis. Order of sampling is bottom-to-top (S1 to S9; S = 'sample'). The temperature of the reactor contents at the time of sampling is given. The groups that give rise to key bands are highlighted.

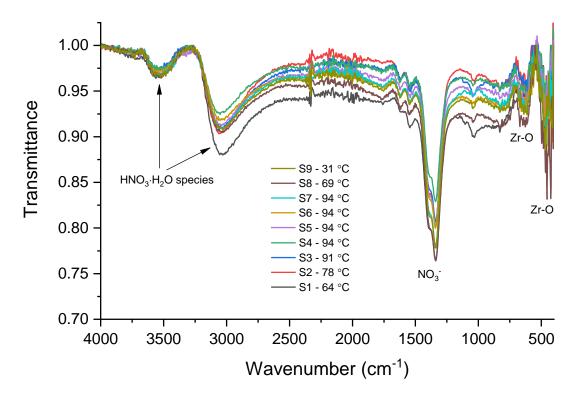


**Figure 3.14** Non-offset baseline corrected infrared spectra of samples of PZN solution taken from the reactor during synthesis, with a water background subtracted. Order of sampling is bottom-to-top (S1 to S9; S = 'sample'). The temperature of the reactor contents at the time of sampling is given. The groups that give rise to key bands are highlighted.

# 3.4.4 Infrared Measurements of PZN Solutions after Aging

Infrared measurements of a PZN solution of composition 1:1 Zr:NO<sub>3</sub> and 1.5 mol% mandelic acid are presented here in Figures 3.15 and 3.16, without and with water background subtraction, respectively. The purposes of this were to ascertain the usefulness of this technique in following any changes after synthesis, i.e. changes in the zirconium solution species due to time, post heat treatment. Figures 3.17 and 3.18 show the same data, without the vertical offset. For fuller discussion of assignment of bands in these spectra, the reader is referred to Section 3.4.1.

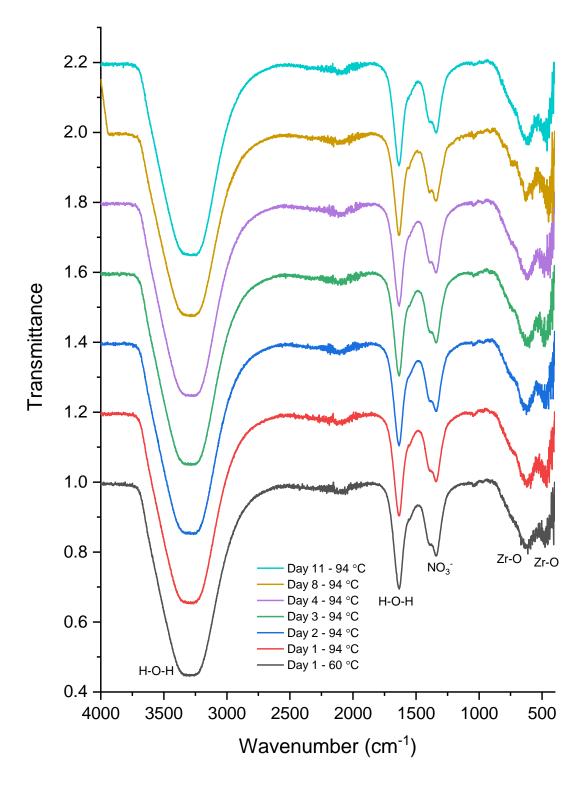


**Figure 3.15** Baseline corrected infrared spectra of a PZN solution of composition 1:1 Zr:NO<sub>3</sub> and 1.5 mol% mandelic acid taken over a time period of 11 days. The 'Day 1-60 °C' measurement is included for comparison. As such the remaining spectra are labelled with '94 °C' as a reminder that these measurements were post full heat treatment. Spectra are vertically offset for clarity. The groups that give rise to key bands are highlighted.

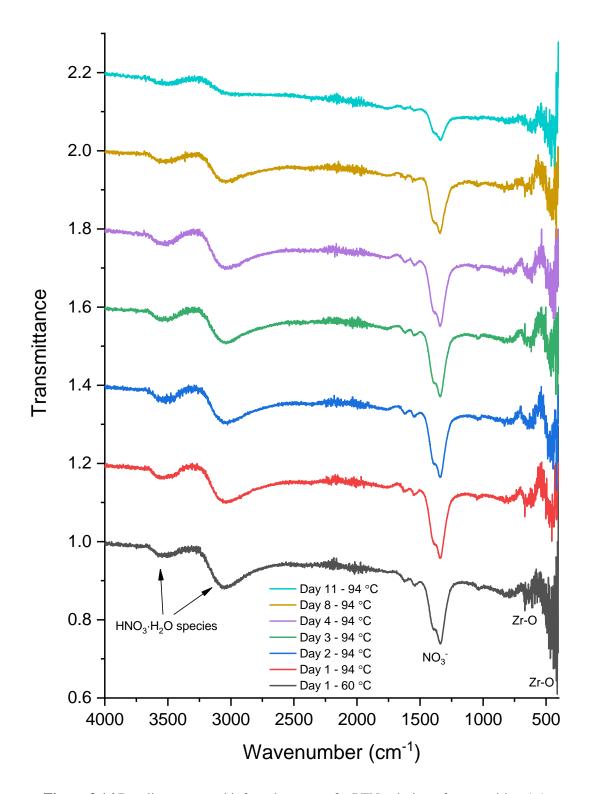


**Figure 3.16** Baseline corrected infrared spectra of a PZN solution of composition 1:1 Zr:NO $_3$  and 1.5 mol% mandelic acid taken over a time period of 11 days, with water background subtraction. The 'Day 1-60 °C' measurement is included for comparison. As such the remaining spectra are labelled with '94 °C' as a reminder that these measurements were post full heat treatment. Spectra are vertically offset for clarity. The groups that give rise to key bands are highlighted.

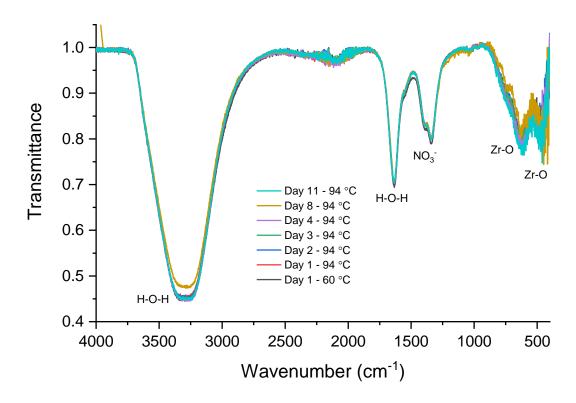


**Figure 3.17** Non-offset baseline corrected infrared spectra of a PZN solution of composition 1:1 Zr:NO<sub>3</sub> and 1.5 mol% mandelic acid from the short aging study. The groups that give rise to key bands are highlighted.

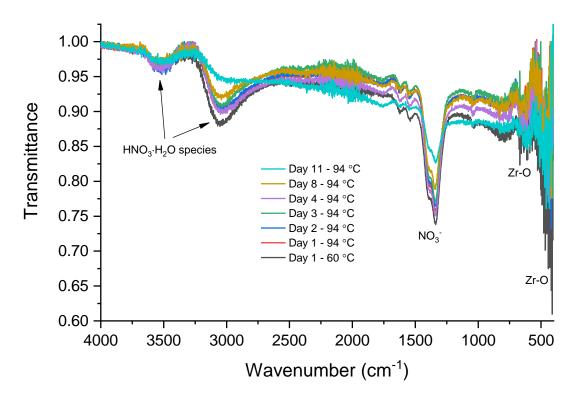


**Figure 3.18** Non-offset baseline corrected infrared spectra of a PZN solution of composition 1:1 Zr:NO<sub>3</sub> and 1.5 mol% mandelic acid from the short aging study, with water background subtraction. The groups that give rise to key bands are highlighted.

## 3.5 Characterisation by Raman Spectroscopy

#### 3.5.1 Initial Benchmarking

Like with the infrared spectra seen previously, Raman spectra of as-made PZN solutions feature a number of easily distinguishable peaks. The full Raman spectrum for a PZN solution of a typical composition is shown in Figure 3.19 as an example. Considering the whole spectral range measured of 3500 – 100 cm<sup>-1</sup>, the spectrum is dominated by an intense broad band with maximum intensity at ~3425 cm<sup>-1</sup>, that arises from symmetric and asymmetric O-H stretching modes of water, and a very intense and sharp peak at ~1050 cm<sup>-1</sup>. The main bands of interest for the purposes of this work lie between 1800 – 300 cm<sup>-1</sup>, as seen in the Figure 3.19 inset. For reference, Figure 3.20 gives a comparison between the spectra of water, nitric acid, and a nitric acid/mandelic acid mix, at an equivalent level to the composition of the solution the spectra of which is shown in Figure 3.19, for this region. As such it is clear that the intense peak at ~1050 cm<sup>-1</sup> arises from a nitric acid or nitrate species, and is, more specifically, due to aquated nitrate ions.<sup>12</sup>

Raman spectra for the five benchmarking solutions studied are given in Figure 3.21. Obvious differences are seen between the spectra for solutions made with nitric acid and those made with hydrochloric acid. Common to all five spectra is a band centred at ~960 cm<sup>-1</sup>, arising due to the quartz cuvette, and a contribution at ~1640 cm<sup>-1</sup> from water; attributable to the H-O-H scissor bending mode of water, as seen in Figure 3.20. From further comparison of Figures 3.20 and 3.21 it can be seen that the bands at ~1658, ~1415, ~1335 and ~720 cm<sup>-1</sup>, as well as the intense band at ~1050 cm<sup>-1</sup> are due to the presence of nitrate, the former of which overlaps with the water band at ~1640 cm<sup>-1</sup>. There are a number of additional bands that feature in the spectrum of pure nitric acid (Fig. 3.20) that do not appear in the spectra of PZN solutions. Raman spectra of aqueous nitric acid can feature a number of bands, which may be present or not depending on the concentration. <sup>26, 34</sup> For the zirconium solutions made with mandelic acid, bands at ~1610, ~1200, ~1160, ~1006 and ~968 cm<sup>-1</sup> are due to the mandelic acid. The band at ~1033 cm<sup>-1</sup> in the spectrum of the PZC solution with mandelic acid is most

likely also due to mandelic acid but is otherwise obscured by the strong nitrate band in the other spectra (shown more clearly in Figure 3.22). It was hoped that Raman measurements would show whether there is coordination of mandelic acid to zirconium centres in the solution species. A band at ~1709 cm<sup>-1</sup>, believed to be a C=O stretch,<sup>35</sup> is absent in spectra of zirconium mandelate<sup>24</sup> and of a PZN solution of 1:1 Zr:NO<sub>3</sub> and 10 mol% mandelic acid, though present in that for mandelic acid; this change was taken as tentative evidence for coordination (Fig. 3.23). Otherwise, other Raman features that are ascribable to O bonds<sup>35</sup> in the carboxyl(ate) are obscured by the intense PZN nitrate band at ~1050 cm<sup>-1</sup>. Mandelic acid is known to have a particularly strong affinity for zirconium,<sup>24</sup> so coordination is not unlikely.

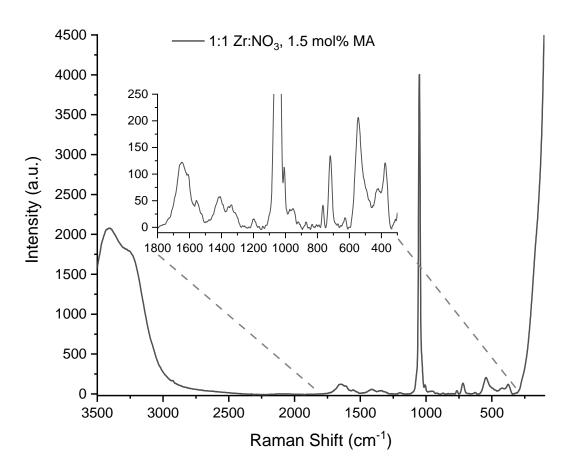


**Figure 3.19** Example Raman spectrum taken of an LMT PZN solution, with an inset highlighting the main region of interest, containing bands from water, nitrate and Zr-OH groups.

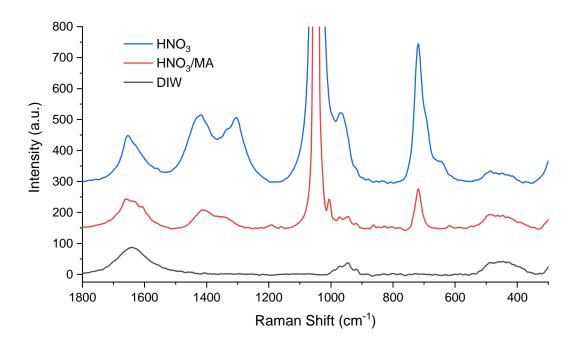


**Figure 3.20** Raman spectra of deionised water ('DIW'), nitric acid, and a mix of nitric acid and mandelic acid (of content equivalent to a PZN solution of 1:1 NO<sub>3</sub> and 1.5 mol% mandelic acid). Spectra are vertically offset for clarity.

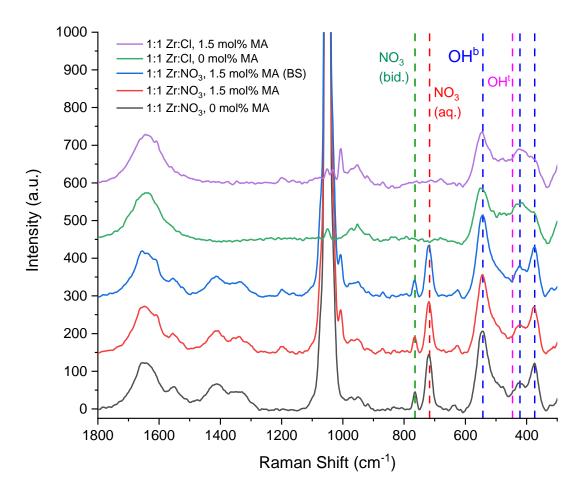


**Figure 3.21** Raman spectra of the PZN and PZC solutions used in the initial benchmarking work. Spectra are vertically offset for clarity. Key bands described in the main text are highlighted with the coloured dashed lines.

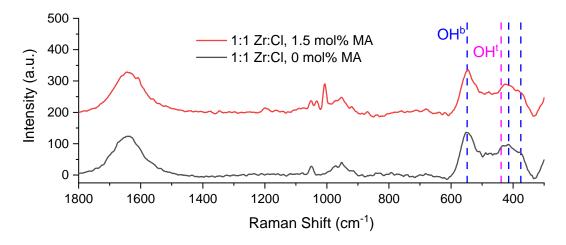


**Figure 3.22** Raman spectra of PZC solutions to more clearly show the changes caused by the presence of mandelic acid. Key bands described in the main text are highlighted with the coloured dashed lines.

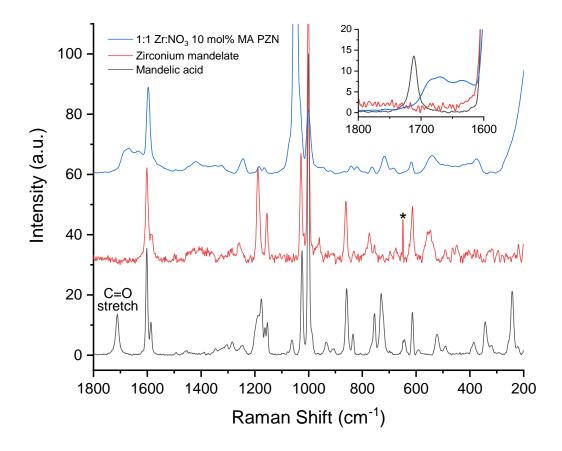


**Figure 3.23** Raman spectra of mandelic acid, zirconium mandelate and PZN solution containing the highest mandelic acid content level studied of 10 mol%. The mandelic acid C=O stretch is labelled (and contained within the inset, top right); the sharp feature marked by an asterisk in the spectrum for zirconium mandelate is an artefact of the instrument. Spectra are vertically offset for clarity.

The following discussion is centred around the region of the spectra between 800 – 300 cm<sup>-1</sup>, in which bands from Zr-O(H) bonds would be expected to be visible (Fig. 3.24). At ~720 cm<sup>-1</sup> is the nitrate band previously mentioned. At ~765 cm<sup>-1</sup> is an additional band that can also be assigned to a nitrate species, given that it does not feature in the spectra of the chloride-based solutions. In fact, it is due to zirconium coordinated nitrate species, not those free in solution. <sup>12, 27</sup> Other than the absence of bands for nitrate, the spectra for the chloride-based solutions are quite different in the region 600 – 350 cm<sup>-1</sup>. Bands in this region can be specifically assigned to the bonding of the Zr-OH groups in the zirconium species themselves – from bridging hydroxy groups that connect zirconium centres, and terminal hydroxy groups (and coordinated water molecules) that do not.<sup>7, 10, 12, 15</sup> Thus, the relative intensities of these

bands reflect the extent of zirconium hydrolysis, and the build-up of zirconium structures in solution. Bands attributable to bridging hydroxy groups are marked by the blue dashed lines at ~545, 420 and 375 cm<sup>-1</sup> in Figure 3.24,<sup>12</sup> and the expected positions of bands of terminal hydroxy groups by the pink dashed lines at ~575 and ~450 cm<sup>-1</sup>. The greater intensity of the two bands at ~545 cm<sup>-1</sup> and ~ 375 cm<sup>-1</sup>, and the decreased intensity at ~450 cm<sup>-1</sup> is interpreted as there being greater numbers of bridging hydroxy groups in the nitrate-based zirconium solutions, due to a greater level of hydrolysis.

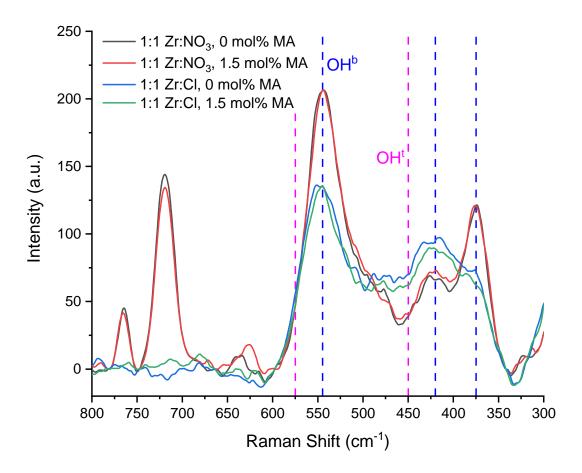


**Figure 3.24** Raman spectra of PZN and PZC solutions containing bands attributable to the Zr-OH groups of solution zirconium species. Bridging OH groups 'OHb' are marked by blue dashed lines with terminal OH groups 'OH' marked by the pink dashed lines.

#### 3.5.2 Raman Measurements During PZN Synthesis

Spectra from Raman measurements of samples taken from the reactor during the synthesis of a PZN solution of composition 1:1 Zr:NO<sub>3</sub> and 1.5 mol% mandelic acid are presented here in Figure 3.25. These formed an initial test of the usefulness of this technique in following any changes during synthesis, i.e. the development of zirconium solution species due to the applied heat treatment. Figure 3.26 shows the  $800 - 300 \text{ cm}^{-1}$  region, where the main changes occur due to zirconium hydrolysis. There are small differences in intensity for the coordinated and free solution nitrate bands at ~765 and ~720 cm<sup>-1</sup>, however the order in which the intensity changes does not follow any obvious trend. Bands attributable to bridging (OH<sup>b</sup>) and terminal hydroxy groups (OH<sup>t</sup>) are highlighted with the blue and pink annotations respectively, like those seen in Figure 3.24. In the case of this sample, bands distinguishable in the Zr-O region between  $600 - 300 \text{ cm}^{-1}$  after the completion of the heat treatment mainly relate to bridging hydroxy groups. The bridging hydroxy band at ~540 cm<sup>-1</sup> is seen to increase in intensity as synthesis progresses, as well as that at ~375 cm<sup>-1</sup>. At the same time, a decrease in intensity is seen in the region of ~450 cm<sup>-1</sup>, where one of the bands for terminal hydroxy groups would be expected. However a distinct band at ~450 cm<sup>-1</sup> is not seen, most likely due to the overlap of a number of peaks in this region. This is consistent with increasing hydrolysis and zirconium connectivity, i.e. the growth of the zirconium particles in solution, which takes place via the formation of bridging hydroxy groups between zirconium centres from pairs of terminal hydroxy groups.

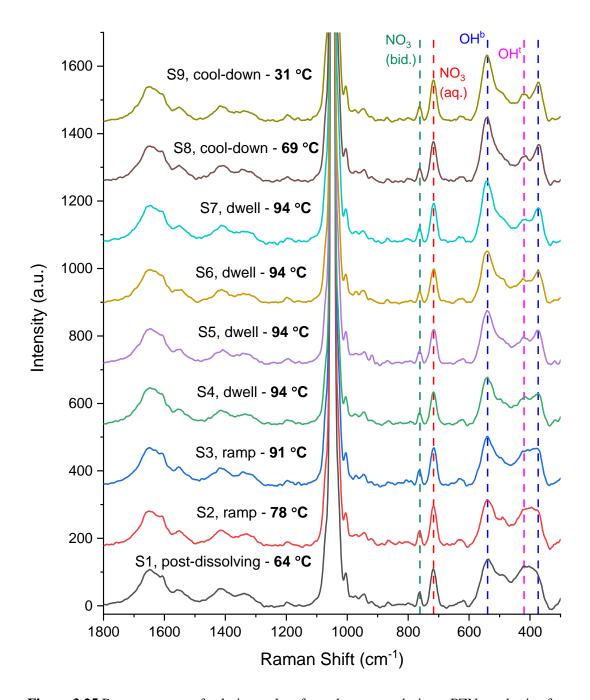


**Figure 3.25** Raman spectra of solutions taken from the reactor during a PZN synthesis of a 1:1 Zr:NO3, 1.5 mol% mandelic acid PZN solution. Spectra are vertically offset for clarity. The stage of synthesis, and the exact temperature of the reactor contents at the time of sampling is given.

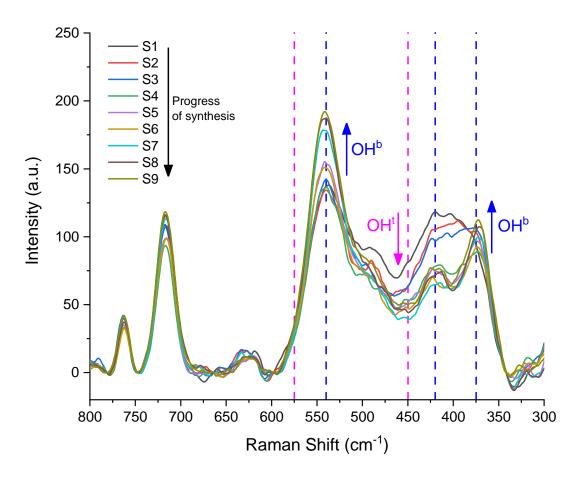


**Figure 3.26** Raman spectra of solutions taken from the reactor during a PZN synthesis of a 1:1 Zr:NO<sub>3</sub>, 1.5 mol% mandelic acid PZN solution, with key bridging and terminal Zr-OH bands<sup>12</sup> highlighted.

# 3.5.3 Testing of PZN Solutions of Varying Composition

Raman measurements of PZN solutions of varying nitric acid and mandelic acid composition are presented here in Figure 3.27. Figures 3.28 – 3.31 show direct comparisons of spectra of solutions according to nitric acid and mandelic acid content. As might be expected, the bands arising due to nitrate and mandelic acid or mandelate increase in intensity as the amounts of the components in the solutions is increased.

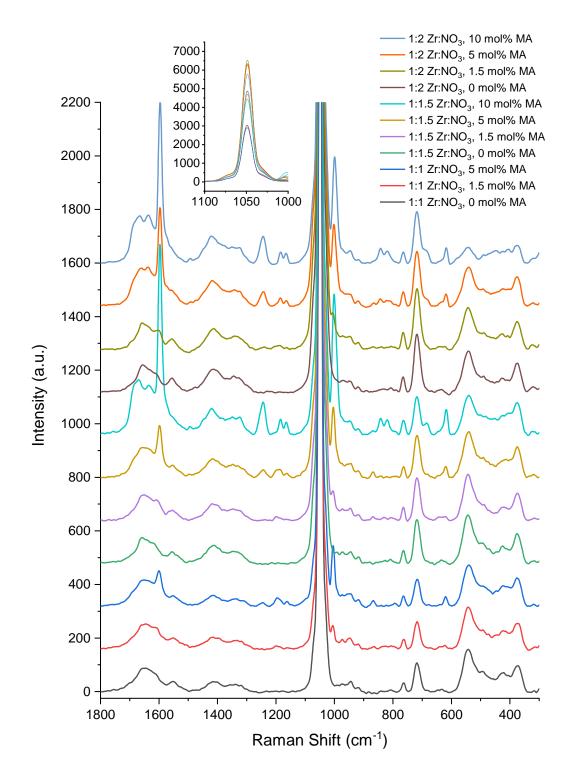


**Figure 3.27** Raman spectra of PZN solutions of a range of nitric acid and mandelic acid composition. Spectra are vertically offset for clarity. The inset graph shows the entirety of the nitrate band at ~1050 cm<sup>-1</sup> for each sample. Assignment of the key bands (nitrate and Zr-OH groups) are the same as those highlighted by the dashed lines in Figure 3.25.

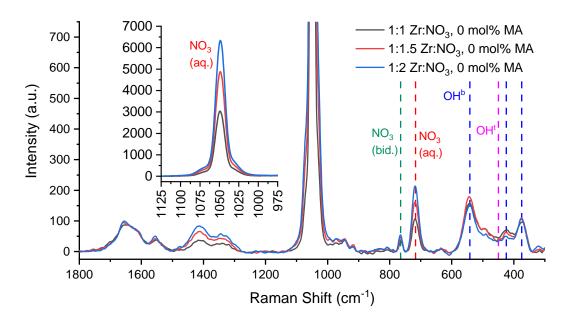


**Figure 3.28** Raman spectra of PZN solutions containing 0 mol% mandelic acid, showing the effects of increasing nitric acid content. Key bands are assigned as previously.

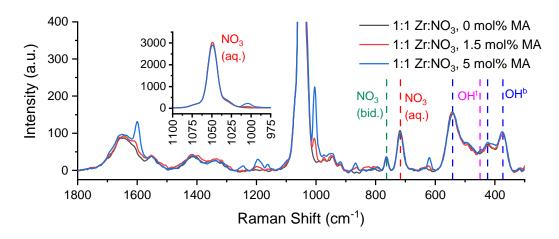


**Figure 3.29** Raman spectra of 1:1 Zr:NO<sub>3</sub> PZN solutions, showing the effects of increasing mandelic acid content. Key bands are assigned as previously.

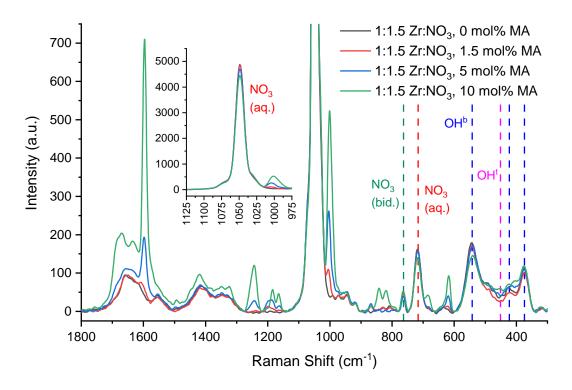


**Figure 3.30** Raman spectra of 1:1.5 Zr:NO<sub>3</sub> PZN solutions, showing the effects of increasing mandelic acid content. Key bands are assigned as previously.

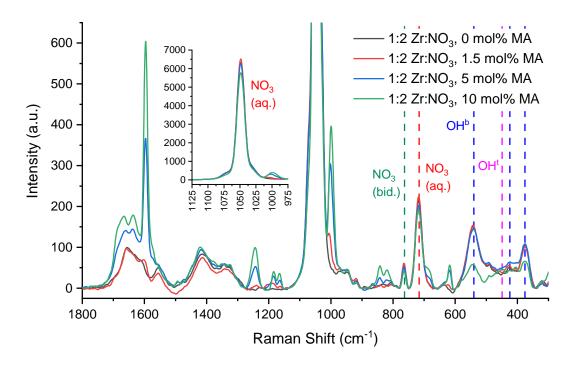


**Figure 3.31** Raman spectra of 1:2 Zr:NO<sub>3</sub> PZN solutions, showing the effects of increasing mandelic acid content. Key bands are assigned as previously.

## 3.5.4 Variation of Heat Treatment Temperature During PZN Synthesis

#### 3.5.4.1 Discussion of Spectra

A batch of PZN solutions were made without any added mandelic acid, with maximum heat treatment temperatures during synthesis of 60, 70, 80, 90 and 100 °C. A Zr:NO<sub>3</sub> ratio of 1:2 was used, the reasoning being that in a solution of greater acidity, zirconium cluster species would be at their smallest or least developed, as the acidity would be inhibiting hydrolysis to a greater extent. Thus it was hoped that initially, spectra would be dominated by bands from terminal hydroxy groups, and a more 'complete' transformation of terminal to bridging hydroxy groups would be seen following heat treatment. Starting with the apparent dissolution of the carbonate precursor, samples were taken from the reactor at 30-minute intervals until the reactor program had run to completion. Thus, the range of samples covered the common ramp starting temperature of 60 °C, the temperature ramp itself and the high temperature treatment, and at a point where the reactor contents were cooling back to near room temperature. Henceforth, Raman measurements of these samples show the changes in solution species bonding during synthesis, in relation to temperature, and time spent at a particular temperature (Figs. 3.32 – 3.37).

At a constant reactor temperature of 60 °C, no changes are seen in the Raman spectra throughout the whole time of synthesis, suggesting that the species that are present in the initial starting solution are the same as those seen after heating has ceased. Similar results are seen for a maximum temperature of 70 °C, so again, at these low temperatures the starting species generally persist. Upon increasing the maximum temperature to 80 °C, changes start to occur by the end of the heat treatment, though not until during the ramp has completed. The biggest differences in the Raman spectra during synthesis are seen for maximum temperatures of 90 and 100 °C, whereby the emergence and disappearance of bands is obvious by the end of the temperature ramp. The changes all occur within a spectral range of 600 – 350 cm<sup>-1</sup>, i.e. the region of the Raman spectra populated by the bands arising from Zr-O(H) bonding. Also seen

in the following plots are the two bands for coordinated and aquated nitrate, which do not appear to change during heat treatment regardless of the temperature.

As can be seen from the peak assignments, the bands that change all relate to the consumption and formation of terminal and bridging hydroxy bridges, respectively. 12 This is most apparent for the bands indicative of terminal Zr-OH groups at ~580 and ~455 cm<sup>-1</sup>, which for heat treatment temperatures of 90 and 100 °C, disappear by the end of PZN synthesis. These bands in particular are known to be a sign of the presence of the zirconium tetramer itself. <sup>6, 7, 9, 14</sup> For two of the bands for the bridging Zr-OH groups, at ~540 and ~420 cm<sup>-1</sup>, it is not clear from just looking at the spectra whether these peaks actually increase in intensity, as they are initially obscured by those for the terminal hydroxy groups; they are a sign of other more hydrolysed or polymeric soluble species in equilibrium with the tetramer. <sup>6,7,14</sup> However, the remaining band for the bridging hydroxy groups, at ~375 cm<sup>-1</sup>, does grow, even with the disappearance of the broad terminal hydroxy band adjacent to it (and the intensity contribution of its tail). This band has been noted in the literature for aqueous solutions of zirconium submitted to reflux, which is similar to what happens during a PZN synthesis. In addition, there is the presence of a further band at  $\sim 480 - 490 \text{ cm}^{-1}$ . This was not noted explicitly or assigned by Southon et. al., though some of their reported spectra possibly show a sign of it, 12, <sup>13</sup> and bands in similar positions have also been reported for other aqueous solutions of zirconium.6 As such it is tentatively assigned as a further Zr-OH band, and marked by the green dotted lines in Figures 3.32 - 3.36.

Thus overall, there is a relative increase in the contribution to the spectra from hydroxy groups linking zirconium centres in the solution species, as the contribution from terminal hydroxy groups greatly diminishes. This is consistent with the idea of hydrolysis, the process behind the 'polymerisation' of zirconium cations in solution, whereby terminal hydroxy groups (and OH groups of coordinated water molecules) condense to form hydroxy bridges, linking more zirconium centres together. In other words, Raman measurements could

potentially give a measure (qualitative or quantitative) of the growth of zirconium species in aqueous solution.

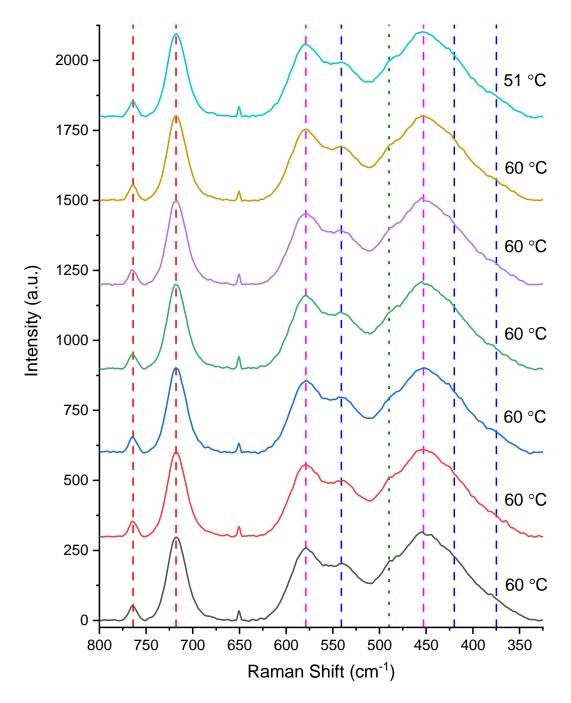


**Figure 3.32** Raman spectra from samples taken during a PZN synthesis, reaching a maximum heat treatment temperature of 60 °C. Order of sampling is bottom-to-top. Bands relating to Zr-OH<sup>t</sup>, Zr-OH<sup>b</sup> and nitrate are highlighted by the vertical dashed lines in magenta, blue and red respectively. The exact PZN temperatures when each sample was taken are labelled on the right. The spike at ~650 cm<sup>-1</sup> is an artefact of the instrument.

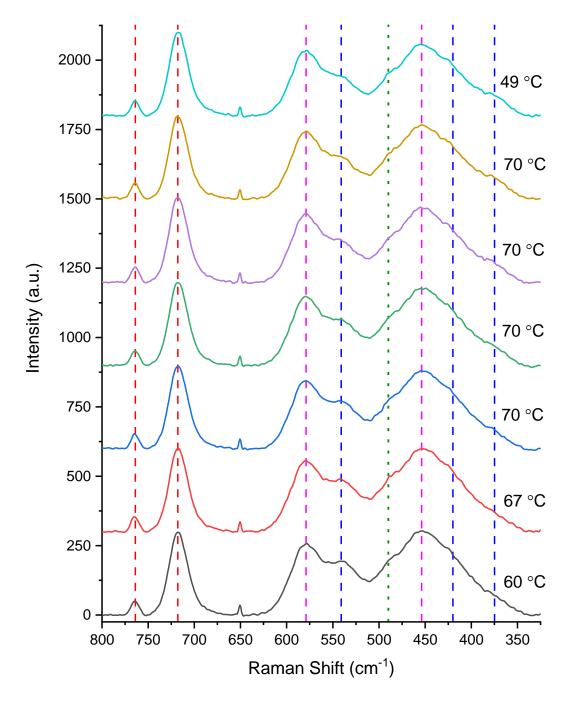


**Figure 3.33** Raman spectra from samples taken during a PZN synthesis, reaching a maximum heat treatment temperature of 70 °C. Order of sampling is bottom-to-top. Bands relating to Zr-OH<sup>t</sup>, Zr-OH<sup>b</sup> and nitrate are highlighted by the vertical dashed lines in magenta, blue and red respectively. The exact PZN temperatures when each sample was taken are labelled on the right. The spike at ~650 cm<sup>-1</sup> is an artefact of the instrument.

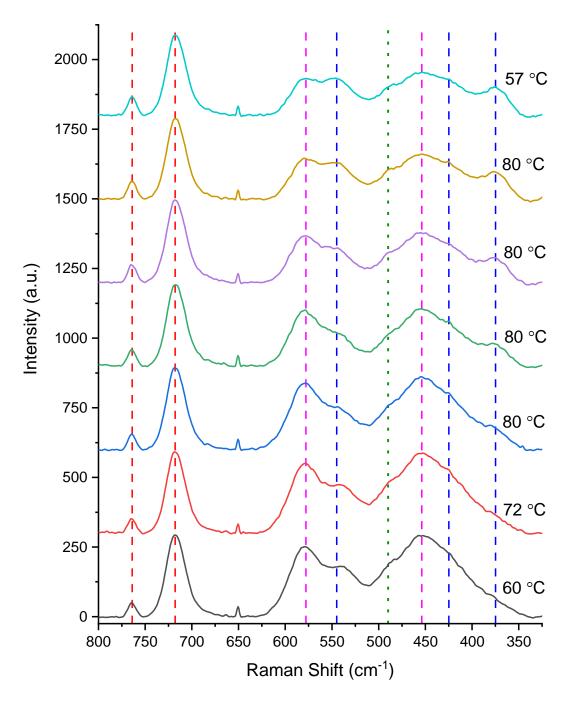


**Figure 3.34** Raman spectra from samples taken during a PZN synthesis, reaching a maximum heat treatment temperature of 80 °C. Order of sampling is bottom-to-top. Bands relating to Zr-OH<sup>t</sup>, Zr-OH<sup>b</sup> and nitrate are highlighted by the vertical dashed lines in magenta, blue and red respectively. The exact PZN temperatures when each sample was taken are labelled on the right. The spike at ~650 cm<sup>-1</sup> is an artefact of the instrument.

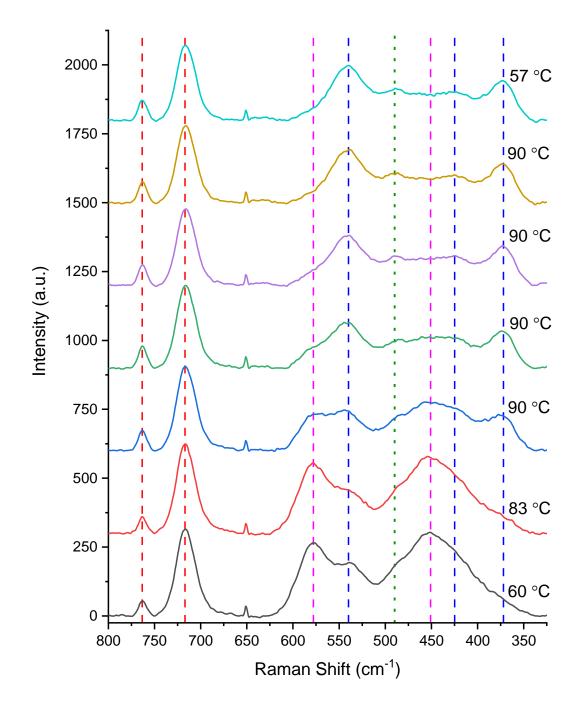


**Figure 3.35** Raman spectra from samples taken during a PZN synthesis, reaching a maximum heat treatment temperature of 90 °C. Order of sampling is bottom-to-top. Bands relating to Zr-OH<sup>t</sup>, Zr-OH<sup>b</sup> and nitrate are highlighted by the vertical dashed lines in magenta, blue and red respectively. The exact PZN temperatures when each sample was taken are labelled on the right. The spike at ~650 cm<sup>-1</sup> is an artefact of the instrument.

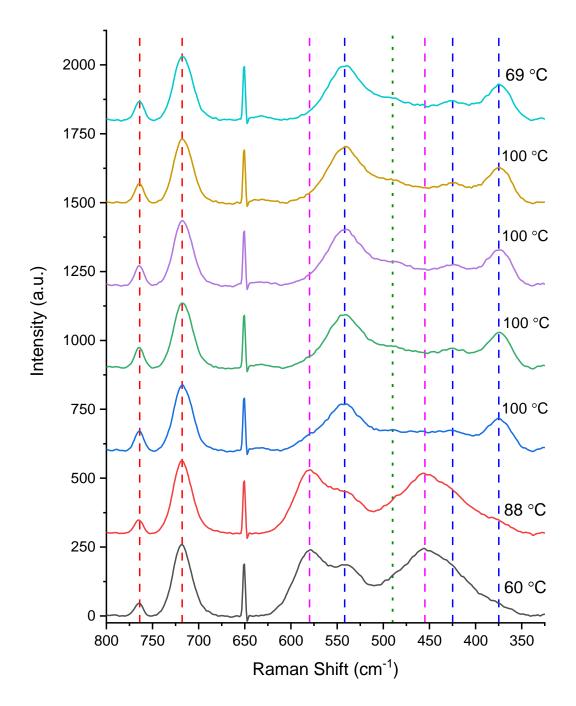


**Figure 3.36** Raman spectra from samples taken during a PZN synthesis, reaching a maximum heat treatment temperature of 100 °C. Order of sampling is bottom-to-top. Bands relating to Zr-OH<sup>t</sup>, Zr-OH<sup>b</sup> and nitrate are highlighted by the vertical dashed lines in magenta, blue and red respectively. The exact PZN temperatures when each sample was taken are labelled on the right. The spike at ~650 cm<sup>-1</sup> is an artefact of the instrument.

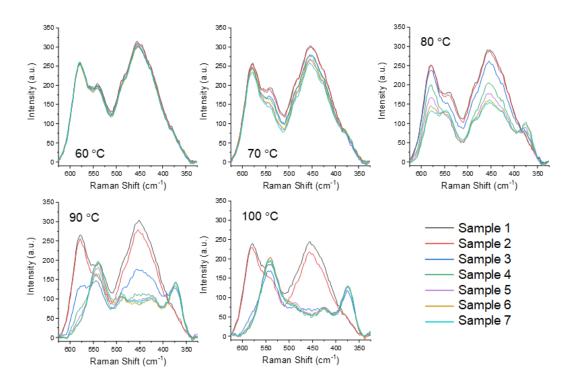


**Figure 3.37** Plots of Raman spectra as depicted in Figures 1-5, more clearly showing the changes in the spectra between subsequent samples. The maximum temperature for each run is given for each plot.

## 3.5.4.2 Quantitative Analysis of Spectra

Figures 3.32 – 3.37 show *qualitatively* the relative changes in the bands seen in Raman spectra of the studied zirconium solutions. To put a number to these changes, it is possible to use the peak intensity (relative or absolute) of a particular band to follow the changes in the abundance of a particular phase or functional group in a material.<sup>36</sup> Alternatively, a Raman band or group of bands can be parameterised by deconvolution and/or peak fitting, giving values for peak position, area, full width at half-maximum, and intensity. Thus taking into account the position of a Raman band and its overall shape, in addition to the intensity. A number of different fitting profiles are commonly used, such as Gaussian and Lorentzian, depending on band and vibrational mode symmetry, or the type of material being analysed.<sup>37</sup>

The Raman spectra are relatively complex in the 650 - 350 cm<sup>-1</sup> spectral region, due to the presence of six overlapping bands. Fitting these truly independently of each other is thus difficult; some compromises were required in order to obtain satisfactory fits that gave

rise to trends that made chemical sense. Peak fitting of spectra was carried out in order to deconvolute individual bands and to allow calculation of the respective peak areas. Fitting with a Gaussian profile was tested but the algorithm would not converge despite hundreds of fitting iterations. Instead, a Voigtian profile was found to work, which is a sum or convolution of a Gaussian and a Lorentzian function. Ultimately, the approach that was finally settled upon was as follows. Given the behaviour and nature of the ~480 and ~420 cm<sup>-1</sup> bands (i.e. the relatively weak intensity and that no significant changes are seen for these bands unlike for the others in the spectra in the same region with time and temperature), all fitting parameters for these (peak position, area, Gaussian width and Lorenztian width) were fixed for all fits. The parameters used were determined from averaging those from four-peak fits of the last four spectra for the 100 °C synthesis (top four spectra, Figure 3.37), assuming that the bands for terminal OH groups at ~580 and ~450 cm<sup>-1</sup> were totally absent. Multiple (six – or four, to be precise) peak fits were then carried out for the five sets of spectra in order of progress of synthesis, with the 'output' of one fit used as the initial parameters for the next. The position of the bridging OH band at ~375 cm<sup>-1</sup> was also fixed at 374 cm<sup>-1</sup> (but with all other parameters allowed to vary) due to it often being obscured due to the intensity of the adjacent bands. Otherwise, its fitted position would vary greatly until its peak maximum became more prominent than just a shoulder.

Plotted peak areas and plotted normalised peak areas from fits following the described routine, used as a measure of the relative abundance of different types of OH group, are presented in Figures 3.38 and 3.39, respectively.

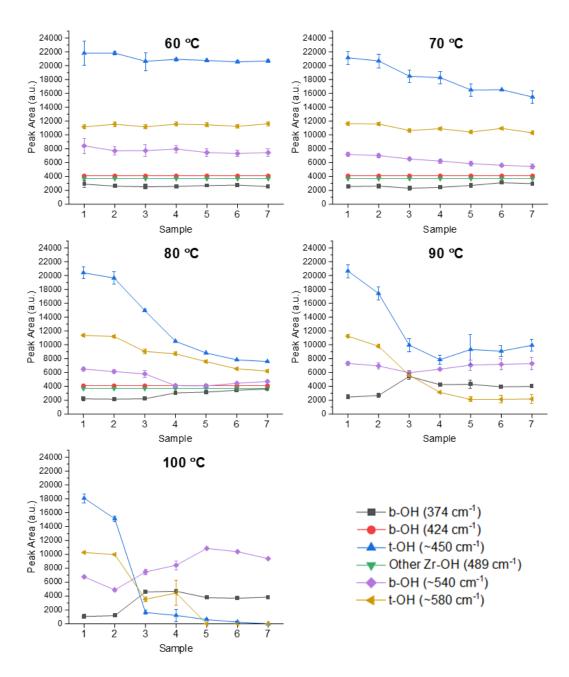


**Figure 3.38** Peak areas determined from Voigt profile fitting to Raman bands for terminal and bridging Zr-OH groups, from the study into variation of PZN heat treatment temperature. Plots for the bridging Zr-OH band at 424 cm<sup>-1</sup> and the band at 489 cm<sup>-1</sup> (those fixed during the fitting procedure) have been omitted from the 90 and 100 °C plots for clarity.

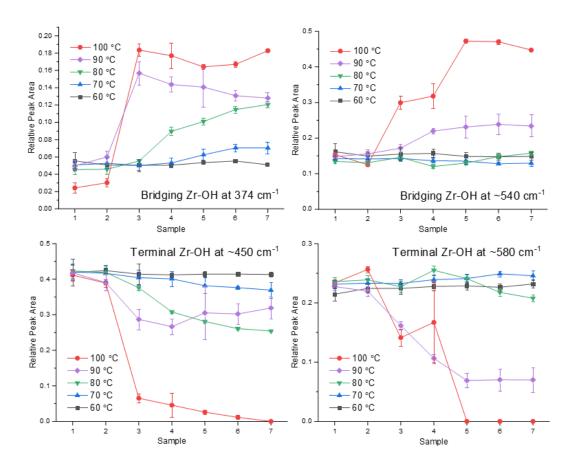


**Figure 3.39** 'Total-area' normalised peak areas determined from Voigt profile fitting to Raman bands for terminal and bridging Zr-OH groups, from the study into variation of PZN heat treatment temperature. Areas are normalised according to the total area of bands covered by the fitting procedure.

As can be seen in Figures 3.38 and 3.39, during the synthesis of PZN solution there is a change in the relative abundance of hydroxy groups, with those of a terminal nature generally decreasing in number and those that bridge zirconium centres correspondingly increasing in number, although the extent to which this occurs is strongly influenced by the temperature. This is direct spectroscopic evidence for increasing connectivity of zirconium cations in solution, which takes place *via* hydrolysis. At 60 °C, the changes are insignificant (Fig. 3.38), suggesting that at this temperature the same size or type of zirconium solution clusters tend to persist. Upon an increase in heat treatment temperature, the conversion of terminal hydroxy groups to bridging hydroxy groups is correspondingly greater. From further comparison, it appears that the bridging band at 374 cm<sup>-1</sup> and the terminal band at ~450 cm<sup>-1</sup> (Fig. 3.39) change more readily, at the lower temperatures especially, than the other bridging and terminal

bands under investigation here. It is noted that the increase in relative peak area for the  $\sim$ 450 cm<sup>-1</sup> terminal hydroxy band and decrease in area of the 374 cm<sup>-1</sup> bridging hydroxy band for samples 4 – 7 at 90 °C is attributed to the effects of significant overlap of adjacent bands, whose change might not be in the same direction. Overall, it has been seen throughout the process of fitting the Raman spectra that 'isolating' individual bands in order to parameterise their changes is non-trivial, particularly due to the overlap of bands arising from terminal hydroxy groups, which are initially significantly larger in area and of a greater intensity that those of bridging hydroxy groups.

Results of normalisation of peak areas to span relative peak areas of between 0 and 1 were also subject to the difficulties described above; the trends being the clearest at the higher temperatures and for one of the bridging and one of the terminal bands in particular. This is shown in Figure 3.40. The decrease in the relative peak area of the bridging OH band at 374 cm<sup>-1</sup> is attributed to the issues already mentioned. Overall however, the key trends are still seen; the disappearance of a band arising due to terminal hydroxy groups and the emergence of a band attributable to bridging hydroxy groups, consistent with the action of hydrolysis of zirconium in the heat-treated solutions. It was also noted that the crossover of the plots, for 90 and 100 °C in particular, occurred at a relative peak area of approximately 0.5. This was interpreted as one sign that the consumption of terminal hydroxy groups is (inversely) proportional to the creation of bridging hydroxy groups, *i.e.* the loss of terminal hydroxy groups is due to the transformation into bridging hydroxy groups with no distinct intermediate species.

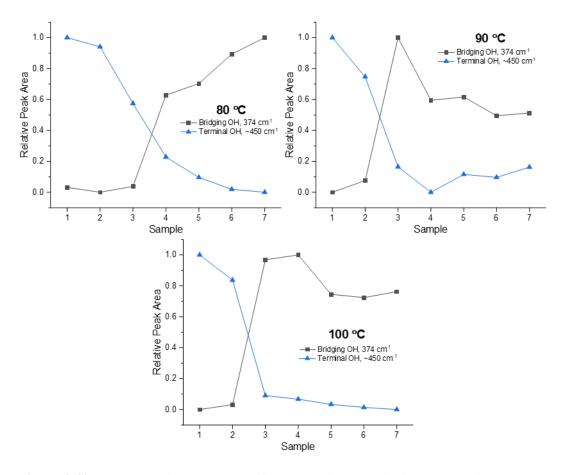


**Figure 3.40** 0 – 1 normalised peak areas for bands of select bridging and terminal hydroxy groups from Raman spectra of samples from PZN syntheses reaching maximum temperatures of 80, 90 and 100 °C.

The bands arising due to free nitrate in solution and nitrate groups coordinated to zirconium centres were also fitted, and the relative areas of these with respect to one another also change with temperature, as shown in Figure 3.41. It is seen that the proportion of coordinated nitrate increases with increasing heat treatment temperature. This builds upon previous observations by Southon *et al.*, who noted that the amount of coordinated nitrate remains roughly constant – although in their work, only a small number of samples were measured and the solutions/sols studied were synthesised at a temperature of only 70 °C.<sup>12</sup> Southon also found *via* <sup>14</sup>N NMR that in general, aquated nitrate anions become weakly associated with the surface of the solution zirconium particles, without directly coordinating. It was considered that in the case of the PZN solutions studied here, that at the higher

temperatures, the larger zirconium species provide a larger 'surface' for association of nitrate, making subsequent coordination of nitrate to zirconium more likely.

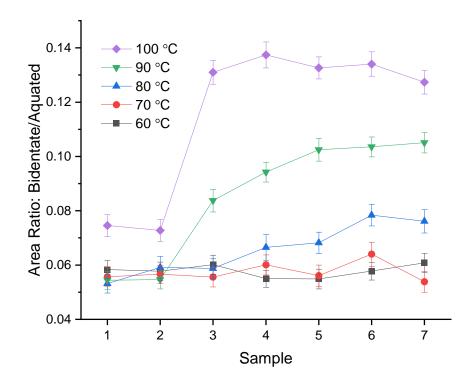


**Figure 41** Ratio of the peak areas of the bands for bidentate (760 cm<sup>-1</sup>) and aquated nitrate groups (715 cm<sup>-1</sup>) seen in Raman spectra of 1:2 Zr:NO<sub>3</sub> PZN solutions, according to synthesis heat treatment temperature.

Plots of all of the fits to Raman spectra carried out can be found in the Appendices (Figs. A.1 (Zr-OH band fits) – A.10 (nitrate band fits)).

## 3.6 Summary and Conclusions

Data from infrared spectroscopy measurements of nitrate based aqueous solutions of zirconium (PZN), known to be uncommon in the literature, have been reported, and a number of bands assigned. Spectra are seen to vary with solution composition (ratio of nitrate to zirconium, and mandelic acid level relative to zirconium). Overall, the usefulness of this technique to industry is likely limited.

Conversely, Raman measurements of aqueous solutions of zirconium have proved much more informative. Bands are easily distinguished and assigned, with the behaviours of which reflecting the chemical changes that take place in solution during or as a result of the heat treatment during synthesis. Spectra also vary accordingly with solution composition, and clear differences are seen between solutions base upon chloride and nitrate, in terms of the bands indicative of Zr-OH groups, as well as the presence or not of the respective anions. Raman spectroscopy also has the benefit here of detecting the mandelic acid or mandelate in solution, unlike with infrared spectroscopy. The growth and development of zirconium species in aqueous solution have been followed during synthesis in more detail than seen previously in the literature, and across a wider range of temperatures, showing the transformation from initial tetramer-like species to more hydrolysed, polymerised species, despite the complexity of fitting the multiple Zr-OH bands between 650 – 350 cm<sup>-1</sup>. Understanding of the behaviour of the nitrate anion in these solutions has also been furthered.

Raman spectroscopy would be a suitable choice of analytical technique for industry to follow and confirm or validate the changes in these solutions during synthesis or manufacture. Spectrum analyser equipment could be combined with optical fibre probes, <sup>38, 39</sup> robust enough to withstand high levels of acidity or high temperatures, to give a truly *in-situ* insight into the properties of PZN and other solutions on plant. As such the progress of the synthesis of a solution can be followed in almost real-time as high-quality spectra can be measured in as little as minutes or seconds. Information such as this can ultimately save industry time and money especially when the scale of manufacture is on the order of many kilograms or tons; where resource expenditure (time, energy, supervisory manpower or other human input) is high.

## 3.7 Bibliography

- S. Thomas, R. Thomas, A. K. Zachariah and R. K. Mishra, Spectroscopic Methods for Nanomaterials Characterization, Elsevier, Amsterdam, 2017.
- 2. F. G. Baglin and D. Breger, *Inorg. Nucl. Chem. Letters*, 1976, **12**, 173-177.
- 3. R. C. Fay and T. J. Pinnavaia, *Inorg. Chem.*, 1968, **7**, 508-514.
- 4. A. Clearfield, *Rev. Pure and Appl. Chem.*, 1964, **14**, 91-108.
- 5. A. S. Solovkin and S. V. Tsvetkova, *Russ. Chem. Rev.*, 1962, **31**, 655-669.
- J.-L. Tosan, B. Durand, M. Roubin, F. Chassagneux, L. Mosoni, F. Bertin and B. Moraweck, *J. Non-Cryst. Solids*, 1993, 160, 167-176.
- 7. J.-L. Tosan, B. Durand, M. Roubin, F. Chassagneux and F. Bertin, *J. Non-Cryst. Solids*, 1994, **168**, 23-32.
- 8. K. A. Burkov, G. V. Kozhevnikova, L. S. Lilich and L. A. Myund, *Russ. J. Inorg. Chem.*, 1982, **27**, 804-806.
- 9. S. Hannane, F. Bertin and J. Bouix, *Bull. Soc. Chim. Fr.*, 1990, **127**, 43-49.
- 10. M. Aberg and J. Glaser, *Inorg. Chim. Acta*, 1993, **206**, 53-61.
- P. D. Southon, J. R. Bartlett, J. L. Woolfrey and M. G. Stevens, *Ceram. Trans.*,
   1998, 81, 75-80.
- P. D. Southon, J. R. Bartlett, K. S. Finnie, J. L. Woolfrey, B. Ben-Nissan and G. S.
   K. Kannangara, J. Aust. Ceram. Soc., 1999, 35, 7-12.
- P. D. Southon, J. R. Bartlett, J. L. Woolfrey and B. Ben-Nissan, *Chem. Mater.*,
   2002, 14, 4313-4319.
- M. Ambrosi, E. Fratini, P. Canton, S. Dankesreiter and P. Baglioni, *J. Mater. Chem.*, 2012, 22, 23497-23505.
- 15. A. Gossard, G. Toquer, S. Grandjean and A. Grandjean, *J. Sol-Gel Sci. Technol*, 2014, **71**, 571-579.
- 16. D. M. Carey and G. M. Korenowski, *J. Chem. Phys.*, 1998, **108**, 2669-2675.
- 17. H. Cohn, C. K. Ingold and H. G. Poole, *J. Chem. Soc.*, 1952, 1952, 4272-4282.

- 18. W. A. Guillory and M. L. Bernstein, *J. Chem. Phys.*, 1975, **62**, 1058-1060.
- C. C. Addison, N. Logan, S. C. Wallwork and C. D. Garner, Q. Rev. Chem. Soc., 1971, 25, 289-322.
- B. M. Gatehouse, S. E. Livingstone and R. S. Nyholm, *J. Chem. Soc.*, 1957, 1957, 4222-4225.
- 21. L. V. Volod'ko and L. T. Huoah, *J. Appl. Spec.*, 1968, **9**, 1100-1104.
- 22. R. A. Marcus and J. M. Fresco, *J. Chem. Phys.*, 1957, **27**, 564-568.
- 23. C. K. Ingold and D. J. Millen, 1950, **1950**, 2612-2619.
- J. M. Crosland, E. K. Corlett, D. Scapens, N. Guillou, S. P. Brown and R. I. Walton,
   Chem. Commun., 2020, 56, 10159-10162.
- 25. G. E. McGraw, D. L. Bernitt and I. C. Hisatsune, *J. Chem. Phys.*, 1965, **42**, 237-244.
- 26. S. A. Stern, J. T. Mullhaupt and W. B. Kay, *Chem. Rev.*, 1960, **60**, 185-207.
- J. Jose, M. J. Bushiri, K. Jayakumar and V. K. Vaidyan, *AIP Conf. Proc.*, 2008,
   1075, 125-127.
- 28. J. H. Meisenhelder and A. A. Siczek, *Radiochim. Acta.*, 1980, **27**, 223-227.
- N. Nakamoto, Infrared and Raman Spectra of Inorganic and Coordination Compounds, John Wiley & Sons, New York, 4th edn., 1986.
- 30. A. B. P. Lever, E. Mantovani and B. S. Ramaswamy, *Can. J. Chem.*, 1971, **49**, 1957-1964.
- 31. E. F. Lopez, V. S. Escribano, M. Panizza, M. M. Carnasciali and G. Busca, *J. Mater. Chem.*, 2001, **11**, 1891-1897.
- 32. F. Bollino, E. Armenia and E. Tranquillo, *Materials*, 2017, **10**, 757-775.
- 33. R. Jin, Y. Zhang, S. Huang, P. Wang and P. Tian, *Chin. J. Chem.*, 2011, **29**, 13-20.
- V. M. Aksenenko, N. S. Murav'ev and G. S. Taranenko, *J. Appl. Spec.*, 1986, 44, 87-91.
- 35. H. M. Badawi and W. Forner, *Spectrochim. Acta A*, 2011, **78**, 1162-1167.
- 36. P. H. Colomban and A. Slodczyk, *Acta Phys. Pol. A*, 2009, **116**, 7-12.
- 37. X. Yuan and R. A. Mayanovic, *Appl. Spectrosc.*, 2017, **71**, 2325-2338.

- 38. C. K. Chong, C. Shen, Y. Fong, J. Zhu, F.-X. Yan, S. Brush, C. K. Mann and T. J. Vickers, *Vib. Spectrosc.*, 1992, **3**, 35-45.
- 39. C. Wang, L. Zeng, Z. Li and D. Li, J. Raman Spectrosc., 2017, 48, 1040-1055.

## **Chapter 4:**

# **Characterisation of Aqueous Zirconium Solutions by Small-Angle X-Ray Scattering**

## 4.1 Introduction

This chapter describes work carried out to investigate the properties of aqueous nitrate-based solutions of zirconium (LMT PZN-type solutions) via small-angle X-ray scattering (SAXS). SAXS<sup>1, 2</sup> is an X-ray scattering technique whereby interaction of X-ray radiation (from a laboratory source or synchrotron) with nanoscale differences in sample electron density (contrast) permits determination of particle size and shape, including pore size and molecular weight for example. 'Particle' in this sense covers solid, liquid and gaseous domains in solid or liquid samples, for example metal oxide clusters suspended in a liquid (whereby the contrast is between the electron-rich solid particles and the less electron dense bulk solution). Every particle or part of the sample illuminated by the X-ray beam will contribute to scattering; thus, it is a measure of average structure. In the ideal case, the best results are obtained from samples exhibiting monodispersity of particles with no inter-particle interaction. SAXS is typically observed over scattering angles of  $0.1 - 5^{\circ} 2\theta$ , providing structural information over distances of 1 – 100 nm, depending on the wavelength of the radiation used. These ranges can be extended to probe larger or smaller particle sizes or interatomic distances; via Ultra Small-Angle X-ray Scattering (USAXS) and Wide-Angle Xray Scattering (WAXS).3 WAXS is commonly encountered in materials characterisation as powder X-ray Diffraction (XRD). SAXS is non-destructive and requires only minimal sample preparation; thus finds use in a very broad range of fields, including biological materials,5,6 polymers and colloids, 7-9 inorganic materials and nanocomposites, 10-12 and pharmaceuticals. 13 Aqueous solutions of zirconium are particularly suited to analysis by this technique, due to the great electron density contrast between the water matrix and hydrolysed zirconium cluster species, allowing for collection of high-quality data over short time frames on the order of minutes. However for measurements of particularly weakly scattering samples, or when greater time resolution is required, the very intense monochromatic X-ray beams generated by synchrotron sources make these facilities the superior choice. <sup>14</sup> Specific results presented here include characterisation of PZN solutions of varying composition, and *in situ* observation of changes taking place in the solutions due to heat treatment.

## 4.2 Explanation of Terms

Definitions of a number of terms regarding small-angle X-ray scattering specific to this chapter are given in this section.

Radius of gyration,  $R_g$ :  $R_g$  is a measure of the effective size of a species and the spread of its mass (or more specifically for SAXS, electron density), calculated as the root mean square distance of an object's parts from its centre of gravity.

<u>Guinier Plot:</u> A plot of scattering data in the form ln[I(q)] vs.  $q^2$ , derived from taking the natural logarithm of the equation describing the relationship at low q between scattered intensity I(q), the intensity at zero scattering angle I(0) and the scattering vector q:

$$I(q) = I(0) \cdot \exp\left(-\frac{q^2 R_g^2}{3}\right) \quad ln[I(q)] = ln[I(0)] - \frac{q^2 R_g^2}{3}$$

The slope of this plot is thus equal to  $-R_g^2/3$  and allows for the determination of the Guinier radius, or radius of gyration  $R_g$ .

<u>Longrods Plot</u>: A 'longrods' plot, or Guinier plot for elongated objects is a modification of the Guinier plot for rod-like scattering objects. Here a plot of  $\ln[q \cdot I(q)]$  vs.  $q^2$  will give a linear region with a slope equal to  $-R_c^2/2$ , where  $R_c$  is the radius of gyration of the cross-section of the scattering particles.

<u>Power law:</u> A power law is a relationship between two quantities whereby a relative change in one results in a proportional relative change in the other, independent of the initial size of the two quantities. In other words, where one quantity varies as an exponent, or power, of the other.

<u>Fractal:</u> An object that displays self-similarity – the same 'type' of structures – on all length scales.

Surface fractal: A solid with a fractal surface.

<u>Mass fractal:</u> A structure containing branching and crosslinking to form a 3D network, or structure composed of monomeric units or small particles that are clustered.

## 4.3 Literature Overview

Reports in the literature of applications of SAXS to investigating the properties of aqueous solutions of zirconium (and similar samples such as metal and metal oxide clusters in solution) in recent decades are plentiful, and include examples of the study of those involving nitrate.

One of the early studies by Toth et al. 15 involved dissolution of zirconium nitrate to produce solutions of concentration of 0.035 - 1.0 M, adjusted to a pH of 2.2 with small amounts of NaOH. Guinier plots produced from scattering data gave  $R_g$  values of 4.6  $\pm$  0.1 Å for all concentrations. They determined that scattering was taking place from species of tetramer dimensions and not from zirconium monomers. The best fits to their scattering data suggested the solution zirconium species took the form of particles that were overall cylindrical in shape. In other work by Toth et al., designed to identify other species in equilibrium with the zirconium tetramer in solution, <sup>16</sup> 0.05 M zirconium oxychloride solutions were prepared with varying amounts of added H<sup>+</sup> and OH<sup>-</sup>. For a [H<sup>+</sup>]<sub>added</sub> of 1.0 to 0.4, both  $R_g$  and I(0) do not change significantly, suggesting the species was largely unchanged in this range, and was identified as the zirconium tetramer. The  $R_g$  for  $[H^+]_{added}$  of 1.0 M is 3.8  $\pm$  0.2 Å, similar to that calculated for the species  $[Zr_4(OH)_8(H_2O)_{16}Cl_6]^{2+}$  and  $Zr_4(OH)_8(H_2O)_{16}Cl_8$ , leading to the conclusion that [Zr<sub>4</sub>(OH)<sub>8</sub>(H<sub>2</sub>O)<sub>16</sub>Cl<sub>x</sub>]<sup>(8-x)+</sup> is to be considered the scattering entity in these solutions. When the solution acidity was further decreased ([H<sup>+</sup>]<sub>added</sub> < 0.4 M), both  $R_g$  and I(0) increase, and at an  $[OH^-]_{added}$  value > 0 M, the  $R_g$  and I(0) increase rapidly, indicative of the formation of larger molecular weight species.  $R_g$  increased from 3.8 to 5.1 Å as  $[H^+]_{added}$  decreases from 0.4 to 0.0 M. The authors noted that the largest  $R_g$  value could be explained by the presence of a zirconium octamer, such as  $[Zr_8(OH)_{20}(H_2O)_{24}Cl_{16}]$ . There were two possible configurations of tetramers that can be considered to make this; two tetramers attached along a matching edge in a sheet-like fashion *via* two double-hydroxy bridges, and two tetramers stacked atop each other linked *via* four single OH bridges. These gave calculated  $R_g$  values of 5.4 and 5.0 Å respectively, but the values are were not sufficiently different to distinguish between the two structures based on  $R_g$  alone. Subsequent comparison to calculated scattering curves did however reveal that the octamer formed from two stacked tetramers was the most plausible structural description.

A 1997 paper by Singhal et al. developed further the work of the previous authors.<sup>17</sup> Three 0.05 M solutions of zirconium oxychloride of pH 1.22, 1.5 & 1.7 were studied in relation to solution pH, aging time and aging temperature. During the initial stages of zirconium cluster growth cross-section Guinier plots at large q revealed cross-section radii of gyration ( $R_c$ ) that were similar across different pH values; for solutions of pH 1.22  $R_c = 4.4$  Å, with  $R_c = 4.75$  Å after an extended period of aging. For solutions of pH 1.7, R<sub>c</sub> started at 4.2 Å, but increased on aging as revealed by non-linear Guinier plots. They interpreted this non-linearity as such: as clusters grow in size with time, they grow in different directions. Solutions with an initial pH of 1.5 were found to behave like those of pH 1.7. A reason for this was a possible change in the bonding in the tetramer due to loss of water. The Zr-Zr distance in the tetramer with Zr-(OH)<sub>2</sub>-Zr bonds increases from 3.56 to 3.89 Å upon condensation to form Zr-O-Zr bonds. Using 'longrods' plots, it was seen that for solutions of pH 1.2, aging for > 1250 min gives a power-law slope close to -1.0 at intermediate q values. Eventually, at higher pH and following further aging, the linear clusters transform into branched clusters or polymers with power-law slopes of -1.4 to -1.45. These scattering data indicate the formation of long rod-like particles with initial  $R_c$  of 4.2 – 4.4 Å. This was slightly larger than the calculated  $R_c$  of 4.0 Å for a single Zr tetramer but smaller than that for the octameric species (5.4 Å), suggesting that these polymeric zirconium species were unlikely to be formed from a species larger than the tetramer. The growth characteristics of the zirconium polymers could be obtained from the low-q region of the scattering data that was obtained as a function of time, aging temperature and initial solution pH. Clusters in the pH 1.7 solution aged at 80.5 & 92 °C grew larger than those in the solution with an initial pH of 1.2, indicating that the growth rate is proportional to [OH] (or correspondingly inversely proportional to [H<sup>+</sup>]). They noted a very slow growth rate at low aging temperatures, reporting that I(0) increases dramatically at the beginning and then displays linear behaviour with time. The initial rapid growth period decreased as the aging temperature is increased. This implied that at the beginning of the aging process, species grew to a particular polynuclear cluster before they condensed to produce large polymers and the rate of formation of these clusters is a function of the aging temperature. The final conclusions of the work are that the primary particles that exist in solution have a shape dictated by pH. Primary particles formed by hydrolysis and condensation coalesce to form larger aggregates which eventually precipitate. Other SAXS results of theirs revealed that the larger aggregates are mass fractals which restructure whilst growing.

Hu *et al.* studied 'thermo-hydrolytically polymerised' solutions of zirconium oxychloride to study early-stage colloid formation. SAXS results for the initial solutions (pre-aging) were consistent with the presence of zirconium tetramers, with  $R_g$  values between 4.0 and 5.0 Å for solutions with concentrations spanning 0.025 to 1.0 M. Following incubation of 0.05 M solutions at 100 °C for 24 hours, significant changes were seen in  $R_g$  values as determined from Guinier plots. 'Large-end' cluster/particle sizes (from the Guinier slope at low q) increase from 4.5 to 110 Å, and the 'small-end' sizes at high q increase slightly from around 4.5 Å to 5 – 6 Å. The radii of gyration of the of the cross-section of the rod-shaped particles ( $R_c$ , found from linear slopes of longrod plots) were found to be 4.3, 4.5, 4.6, 4.8 and 4.8 Å for the 2, 4, 10, 16, and 24 hour incubated samples respectively. The constant presence of the small-sized species suggested that the consumption of the species to form the rods is a slow process and thus rate limiting for the transition of the solution into sol. Results for 0.1 M solutions showed similar behaviour, except that the initial solution did not appear to be

polymerised even after a few days of storage at room temperature. It is possible that the higher acidity of the solution inhibited the hydrolytic polymerisation process. Increasing the initial zirconium concentration was found to increase the rate of polymerisation at elevated temperatures, and for a given incubation time, the particle sizes were larger for 0.1 M compared to 0.05 M.

SAXS of nitrate-based solutions and sols of zirconium made from zirconium carbonate and nitric acid were covered by Southon.<sup>19</sup> The results were consistent with scattering by spherical particles; best fitted by a sphere with an  $R_g$  of 0.4  $\pm$  0.04 nm and diameter 0.52 nm. For sol samples, scattering data were best fitted by a plate model, with a plate size of 2.8  $\pm$  0.4 nm wide by 0.5  $\pm$  0.1 nm thick.

Kanazhevskii *et al.* briefly discussed SAXS results for zirconium hydroxide and oxychloride solutions with varying amounts of added sulfuric acid, as well as for zirconium sulfate solution. They only said that in all solutions studied that the particles present had a typical diameter of the equivalent sphere of an order of 12 - 18 Å, and the size of the 'mononuclear complex' did not exceed 6 - 7 Å, so larger than that expected for an individual tetramer. No other details on their interpretation of this data were provided.

In a study of ammonia-induced precipitation from zirconium oxychloride and zirconium-yttrium chloride solutions, Carter *et al.* reported that SAXS results implied that all solutions studied (either [Zr] = 0.81 or 1.62 M) contained species of an  $R_g$  of 3.9 – 4.4 Å (± 0.3 Å),<sup>21</sup> which is a very small size to be determined from SAXS data. No comment was made on particle shape or morphology but that the results were otherwise consistent with the literature.

Ambrosi *et al.* investigated the synthesis of tetragonal zirconia *via* zirconium hydroxide nanoparticles prepared from aqueous 0.39 M solutions of zirconium oxychloride.<sup>22</sup> Addition of sodium hydroxide resulted in the precipitation of a white, gelatinous solid that restructured upon aging. Fitting of SAXS data revealed the presence of large aggregates with

an  $R_g$  of around 150 Å. Over time these aggregates re-arranged, and after 1 week of aging elongated or rod-like species formed which were about 70 Å long with a cross-section of about 5.5 Å. After this further de-aggregation took place and a clear solution was formed within two months. This solution contained spherical particles with an  $R_g$  of about 6.2 Å. Intermediate samples contained species with an apparent overall radius of 50 – 80 Å. All results showed the presence of oligomeric species with  $R_g$  values spanning 5.3 – 6.3 Å – both slightly too large for an individual zirconium tetramer.

A study of zirconium nitrate solutions of [Zr] = 0.03, 0.1, 0.16, 0.22 and 1.26 M, with added acetylacetonate and ammonia was carried out by Gossard *et al.* using SAXS.<sup>23</sup> For the pure zirconium nitrate solutions a pseudo Bragg peak was seen in the scattering data for the solution of [Zr] = 1.26, which they interpreted as a sign of object interacting in solution. None of the solutions were seen to change with time, and scattering data were consistently fit with a monodisperse rod-like particle form factor – assumed to be stacks of tetramers. Radii of the tetramer stacks were found to decrease slightly as [Zr] increased, though always appear to be around 3 – 5 Å. The length of the tetramer stacks changed more dramatically with concentration; for the 0.03 M solution the length was approximately 44 - 45 Å whereas it is close to 14 - 15 Å for the 0.22 M solution.

Solutions of zirconium acetate in dilute acetic acid of a range of zirconium concentrations with added NaCl at different concentrations were studied by Brenholm *et al.*<sup>24</sup> Their data showed that even at room temperature extended oligomers were present with an approximate length of  $100 \pm 15$  Å and radii of  $4.9 \pm 0.9$  Å. This radius was found to be independent of zirconium concentration. They noted that the calculated radius of gyration for an individual tetramer, based upon the structure of crystalline zirconium oxychloride, is 3.8 Å. The true shape is an intermediate between a sphere  $(R = (5/3)^{1/2} \cdot R_g)$  and a thin disc  $(R = \sqrt{2R_g})$ , which constrains the geometric cross-section radius of an individual tetramer to 4.9 - 5.4 Å.

## **4.4 Experimental Methods**

## 4.4.1 Theory of SAXS

Upon irradiation of a sample with an X-ray beam, one process that may occur is absorption. There is a chance that an incoming X-ray photon can eject an electron from an atom of the sample, leaving a vacancy in an atomic orbital (Fig. 4.1 A(i)). Electrons of higher energies in the atom can then switch orbitals to fill this vacancy, and in doing so give off excess energy in the form of fluorescence (Fig. 4.1 A(ii)). Alternatively, a sample can scatter the X-ray beam. Atoms can scatter the incident radiation in all directions, giving an almost constant background scatter across small angles. In addition, 'particles' (see Section 4.1) within the sample can give rise to so-called 'excess scattering' due to the differences in composition or electron density within the sample. These particles are of sizes comparable to the wavelength of the incoming X-rays. Measuring the angle-dependent distribution of the scattered radiation allows for conclusions to be drawn about the average structure of a material. In the case of Thomson scattering, X-ray photons can strike electrons bound to atoms of the sample without transferring energy to the electrons (elastic scattering). These electrons then oscillate with the same frequency as the incoming radiation, and subsequently emit their own radiation of the same frequency. This results in coherent scattering, as the radiation emitted by groups of neighbouring atoms occurs simultaneously. As such, interference patterns may be produced which contain structural information about a sample. The extent to which the interference is constructive or destructive depends on the angle of observation 20 and the distance r between the atoms causing the scattering (Fig. 4.1 B). These distances that are measured are done so in relation to the wavelength  $\lambda$  of the incoming X-rays, so in order to make them independent of  $\lambda$ , the scattered intensity I(q) is given as a function of the scattering vector q, where  $q = (4\pi/\lambda) \cdot \sin(\theta)$ . q therefore takes units of inverse distance, usually reciprocal Ångströms, Å-1. As such, scattering patterns are referred to as 'the structure in reciprocal space' whereas the sample causing the scattering is said to have a 'structure in real space.'

**Figure 4.1** Possible processes that may occur when an X-ray photon interacts with an atom of a sample (A, top), and the creation of an interference pattern seen by an X-ray detector from the scattering of X-rays by atoms in a sample (B, bottom). Diagrams have been adapted by the author from Ref. 3.

The scattering of a single particle can be thought of as the interference pattern created by all of the scattered X-rays from all of the atoms (electrons) inside the particle, and is known as the form factor, P(q), which varies in a manner characteristic to the shape (or form) of the particle in question. If one considers the example of scattering from solid particles suspended in a liquid, only if the particles are all identical in size and shape, i.e. they are monodisperse, and the solution is sufficiently dilute that the particles are spaced far apart, does the overall observed scattering pattern resemble the form factor of that particle. However in reality, it is more likely that the sample in question contains particles of a number of different sizes, in which case the overall scattering pattern is considered to be the sum of all of the form factors of the different sized particles. If a sample or particle system is densely packed (e.g. a concentrated solution of particles, or aggregated particles), then it is possible that the distances between particles may be comparable to the distances between atoms within the particles, in which case the overall scattering will contain contributions from neighbouring particles. This additional scatter scales with the form factor P(q) of the particles and is known as the structure factor; it contains information regarding the relative positions of particles or scattering elements. This effect can become visible in scattering patterns as Bragg-like peaks; the distances in question can be related to the position of the peak in the scattering curve by  $d_{Bragg}$  $=2\pi/q_{peak}$  (Å).

## 4.4.2 Experimental Setup

SAXS measurements were carried out using a Xenocs Xeus 2.0 5m laboratory SAXS beamline. X-ray radiation was generated using a Cu K- $\alpha_1$  source ( $\lambda = 1.5406$  Å) and scattered intensity collected with a Dectris PILATUS3 R 300K hybrid photon counting detector. These items and other key components of this instrument are outlined in Figure 4.2.

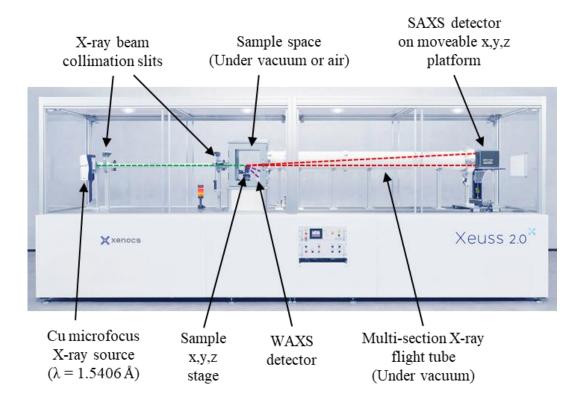


**Figure 4.2** The Xeus 2.0 SAXS instrument. The green dashed line indicates the incident X-ray beam, with scattered X-ray intensity represented by the red dashed lines. Wide-angle-scattered X-rays (short purple dashed lines) are collected by the WAXS detector (partially hidden, not used in this project).

The position of the SAXS detector was changed depending on the q range accessed during a particular measurement. Calibration or determination of the exact sample-detector distance was by means of a measurement of a sample of silver behenate, which gave a scattering pattern with easily distinguishable peaks. Knowing the measured q positions of these peaks compared to the theoretical positions, the sample-detector distance could be accurately determined. This was carried out by Steven Huband whenever the instrument setup was changed, using custom-made macros in Microsoft Excel. Calibration of X-ray intensity was carried out by means of a measurement of a glassy carbon NIST standard, the scattering data of which was compared to data provided by NIST to generate a scaling factor that could be used to normalise the scattering data of samples to absolute intensity<sup>25</sup> using the IRENA SAS analysis package<sup>26</sup> in Igor Pro software. Measurements of the X-ray beam itself (with no

samples or standards in place) were used to check the beam intensity and the alignment of the beam-stop in front of the detector.

SAXS measurements of aqueous zirconium solutions under ambient conditions were carried out using a multi-position sample holder occupied with solution-filled quartz glass capillaries, atop a motorised. x,y,z stage. In this way many measurements of different samples could be easily made using software macros to automate the process. Scattering patterns were collected for up to 10 minutes each. With each batch of samples, a measurement of deionised water in a quartz capillary was also taken, allowing the background scatter (scattering from the bulk water and walls of the capillary itself) to be subtracted from sample data. With each sample measurement, a measurement of the 'straight through beam' intensity was made with the beam-stop moved aside, to allow any X-ray absorption (and subsequent drop in intensity at the detector) to be accounted for, allowing for normalisation of intensity data on an absolute scale. An insert was used within the sample space to extend the distance over which the scattered X-rays could travel to the detector whilst still under vacuum. Otherwise, scatter from the air within the sample space was negligible, compared to that from the zirconium samples.

SAXS measurements with *in situ* heating were carried out using quartz capillaries inserted into a Linkam capillary heating stage, mounted atop the x,y,z platform. Macros were used to control the heating of the capillaries and measurement taking; measurement conditions were otherwise the same as the static studies. Measurement times were shortened to 1 minute to allow many snapshots of the sample to be taken during each heating run. The background measurement also took into account additional scatter from the Kapton® windows of the heating stage.

For SAXS measurements accessing the higher values of q, the sample stage and detector were positioned such that the sample-detector distance was as short as possible. This enabled higher-angle scattering to be picked up by the detector, which corresponds to the ability to probe smaller interatomic distances. This can be inferred from Bragg's Law,  $\lambda = 2d\sin\theta$ , where d is the interatomic distance and  $2\theta$  the scattering angle.  $\lambda$  is the X-ray

wavelength, and is constant. Some disassembly of the sample cabinet itself was required for this, the end result being that the entire sample space had to be under vacuum. As such, sample solutions were contained within quartz capillaries that had the top openings sealed with two-part epoxy resin (to avoid evaporation of the solutions and/or bubble formation). Otherwise, the experimental setup was as described previously, including the taking of a measurement of water to account for background scatter.

Data reduction<sup>27</sup> was carried out with Foxtrot software<sup>28</sup> supplied with the instrument. The overall goal here was to convert the 2D image from the detector into a 1D scattering curve, I(q) (y-axis) vs. q (x-axis), for each sample. Firstly, detector images are masked in certain areas to exclude regions of the detector where X-rays are not collected. This included the outer edges of the detector, the joins between the three individual sensor plates of the detector, the 'shadow' and close vicinity of the beam-stop and its supporting arm, and any dead pixels the detector was known to possess. Next, an azimuthal integration summed the intensity of all of the un-masked pixels in order to generate the data for the 1D plots of the intensity with respect to q. At this stage, data could be scaled according to the duration of collection time, the absolute intensity calibration and through-beam measurement, and the background scattering data subtracted (which was generated by treating the raw scattering data for the water-filled capillaries in the same way as the zirconium solution samples). This was carried out using a custom macro in Microsoft Excel created by Steven Huband.

#### 4.5. Results and Discussion

## 4.5.1 Characterisation of PZN Solutions of Varying Composition

## 4.5.1.1 Discussion of Results

SAXS measurements of aqueous solutions of zirconium with varying amounts of nitrate and mandelic acid are presented here, in Figures 4.3 - 4.5. Figure 4.3 shows the scattering from solutions with an equal molar amount of zirconium and nitric acid, and up to

5 mol% added mandelic acid, relative to Zr. The scattering curves are all of the same shape and thus may be assumed to be of the same form factor. The plateau in the scattering curves at low q suggests that no scattering particles are present which are of sizes greater than those corresponding to the probed range of q in these measurements; otherwise, the scattered intensity would continue to increase with decreasing q. This plateau, and the initial downwards slope with increasing q ( $q = 0.02 - 0.06 \text{ Å}^{-1}$ ), is characteristic of a Guinier region, which arises from scattering of particles that are of an overall size smaller than the distances being probed at that particular value of q. This region defines the radius of gyration,  $R_{\rm g}$ , of scattering particles, which is a shape-independent measure of the particle size. It is useful to note that a smaller scattering vector q corresponds to larger distances being probed (or the scattering from larger particles being measured), and at larger q, correspondingly smaller distances are probed (or the scattering from smaller particles detected). The curve for the 5 mol% mandelic acid solution shows a slight deviation at around  $q = 0.01 \text{ Å}^{-1}$ , which can be interpreted as a shift of the Guinier region to lower q, as a result of the presence of slightly larger particles, on average. The scattered intensity at lowest q is in turn greater. In Figures 4.3 and 4.4, the scattering curves for the solutions of 0-5 mol% mandelic acid are of the same overall shape, but with a low q plateau that does not span the same range of q; i.e., for these plots the Guinier region has shifted further to lower q with the increased level of nitrate present, due to the presence of overall larger particles in solution. The effect on the scattering of the amount of nitrate present is seen more clearly in Figure 4.6, where the shift of the Guinier region to lower q is manifested in the deviation at intermediate q, and increased scatter at lowest q (due to the presence of particles that are on average, significantly larger). On the other hand, the effects of varying the amount of mandelic acid present, for the most part, are more subtle, with the exception of the solutions containing 10 mol% mandelic acid. For these, the effect is similar to that arising from increasing the nitrate content, but to a greater extent, i.e., the chemistry of these solutions has been altered further to promote the formation of even larger scattering species. This is particularly interesting as solutions containing this amount of mandelic acid were seen to

noticeably change post-synthesis, in that a precipitate formed which subsequently settled over time.

Figure 4.7 shows the same scattering data, with the exception of the 10 mol% mandelic acid solutions, as a double logarithmic (base 10) plot, in which informative power-law regimes can be visualised. These linear sections are more obvious for the solutions containing higher levels of mandelic acid; these have been fitted and the gradients are reported in the figure. At intermediate values of q, the slope of the scattering profiles varies according to  $q^{-1} - q^{-2}$ , which is indicative of cylindrical or rod-like particles, *i.e.*, those whose (mode of) growth is predominantly along one particular axis. At highest q, the power-law slope here forms the Porod region, whereby scatter arises from the surfaces of particles. This region also contains information about the so-called fractal dimension of the scattering particles. In the case of the solutions studied here, this slope is approximately -3, which is suggestive of particles that are mass-fractal in nature.

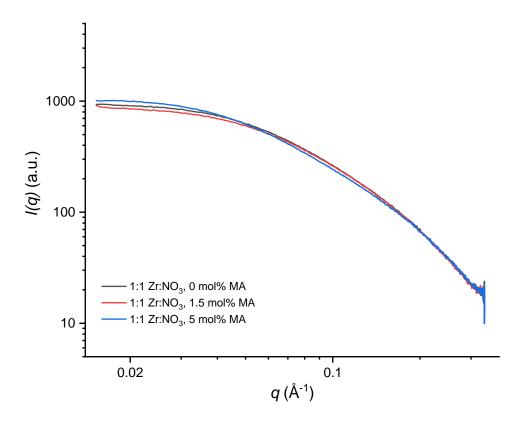


Figure 4.3 Scattering profiles for PZN solutions of 1:1 Zr:NO<sub>3</sub> composition.

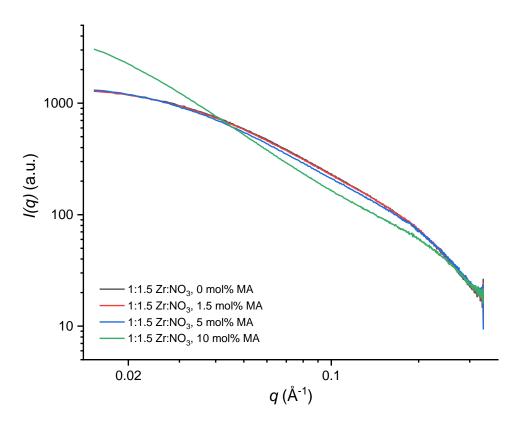
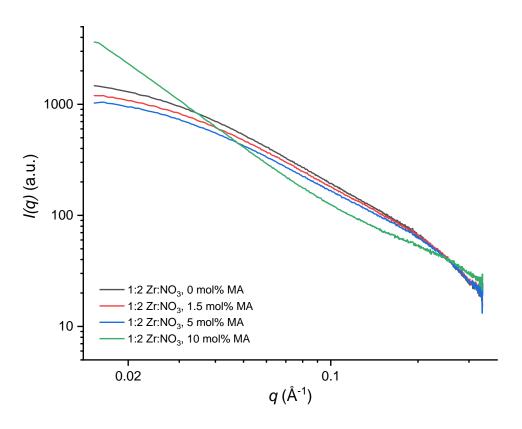


Figure 4.4 Scattering profiles of PZN solutions of 1:1.5 Zr:NO<sub>3</sub> composition.



**Figure 4.5** Scattering profiles of PZN solutions of 1:2 Zr:NO<sub>3</sub> composition.

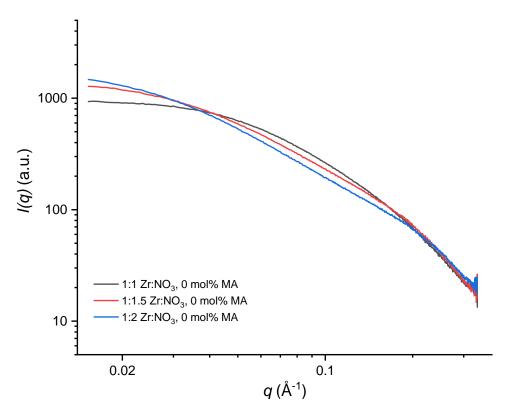
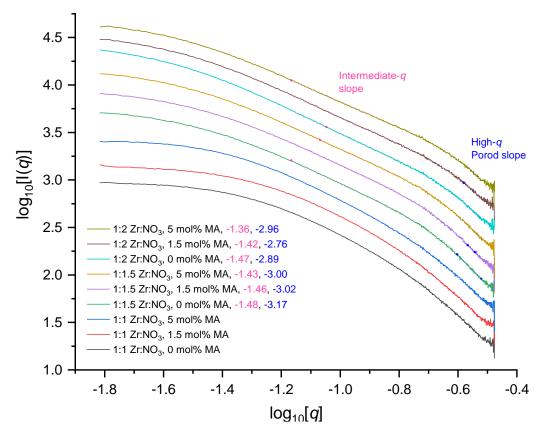
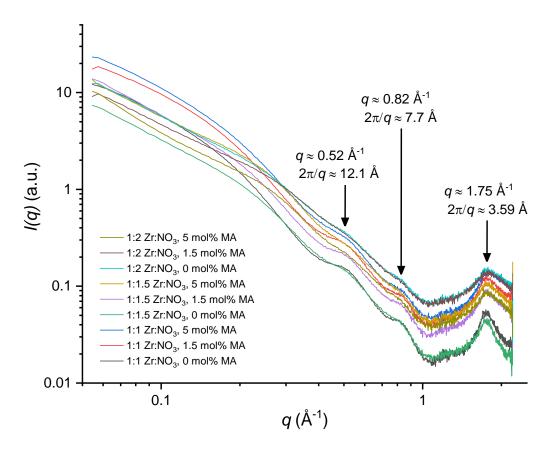


Figure 4.6 Scattering profiles showing the effect of varying the solution nitrate content.



**Figure 4.7** Vertically offset scattering data for PZN solutions of varying composition as  $\log_{10}$  of q and I(q). The gradients of the highlighted linear regions are reported in the legend for the different samples. Plots are vertically offset for clarity.

Scattering data for solutions studied here were also measured utilising a shorter sample-to-detector distance, which has the effect of moving the probed q range to higher values of q, where smaller structural features may be detected. Figure 4.8 contains the results of this. The most significant feature of these scattering curves is the Bragg-like peak at around approximately  $q = 1.75 \text{ Å}^{-1}$ , which corresponds to a physical distance d of around 3.5 Å (d = $2\pi/q$ ), which is consistent with the separation distance of zirconium atoms in the zirconium tetramer. It is suggestive of some sort of ordering of zirconium atoms in solution, as a significant number of repeating planes of atoms would be required to give such a signal in the scattering data. Such an observation has only been reported once previously in the literature for aqueous solutions of zirconium, in recent work by Sommers et al., 29 who found that the scattering of their solutions containing the tetramer was best described as that of a chain of three linked tetramers, suggesting a 'ladder-type' polymerisation of zirconium in solution. This idea is consistent with the observation that the PZN solutions studied here feature particles of a rod-like or cylindrical morphology. Not seen in the work of Sommers et al., however, were the additional features at  $q \approx 0.52$  and  $q \approx 0.82$  Å<sup>-1</sup> (corresponding to physical distances of 12.1 and 7.7 Å, respectively), seen in the scattering data of solutions studied as part of this project (Fig. 4.8). It was noted that these features diminish and eventually disappear from the scattering curves when the solutions were made to be of a lower zirconium concentration (blue curve, left, Fig. 4.9). These features may arise from the arrangement (e.g., stacking) of zirconium particles in solution, however this has not been proved definitively. In addition, it was also noted that if a PZN solution of the standard concentration was taken and then diluted, that the additional features remained (Fig 4.9, right). As such, it was considered that if indeed these features are due to particle arrangement, that the interactions holding them together in solution are relatively strong, and so are not disrupted by the dilution process.



**Figure 4.8** Scattering data from PZN solutions of varying composition measured at a higher range of q than previously reported. Key features, including the Bragg-like diffraction feature at highest q, are highlighted with the corresponding physical distances determined from q values.

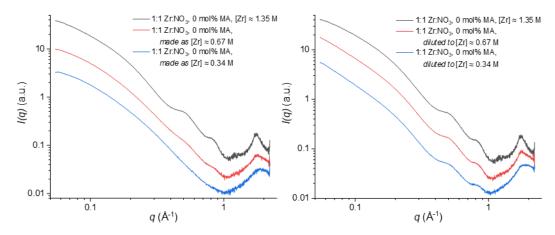


**Figure 4.9** Higher-*q* scattering data of PZN solutions intentionally made to be of a lower zirconium concentration (left), and of PZN solutions of a lower zirconium concentration achieved through dilution (right). Plots are vertically offset for clarity.

#### 4.5.1.2 Determination of Particle Sizes

A typical first step in the analysis of scattering data is to transform the data into a Guinier plot, from which  $R_g$  values can be determined. Such plots, of ln[I(q)] vs.  $q^2$ , are given in Figure 4.10, for the PZN solutions of varying composition. For a monodisperse solution of particles, a Guinier plot should be linear, and the slope of which can give a value for  $R_g$ , as this slope is equal to  $-R_g^2/3$ , according to Guinier (see section 4.2). Curvature of Guinier plots indicates polydispersity or aggregation, and this is seen in the plots in Figure 4.10. It is still possible to calculate the initial and final slope of a Guinier plot as an estimation of the largest and smallest particles in a scattering sample, however. Although, the choice of points on the plot to use in determining the slope is somewhat arbitrary, so here the procedure of 'Guinier peak analysis' (GPA) was employed to confirm which data points to use. A GPA plot of  $q \cdot I(q)$ vs.  $q^2$  transforms the Guinier region into a peak, with the data points forming the initial rise of the peak, up to ' $q^2_{\text{max}}$ ,' being part of the Guinier region. These plots are given in Figure 4.11. For the solutions containing 10 mol% mandelic acid, a peak is not seen, due to the shift of the Guinier region to low enough values of q that it is not seen with the current experimental setup - due to the presence of much larger particles or aggregates in solution for these two samples. Guinier plots with linear fits to the data identified by GPA for the samples of 0-5 mol% mandelic acid are given in Figure 4.12. The fitting did not necessarily encompass all the data points in question, in order not to give a result that passed the limit for the Guinier approximation of  $q \cdot R_g \le \sim 1.3$ . For the solution of composition 1:2 Zr:NO<sub>3</sub> and 0 mol% mandelic acid, the plot still featured significant curvature, so the fit was restricted to the linear region at lowest q.

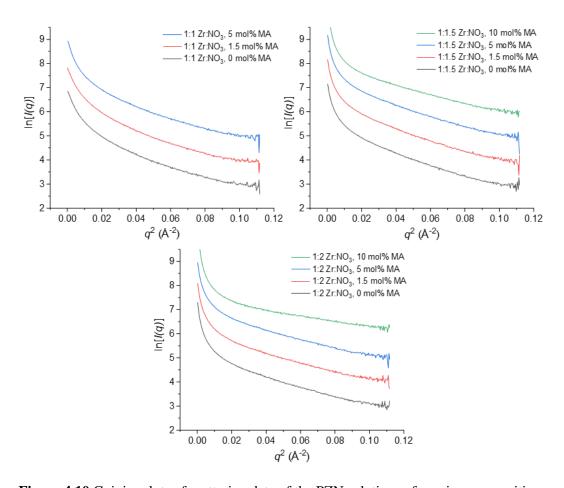


**Figure 4.10** Guinier plots of scattering data of the PZN solutions of varying composition. Plots are vertically offset for clarity.

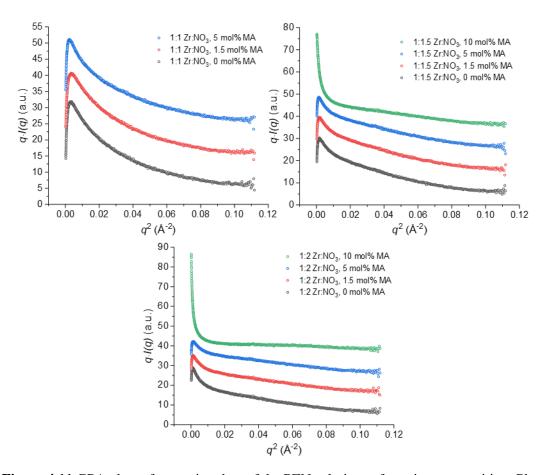


**Figure 4.11** GPA plots of scattering data of the PZN solutions of varying composition. Plots are vertically offset for clarity.

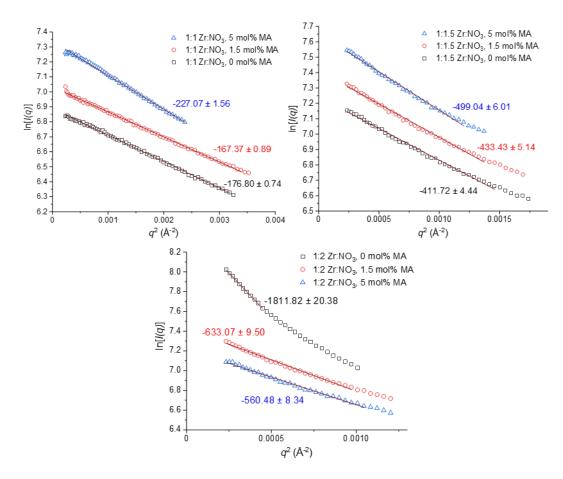


**Figure 4.12** Guinier plots of scattering data of the PZN solutions of varying composition, displaying those data points indicated by GPA to lie within the Guinier region. Labels give the gradients of the linear-fitted regions.

Results of the conversion of Guinier slopes (Fig. 4.12) to radii of gyration are given in Table 4.1 below, along with the corresponding geometric length L of a rod-like particle ( $L \approx R_{\rm g} \cdot \sqrt{12}$ ), which would be the expected shape assuming a ladder-like connectivity of tetramers as seen previously in the literature.

**Table 4.1** Particle size parameters for the solutions of varying composition determined from Guinier-type analysis of scattering data. Uncertainty values originate from the uncertainties in the original linear fits to Guinier plots. The entry in italics should be considered an outlier (discussed in due course).

Zr:NO <sub>3</sub> Ratio	MA Content (mol%)	$R_{\mathrm{g}}(\mathrm{\mathring{A}})$	L (Å)
1:1	0	$23.03 \pm 0.05$	$79.78 \pm 0.17$
1:1	1.5	$22.41 \pm 0.06$	$77.62 \pm 0.21$
1:1	5	$26.10 \pm 0.09$	$90.41 \pm 0.31$
1:1.5	0	$35.15 \pm 0.19$	$121.75 \pm 0.66$
1:1.5	1.5	$36.06 \pm 0.21$	$124.91 \pm 0.74$
1:1.5	5	$38.69 \pm 0.23$	$134.04 \pm 0.81$
1:2	o	$73.73 \pm 0.41$	$255.39 \pm 1.44$
1:2	1.5	$43.58 \pm 0.33$	$150.96 \pm 1.13$
1:2	5	$41.01 \pm 0.31$	$142.05 \pm 1.06$

Table 4.1 gives an insight into the effect of the composition of the PZN solution on particle size. The effect of the amount of mandelic acid present is not clear in terms of an overall trend, although the proportions used in PZN solutions are relatively small, so the effect could be 'outweighed' by other influences - though differences between samples due to mandelic acid are seen. It can be seen that increasing the nitrate or nitric acid content of the solutions results in larger particle sizes following heat treatment. This might seem counterintuitive, as solutions made with more nitric acid would be expected to be more acidic, which would inhibit hydrolysis to a greater extent, resulting in smaller particles. However, introducing more nitric acid into the solutions increases the amount of charge-balancing counterions in solution. The hydrolysed zirconium species have an overall positive charge, and nitrate anions are negatively charged. This balancing of charges would be expected to allow a closer approach of zirconium species in solution, due to diminished repulsive electrostatic forces between them, allowing hydrolysis to join zirconium species together more readily. It might be possible that mandelic acid could have the same effect, although it is present in much lower amounts as compared to nitric acid. However, mandelic acid also coordinates to zirconium much more readily than nitrate, and this bulky organic ligand could be expected to inhibit hydrolysis. It is likely that there are competing factors in effect here, though it is clear that it is the use of nitric acid that has the most significant influence upon the zirconium solution species.

It has been mentioned previously that the particles in the PZN solutions measured appear to be rod-like or cylindrical. In addition to the length of these particles, it is possible to estimate the *radius of gyration of the cross-section* of the particles,  $R_c$ , with so-called 'longrods' plots or intermediate-q Guinier plots, of  $\ln[q \cdot I(q)]$  vs.  $q^2$ . In this case, the slope of linear sections is equal to  $-R_g^2/2$ , and this can then give the geometric radius  $R_{cyl}$  of the cylinder with  $R_{cyl} = R_c \cdot \sqrt{2}$ . Longrods plots of the scattering data of PZN solutions of composition 0-5 mol% mandelic acid are given in Figure 4.13 and resulting  $R_c$  values and particle sizes in Table 4.2.

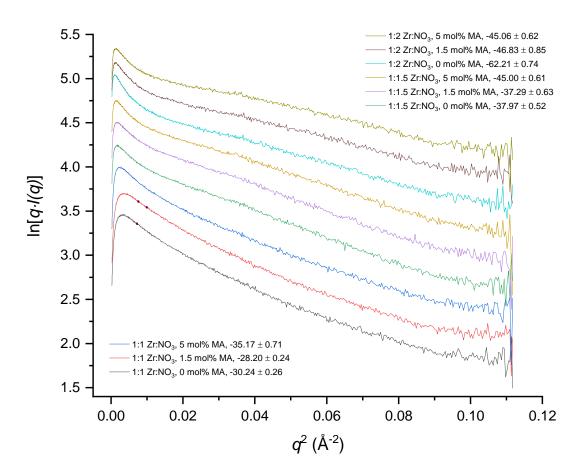


**Figure 4.13** 'Longrods' plots of scattering data for PZN solutions of varying composition. The slope of the linear-fitted region for each plot is given in the legend. The fitted regions of the plots are marked with brown dots.

**Table 4.2** Particle size parameters for the solutions of varying composition determined from longrods-type analysis of scattering data. Uncertainty values originate from the uncertainties in the original linear fits to Guinier and longrods plots. The last column gives an estimate of the approximate number of connected whole tetramers (to the nearest whole number) that would make up a ladder-like structure with a length *L*. The entry in italics should be considered an outlier (discussed in due course).

Zr:NO <sub>3</sub> Ratio	MA Content (mol%)	L (Å)	$R_{\rm c}$ (Å)	$R_{\mathrm{cyl}}(\mathring{\mathbf{A}})$	No. Tetramers in
					Ladder
1:1	0	$79.78 \pm 0.17$	$7.78 \pm 0.03$	$11.00 \pm 0.05$	11
1:1	1.5	$77.62 \pm 0.21$	$7.51 \pm 0.03$	$10.62 \pm 0.05$	11
1:1	5	$90.41 \pm 0.31$	$8.39 \pm 0.08$	$11.86 \pm 0.12$	13
1:1.5	0	$121.75 \pm 0.66$	$8.71 \pm 0.06$	$12.32 \pm 0.08$	17
1:1.5	1.5	$124.91 \pm 0.74$	$8.64 \pm 0.07$	$12.21 \pm 0.10$	17
1:1.5	5	$134.04 \pm 0.81$	$9.49 \pm 0.05$	$13.42 \pm 0.08$	19
1:2	0	$255.39 \pm 1.44$	$11.15 \pm 0.07$	$15.78 \pm 0.09$	36
1:2	1.5	$150.96 \pm 1.13$	$9.68 \pm 0.09$	$13.69 \pm 0.12$	21
1:2	5	$142.05 \pm 1.06$	$9.49 \pm 0.07$	$13.43 \pm 0.09$	20

The plots in Figures 4.14 and 4.15 below give a visual representation of the data contained within Tables 4.1 and 4.2; particle radii of gyration and corresponding particle sizes assuming a cylindrical model, respectively.

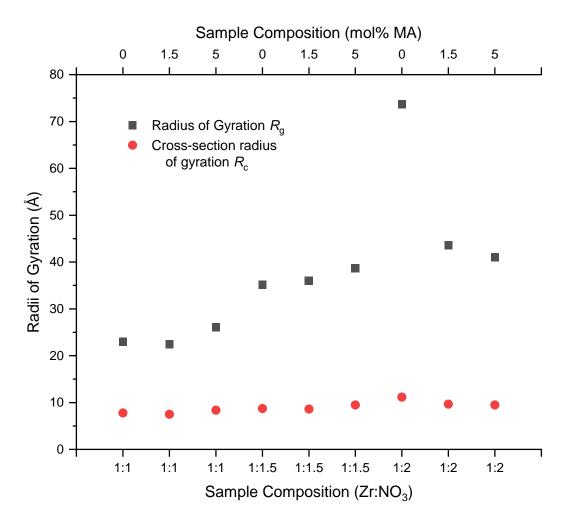


**Figure 4.14** Radii of gyration for solution species determined from analysis *via* Guinier and longrods plots of scattering data from PZN solutions of varying composition.

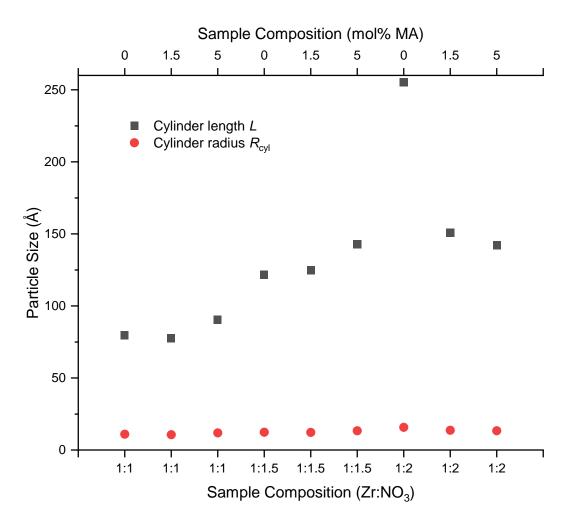


**Figure 4.15** Particle size parameters calculated from radii of gyration values for solution species determined from analysis *via* Guinier and longrods plots of scattering data from PZN solutions of varying composition.

It should be noted that, as is clear from the plots in Figures 4.14 and 4.15, the data point for the sample of composition 1:2 Zr:NO<sub>3</sub> and 0 mol% mandelic acid does not follow the same trends for this set of data. It is a definite outlier, most likely due to the sample solution itself. In general the synthesis behaviour of the 1:2 Zr:NO<sub>3</sub> solutions was less predictable, with these solutions more likely to gel in the reactor. Further measurements on different samples of the same compositions were not carried out, as the additional project goal of solution reproducibility studies was ultimately not realised in the time available.

#### 4.5.2 SAXS Measurements of PZN Solutions During Synthesis

Small-angle X-ray scattering measured from samples taken from the reactor during the synthesis of a PZN solution of composition 1:1 Zr:NO<sub>3</sub> and 1.5 mol% mandelic acid is presented here. Scattering data for these samples is given in Figure 4.16. Analysis of the scattering data was carried out in the same manner as for the samples studied in Section 4.5.1 (Guinier, GPA and longrods plots).

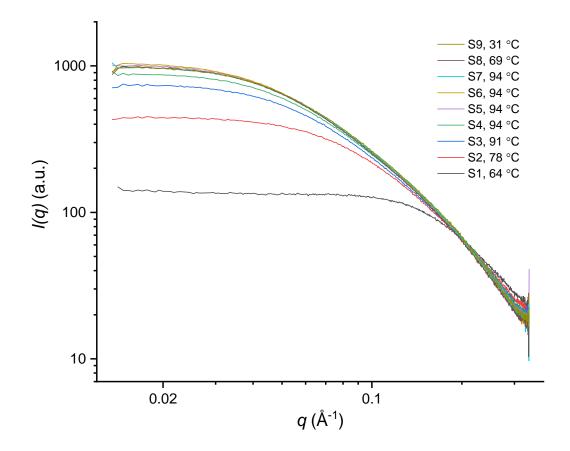


**Figure 4.16** Scattering data of samples ('S1' – 'S9') taken from the reactor during the synthesis of a PZN solution of composition 1:1 Zr:NO<sub>3</sub> and 1.5 mol% mandelic acid. The temperature of the reactor contents at the time of sampling is given in the legend for each sample.

The evolution of scattering curves during a PZN synthesis with time and temperature is seen in Figure 4.16. The overall shape of the scattering curves by the end of synthesis, which reflects the form factor of particles, is like that seen for the solutions studied in Section 4.5.1.

The intensity at low q is seen to increase over time as a result of the synthesis heat treatment, which indicates the growth of larger zirconium particles in solution. There is not such a significant change at high q, which may suggest the persistence of a smaller zirconium species in solution throughout synthesis. It appears that once the PZN solution has reached the highest temperature of 94 °C, that the scattering curves change very little, despite the continuing application of heat. It is possible that an equilibrium is reached, whereby the forcing effects of the heat treatment are offset by the increased acidity of the solution (due to release of  $H^+$  from hydrolysis); the former otherwise results in the increase in size of solution species, whereas the latter would act to inhibit the further growth of individual particles. Guinier plots of the above scattering data are given in Figure 4.17, and the curvature of which is seen to increase with time and temperature, most notably during the temperature ramp up to 94 °C. This change in curvature is indicative of the increased polydispersity of the solution during synthesis; larger particles (or aggregates) form yet there is still a significant population of smaller species present. Scattering is generally dominated from that by the largest of particles;  $I(q) \propto r^6$ .

Table 4.3 contains the particle size parameters determined from the Guinier, GPA and longrods analysis of scattering data discussed here. GPA and longrods plots, plots of the Guinier regions and the results of the relevant linear fits can be found in the Appendices (Figs. A.11 – A.15). Figure 4.18 shows the plotted particle sizes; radii of gyration and geometric sizes of a cylinder model. The data are consistent with the idea of growth of particles predominantly occurring in one direction during synthesis: the smallest dimension of the cylinder changes relatively little whilst the overall length of the particles increases to approximately four times their diameter, an idea proposed previously with solutions of zirconium oxychloride, in a study that also analysed SAXS data *via* Guinier and longrods plots.<sup>30</sup>

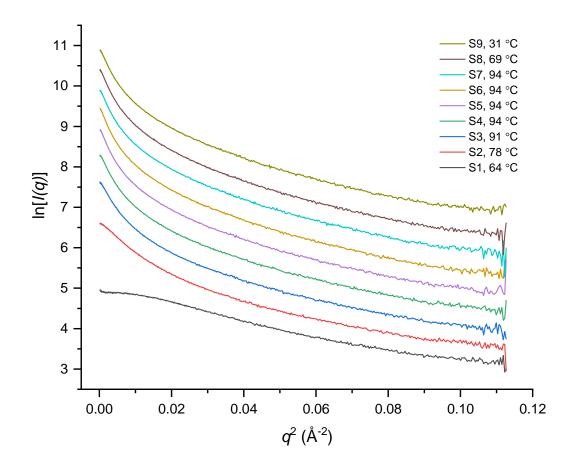


**Figure 4.17** Guinier plots of scattering data of samples ('\$1' - '\$9') taken from the reactor during the synthesis of a PZN solution of composition 1:1 Zr:NO<sub>3</sub> and 1.5 mol% mandelic acid. The temperature of the reactor contents at the time of sampling is given in the legend for each sample. Plots are vertically offset for clarity.

**Table 4.3** Particle size parameters determined from analysis of scattering data, for samples from a synthesis of a PZN solution of standard composition. Uncertainty values originate from the uncertainties in the original linear fits to Guinier and longrods plots.

Sample	$R_{\mathrm{g}}(\mathring{\mathrm{A}})$	$L(\mathring{\mathbf{A}})$	$R_{\rm c}$ (Å)	$R_{\text{cyl}}(\mathring{\mathbf{A}})$
S1, 64 °C	$8.30 \pm 0.16$	$28.77 \pm 0.54$	$4.45 \pm 0.02$	$6.29 \pm 0.03$
S2, 78 °C	$15.44 \pm 0.03$	$53.48 \pm 0.12$	$6.28 \pm 0.03$	$8.89 \pm 0.04$
S3, 91 °C	$21.48 \pm 0.04$	$74.42 \pm 0.16$	$7.43 \pm 0.04$	$10.50 \pm 0.05$
S4, 94 °C	$23.40 \pm 0.05$	$81.07 \pm 0.19$	$8.05 \pm 0.05$	$11.38 \pm 0.07$
S5, 94 °C	$25.03 \pm 0.10$	$86.69 \pm 0.35$	$8.43 \pm 0.06$	$11.92 \pm 0.08$
S6, 94 °C	$25.42 \pm 0.06$	$88.05 \pm 0.21$	$8.54 \pm 0.04$	$12.07 \pm 0.06$
S7, 94 °C	$24.43 \pm 0.08$	$84.64 \pm 0.29$	$8.31 \pm 0.06$	$11.75 \pm 0.08$
S8, 69 °C	$24.77 \pm 0.07$	$85.82 \pm 0.23$	$8.56 \pm 0.04$	$12.11 \pm 0.06$
S9, 31 °C	$23.98 \pm 0.07$	$83.07 \pm 0.24$	$8.22 \pm 0.05$	$11.62 \pm 0.07$

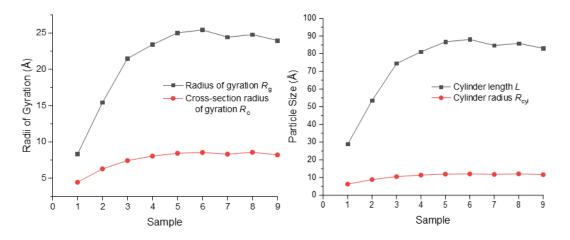


**Figure 4.18** Radii of gyration and corresponding geometric sizes of particles determined from scattering data of samples taken during a synthesis of PZN solution of standard composition.

### 4.5.3 SAXS Measurements of Aged PZN Solutions

Small-angle X-ray scattering measured over a period of several days for a PZN solution of composition 1:1 Zr:NO<sub>3</sub> and 1.5 mol% mandelic acid is discussed here. It was found that the changes over time in the scattering data post-synthesis are small, suggesting that solution species originally formed during synthesis tend to remain intact, *i.e.* there is not a significant continuation of hydrolysis such that larger particles are formed, and particles are generally not re-dissolving into solution resulting in particles of a smaller size. Scattering data measured up to day 45 following synthesis (the day of synthesis is denoted day 1) can be seen in Figure 4.19, with the corresponding Guinier plots in Figure 4.20. Particle size parameters determined from Guinier, GPA and longrods analysis of scattering data are given in Table 4.4; these are plotted in Figure 4.21. The as-mentioned plots from which these values are determined may be found in the Appendices (Figs. A.16 – A.19).

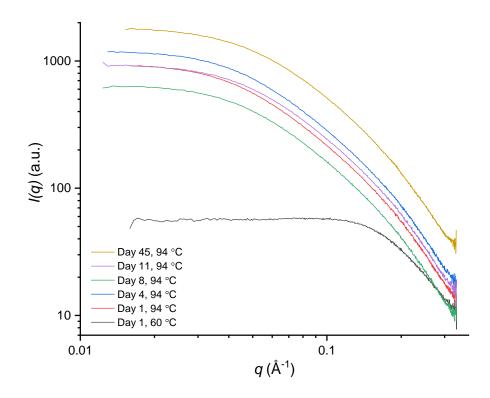


**Figure 4.19** Offset scattering data from a PZN solution of standard composition measured over time following synthesis. Data for a sample taken from the reactor pre-heat treatment is given for comparison. The temperatures in the legend show the maximum temperature that the solution was subjected to.

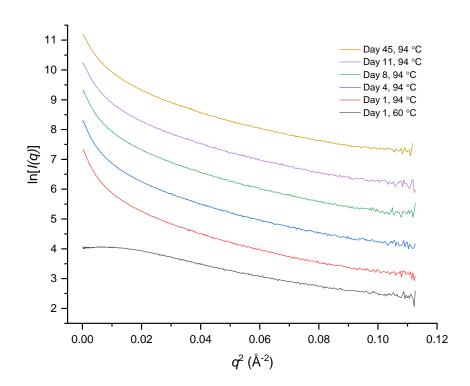


**Figure 4.20** Offset Guinier plots of scattering data from a PZN solution of standard composition measured over time following synthesis. Data for a sample taken from the reactor pre-heat treatment is given for comparison. The temperatures in the legend show the maximum temperature that the solution was subjected to.

**Table 4.4** Particle size parameters determined from analysis of scattering data, from post-synthesis measurements of a PZN solution of standard composition. Uncertainty values originate from the uncertainties in the original linear fits to Guinier and longrods plots.

Sample	$R_{\mathrm{g}}(\mathring{\mathrm{A}})$	L (Å)	$R_{c}$ (Å)	$R_{\mathrm{cyl}}(\mathring{\mathbf{A}})$
Day 1, 60 °C	$7.85 \pm 0.29$	$27.20 \pm 1.00$	$4.49 \pm 0.02$	$6.36 \pm 0.03$
Day 1, 94 °C	$26.26 \pm 0.05$	$90.95 \pm 0.17$	$8.60 \pm 0.03$	$12.16 \pm 0.05$
Day 4, 94 °C	$25.45 \pm 0.06$	$88.17 \pm 0.20$	$8.40 \pm 0.03$	$11.88 \pm 0.05$
Day 8, 94 °C	$24.85 \pm 0.05$	$86.09 \pm 0.17$	$8.37 \pm 0.04$	$11.83 \pm 0.06$
Day 11, 94 °C	$24.01 \pm 0.05$	$83.18 \pm 0.17$	$8.19 \pm 0.04$	$11.59 \pm 0.06$
Day 45, 94 °C	$23.00 \pm 0.04$	$79.67 \pm 0.14$	$7.69 \pm 0.03$	$10.87 \pm 0.05$

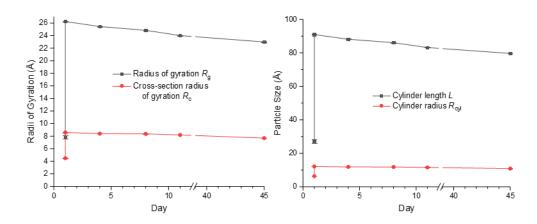


**Figure 4.21** Radii of gyration and corresponding geometric sizes of particles determined from scattering data of from SAXS measurements upon an aged PZN solution of composition 1:1 Zr:NO<sub>3</sub> and 1.5 mol% mandelic acid.

#### 4.5.4 Variation of Heat Treatment Temperature During PZN Synthesis

SAXS measurements of samples taken from the reactor during the synthesis of a PZN solution of composition 1:2 Zr:NO $_3$  and 0 mol% mandelic acid, reaching different maximum heat-treatment temperatures, are reviewed in this section. These analyses complement the Raman measurements of the same type of samples in Chapter 3 Section 3.5.4. Plots of the X-ray scattering data are given in Figure 4.22 with the corresponding Guinier plots displayed in Figure 4.23. Particle Size parameters from Guinier, GPA and longrods analysis of scattering plotted in Figure 4.24. The as-mentioned plots from which these values are determined may be found in the Appendices (Figs. A.20 – A.29).

In general, increases in scattered X-ray intensity, particularly at lower values of q, are more prominent at the higher temperatures of heat treatment, which is not unexpected. This is indicative of the emergence of larger and larger scattering species in solution. There is less of a change in scattered intensity at the higher values of q, consistent with a much smaller dimension being detected throughout heat treatment. This is consistent with particle growth considered to be analogous to that of a cylinder of increasing length; the increases in length are reflected in the increased scatter at lowest q with the cross-section of the cylinder, which would be expected to change relatively little compared to the length, contributing to the scatter at highest q. The scattering curves also level off-before minimum q is reached, so it is unlikely that there are particles present in solution bigger than those seen via the q-range employed in this experiment. There is essentially no change during synthesis for the PZN solution heated up to 60 °C, i.e. the temperature required to ensure complete dissolution of the zirconium carbonate precursor in the first instance. Guinier plots, given in Figure 4.23, show increasing curvature due to heat treatment as the maximum heat treatment temperature is increased; reflecting increased polydispersity of the solution particles. This is consistent with the idea of the growth of cylindrical or rod-like particles of varying lengths. Particle size parameters, determined from the methods already mentioned (Figure 4.24), show little change at 60 °C, but indicate that at 70 °C, the temperature is high enough to promote particle growth throughout the extent of heat treatment. However at 80 and 90 °C, the growth of particle sizes is initially faster, but then settles, which could be due to an equilibrium between the hydrolysis-inhibiting effects of increased solution pH and the forcing conditions (heating) increasing the rate of any reactions taking place. This is interesting as it suggests a possible route to tailoring the sizes of the particles reached in solution just by selecting a particular heat treatment temperature, without the worry of a 'run-away' increase in particle size. It should be noted that the data from longrods analysis (to estimate particle cross-section radii of gyration) is incomplete as these plots were of a positive slope, in contradiction to the usual method of determining sizes from these plots. It is considered that for samples from synthesis with the lower heat treatment temperatures, and from early in the synthesis procedure, the

particles present in solution are of a small enough size that their overall size is enough to contribute to the X-ray scattering, but that their cross-section is too small to be detected. This idea is consistent with there being initially much smaller particles in these solutions due to the higher amount of nitric acid relative to zirconium; the increased acidity in this case inhibiting particle growth by hydrolysis.

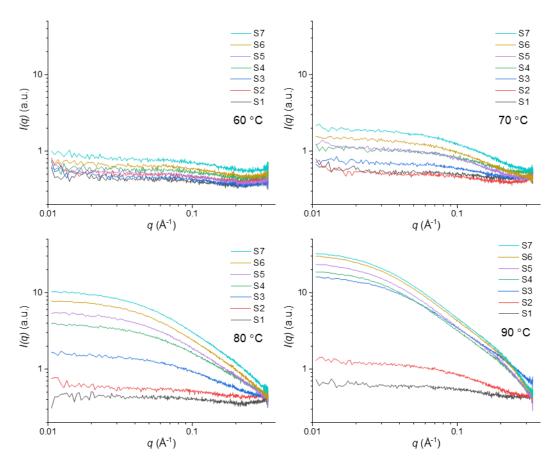


**Figure 4.22** Scattering data of samples of PZN solutions subjected to different maximum heat treatment temperatures during synthesis.

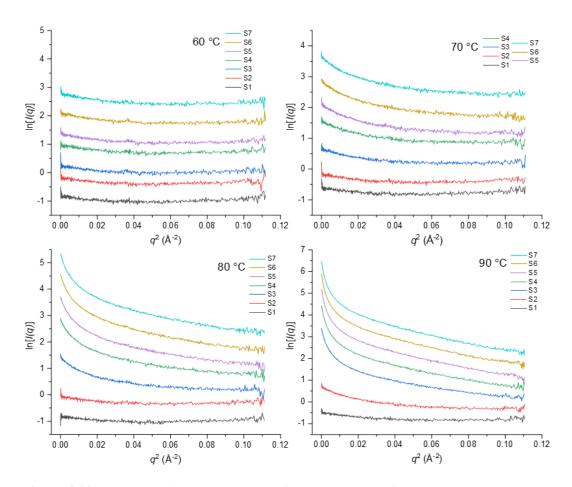


**Figure 4.23** Vertically offset Guinier plots of scattering data of PZN solutions subjected to different maximum heat treatment temperatures during synthesis.

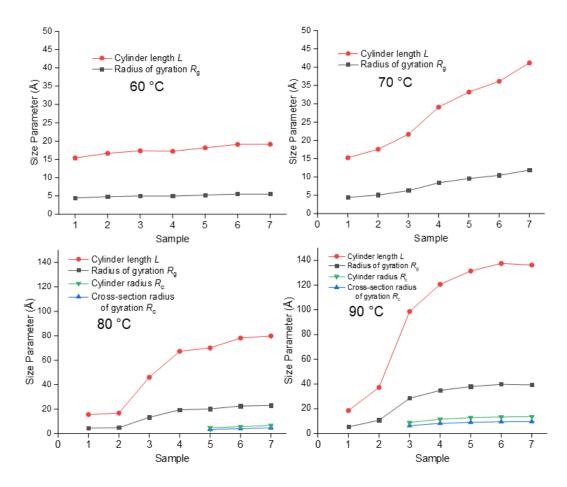


**Figure 4.24** Radii of gyration and corresponding geometric sizes of particles determined from scattering data of samples taken during syntheses of PZN solution of a composition 2:1 Zr:NO<sub>3</sub> and 0 mol% mandelic acid, at different maximum heat treatment temperatures.

#### 4.5.5 SAXS Measurements of PZN Solutions with In-Situ Heating

In this section, the results of experimentation utilising *in-situ* heating of PZN solutions is discussed. In the previous section samples were taken from the reactor at different temperatures and then measured at a later time. Here however, initially non-heat treated PZN solution was heated on the SAXS instrument with the use of a capillary heating stage, whilst scattering measurements took place. The experimental conditions therefore are thus slightly different, though the outcome of results would be expected to be similar, and show the same trends, if not the same values for particle sizes, for example. Plots of the X-ray scattering data are given in Figure 4.25 with the corresponding Guinier plots displayed in Figure 4.26. Particle

Size parameters from Guinier, GPA and longrods analysis of scattering data are plotted in Figure 4.27.

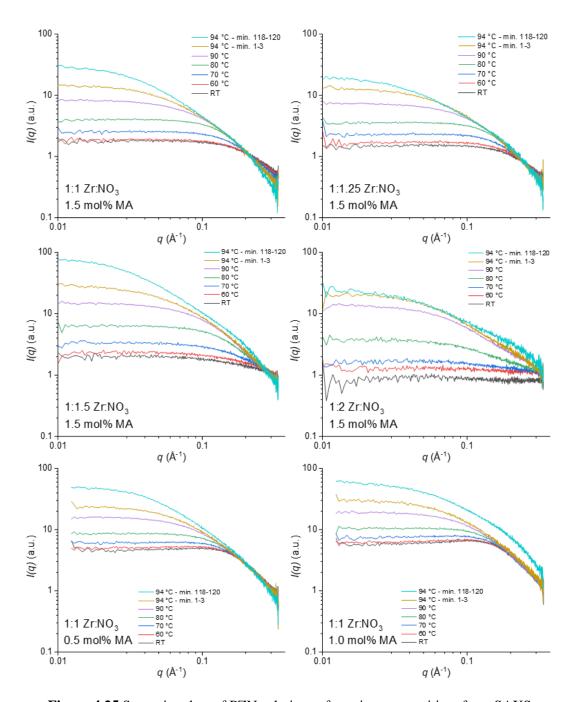


**Figure 4.25** Scattering data of PZN solutions of varying composition, from SAXS experiments with *in-situ* heating.

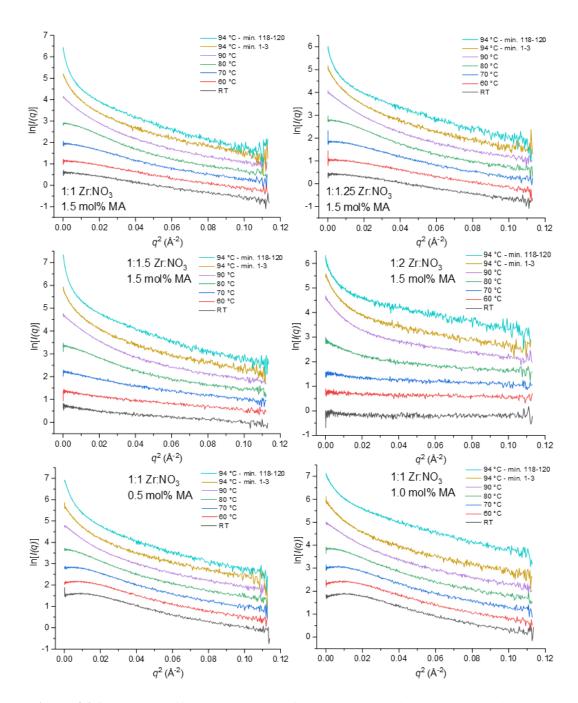


**Figure 4.26** Vertically offset Guinier plots of scattering data of PZN solutions of varying composition, from SAXS experiments with *in-situ* heating.

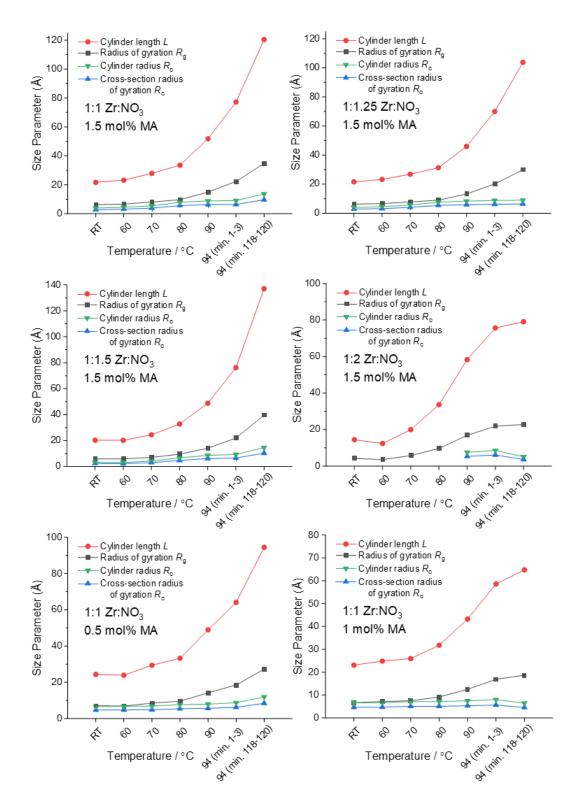


**Figure 4.27** Radii of gyration and corresponding geometric sizes of particles determined from scattering data of PZN solutions of varying composition, from SAXS experiments with *in-situ* heating.

As seen previously with the other experiments discussed, the changes in the plots of scattering data (Figure 4.27) reflect the presence of particles of increasing size due to the effects of heat treatment, with particles tending to grow to a range of lengths as indicated by the increasing curvature of the corresponding Guinier plots (Figure 4.26). The trends in particle size parameters determined *via* analysis using Guinier, GPA and longrods plots mirror these changes, showing overall growth of particles but with a population of much smaller particle dimensions always detected. Relative changes in particle size are greatest for the particles overall size or length, given a cylinder model, with the changes in the particles cross-sectional size being less so. This is consistent, again, to growth of particles that ocurrs predominantly in one direction or along one axis.

Previous results from Section 4.5.1 looking at variation of PZN solution composition suggested that the changes in particle sizes (following heat treatment) due to the different amounts of nitric acid and mandelic acid used to make the solutions was predominantly a result of changing the ratio of nitrate to zirconium, with the largest particles seen when more nitric acid was employed. Considering the samples here in terms of the variation in the Zr:NO<sub>3</sub> ratio, the final particle sizes do not reflect the same trend (Figure 4.28, left), however initially, the sizes for the most acidic solution are smaller, consistent with the effects of inhibition of hydrolysis. Though there is a noticeable deviation from the data for the other samples of different Zr:NO<sub>3</sub> ratios, the overall trend (increase in particle size due to heating) is the same. There is not initially a significant change in particle sizes due to varying the amount of mandelic acid present (Figure 4.28, right); the changes occur mostly, relatively speaking, when the temperature of the solution is highest. The trend in final sizes seen here also do not reflect an increase or decrease in mandelic acid content; however the amounts used are very small compared to the amount of zirconium in the solutions, so the effects of the mandelic acid could be easily overshadowed by other effects at work.

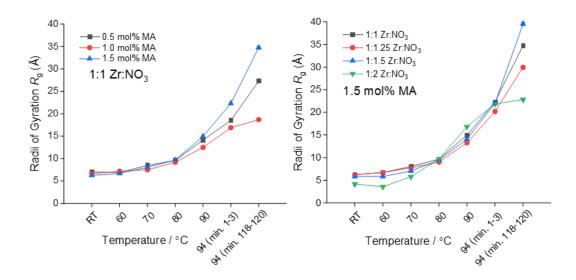


**Figure 4.28** Radii of gyration of particles determined from scattering data of PZN solutions of varying composition, from SAXS experiments with *in-situ* heating. Left: samples of constant Zr:nitrate ratio but varying mandelic acid content. Right: samples of constant mandelic acid content but varying Zr:nitrate ratio.

#### 4.6 Summary and Conclusions

Aqueous nitrate-based solutions of zirconium and mandelic acid of varying composition have been characterised by small-angle X-ray scattering to further understand the properties of these solutions on a different length scale to that probed by other experimental techniques in this project. The data have demonstrated the usefulness of SAXS in determining zirconium oxy-cluster particle sizes in solution and how it can be used to characterise material both during and after synthesis; showing how particle sizes change in response to solution composition, time, and temperature of heat treatment of solutions. In particular, experiments to follow the changes in solution such as those described in Sections 4.4 and 5.5 have not previously been reported in the literature for nitrate-based aqueous solutions of zironium. Results seen here suggest that for these solutions, modification of particle sizes of solution species is primarily due to the amount of nitrate or nitric acid used to make the solutions, with the presence of mandelic acid in solution having a much smaller effect, though this was not necessarily the case for all solutions. A reproducibility study on these solutions would be expected to more definitively confirm this. A fuller understanding would be achieved from a

study of solutions of a wider range of compositions, however this would have deviated from the overall goal of this project of characterising solutions like those as might be used in industry to create commercial products. Evidence has also been seen to suggest that in terms of the sizes of particles in these solutions, the solutions are reasonably stable with respect to aging over time, which is useful for industry as this will help to inform how long precursor material (solution precursors to zirconium) can be kept in storage without an adverse effect on solution properties. From measurements upon samples taken from a reactor setup used to synthesise PZN solutions, it has been seen that the largest particle sizes are achieved at the highest heat treatment temperatures, but that growth of particles is not necessarily constant throughout the heat treatment process, and given enough time, will reach an upper limit. Thus, it could be possible to control particle sizes for a given solution composition just by choice of heat treatment temperature. Such an insight would be useful to industry as it would help to save time and energy by ensuring that solutions are not heated for longer than is necessary to achieve the desired properties. SAXS measurements involving in-situ heating of PZN solutions have not always given results consistent with the sampling method. When sampling from the reactor, the setup is such that the solution is constantly stirring, so that in theory the heating of the reactor contents is as uniform as possible. Whereas, in a capillary, the only mixing of solution is due to convection, and the measured temperature is not of the solution itself.

#### 4.7 Bibliography

- A. Guinier and G. Fournet, Small-Angle Scattering of X-Rays, John Wiley & Sons, Inc., New York, 1955.
- 2. L. A. Feigin and D. I. Svergun, *Structure Analysis by Small-Angle X-Ray and Neutron Scattering*, Plenum Press, New York, 1987.
- 3. H. Schnablegger and Y. Singh, *The SAXS Guide Getting acquainted with the principles*, Anton Paar GmbH, Austria, 2017.
- 4. C. F. Holder and R. E. Schaak, *ACS Nano*, 2019, **13**, 7359-7365.
- 5. C. E. Blanchet and D. I. Svergun, *Annu. Rev. Phys. Chem.*, 2013, **64**, 37-54.
- 6. J. Lipfert and S. Doniach, Annu. Rev. Biophys. Biomol. Struct., 2007, 36, 302-327.
- 7. S. Sakurai, *Polym. Int.*, 2017, **66**, 237-249.
- 8. B. Chu and B. S. Hsiao, *Chem. Rev.*, 2001, **101**, 1727-1761.
- 9. M. Ballauf, Adv. Eng. Mat., 2011, 13, 793-802.
- 10. M. Nyman, Coord. Chem. Rev., 2017, 352, 461-472.
- 11. P. Fratzl, J. Appl. Cryst., 2003, 36, 397-404.
- 12. T. Li, A. J. Senesi and B. Lee, *Chem. Rev.*, 2016, **16**, 11128-11180.
- B. J. Boyd and T. Rades, in *Advances in Delivery Science and Technology*, eds. A.
   Mullertz, Y. Perrie and T. Rades, Springer-Verlag, New York, 2016, pp. 339-360.
- 14. A. F. Craievich, Mat. Res., 2002, 5, 1-11.
- 15. L. M. Toth, J. S. Lin and L. K. Felker, *J. Phys. Chem.*, 1991, **95**, 3106-3108.
- A. Singhal, L. M. Toth, J. S. Lin and K. Affholter, J. Am. Chem. Soc., 1996, 118, 11529-11534.
- A. Singhal, L. M. Toth, G. Beaucage, J.-S. Lin and J. Peterson, *J. Colloid Interface Sci.*, 1997, **194**, 470-481.
- M. Z.-C. Hu, J. T. Zielke, J.-S. Lin and C. H. Byers, J. Mater. Res., 1999, 14, 103-113.

- P. D. Southon, J. R. Bartlett, J. L. Woolfrey and B. Ben-Nissan, *Chem. Mater.*, 2002,
   14, 4313-4319.
- V. V. Kanazhevskii, V. P. Shmachkova, N. S. Kotsarenko, V. N. Kolomiichuk and D. I. Kochubei, *J. Struct. Chem.*, 2006, 47, 860-868.
- 21. G. A. Carter, M. I. Ogden, C. E. Buckley, C. Maitland and M. Paskevicius, *Powder Technol.*, 2009, **188**, 222-228.
- M. Ambrosi, E. Fratini, P. Canton, S. Dankesreiter and P. Baglioni, *J. Mater. Chem.*, 2012, 22, 23497-23505.
- A. Gossard, G. Toquer, S. Grandjean and A. Grandjean, J. Sol-Gel Sci. Technol, 2014,
   71, 571-579.
- M. Brenholm, H. Birkedal, B. B. Iversen and J. S. Pedersen, *J. Phys. Chem. C*, 2015,
   119, 12660-12667.
- A. J. Allen, F. Zhang, R. J. Kline, W. F. Guthrie and J. Ilavsky, *J. Appl. Cryst.*, 2017,
   50, 462-474.
- 26. J. Ilavsky and P. R. Jemain, J. Appl. Cryst., 2009, **42**, 347-353.
- 27. B. R. Pauw, J. Phys. Condens. Matter, 2013, 25, 383201-383224.
- 28. R. Girardot, G. Viguier, J. Perez and M. Ounsy, Foxtrot: A Java-Based Application to Reduce and Analyse SAXS and WAXS Piles of 2D Data at Synchrotron Soleil, canSAS-VIII, J-PARC, Tokai, Japan, 2015.
- J. A. Sommers, D. C. Hutchison, N. P. Martin, K. Kozma, D. A. Keszler and M. Nyman, *J. Am. Chem. Soc.*, 2019, **141**, 16894-16902.
- 30. J. A. Jutson, R. M. Richardson, S. L. Jones and C. Norman, *Mat. Res. Soc. Symp. Proc.*, 1990, **180**, 123-128.

# Chapter 5:

# Characterisation of Aqueous Zirconium Solutions by Synchrotron X-Ray Techniques: EXAFS and XPDF

#### 5.1 Introduction

This chapter describes work carried out to investigate the properties of aqueous nitrate-based solutions of zirconium using two synchrotron-based characterisation methods: EXAFS (Extended X-ray Absorption Fine Structure) and XPDF (X-ray Pair Distribution Function) analysis. Work utilising EXAFS was carried out during beamtime at the B18 core XAS (X-ray Absorption Spectroscopy) beamline at Diamond Light Source; XPDF experimentation was carried out during rapid access beamtime on the I15-1 XPDF beamline at Diamond Light Source.

XAS, or more specifically XAFS (X-ray absorption fine structure), 2,3 encompasses both EXAFS and XANES (X-ray absorption near-edge structure), widely used techniques for probing the structure of matter on a local level. Both effects arise from the absorption of X-ray energy by an element of interest in a sample, and the subsequent excitation or ejection of a core (photo)electron, which then interacts with other atoms in the vicinity. Such experiments are usually carried out at synchrotron facilities, where the intense X-ray beams possible allow for measurement of minute amounts of sample, and the ability to tune the energy of the beam allows for elemental selectivity. The use of EXAFS is common in modern materials science due to the advent of such facilities and may be applied to the study of many different types of samples, whether they be crystalline or amorphous solids, or liquid.<sup>4-9</sup> Although, laboratory X-ray sources for measuring EXAFS data are becoming more common. The XPDF method<sup>10.</sup> is also applicable to such samples<sup>12, 13</sup> for probing local and medium-range structure, especially for amorphous glasses and fluids. It may also be carried out at synchrotron facilities but is also possible with laboratory-based equipment, if X-ray sources capable of producing short wavelength radiation are available (Ag Kα for example).<sup>14</sup> Also known as total

scattering, it is an analytical technique for gathering structural information from the entirety of an X-ray diffraction pattern; making use of Bragg scattering from the crystalline arrangement of atoms, and the underlying diffuse scattering present across all  $2\theta$ . The Bragg features contain information about the long-range order of atoms in a material, and the local structure, or short-range order (or disorder) is contained within the diffuse scattering.

## **5.2 Experimental Methods**

#### **5.2.1 Extended X-Ray Absorption Fine Structure (EXAFS)**

As previously mentioned, the EXAFS characterisation technique is a form of X-ray Absorption Spectroscopy,<sup>2, 3</sup> and is underpinned by the photoelectric effect.<sup>15, 16</sup> Here, the absorption of X-rays of a definite energy by a sample can result in the excitation or ejection of a core election from an atom present within the sample. The residual energy left over from the excitation process is the energy of this so-called photo-electron, which leaves behind a core hole (Fig. 5.1a). The X-ray absorption  $\mu(E)$  can be quantified from the logarithmic ratio of the intensity of the transmitted X-ray beam I to that of the incident beam  $I_0$ , and the sample thickness t ( $\mu(E)t = -\ln(I/I_0)$ ). Or alternatively, by measuring the X-ray fluorescence intensity given off by the excited atoms as core holes are filled by electrons from higher energy orbitals  $(I_{\rm F})$ , in combination with the incident intensity  $(\mu(E) \sim I_{\rm F}/I_0)$ . By scanning through a range of incident X-ray energies, an X-ray absorption spectrum may be produced. The chosen range of energies allows for elemental selectivity - it is chosen to encompass a particular edge of a particular atom type, such as the zirconium K-edge at 17.9976 keV for example. The most obvious feature of a typical XAS spectrum is a sudden jump in absorption coefficient – an edge, at an energy sufficient to result in atomic excitation. At energies below the absorption edge, incoming X-ray photons are not energetic enough to induce an excitation. At higher energies, the likelihood of absorption and excitation decreases as the X-ray energy increases, resulting in a steady decay in the absorption coefficient. The additional features superimposed

on this decay after the absorption edge are the origin of the extended X-ray absorption fine structure; the source of the structural information generated by this characterisation method, and arise from the interference or interaction of the ejected photo-electron with itself *via* nearest-neighbour atoms.

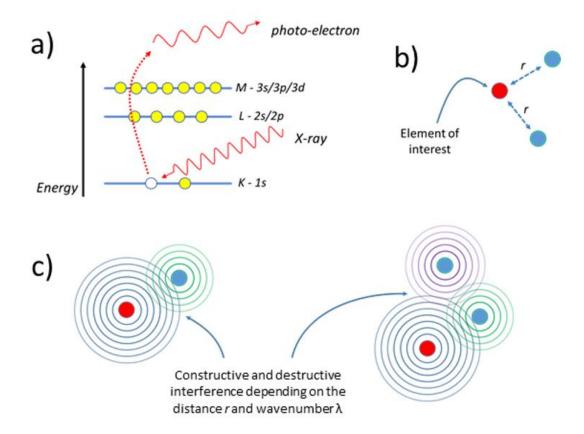


**Figure 5.1** Depictions of key concepts during X-ray irradiation of a sample leading to the structural information generated by EXAFS measurement: a) the photo-electric effect, b) selection of a particular element within a sample as opposed to its neighbours of the same or differing elements, c) the interactions of the outgoing photo-electron wave (blue) with itself following scattering by single atom neighbours (green, left) or *via* multiple neighbours (green then purple, right).

The ejected photo-electron can be considered a spherical electromagnetic wave propagating outwards from a source atom in all directions. This wave is then scattered by other atoms in the vicinity, returning to the original absorbing atom. This can happen by single or multiple scattering events, and can give rise to constructive or deconstructive interference

between the outgoing and returning wave (Fig. 5.1b, c). The extent of such interference is influenced by the distance between the absorbing and scattering atoms, and the wavelength of the photo-electron, and results in the oscillations seen post-edge in the absorption spectrum. However, the lifetime of the ejected photo-electron wave is not certain; it could for example scatter inelastically off a nearby atom which would change the photo-electron energy, its wavelength and its interference pattern. It could fail to scatter completely. An atom of high atomic number, with a relatively large number of electrons will generally scatter with a greater probability than an atom with fewer electrons (of lower atomic number), and in this way EXAFS can yield information about the types of atoms present in the local environment, in addition to how far away they are. After measurement of the absorption spectrum (Fig. 5.2a), the data are normalised and a background function subtracted to leave the EXAFS data  $\chi(E)$ remaining. EXAFS features may extend out to many 100s of eV above the absorption edge. This is in contrast to the XANES, the features at or just above and below the absorption edge, where multiple scattering events dominate. The energy of demarcation between the two is somewhat arbitrary. 16 It is convenient to think of the data in terms of a photo-electron wavenumber k (units of Å<sup>-1</sup>), rather than energy. These data  $\chi(k)$  are usually 'k-weighted' in order to give a more uniform amplitude to the EXAFS oscillations across the range of k and are known as the data in 'k-space' (Fig. 5.2b). Carrying out a Fourier-transform of the k-space data transforms those data into that in 'R-space.' The R-space data resembles a type of radial distribution function and features peaks at particular (radial) distances corresponding to the different atomic shells around the absorbing atom (Fig. 5.2c). Although, it is not quite a true distribution function as the distances are phase shifted, typically by ~0.5 Å. An R-space plot of EXAFS data provides a much more intuitive representation of the data from an EXAFS experiment, compared to the same data in k-space.

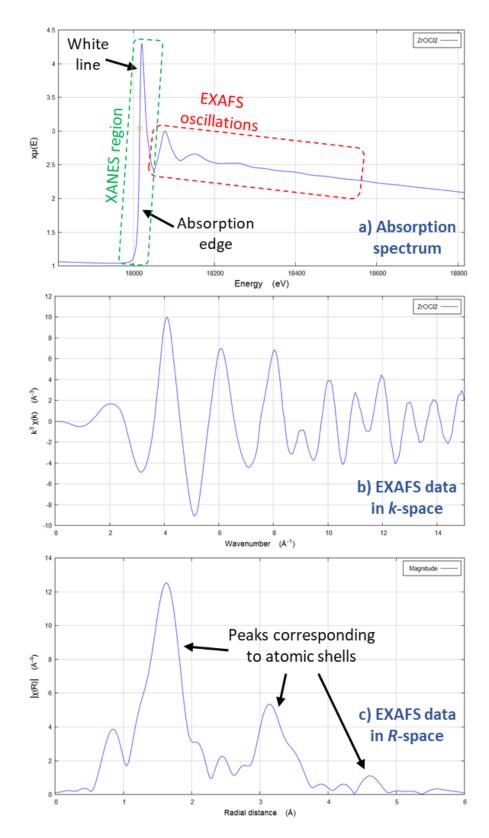


**Figure 5.2** Example of an X-ray absorption spectrum exhibiting EXAFS features (a, highlighted red), and the corresponding EXAFS data in *k*-space (b) and in *R*-space, which resembles a radial distribution function (c). The XANES region or the near-edge structure is highlighted in green.

Transmission EXAFS measurements were carried out at the Zr K-edge on the B18 Core XAS beamline at the Diamond Light Source X-ray synchrotron<sup>1</sup> with the assistance of Giannantonio Cibin. 10 scans were made for each sample with simultaneous measurement of a Zr metal reference foil. Incident energies were selected using a water-cooled, fixed-exit, double-crystal monochromator with Si(311) crystals. The beam was focussed horizontally and vertically using a double toroidal mirror, coated with Pt, 25 m from the source, while a pair of smaller plane mirrors were used for harmonic rejection. The beamline was operating in 'quick-EXAFS' mode. Solution samples were suspended in the path of the X-ray beam by means of a custom-made sample holder previously built by the School of Engineering, University of Warwick (Fig. 5.3). Aqueous solutions were contained within a Teflon® ring between two circular sheets of Kapton® film, all within a brass container with open ends. This container could be rotated along the axis of the incoming beam by means of a worm drive and heating could be applied via elements inserted into the main body of the sample holder. Thus samples could be measured both under ambient conditions and with in situ heating. Temperature calibration of the solution heating system was carried out at Warwick using a graphite insert in place of a solution sample; the temperature of which could be read externally by an infrared temperature probe. Measurements of solid samples (solid powders pressed into pellets) were carried out similarly with the pellets suspended in the path of the X-ray beam. Reduction of raw sample data (normalisation, background subtraction and conversion of EXAFS data  $\chi(E)$ to a function of wavenumber  $\chi(k)$ ) was carried out using the software ATHENA, to produce EXAFS spectra that could be fitted with the software ARTEMIS, both part of the Demeter XAS data processing package. 17 Ultimately, what this fitting process does is determine the parameters present in the 'EXAFS equation.' The form of this used as by ARTEMIS is presented in below in Equation 5.1.

$$\chi(k) = S_0^2 \sum_j \frac{N_j f_j(k) e^{-2Rj/\lambda(k)} e^{2k^2 \sigma_j^2}}{kR_j^2} sin[2kR_j + \delta_j(k)]$$
 Equation 5.1

f(k) and  $\delta(k)$  are the photo-electron scattering amplitude and phase respectively. These depend on the atomic number Z of the scattering atoms(s) and must be calculated from the measured spectra. The sum includes all scattering paths of the photo-electron from the central absorber to the neighbouring atoms and back;  $\lambda(k)$  describes how far this photo-electron can travel. Knowing these three parameters, it is then possible to determine R, N and  $\sigma^2$ . These are the nearest neighbour distance, coordination number of the absorbing atom and mean-square disorder in R, respectively. Finally,  $S_0^2$  is the amplitude reduction factor, an empirical parameter that accounts for processes that contribute to the X-ray absorption coefficient, but not the EXAFS. It has a characteristic dependence on the atomic number of the absorbing atom in question, and is closely linked to the coordination number.

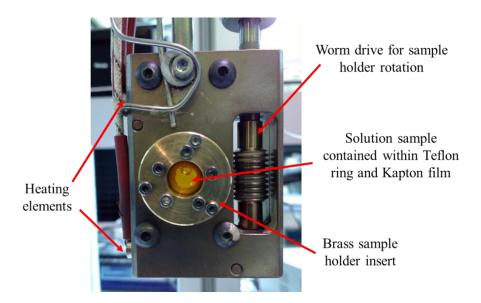


**Figure 5.3** Photograph of the sample holder with key components annotated. Not shown is the aluminium framework that suspends the holder, and connections to the sample rotation motor and heating control and associated power supply. Also visible in the sample space is an air bubble, the likes of which often formed *in situ* during heating experiments.

#### **5.2.2** X-Ray Pair Distribution Function (XPDF)

Powder X-ray diffraction is a powerful method to characterise solid materials. The powder diffraction pattern of a crystalline material typically features sharp Bragg peaks, which contain atomic-scale structural information about the material in question. For a material that is not fully crystalline, or only crystalline on the nanoscale, the Bragg peaks may become broad and diffuse, such that the information content of the diffraction pattern is reduced. The XPDF method is one approach to overcoming this problem. <sup>10</sup> Here, high-energy X-rays are scattered from a sample and detected, however in contrast to a typical powder diffraction experiment, the short X-ray wavelength and detection of scatter over much wider angles allows much more reciprocal space to be probed. As a result of this, and because both Bragg and diffuse scattering are detected and analysed, the technique is often referred to as total scattering. The link between reciprocal and real space is described by a scattering vector Q. This scattering vector Q may be related to the wavelength  $\lambda$  of incoming X-ray radiation by Q  $= 4\pi \cdot \sin(\theta/\lambda)$ , where  $\theta$  is half the scattering angle,  $2\theta$ . Q is often measured out to a value of  $Q_{\rm max}=30~{\rm \AA^{-1}}$  or more, to gain as much useful structural information about a sample as possible, though the coherent scattering at high-Q may be affected by the presence of incoherent Compton scattering and fluorescence. In practise  $Q_{\min}$  and  $Q_{\max}$  are determined by the experimental setup, though  $Q_{\max}$  is often deliberately reduced to eliminate data of low signal-to-noise, and artefacts that arise from truncation of signals during Fourier transformation. In this way maximising  $Q_{\text{max}}$  via experimental setup gives a higher resolution PDF with easily distinguishable atomic shells, and more real features that might otherwise be obscured.

The pair distribution function (PDF) is a measure of the probability of finding a pair of atoms a distance r apart and is related to the density of these atom pairs. A plot of a PDF or G(r) features peaks corresponding to particular atomic shells in a material and is relatively easy to interpret as the position of these peaks relates to specific inter-atomic distances. The function G(r) (Equation 5.2), contains a wealth of real-space structural information, such as

atomic distances, coordination number, disorder and particle size, independent of any structural model.  $^{12}$  S(Q) is the structure function, arising from intensities of features in the original scattering or diffraction pattern.

$$G(r) = \frac{2}{\pi} \int_0^\infty Q[S(Q) - 1] \sin Qr dQ$$
 Equation 5.2

Calculation of a PDF given a particular atomic structure is relatively straightforward, however realising a structure of a material from its PDF is difficult. As such, interpretation of PDF data is often made by comparison to other samples or reference materials that provide a model structure. The PDF data for a sample material is generated *via* a Fourier transform of the original X-ray diffraction data as outlined in Figure 5.4.<sup>10</sup>

**Figure 5.4** Outline of the steps involved in transforming X-ray diffraction or scattering data into a pair distribution function, reproduced from ref. 10. Collection of scattered X-ray intensity as a function of angle  $(2\theta)$  (top left) produces an X-ray diffraction pattern (bottom left). Raw data is corrected, and the intensity of the Bragg and diffuse components of the X-ray scatter gives rise to the structure function S(Q) (top right). The final atomic pair distribution function G(r) (bottom right) is calculated *via* a truncated Fourier transform of the structure function S(Q).

PDF data discussed in this chapter were collected from a number of aqueous zirconium solutions in sealed, rotating quartz capillaries mounted on the beamline, measured by the beamline scientists at the I15-1 beamline at Diamond Light Source as part of the 'Rapid Access' data collection programme. Data collected over an angular range of  $0.25 - 25^{\circ} 2\theta$  ( $0.02^{\circ}$  steps) with X-rays of  $\lambda = 0.161669$  Å were used to produce the D(r) PDF data provided, which is r-weighted to accentuate the data at higher r. Processing of data, including normalisation and subtraction of the background contribution from an empty capillary was carried out with an automated script in the software GudrunX. <sup>18, 19</sup> This was envisaged to be a prelude to further experimentation; however, this was ultimately not realised due to delays caused by equipment failure and the subsequent unavailability of the Diamond facility during the remaining time of this project. Ideally, for each sample a background measurement of a solution of nitric acid of the appropriate concentration would have been measured also and the data subtracted from those of the sample, however there was only the opportunity to run measurements on a total of five capillaries (due to the nature of the rapid access programme). This presents an important point to improve upon for further investigation.

#### **5.3 Literature Overview**

From a survey of the available literature concerning the application of EXAFS to aqueous solutions of zirconium, a relatively large number of papers were found compared to the other analytical techniques used in this project. However, reports of research making use of XPDF to study such samples were limited in comparison, and did not include any investigation of nitrate-based aqueous solutions of zirconium.

The earliest papers found are predominantly concerned with the study of precursors to zirconia, which can be formed from aqueous solutions of *e.g.*, zirconium oxychloride, transformed into zirconia via amorphous zirconium hydroxides using precipitation and calcination methods, in a sol-gel process.<sup>20-23</sup> EXAFS measurements show the zirconium hydroxide intermediate to have a structure resembling sheets of the zirconium tetramer; a

distorted square array of zirconium atoms connected by double hydroxy bridges (or oxo bridges), with additional coordinated water or hydroxy groups. In this arrangement the zirconium atoms typically have a spacing between nearest neighbours of ~3.5 Å (the side length of squares of zirconium atoms) with Zr-O bonds of around ~2.1 Å.<sup>20, 21</sup> Zirconium alkoxides may also be used as sol-gel precursors to zirconia, however are typically studied in alcoholic media, whereby the species that form consist of dimeric and trimeric linear alkoxide chains, though with similar interatomic distances.<sup>24, 25</sup>

At the turn of the 21st century, studies begin to appear in the literature regarding the structural properties of aqueous zirconium solutions themselves. Kanazhevskii et al. reported in 2001 work covering solutions of oxychloride, oxynitrate and sulfate salts. <sup>26</sup> They noted that previous studies using spectroscopic techniques on such solutions reveal structures like that in crystalline zirconium oxychloride, i.e. a tetrameric arrangement of zirconium atoms. They concluded with EXAFS measurements that the complexes formed in the three types of solutions studied were structurally similar, exhibiting a square-planar configuration of zirconium atoms. Small differences in Zr-Zr and Zr-O distances were attributed to different charges present on the complex ions, determined by the number of coordinated anions and weakly by the nature of the anions themselves. The same effect was seen to be induced by solution aging also, with aged solutions having generally shorter Zr-Zr and Zr-O distances and increased Zr-Zr connectivity. The same authors later expanded on this work to show via EXAFS measurements that solutions of zirconium oxychloride and hydroxide that originally feature tetrameric zirconium species may be modified by addition of sulfuric acid to create open zirconium trimer species. The introduction of sulfate groups into solution results in a displacement of hydroxy bridges such that zirconium ions become linked by sulfate bridges instead.27

A study reported in 2010 by Takasaki *et al.* reported on EXAFS measurements of solutions of zirconium oxychloride of varying compositions, with different amounts of added hydrochloric and perchloric acids.<sup>28</sup> For the range of solutions studied, they were able to show that the form of Zr-Zr bonding is a structure with double hydroxy bridges connecting

zirconium centres, as in the tetramers of zirconium oxychloride. However, the overall structure of solution species present resembled both tetramers and trimers depending on the exact amounts of added acid and zirconium concentration. Change of these parameters was reflected in Zr-Zr coordination number and interatomic distances. Irrespective of zirconium concentration, an increase in hydrogen ion concentration is accompanied by a decrease in Zr-Zr coordination number, attributed to the presence of trimer and smaller species. Later work covering similar solutions provided further evidence that the hydrolysis products of zirconium in aqueous solution are structurally similar to the zirconium tetramer.<sup>29</sup>

In general, the idea that the zirconium tetramer is a persistent species in solution as measured by EXAFS is common in the literature, but the presence of species smaller, and larger than the tetramer (*e.g.* zirconium octamers) is possible dependent on the exact conditions.<sup>30, 31</sup> The tetramer is also known to be present in acidic aqueous solutions of hafnium,<sup>32</sup> as well as in alkaline solutions of zirconium.<sup>33</sup> Deviations from this observation are exemplified by solutions of carbonate complexes, which are known to be monomeric,<sup>34, 35</sup> and seen for solutions of zirconium with added complexing agents such as acetic acid, which results in the formation of hexameric species.<sup>36</sup>

Recent work making use of XPDF measurement of precursors to zirconia also reveal the presence of species that are tetramer-like in structure. Tyrsted *et al.* reported in 2014 the presence of polymerised tetramer chains during a study of the synthesis of yttria-zirconia.<sup>37</sup> These could be considered tetramers joined together along the edges of the square of the tetramer, thus forming long chains with a characteristic persistence length of ~10 Å, consistent with two zirconium tetramers connected side-on. However, the PDF data revealed that the chains were not flat, but kinked or twisted, exhibiting Zr-Zr-Zr angles of 145°. As well as the 'nearest neighbour' Zr-Zr correlation of ~3.5 Å, and the second nearest neighbour correlation of ~5 Å, a third Zr-Zr correlation of ~6.7 Å was detected. This structural arrangement has since been reported by Dippel *et al.*, in another study regarding the species in solution during the solvothermal synthesis of zirconia;<sup>38</sup> here, characteristic diagonal distances along the tetramer chains of ~7.6 Å and ~10.2 Å were also seen. Hu *et al.* have also reported the presence

of the tetramer in aqueous solutions of zirconium, and the effect on these species when in the presence of sulfate; species larger than the tetramer were observed.<sup>39</sup>

#### **5.4 EXAFS Results**

The measurement of EXAFS data to determine the local atomic structure of samples was envisaged as an immediate gauge of whether the zirconium solutions studied here contained species whose structure were based upon the zirconium tetramer or not. The results presented here consist of k-space fits of  $k^2$ -weighted EXAFS data, and the R-space data with calculated R-space data from the k-space fits. Data normalisation, correction of absorption edge position and subtraction of pre- and post-edge background functions were carried out in the software ATHENA<sup>17</sup> to produce the EXAFS data. Fits to the EXAFS data over a k range of 3-14 Å<sup>-1</sup> were done with the software ARTEMIS.<sup>17</sup> Here, calculation of the possible scattering paths for a zirconium-tetramer like structure were performed with the built-in FEFF program,<sup>40</sup> from existing crystal structure data for zirconium oxychloride from the literature,<sup>41</sup> and the corresponding waveforms were fitted to the EXAFS data. The same was done for the sample of zirconia with the appropriate structural information.<sup>42</sup> The zirconium oxychloride structural model was chosen as it already contains suitable Zr-Zr and Zr-O shells, and a tetramer structure that is expected to be the basis of the structure of the species present in the zirconium solutions studied in this project.

EXAFS measurements of solid samples of zirconium oxychloride (ZrOCl<sub>2</sub>·8H<sub>2</sub>O) and zirconia (ZrO<sub>2</sub>) were carried out to provide reference data. Results of the fits to these data can be seen in the *k*- and *R*- space plots in Figure 5.5. Structural parameters generated during the fitting process may be found in Table 5.1. The atomic correlations that give rise to the features in the *R*-space plots are given in the annotations. These plots are dominated by a contribution from Zr-O correlations. Zirconia contains 7-coordinate Zr centres with respect to O whereas Zr is 8-coordinate in zirconium oxychloride (from hydroxy bridges and coordinated hydroxy and water groups). The next most intense features arise due to Zr-Zr correlations. It should be

noted that the radial distances implied by the *R*-space plots are not the true interatomic distances, though for the purposes of comparison of data of different samples this is not so important.

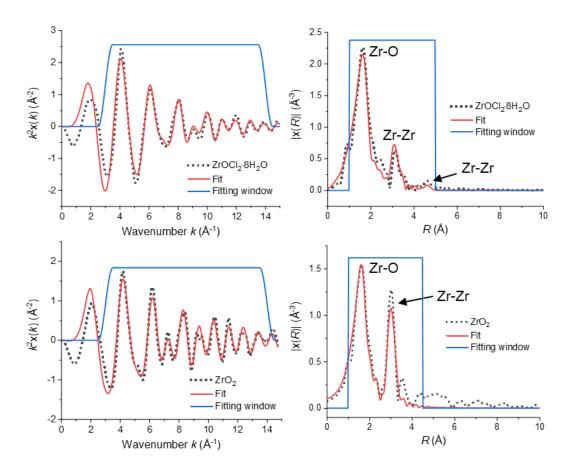


**Figure 5.5** Results of best fits to Zr K-edge EXAFS data measured for zirconium oxychloride and zirconia. The atomic correlations that give rise to the features in the R-space plots are given. At higher k and R, amplitudes and intensities drop as a result of the quick decay of the raw EXAFS  $\chi(k)$ , hence the use of 'k-weighting' (see Section 5.2.1) to try and mitigate this.

**Table 5.1** Refined EXAFS parameters from the Zr K-edge data analysis in Figure 5.5. The atom label in the Shell column denotes a particular scattering path included in the fit.  $R_{\rm eff}$  is the average interatomic distance as per the crystal structure; R is the refined distance adjusted during the fit. N,  $\sigma^2$ ,  $S_0^2$  &  $E_0$  represent coordination number, atomic position meansquared disorder, amplitude reduction factor and threshold energy, respectively.

Zirconium oxychloride					Zirconium dioxide				
Shell	Reff / Å	N	$\sigma^2$ / Å <sup>2</sup>	R / Å	Shell	Reff / Å	N	$\sigma^2$ / $\mathring{\mathbf{A}}^2$	R / Å
0	2.207	8	0.00985 ± 0.00149	2.177 ± 0.011	0	2.054	2	0.00326 ± 0.00292	2.092 ± 0.031
Zr	3.559	2	0.00494 ± 0.00087	3.560 ± 0.010	0	2.157	2	0.02523 ± 0.04857	2.156 ± 0.039
Zr	5.032	1	0.00796 ± 0.00707	5.010 ± 0.011	0	2.231	3	0.00612 ± 0.00438	2.221 ± 0.050
					Zr	3.333	1	0.00686 ± 0.00149	3.636 ± 0.022
					Zr	3.446	4	$0.00576 \pm 0.00214$	3.463 ± 0.018
$S_0^2 =$	= 1.650 ±	0.2	$21, E_0 = -7.861 \pm$	1.650 eV		$S_0^2 = 1.6$	50, 1	$E_0 = -6.717 \pm 4.33$	31 eV

For all of the zirconium solutions measured, EXAFS data were fitted with a structure based upon that of the zirconium tetramer. This was the case independent of exact solution composition (Zr:NO<sub>3</sub> – or Zr:Cl – ratio, and level of mandelic acid present) or temperature of heat treatment. It should be noted that the amount of mandelic acid used in these solutions is very low, compared to the amount needed to make zirconium mandelate.<sup>43</sup> The same was seen for samples of zirconium solutions dried to a solid gel, and two commercial solutions produced by industry. For solutions subjected to the full heat treatment at 94 °C (either as-made solutions or those heated *in-situ*), the best fits to EXAFS data were achieved by considering that the structures present in solution were possibly not individual tetramers. Here, the 'coordination number' for nearest-neighbour Zr-Zr correlations was increased from 2 to 3, and that for the Zr-Zr correlations across the tetramer increased from 1 to 2, to take into account connectivity of zirconium tetramers. This idea is analogous to the interpretation of XPDF data discussed later in this chapter. However fits to EXAFS data for solutions only subjected to heating at 60 °C were not improved in the same manner, suggestive of solution species that

are more like individual zirconium tetramers. Though it could be possible that if these species are agglomerated, then it is in a disordered manner such that the second Zr-Zr shell makes little contribution to the EXAFS. It should be noted that for the solution and gel samples measured the resulting amplitude reduction factors  $S_0^2$  are much higher than would be expected. In general, they should be in the region of 0.7 - 1.0, and fixed to be the same in value as that for a reference material of the same absorbing element of interest, measured at the same time. Multiple attempts were made to try and remedy this, though a way of satisfactorily improving this in fitting could not be found. It was considered that perhaps a sample preparation issue could be the cause of this;  $S_0^2$  is also inherently linked with coordination number which can be non-trivial to refine. 48 Reduced coordination numbers Nfor the Zr-Zr shells were tested (also with using an alternative zirconium nitrate starting structural model) to see if assuming the presence of chain-like species instead of those based upon the tetramer improved the result, however  $S_0^2$  was instead very greatly increased. Increasing the coordination numbers for the Zr-Zr shells – to simulate a close interaction between individual zirconium solution species (in a particle stacking-like manner for example) improved the results slightly but other errors regarding the structural disorder  $\sigma^2$  values arose. Otherwise, it was not possible to refine N in the same manner as for the other parameters as ARTEMIS does not accept variables as a starting input for N (only integers). A last point of note is that when the  $S_0^2$  values for the fits to solution/gel EXAFS data were fixed at 1.0, the fits, as judged by the k and R-space plots, were satisfactory for the Zr-Zr shells, but much worse for the Zr-O shells. It was thus thought that it may be the interpretation of the local oxygen environment that is the issue here, perhaps affected by the coordination of nitrate species and/or mandelic acid. The uncertainties in the structural disorder  $\sigma^2$  values for the Zr-O shells were also generally larger than those for the Zr-Zr shells. This would be an interesting hypothesis to look into for further investigation. Lastly, the intensities of Zr-Zr peaks in the R-space plots for two commercial zirconium oxynitrate and oxychloride samples included for comparison were noticeably reduced. This is attributed to the fact that they were produced with the *current* generation manufacturing process (not the background of this project), in a larger scale synthesis on plant, and were also aged to a greater extent. Thus the species present in these solutions may be slightly different in form. The intensity of the Zr-O peaks were much more intense (like with the other samples measured), which is unsurprising as the ready hydrolysis of zirconium ions in solution would produce an abundance of Zr-O bonding. Figures 5.6 and 5.7 show the results of fits to EXAFS data for aqueous zirconium solutions of varying composition. Representative structural parameters generated during the fitting process for these solutions may be found in Tables 5.2 – 5.5. The plots of EXAFS fits in Figure 5.8 show the 'before and after' from *in situ* heating in the sample holder whilst on the beamline. Figures 5.9 and 5.10 show the results of fitting to data for solutions dried to solid gels, and two commercial industry solution samples (made on plant using LMT's current generation manufacturing process) respectively. Structural parameters generated during the fitting of EXAFS data in the figures just described may be found in the Appendices (Tables A.2 – A.6).

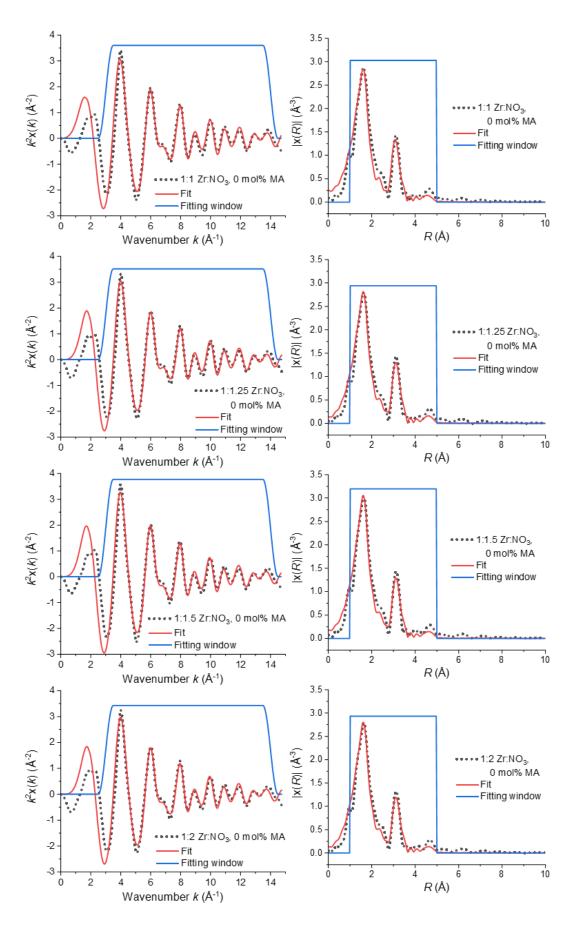


**Figure 5.6** Results of best fits to EXAFS data measured for as-made aqueous zirconium solutions of varying composition.

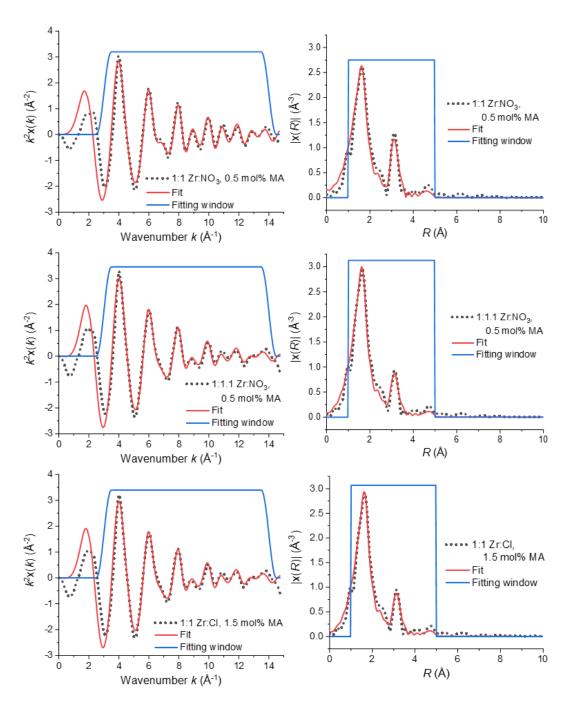


**Figure 5.7** Results of best fits to EXAFS data measured for as-made aqueous zirconium solutions of varying composition.

**Table 5.2** Refined EXAFS parameters from the Zr K-edge data analysis of PZN solutions of varying composition. An explanation of column designations may be found in the caption for Table 5.1

1:1 Zr:NO <sub>3</sub> , 0 mol% mandelic acid						1:1.25 Zr:NO <sub>3</sub> , 0 mol% mandelic acid				
Shell	Reff / Å	N	$\sigma^2$ / $\mathring{\mathbf{A}}^2$	R / Å		Shell	Reff / Å	N	$\sigma^2$ / $\mathring{\mathbf{A}}^2$	R / Å
0	2.124	3	0.00696 ± 0.00760	2.086 ± 0.032		0	2.124	3	0.00811 ± 0.01280	2.112 ± 0.068
0	2.210	3	0.00204 ± 0.00382	2.172 ± 0.024		0	2.210	3	0.00347 ± 0.00505	2.181 ± 0.058
0	2.326	2	0.00136 ± 0.00340	2.302 ± 0.016		0	2.326	2	0.00251 ± 0.00428	2.318 ± 0.027
Zr	3.559	3	0.00617 ± 0.00124	3.565 ± 0.010		Zr	3.559	3	0.00612 ± 0.00099	3.581 ± 0.010
Zr	5.032	2	0.00996 ± 0.00996	5.039 ± 0.045		Zr	5.032	2	0.00932 ± 0.00398	5.063 ± 0.041
$S_0^2 =$	2.585 ±	0.45	$E_0 = -11.243 \pm 1$	1.018 eV		$S_0^2 =$	= 2.520 ±	0.4	$78, E_0 = -8.550 \pm$	1.963 eV

**Table 5.3** Refined EXAFS parameters from the Zr K-edge data analysis of PZN solutions of varying composition. An explanation of column designations may be found in the caption for Table 5.1

1:1.5 Zr:NO <sub>3</sub> , 0 mol% mandelic acid					1:2 Zr:NO <sub>3</sub> , 0 mol% mandelic acid				
Shell	Reff / Å	N	$\sigma^2$ / $\mathring{\mathbf{A}}^2$	R / Å	Shell	Reff / Å	N	$\sigma^2$ / $\mathring{\mathbf{A}}^2$	R / Å
0	2.124	3	0.00741 ± 0.01395	2.115 ± 0.083	0	2.124	3	0.00724 ± 0.01270	2.112 ± 0.072
0	2.210	3	0.00357 ± 0.00653	2.184 ± 0.072	0	2.210	3	0.00326 ± 0.00594	2.184 ± 0.062
0	2.326	2	0.00266 ± 0.00494	2.319 ± 0.023	0	2.326	2	0.00236 ± 0.00459	2.318 ± 0.028
Zr	3.559	3	0.00658 ± 0.00107	3.589 ± 0.011	Zr	3.559	3	0.00638 ± 0.00102	3.587 ± 0.010
Zr	5.032	2	0.00992 ± 0.00458	5.077 ± 0.047	Zr	5.032	2	0.00979 ± 0.00447	5.075 ± 0.046
$S_0^2 =$	= 2.693 ±	0.5	$27, E_0 = -8.802 \pm$	2.034 eV	$S_0^2 =$	= 2.407 ±	0.4	$57, E_0 = -8.354 \pm$	1.985 eV

**Table 5.4** Refined EXAFS parameters from the Zr K-edge data analysis of PZN solutions of varying composition. An explanation of column designations may be found in the caption for Table 5.1

1:1 Zr:NO <sub>3</sub> , 0.5 mol% mandelic acid						1:1.1 Zr:NO <sub>3</sub> , 0.5 mol% mandelic acid				
Shell	Reff / Å	N	$\sigma^2$ / $\mathring{\mathbf{A}}^2$	R / Å		Shell	Reff / Å	N	$\sigma^2$ / $\mathring{\mathbf{A}}^2$	R / Å
0	2.124	3	0.00725 ± 0.01273	2.113 ± 0.074		0	2.124	3	0.00494 ± 0.01574	2.124 ± 0.135
0	2.210	3	0.00339 ± 0.00623	2.185 ± 0.064		0	2.210	3	0.00331 ± 0.01471	2.199 ± 0.116
0	2.326	2	0.00244 ± 0.00463	2.319 ± 0.028		0	2.326	2	0.00244 ± 0.00708	2.323 ± 0.042
Zr	3.559	3	0.00625 ± 0.00100	3.586 ± 0.010		Zr	3.559	3	0.00825 ± 0.00133	3.609 ± 0.013
Zr	5.032	2	0.009702 ± 0.00433	5.072 ± 0.044		Zr	5.032	2	0.00979 ± 0.00543	5.108 ± 0.054
$S_0^2 =$	= 2.316 ±	0.4	$35, E_0 = -8.897 \pm$	1.957 eV		$S_0^2 =$	= 2.282 ±	0.4	$52, E_0 = -6.779 \pm$	2.103 eV

**Table 5.5** Refined EXAFS parameters from the Zr K-edge data analysis of PZN solutions of varying composition. An explanation of column designations may be found in the caption for Table 5.1

1:1 Zr:Cl, 1.5 mol% mandelic acid							
Shell	Reff / Å	N	$\sigma^2$ / Å <sup>2</sup>	R / Å			
0	2.124	3	0.00489 ± 0.01390	2.122 ± 0.110			
0	2.210	3	0.00306 ± 0.01247	2.199 ± 0.094			
0	2.326	2	0.00225 ± 0.00654	2.323 ± 0.038			
Zr	3.559	3	0.00804 ± 0.00128	3.608 ± 0.013			
Zr	5.032	2	0.009702 ± 0.00511	5.107 ± 0.052			

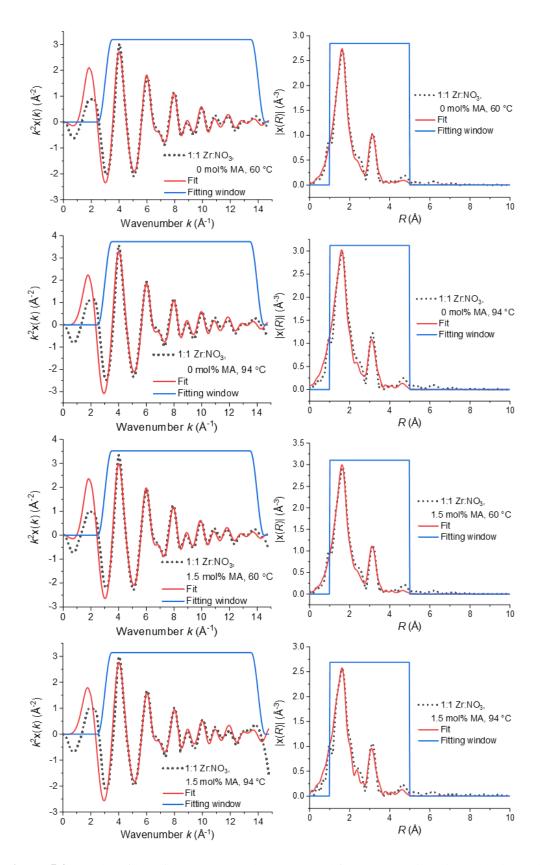


**Figure 5.8** Results of best fits to EXAFS data measured for aqueous zirconium solutions of varying composition, heated *in situ* from 60 to 94 °C.

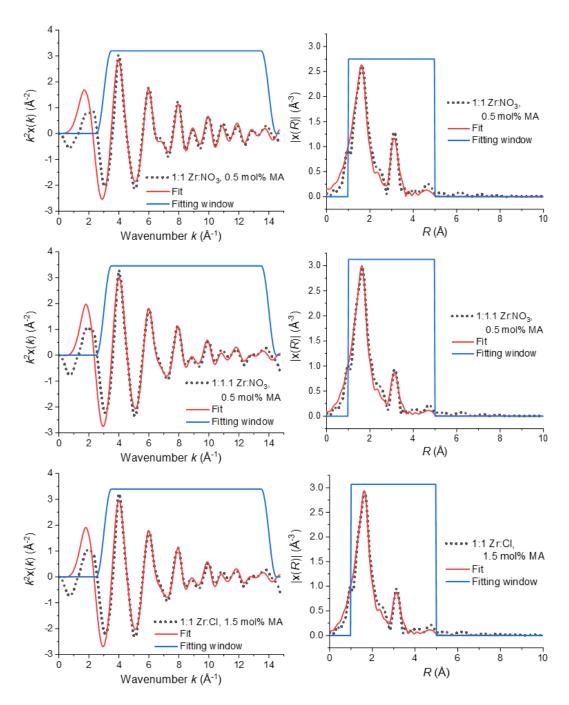


**Figure 5.9** Results of best fits to EXAFS data measured for as-made aqueous zirconium solutions of varying composition dried to solid gels.

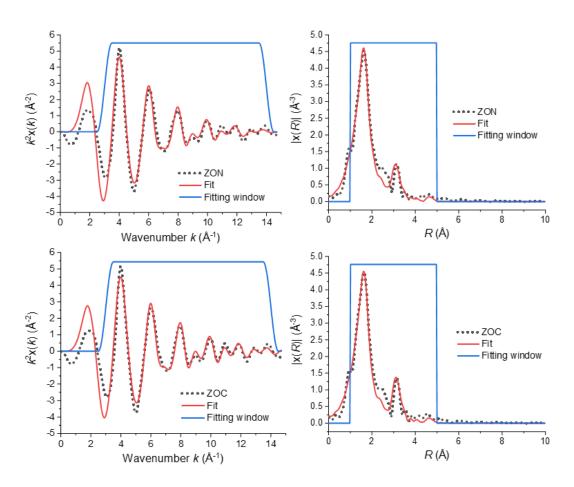


**Figure 5.10** Results of best fits to EXAFS data measured for as-made commercial aqueous zirconium solutions. 'ZON' = zirconium oxynitrate and 'ZOC' = zirconium oxychloride.

## **5.5 PDF Results**

X-ray PDF data were determined for samples of aqueous solutions of zirconium of varying composition and for one differing in maximum heat treatment temperature (Fig. 5.11). The plots of PDF data D(r) are broadly similar for all 5 samples, suggestive of the presence of some of the same structures for the zirconium species present in all these solutions, *i.e.*, similar short- and medium-range order. Although, peak intensities were seen to vary which could result from differences in coordination numbers, so ultimately there is likely a range of types (sizes, with species smaller than tetramer perhaps, due to the great acidity of the solutions) of species present, albeit all based upon zirconium – oxygen bonding. Further investigation, with subtraction of suitable background data for each sample tested, would be required to fully understand these variations. This could be due in part to small differences in

the concentration of the solutions although every effort was made to create them in the same manner. Strong correlations are seen up to 7-8 Å. The key features of these plots are the four intense peaks between r=2-8 Å; these correspond to Zr-O and Zr-Zr correlations (those most important in understanding the connectivity of the zirconium centres). The specific interatomic distances are highlighted in red in Figure 5.12 for the 1:1 Zr:NO<sub>3</sub> 0 mol% mandelic acid sample heated to 94 °C. The correlation at ~2.2 Å is assigned to the Zr-O pairs of the bridging hydroxy groups between zirconium centres and of coordinated water and hydroxy groups. The next two most intense peaks at ~3.6 Å and ~5.1 Å are at an r value consistent with the Zr-Zr distance that forms the edge of the square zirconium tetramer, and the Zr-Zr square diagonal distance respectively (Fig. 5.13a).  $^{37,38}$  This strongly suggests that the species in these aqueous solutions of zirconium are based upon the zirconium tetramer, in line with the results of other characterisation methods used in this project.

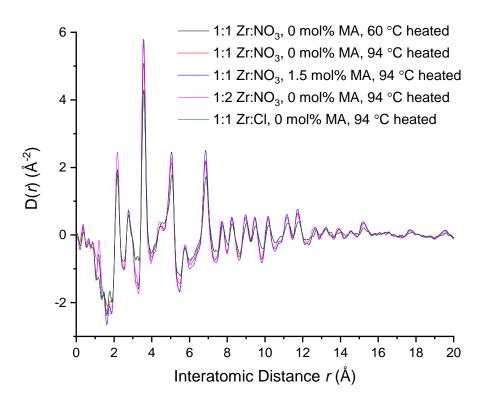


**Figure 5.11** Plots of X-ray PDF data for aqueous zirconium solutions measured on the I15-1 beamline at Diamond Light Source. The different compositions of the solutions are described in the legend; 'MA' refers to mandelic acid. The maximum temperature of heat treatment is also given.

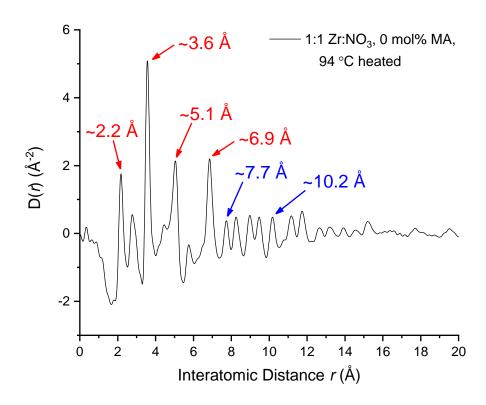
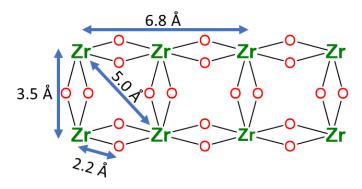


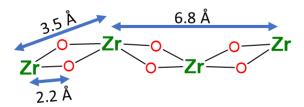
**Figure 5.12** PDF data for the 1:1 Zr:NO<sub>3</sub> 0 mol% mandelic acid solution heated to 94 °C, with the main features of interest, as discussed in the main text, highlighted. 'MA' = mandelic acid.

A further intense peak is also seen at  $\sim$ 6.9 Å, in addition to those relating to the zirconium tetramer itself. This is also likely to be a Zr-Zr correlation, and is the next longest Zr-Zr distance seen due to connectivity of individual tetramers. This atomic spacing is slightly shorter than twice the Zr-Zr tetramer edge distance; and is interpreted as if the connected tetramers are buckled along the chain axis.<sup>37, 38</sup> This concept is visualised in the chain edge view in Figure 5.13b. Also present in the data collected here are less intense peaks at  $\sim$ 7.7 Å and  $\sim$ 10.2 Å (highlighted in blue in Fig. 5.12). These two r values are consistent with two further Zr-Zr diagonal distances seen in the literature<sup>38</sup> for buckled tetramer chains (Fig. 5.13c). No evidence is seen for the alternative, flat sheet-like connectivity of zirconium tetramers that would otherwise be indicated by a Zr-Zr correlation at 7.1 Å (Fig. 5.13d).<sup>38, 44</sup> The idea of chains of linked zirconium tetramers in solution has also been proposed following SAXS measurements of zirconium acetate solutions.<sup>45</sup>

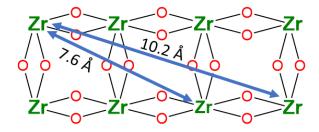
# (a) Tetramer chain top-down 'ladder' view



# (b) Tetramer chain edge view



# (c) Tetramer chain ladder view – next longest Zr-Zr diagonals



# (d) Flat sheet of connected tetramers

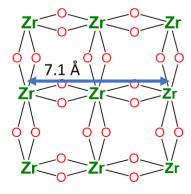


**Figure 5.13** Diagrams of structures formed by the joining of individual tetramers. The tetramer edge view (b) visualises the idea of the buckled tetramer chains. The structure in (d) is that of a flat sheet-like structure formed by joined tetramers. H atoms of the hydroxy bridges and other coordinated water and/or hydroxy groups are omitted for clarity. The Zr-O and Zr-Zr distances discussed in the main text are labelled.

Three further features in the PDF data may be assigned based upon the work by Hu *et al.* These are highlighted in Figure 5.14. The peak at ~2.8 Å may be attributable to protons of coordinated water groups,<sup>39</sup> and that at ~4.5 Å is possibly a Zr-O correlation with O atoms of hydroxy bridges opposite to Zr. The peak at ~5.8 Å is likely due to the O atoms of coordinated water groups on adjacent zirconium centres.<sup>39</sup> These correlations are visualised in Figure 5.15. Of course, O-O correlations might also be expected to be seen, although the literature that was found that enabled the interpretation of the PDF data presented here did not specifically report such correlations. In addition, there were no peaks in this PDF data, otherwise unassigned, that might have been assignable as such. This may have not been the case if subtractions of appropriate backgrounds could be carried out for each sample measured, which would have eliminated contributions from the solvent (water) and free nitrate groups. *Coordinated* nitrate groups (though small in number) would also have also added further O-O correlations.

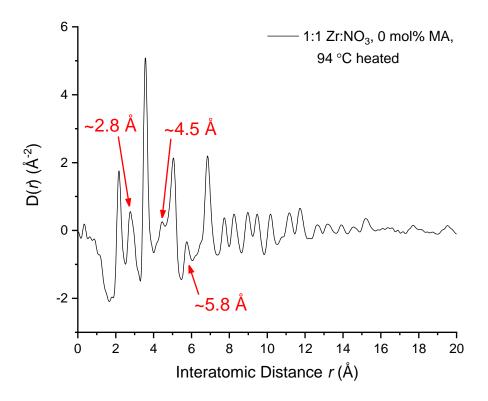


**Figure 5.14** PDF data for the 1:1 Zr:NO<sub>3</sub> 0 mol% mandelic acid solution heated to 94 °C, with the main features of interest, as discussed in the main text, highlighted. 'MA' = mandelic acid.

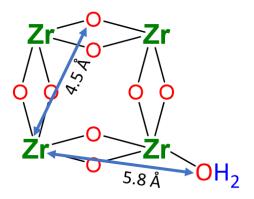


**Figure 5.15** A schematic of the zirconium tetramer with assignments of correlations that give rise to the additional PDF features noted in Figure 5.14 (discussed in the main text). H atoms of the hydroxy bridges and other coordinated water and/or hydroxy groups are omitted for clarity.

The plots in Figure 5.16 show the differences between select samples. The differences are the greatest for the four most intense peaks between r = 2 - 8 Å, suggesting variation in the zirconium and oxygen local environments. The differences imparted on the PDF data by changing the heat treatment temperature of an otherwise identical solution are minimal (Fig. 5.16b). The effect of introducing mandelic acid is also relatively small (Fig. 5.16c) though the sample investigated here only had it present at a level of 1.5 mol% relative to zirconium. Greater differences are seen when the Zr:NO<sub>3</sub> ratio is doubled (Fig. 5.16a) or when nitrate is replaced by chloride (Fig. 5.16d). It is interesting that the peaks affected by increasing the nitrate content are mainly those at ~2.2 and ~3.6 Å, whereas the effect of using chloride instead of nitrate more affects the higher r peaks at ~3.6, ~5 and ~6.8 Å. This could be a reflection of the behaviour of the respective anions (nitrate may coordinate to zirconium in these types of solutions,  $^{46.47}$  unlike chloride); this would be a suitable target for further investigation.

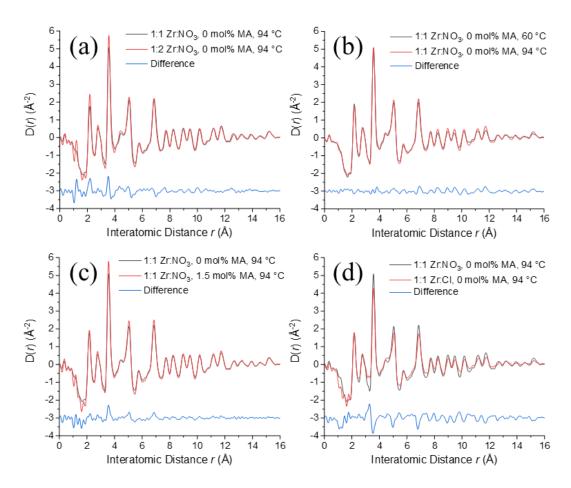


**Figure 5.16** Plots highlighting the differences between X-ray PDF data for aqueous zirconium solutions ((a) nitrate ratio, (b) heat treatment temperature, (c) MA content and (d) acid anion) measured on the I15-1 beamline at Diamond Light Source. The different compositions of the solutions are described in the legends; 'MA' refers to mandelic acid. The maximum temperature of heat treatment is also given.

# 5.6 Summary and Conclusions

EXAFS measurements of aqueous solutions of zirconium, mainly those featuring nitrate as the acid anion have been presented. EXAFS data could be described by solution species with structures like that of the zirconium tetramer, *via* the appropriate fitting, regardless of solution composition or temperature of heat treatment. This is consistent with the idea that the species prevalent in these solutions have a structure which on the local scale is like that of the zirconium tetramer. The same was seen for samples made from drying solutions to solid gels. No detectable effect of the presence of mandelate was seen by EXAFS. Fits to EXAFS data from solutions treated to heating at 94 °C were best when connectivity

between individual tetramers was considered, whereas fitting suggested that solutions not subject to the usual full heat treatment contained species with structures more resembling individual zirconium tetramers. X-ray PDF measurement of nitrate-based aqueous solutions of zirconium has also been reported, and preliminary results suggest the presence of solution species with a structure based upon that of the zirconium tetramer. Medium-range Zr-Zr correlations seen in the data are consistent with the idea that these species may grow to increasing lengths by the combination of multiple individual tetramers, forming buckled, ladder-like chains, as opposed to sheets. Data interpretation was by comparison to the limited literature. Such data on nitrate-based solutions of zirconium specifically is as of yet unreported in the literature. For this reason, and due to first signs of differences seen in the PDF data for solutions of varying composition, these types of solutions would make ideal samples for further investigation *via* XPDF, bringing to light further knowledge on the complex aqueous chemistry of zirconium.

### 5.7 Bibliography

- A. J. Dent, G. Cibin, S. Ramos, A. D. Smith, S. M. Scott, L. Varandas, M. R.
   Pearson, N. A. Krumpa, C. P. Jones and P. E. Robbins, *J. Phys.: Conf. Ser.*, 2009, 190, 12039-12042.
- 2. R. S. von Bordwehr, Ann. Phys. Fr., 1989, **14**, 377-465.
- 3. E. Stern, J. Synchrotron Rad., 2001, **8**, 49-54.
- 4. S. J. Gurman, *J. Mater. Sci.*, 1982, **17**, 1541-1570.
- 5. S. Gross and M. Bauer, *Adv. Funct. Mater.*, 2010, **20**, 4026-4047.
- 6. J. G. Parsons, M. V. Aldrich and J. L. Gardea-Torresdey, *Appl. Spectrosc. Rev.*, 2002, **37**, 187-222.
- 7. A. I. Frenkel, *Chem. Soc. Rev.*, 2012, **41**, 8163-8178.
- A. Gaur, B. D. Shrivastava and H. L. Nigam, *Proc. Indian Natn. Sci. Acad.*, 2013,
   79, 921-966.

- 9. S. Bordiga, F. Bonino, K. P. Lillerud and C. Lamberti, *Chem. Soc. Rev.*, 2010, **39**, 4885-4927.
- 10. S. J. L. Billinge, *Phil. Trans. R. Soc. A*, 2019, **377**, 20180413.
- 11. D. A. Keen, Crystallogr. Rev., 2020, 26, 143-201.
- 12. K. W. Chapman, *Mater. Res. Soc.*, 2016, **41**, 231-238.
- 13. C. Castillo-Blas, J. M. Moreno, I. Romero-Muniz and A. E. Platero-Prats, *Nanoscale*, 2020, **12**, 15577-15587.
- R. K. Biswas, J. Ghosh and M. Kuttanellore, *T. Indian Ceram. Soc.*, 2020, **79**, 158-165.
- 15. G. Bunker, *Introduction to XAFS: A Practical Guide to X-ray Absorption Fine Structure Spectroscopy*, Cambridge University Press, Cambridge, 2010.
- 16. S. Calvin, *XAFS for Everyone*, CRC Press, New York, 2013.
- 17. B. Ravel and M. Newville, *J. Synchrotron Radiat.*, 2005, **12**, 537-541.
- 18. A. K. Soper, GundrunN and GudrunX: Programs for Correcting Raw Neutron and X-ray Diffraction Data to Differential Scattering Cross Section, RAL-TR-2011-013, Science and Technology Facilities Council, Great Britain, 2011.
- 19. D. A. Keen, J. Appl. Cryst., 2004, **34**, 172-177.
- X. Turrillas, P. Barnes, A. J. Dent, S. L. Jones and C. J. Norman, *J. Mater. Chem.*, 1993, 3, 583-586.
- X. Turrillas, P. Barnes, D. Gascoigne, J. Z. Turner, S. L. Jones, C. J. Norman, C. F.
   Pygall and A. J. Dent, *Radiat. Phys. Chem.*, 1995, 45, 491-508.
- L. A. Chiavacci, S. H. Pulcinelli, C. V. Santilli and V. Briois, *Chem. Mater.*, 1998,
   10, 986-993.
- 23. P. Li, I.-W. Chen and J. E. Penner-Hahn, *Phys. Rev. B*, 1993, **48**, 10063-10073.
- 24. D. Peter, T. S. Ertel and H. Bertagnolli, J. Sol-Gel Sci. Technol, 1994, 3, 91-99.
- 25. D. Peter, T. S. Ertel and H. Bertagnolli, J. Sol-Gel Sci. Technol, 1995, 5, 5-14.
- V. V. Kanazhevskii, B. N. Novgorodov, V. P. Shmachkova, N. S. Kotsarenko, V. V.
   Kriventsov and D. I. Kochubey, *Mendeleev Commun.*, 2001, 11, 211-212.

- V. V. Kanazhevskii, V. P. Shmachkova, N. S. Kotsarenko, V. N. Kolomiichuk and
   D. I. Kochubei, *J. Struct. Chem.*, 2006, 47, 860-868.
- F. Takasaki, N. Ogawa, I. Watanabe, T. Suzuki, Y. Nakajima, T. Wakita and R. Suzuki, *Bunseki Kagaku*, 2010, 59, 447-454.
- F. Takasaki, K. Fujiwara, Y. Nakajima, T. Nishikawa and N. Ogawa, *Chem. Lett.*,
   2014, 43, 196-198.
- 30. C. Walther, J. Rothe, M. Fuss, S. Buchner, S. Koltsov and T. Bergmann, *Anal. Bioanal. Chem.*, 2007, **388**, 409-431.
- J. Rose, T. J. M. D. Bruin, G. Chauveteau, R. Tabary, J.-L. Hazemann, O. Proux, A.
   Omari, H. Toulhoat and J.-Y. Bottero, J. Phys. Chem. B, 2003, 107, 2910-2920.
- 32. C. Hagfeldt, V. Kessler and I. Persson, *Dalton Trans.*, 2004, **2004**, 2141-2151.
- 33. T. Kobayashi, S. Nakajima, R. Motokawa, D. Matsumura, T. Saito and T. Sasaki, *Langmuir*, 2019, **35**, 7995-8006.
- F. Takasaki, K. Fujiwara, Y. Nakajima, T. Nishikawa, H. Masu, M. Imanari, Y. Hidaka and N. Ogawa, *Dalton Trans.*, 2015, 44, 645-652.
- F. Takasaki, K. Fujiwara, T. Kikuchi, T. Tanno, Y. Nakajima, Y. Toyoda and N.
   Ogawa, Anal. Sci., 2017, 33, 1007-1012.
- C. Hennig, S. Weiss, W. Kraus, J. Kretzschmar and A. C. Scheinost, *Inorg. Chem.*,
   2017, 56, 2473-2480.
- 37. C. Tyrsted, N. Lock, K. M. O. Jensen, M. Christensen, E. D. Bojesen, H. Emerich,G. Vaughan, S. J. L. Billinge and B. B. Iversen, *IUCrJ*, 2014, 1, 165-171.
- A.-C. Dippel, K. M. O. Jensen, C. Tyrsted, M. Bremholm, E. D. Bojesen, D. Saha,
   S. Birgisson, M. Christensen, S. J. L. Billinge and B. B. Iversen, *Acta Cryst.*, 2016,
   A72, 645-650.
- Y.-J. Hu, K. E. Knope, S. Skanthakumar, M. G. Kanatzidis, J. F. Mitchell and L. Soderholm, *J. Am. Chem. Soc.*, 2013, 135, 14240-14248.
- 40. S. I. Zabinsky, J. J. Rehr, A. Ankudinov, R. C. Albers and M. J. Eller, *Phys. Rev. B*, 1995, **52**, 2995-3009.

- 41. T. C. W. Mak, Can. J. Chem., 1968, 46, 3491-3497.
- 42. D. K. Smith and H. W. Newkirk, *Acta Cryst.*, 1965, **18**, 983-991.
- J. M. Crosland, E. K. Corlett, D. Scapens, N. Guillou, S. P. Brown and R. I. Walton,
   Chem. Commun., 2020, 56, 10159-10162.
- 44. A. Clearfield, *J. Mater. Res.*, 1990, **5**, 161-162.
- M. Bremholm, H. Birkedal, B. B. Iversen and J. S. Pedersen, *J. Phys. Chem. C*, 2015, 119, 12660-12667.
- P. D. Southon, J. R. Bartlett, K. S. Finnie, J. L. Woolfrey, B. Ben-Nissan and G. S.
   K. Kannangara, J. Aust. Ceram. Soc., 1999, 35, 7-12.
- P. D. Southon, J. R. Bartlett, J. L. Woolfrey and B. Ben-Nissan, *Chem. Mater.*,
   2002, 14, 4313-4319.
- 48. B. Ravel and S. D. Kelly, AIP Conf. Proc., 2007, **882**, 150.

# Chapter 6:

# Synthesis and Characterisation of Zirconium Mandelate: First Structure Elucidation *via* NMR Crystallography

#### 6.1 Introduction

This chapter describes work undertaken to investigate the structure of the zirconiumbased metal-organic complex zirconium (tetra)mandelate. Mandelic acid (2-hydroxy-2phenylacetic acid) is used as an additive in some LMT zirconium solutions, specifically those used as possible precursors to solid zirconium materials (oxides and hydroxides for example).<sup>1</sup> The strong affinity of mandelic acid for zirconium is such that material properties (surface areas and pore sizes for example) of e.g. zirconia made from LMT zirconium solutions, may depend on the level of mandelic acid present. In the industrial setting, relatively low levels are used, typically <10% relative to zirconium. It is thought that the presence of the mandelic acid influences the development of solution zirconium species, which in turn modifies the properties of any materials derived from these solutions.<sup>2</sup> Mandelic acid may direct the growth of individual zirconium species in solution, and the coalescence of these solution zirconium species into larger ones during a subsequent precipitation process (by addition of base for example) thus defining the final product properties following calcination or high-temperature firing. However, these hypotheses are speculative, and a proper understanding is yet to be developed, so knowing the crystal structure of zirconium mandelate will make this more achievable.

It was deemed appropriate to investigate zirconium mandelate further: as a complex in its own right, providing a potentially useful reference material to understand the binding of mandelate in zirconia precursors, as well as expanding the literature knowledge about this substance in general. Zirconium mandelate has been known of and used in selective gravimetric analysis of zirconium for over 70 years.<sup>3</sup> Most notably, its crystal structure is herein described for the first time<sup>4</sup> from a combination of advanced techniques including

synchrotron powder X-ray diffraction (PXRD), <sup>13</sup>C and <sup>1</sup>H solid-state nuclear magnetic resonance (NMR), and extended X-ray absorption fine structure (EXAFS) spectroscopy. As will be revealed, it is a rare example of isolated zirconium cations in the solid state, captured from solution, rather than the clusters that are so often prevalent in aqueous solutions of zirconium.

# 6.2 The Chemistry of Mandelic Acid

Mandelic acid, or 2-hydroxy-2-phenylacetic acid, is a chiral, aromatic, alpha-hydroxy carboxylic acid described by the molecular formula C<sub>6</sub>H<sub>5</sub>CH(OH)CO<sub>2</sub>H. It can exist in two stereochemical forms: a pair of enantiomers that differ in the relative orientations of the four different functional groups around the stereocentre (Fig. 6.1). The combination of both hydroxy and carboxylic acid groups leads to enhanced coordinative abilities; there are several mandelate complexes known of metals other than zirconium, featuring chelating and bridging coordination or a combination of both. These will be referred to later in this chapter. Coordination of this molecule to metal centres is possible via the alpha-hydroxy oxygen electron lone pair, and/or the negative charge on the acidic carboxylic oxygen, when deprotonated. Mandelic acid takes the form of a white crystalline solid and is soluble in water and many polar organic solvents. This is in great contrast to benzoic acid, C<sub>6</sub>H<sub>5</sub>COOH, which lacks the additional C(OH)H moiety and has a very limited solubility in water. It was originally discovered in 1831 as a product of heating amygdalin (a bitter almond extract) with hydrochloric acid.<sup>5</sup> Its name derives from the German word for almond, 'mandel.' Mandelic acid exhibits antibacterial properties<sup>6, 7</sup> and is most well known as an active ingredient in cosmetic products.8

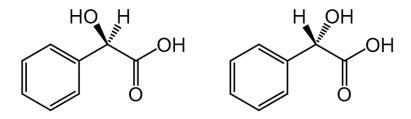


**Figure 6.1** The two enantiomeric forms of mandelic acid ((R)- left, (S)- right).

# 6.3 Zirconium Mandelate as a Gravimetric Analysis Reagent

#### 6.3.1 Discovery and Development of Knowledge Regarding the Complex

In 1947, Kumins first reported the precipitation of zirconium by mandelic acid,<sup>3</sup> and most importantly, this was in the presence of a number of other metal cations, meaning it could be used as a selective and quantitative gravimetric analysis for zirconium. Alternative methods of separation or determination of zirconium content included spectrophotometry, using alizarin, 9, 10 or with other gravimetric agents such as 8-hydroxyquinoline, 11 or the first to be reported, cupferron. 12 Alternatively zirconium can be separated as a phosphate or basic selenite. 13 The use of halogenated and other derivatives of mandelic acid are also effective, 14-<sup>16</sup> and work in *volumetric* determinations of zirconium content also.<sup>17</sup> Kumins' method arguably has become the most commonly used, subject to various improvements over time<sup>18</sup>-<sup>21</sup> and applicable in a range of applications. <sup>22, 23</sup> The affinity of mandelic acid for zirconium is such that it can selectively operate in the presence of an impressive range of other metal cations in solution including titanium, iron, vanadium, aluminium, chromium, thorium, cerium, tin, barium, calcium, copper, bismuth, antimony and cadmium.<sup>3</sup> Kumins proposed that zirconium mandelate was most likely a tetramandelate, a simple salt composed of four mandelate anions per zirconium atom: Zr(C₀H₅CH(OH)CO₂H)₄, but its actual crystal structure was never determined.

A number of other authors expanded on Kumins' work; Hahn found that the method was still applicable in strongly acidic solution, and that hafnium was also precipitated by

mandelic acid. <sup>24</sup> Feigl proposed a chelate-type structure whereby coordination of mandelate to zirconium took place through the alpha-hydroxy oxygen and the deprotonated carboxylate oxygen, <sup>25</sup> an idea later confirmed by Hahn and Weber<sup>26</sup> (Fig. 6.2). It was subsequently found that the use of strongly acidic conditions is key in ensuring the formation of the tetramandelate; otherwise other compositions such as Zr(OH)(C<sub>6</sub>H<sub>5</sub>CH(OH)CO<sub>2</sub>H)<sub>3</sub> result.<sup>27, 28</sup> In contrast to the idea of a simple ML<sub>4</sub> complex, Larsen and Homeier formed the hypothesis that zirconium tetramandelate is in fact polymeric, <sup>29</sup> despite the use of concentrated hydrochloric acid during the synthesis that would solubilise Zr<sup>4+</sup>. They proposed that initially, polymeric zirconium species can act as a template for the formation of a polymeric zirconium mandelate, forming overall linear species that are subsequently coordinated by both chelating and bridging mandelate anions. This idea is consistent with the oxophilic nature of zirconium and its propensity for hydrolysis in aqueous solution even down to very low pH.<sup>30</sup> Indeed, the most studied solution zirconium species are based upon the so-called zirconium tetramer, a slightly distorted square array of zirconium atoms linked together by double hydroxy bridges, formed by hydrolysis processes. Such an arrangement was first found to be the basis of the structure of solid zirconium oxychloride,<sup>31</sup> and then later found to also exist in aqueous solution.<sup>32</sup> It is common in the solid state to find zirconium intricately linked with oxygen in chains or clusters, for example the [Zr<sub>6</sub>O<sub>4</sub>(OH)<sub>4</sub>] octahedral clusters that form part of the structure of the archetypal metal-organic framework (MOF) UiO-66 (Fig. 6.3a),<sup>33</sup> and individual clusters capped by carboxylate ligands. 34, 35 Chains featuring oxygen and anion-linked zirconium atoms can be found in the layered structures of the hydrated zirconium sulfates and nitrates.<sup>36</sup>-<sup>38</sup> Chains of edge-sharing ZrO<sub>7</sub> polyhedra are found in the structure of the MOF MIL-140 (Fig. 6.3b),<sup>39</sup> and chains of edge-shared ZrO<sub>8</sub> units commonly feature in MOFs with phenolate linkers (Fig 6.3c).<sup>40</sup>

**Figure 6.2** A depiction of the composition and nature of bonding of zirconium tetramandelate, as per the original literature, <sup>25, 26</sup> showing the coordination of mandelate to zirconium through both the alpha-hydroxy oxygen and acidic carboxylate oxygen.

**Figure 6.3** Illustrations of the structures of aforementioned zirconium metal-organic frameworks: a) the  $Zr_6$  cluster of UiO-66 and its connectivity via benzenedicarboxylate linkers; b) the edge-sharing chains of  $ZrO_7$  units (right) that make up the MIL-140 series of MOFs (left); c) the edge-sharing chains of  $ZrO_8$  units found in the MOF MIL-163. Images are reproduced from the literature.  $^{33,39,40}$ 

#### **6.3.2 Historical Syntheses**

Early studies on zirconium mandelate used a broadly similar synthesis method, involving mixing of solutions of mandelic acid and zirconium (e.g zirconium oxide or zirconium oxychloride) in the presence of hydrochloric acid, either immediately or dropwise over time, with heating to 80-90 °C.<sup>3, 18, 26, 27</sup> Reaction was also found to take place with zirconium isopropoxide in benzene.<sup>28</sup> A common observation made as part of these studies was that the initial precipitation of zirconium mandelate was not necessarily immediate and could depend on the relative amount of mandelic acid added at a given point. A range of stoichiometries of the products (basic salts featuring O and OH ligands in addition to mandelate) were detected. It was postulated that intermediate soluble complexes of zirconium and mandelic acid were possible whereby the zirconium did not have the full complement of mandelate anions. This phenomenon was eventually attributed to the concentration of the hydrochloric acid at the time of precipitation, which should be sufficiently high that hydrolysis of zirconium is at a minimum.<sup>27</sup>

#### **6.4 Experimental Methods**

#### **6.4.1** Thermogravimetric Analysis (TGA)

Analysis of sample material (5-10 mg) was carried out in open 70  $\mu$ l alumina pans with a Mettler Toledo STARe TGA/DSC, with heating and simultaneous sample mass measurement from room temperature to 1000 °C at 10 °C/min under an air atmosphere (gas flow of 50 ml/min).

# **6.4.2. Fourier-Transform Infrared Spectroscopy (FTIR)**

Infrared spectra were taken using a Bruker ALPHA Platinum ATR spectrometer across a spectral range of  $400 - 4000 \text{ cm}^{-1}$  with a resolution of 2 cm<sup>-1</sup>. Each spectrum was

generated as an average of 16 scans combined for noise reduction purposes. Solid material was pressed against the diamond ATR (attenuated total reflectance) cell with the instrument anvil. Pre-sample-measurement background measurements were performed under the same conditions but with the anvil unused. Spectra were baseline corrected using the software supplied with the instrument.

#### **6.4.3 Extended X-Ray Absorption Fine Structure (EXAFS)**

EXAFS measurements were carried out at the Zr K-edge on the B18 Core XAS (X-ray absorption spectroscopy) beamline<sup>41</sup> at the Diamond Light Source X-ray synchrotron. Data were collected from samples diluted with appropriate amounts of polyethylene powder and pressed in self-supporting discs around 1 mm thick in transmission mode. Incident energies were selected using a water-cooled, fixed-exit, double-crystal monochromator with Si(311) crystals. The beam was focussed horizontally and vertically using a double toroidal mirror, coated with Pt, 25 m from the source, while a pair of smaller plane mirrors were used for harmonic rejection. The raw data were normalised using the software ATHENA to produce EXAFS spectra for modelling using the software ARTEMIS, both part of the Demeter XAS data processing package.<sup>42</sup>

#### **6.4.4 Powder X-Ray Diffraction (PXRD)**

Laboratory PXRD patterns spanning a  $2\theta$  range of  $5-60^\circ$  were collected on a Siemens D5000 diffractometer (Bragg-Brentano geometry) operating with Cu K $\alpha_{1/2}$  radiation, with a step size of  $0.05^\circ$  using a background-free silicon sample holder. Patterns were collected over the course of 1 hour and are presented as measured without any further processing.

High-resolution PXRD data were measured on the I11 beamline at the Diamond Light Source X-ray synchrotron under ambient conditions. A finely-ground sample was mounted in a spinning quartz capillary, and patterns measured across a  $2\theta$  range of  $2-92^{\circ}$  with a step size of  $0.004^{\circ}$ . The incident X-ray beam wavelength was 0.82445(2) Å. Structure solution from

these data was carried out by Dr Nathalie Guillou of the Institut Lavoisier, Versailles. Extraction of peak positions, pattern indexing, charge flipping, simulated annealing processes and Rietveld refinements were carried out with the TOPAS V5 program, 43 while the EXPO package<sup>44</sup> using EXTRA for extracting integrated intensities and SIR97 for direct-method structure solutions was used to initialise the structural model. The LSI (Least Squares Indexing) method based on the first 20 peaks converged unambiguously to a monoclinic unit cell (a = 17.0775(7) Å, b = 5.63423(10) Å, c = 16.9860(4) Å,  $\beta = 114.885(3)^{\circ}$  &  $V = 114.885(3)^{\circ}$ 1482.62(8) Å<sup>3</sup>) with a satisfactory figure of merit ( $M_{20} = 29$ ). A careful examination of the small peaks concluded that only extinctions compatible with a c glide plane were possible. Taking into account the chirality of the organic ligand, the non-centrosymmetric Pc space group was chosen to initialise the structural determination, and charge flipping and directmethods simultaneously allowed the Zr localisation. The atomic coordinates of Zr were used as a starting model in the Rietveld refinement and the direct space strategy was then used to localise the four mandelate anions, which were added and treated as rigid bodies in a simulated annealing process. The organic ligands were treated as rigid bodies and C-C distances subsequently refined. The first structure solution yielded a set of atomic coordinates from which, by comparison of the GIPAW calculated and experimental NMR chemical shifts, the structure was adjusted to reach a structural model which agreed with both PXRD and NMR. At the final stage, Rietveld refinement involved the following structural parameters: 1 atomic y coordinate for Zr, 24 parameters for the localization of the organic ligands, 4 mean C-C C-O distances, 8 torsion angles, 1 overall thermal factor and 1 scale factor for 1720 reflections. The anisotropic line broadening effect was modelled using the Stephens' model. Hydrogen atoms were placed by geometric constraint, with the H atoms of OH groups placed to counterbalance the charge but allowed to rotate freely. The final Rietveld plot corresponds to a satisfactory model indicator  $R_B = 0.017$  and profile factors  $R_p = 0.035$  and  $R_{wp} = 0.049$ . The above data analysis was aided by density measurement of the as-made material using helium pycnometry (1.17 gcm<sup>-3</sup>), which suggested the number of zirconium centres in the unit cell to be two, and by SEM imaging of the solid material which revealed individual crystallites to be of an elongated needle-like morphology.

# 6.4.5 Solid-State <sup>1</sup>H and <sup>13</sup>C Nuclear Magnetic Resonance (NMR)

Solid-state NMR magic angle spinning (MAS) experiments were performed on a Bruker Avance II+ spectrometer, operating at <sup>1</sup>H and <sup>13</sup>C Larmor frequencies of 600.0 MHz and 150.7 MHz, respectively, using a 4 mm HX probe and a 1.3 mm HXY probe for <sup>1</sup>H-<sup>13</sup>C cross polarisation (CP) and <sup>1</sup>H one-pulse experiments. A <sup>1</sup>H 90° pulse length of 2.5 μs was used. SPINAL64<sup>45</sup> <sup>1</sup>H heteronuclear decoupling was applied during the acquisition of the <sup>13</sup>C FID, with a pulse duration of 5.9 μs at a nutation frequency of 100 kHz, and a 70 to 100% ramp<sup>46</sup> on the <sup>1</sup>H channel was used for the CP contact time with nutation frequencies of 47.5 and 60 kHz for <sup>13</sup>C and <sup>1</sup>H, respectively.

Density functional theory (DFT) calculations were performed using CASTEP Academic Release version 16.1.<sup>47</sup> All calculations used the Perdew Burke Ernzerhof (PBE) exchange correlation functional, <sup>48</sup> a plane-wave basis set with ultrasoft pseudopotentials and a plane-wave cut-off energy of 700 eV. Integrals over the Brillouin zone were taken using a Monkhorst-Pack grid of minimum sample spacing  $0.08 \times 2\pi$  Å<sup>-1</sup>. Geometry optimisations were performed with unit cell parameters fixed but all atoms free to move. NMR parameters were calculated for the geometry optimised structure using the gauge-including projector-augmented wave (GIPAW) approach.<sup>49</sup> The calculated isotropic chemical shifts ( $\delta_{iso}^{calc}$ ) were determined from the calculated chemical shieldings ( $\sigma_{calc}$ ) by  $\delta_{iso}^{calc} = \sigma_{ref} - \sigma_{calc}$ , with a  $\sigma_{ref}$  value of 169.0 ppm for <sup>13</sup>C.  $\sigma_{ref}$  was determined for <sup>13</sup>C by taking the sum of the experimental chemical shift and the GIPAW calculated absolute isotropic chemical shieldings. The resulting y-intercept was taken as  $\sigma_{ref}$ . <sup>50</sup>, <sup>51</sup> The NMR experiments and simulations were carried out by Emily Corlett.

#### **6.4.6 Scanning Electron Microscopy (SEM)**

SEM imaging of zirconium mandelate was undertaken using a Zeiss SUPRA 55-VP scanning electron microscope by Ehsan Ghadim. An ultrasonically dispersed suspension of zirconium mandelate in acetone, applied to the top surface of a thin carbon pad which was stuck to an aluminium sample stub, was allowed to dry before being carbon-coated prior to imaging with an Emitech Evaporator.

#### **6.4.7 Helium Pycnometry**

Density measurement of zirconium mandelate was carried out using a Micromeritics AccuPyc 1330 pycnometer with helium gas, with the assistance of David Hammond. Sample material was oven-dried (75-80 °C) overnight to minimise moisture contamination, and left to 'soak' in helium gas inside the instrument prior to measurement. Repeat measurements were taken until pressure readings were consistent. The instrument was calibrated beforehand with a stainless steel ball bearing of known volume.

#### 6.5 Initial Results and Discussion

# 6.5.1 Testing of (Alternative) Methods of Synthesis for Zirconium Mandelate and Preliminary Results

Initial attempts at producing solid zirconium mandelate demonstrated the process to be straightforward. A simple mixing of solutions of mandelic acid and zirconium oxychloride, acidified with hydrochloric acid, in a beaker would rapidly produce a solid precipitate with minimal stirring. Heating to 80-90 °C was employed as per the original literature. Isolation of the solid was by means of vacuum filtration with washing with deionised water and acetone, followed by overnight drying at 75 °C. It was noted that the as-made product was seemingly non-soluble in water, at least sparingly, thus water could be used for washing without

significant loss of product. This is not surprising, given that the material forms so readily in aqueous conditions in the first instance.

An increasingly common method of synthesis in materials/inorganic chemistry is hydrothermal or solvothermal synthesis.<sup>52-54</sup> Here, reagents are combined with a suitable solvent and enclosed in a Teflon<sup>®</sup>-lined stainless steel pressure vessel, or autoclave. The vessel is then heated in an oven, for anywhere from minutes to many hours (even days) usually at temperatures up to 240 °C (the melting point of Teflon<sup>®</sup>), whereby the vapour pressure of the solvent generates an 'autogenous' pressure thus creating reaction conditions otherwise inaccessible under ambient conditions. Synthesis of zirconium mandelate was trialled with this method, successfully producing solid material, in the form of a powder and what appeared to be larger agglomerates.

In general no individual crystals suitably large enough for single-crystal X-ray diffraction were seen. Characterisation by thermogravimetric analysis (TGA) showed the number of ligands per zirconium atom to be close to 4, although the result varied slightly between attempts. Fourier-transform infrared spectroscopy (FTIR) revealed an obvious difference in bonding of carboxyl(ate) moieties between precursor and product; evidence for the formation of a new metal-organic material. Diffraction patterns obtained by laboratory powder X-ray diffraction also showed the material to be crystalline, although with many lowintensity peaks. It was also found that increasing the reaction temperature to 150 °C resulted in decomposition of the mandelic acid, and at a temperature of 110 °C moderate decomposition could also occur depending on the time of synthesis. The additionally formed material, a brown sticky substance (most-likely decomposition products of mandelic acid), could however be removed by acetone washing, leaving behind a white solid. Attempts at recrystallisation of zirconium mandelate to afford larger crystals for single-crystal X-ray analysis were unsuccessful. The material was found to be insoluble in dichloromethane, N,Ndimethylformamide (DMF), dimethyl sulfoxide, methanol, diethyl ether, ethanol and hexane, both at room temperature and 60 °C. Solvothermal synthesis using dimethylamine as solvent was also tested, though this method resulted in no solid material. All attempts using DMF as solvent also failed.

An attempt at recrystallising zirconium mandelate in DMF in a heated autoclave also proved to be unpromising. Reaction in the form of an autoclave 'molten ligand'-type synthesis did produce solid material. In this case, zirconium ethoxide was combined with a 30-fold molar excess of mandelic acid, such that when the autoclave was heated to 150 °C, the mandelic acid melted (having a melting point of 132-135 °C), and reaction was intended to have taken place within the melt. This method produced an off-white sticky mass, thought to be zirconium mandelate and mandelic acid in ethanol, from which a fine white solid powder could be obtained after extensive washing with water and acetone, followed by filtration and drying as previously described. This material was seen to show some differences in its powder XRD compared to optimised zirconium mandelate, but still did not contain large enough single crystals for structure determination.

Other synthesis variations such as leaving mixes of relevant solutions in a fridge at 4°C did not produce any solid material. Substitution of hydrochloric acid by nitric acid, in an autoclave synthesis, gave no solid product, but cooling of the mix resulted in the formation of crystals. However, these crystals were later identified as benzoic acid, possibly formed through reaction of mandelic acid with the nitric acid. The zirconium may also have had a catalytic effect here. Leaving the same mix of reagents in the fridge, *i.e.* without autoclave heating, resulted in a yellow solution, suggestive of some sort of solution complex between zirconium, mandelic acid and nitrate. Indeed, PZN solutions with higher levels of mandelic acid also possess a yellow colouration. This led to the idea that the mandelic acid in PZN solutions actually survives heating in the presence of the nitric acid. A PZN synthesis was carried out but with the zirconium precursor omitted (*i.e.* a solution of nitric acid and mandelic acid only); upon cooling the resulting solution no crystals of benzoic acid were seen, suggesting that the mandelic acid remains intact following synthesis (at least with respect to the solution acidity and application of heat).

The main objective to investigating so many synthesis methods was to see if the zirconium mandelate made was sufficiently crystalline, or the crystals large enough, to allow characterisation by single-crystal X-ray analysis. It was thought that if the formation of zirconium mandelate could be greatly slowed, then this might give the opportunity for larger crystals to grow. Unfortunately, a gel method, where a solution of mandelic acid was left sitting on top of a gel containing zirconium, the idea being that crystals might grow at the gelsolution boundary, was also unsuccessful. In addition, reaction in H-tubes was similarly so. In this case, saturated solutions of zirconium oxychloride and mandelic acid were added to either side of a H-shaped glass tube; the 'bridge' of the H was then filled with water, the intention being that slow diffusion of zirconium and mandelic acid would take place through this water bridge, with individual crystals potentially growing at the point of mixing. However all this method produced over a period of many weeks was a fine white solid powder, like that seen with other methods employed. One interesting observation though was that with sodium mandelate in place of mandelic acid, the amount of solid produced was visually greater.

Another idea considered was that use of a zirconium precursor with zirconium centres 'pre-hydrolysed' i.e. already connected to other zirconium atoms with hydroxy bridges, might not be the best choice for trying to make zirconium mandelate. However, it appears that mandelic acid has such a strong affinity for zirconium that it is able to displace the connecting hydroxy bridges of otherwise hydrolysed zirconium centres, resulting in successful complexation of mandelic acid to zirconium, as demonstrated in all measured FTIR spectra.

# 6.5.2 An Optimised Synthesis Method

Further approaches to synthesising zirconium mandelate were tested. Through modification of variables such as reaction temperature, choice of zirconium salt precursor and the stereochemical form of the mandelic acid, a specific method was developed that was found to give the most crystalline product (as evaluated by the appearance of powder X-ray

diffraction patterns). Although single crystals of material were not obtained, a complete structural characterisation was still possible via analysis of the powder diffraction pattern.

In the optimised method, a 4.5-fold molar excess of (*R*)-mandelic acid was used, more than enough needed to result in a full complement of mandelate ligands around each zirconium centre, making the formation of other solution species such as Zr(OH)(C<sub>6</sub>H<sub>3</sub>CH(OH)CO<sub>2</sub>H)<sub>3</sub> less likely. Reactions were carried out under strongly acidic conditions, intended to completely solubilise the zirconium and prevent formation of condensed zirconium species by hydrolysis. This was achieved by dissolution of solids in a 9:1 mix (by volume) of deionised water and 35% hydrochloric acid respectively, of a total volume of 10 cm<sup>3</sup> (limited by the size of the reaction vessel). Solid reagents were added to a Teflon®-lined autoclave followed by hydrochloric acid solution (Fig. 6.4). The mix was stirred magnetically for 20 minutes prior to heating in an oven at 90 °C for 18 hours. The autoclave was allowed to cool slowly to room temperature (1 °C min<sup>-1</sup>) before the contents were collected. The resulting solid product was isolated by vacuum filtration and thoroughly washed with deionised water and acetone before being dried at 75 °C in air overnight prior to further study.

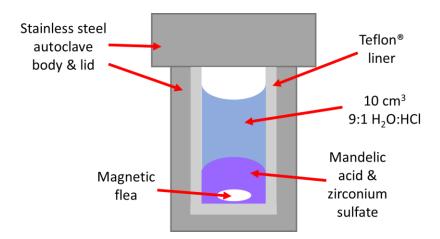


**Figure 6.4** A schematic of the autoclave reaction vessel used for the as-described synthesis of zirconium mandelate.

The most crystalline product was found to be made from zirconium sulfate tetrahydrate, in combination with (R)-mandelic acid (Fig. 6.5). It was observed that the intitial precipitation of solid, seen whilst stirring the reaction mix, was delayed when compared to the other zirconium precursors tested. This was interpreted as a kinetic effect in the solution formation of the salt; a possible reason for the increased quality of the product when using this precursor. Compared to zirconium oxychloride, the structure of which is based upon the tetramer, zirconium sulfates are typically formed of zirconium chains or dimers with linking sulfate groups. 55 The sulfate anion has a stronger affinity for zirconium than chloride or nitrate. It may be the case that use of a zirconium precursor that is initally hydrolysed to a lesser extent (i.e. is not complexed by only (bridging) hydroxy groups) in combination with acidic conditions makes complexation by mandelate more likely. It was noted that in general use of the R isomer of mandelic acid as opposed to the S isomer gave a slightly more crystalline material (Fig. 6.6). Use of a 50:50 mix of both enantiomers resulted in material whose powder diffraction patterns were noticeably different to those from syntheses involving either enantiomer as a precursor. The underlying reasons for this are unknown. In stark contrast, reaction at only room temperature with stirring resulted in a product that was of greatly inferior crystallinity compared to that made hydrothermally (Fig. 6.7); this has also been observed in the crystallisation of other metal mandelates, such as those of divalent transition-metal cations.56

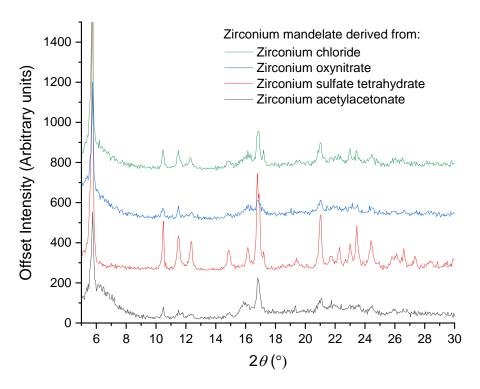


**Figure 6.5** PXRD ( $\lambda = 1.5406 \text{ Å}$ ) patterns for zirconium mandelate derived from various zirconium precursors.

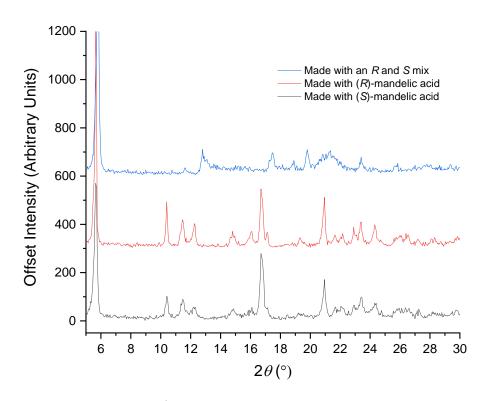


**Figure 6.2** PXRD ( $\lambda = 1.5406 \text{ Å}$ ) patterns for zirconium mandelate made via an autoclave synthesis route with either *R* or *S* mandelic acid or a mixture of both.

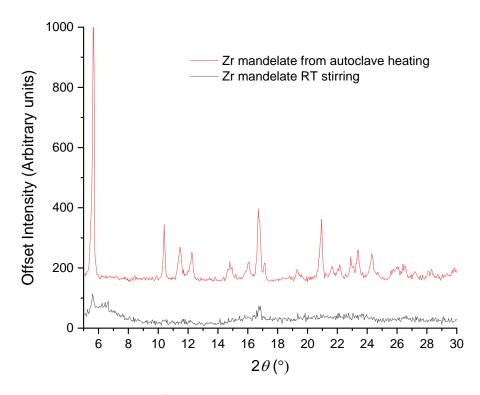


**Figure 6.3** PXRD ( $\lambda = 1.5406$  Å) patterns for zirconium mandelate made from zirconium sulfate tetrahydrate and (R)-mandelic acid, utilising the autoclave method of synthesis (top) and from mixing precursors at room temperature in a glass vial (bottom).

# 6.6 Discussion of Results from the Optimised Synthesis Method

# 6.6.1 Experimental Results and Structural Solution

Use of TGA allowed for an easy determination of the number of mandelate ligands per zirconium cation in the mandelate complex. Heating of the material up to 1000 °C results in decomposition of the complex and combustion of the organic ligand leaving ZrO<sub>2</sub> behind. By considering the changes ocurring in this reaction and the starting and final masses it is possible to calculate the amount of organic matter present in an otherwise inorganic material. The result here for zirconium mandelate made via the optimised synthesis method matches the expected mass loss for a tetra-ligated complex of 82.3%. As such it was possible to confirm the number of ligands in the complex to be 4 (Fig. 6.8).

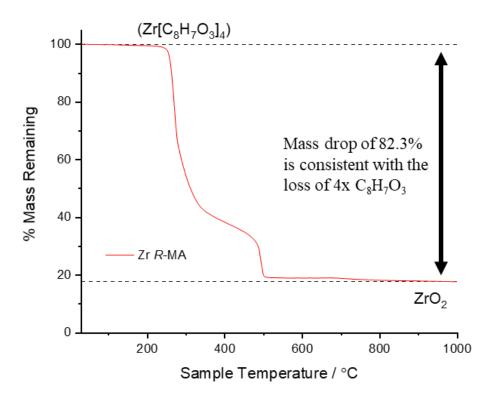


**Figure 6.8** A plot of the mass loss during heating from the thermogravimetric analysis of zirconium mandelate.

FTIR spectroscopy was employed to probe the changes in bonding between the mandelic acid precursor and the mandelate ligands in the zirconium complex, thus revealing if coordination to zirconium had taken place (Fig. 6.9). Bands relating to the alpha-hydroxy O-H stretch<sup>57</sup> at ~3438 cm<sup>-1</sup>, and to the free carbonyl C=O stretch at ~1712 cm<sup>-1</sup>, as seen in the spectrum for mandelic acid, were absent in the case of the zirconium mandelate product. A very broad band was seen in the product spectrum centred at ~3392 cm<sup>-1</sup>, which is assigned as the coordination of the alpha-hydroxy group. The presence of a pair of C=O stretches at ~1579 cm<sup>-1</sup> and ~1381 cm<sup>-1</sup>, separated by approximately 202 cm<sup>-1</sup>, was consistent with a unidentate mode of coordination of the carboxylate group<sup>58</sup> of the mandelate ligands. Such a bonding mode is also known for magnesium and barium mandelates, though in these cases the alpha-hydroxy group is not also involved in ligand-metal coordination.<sup>59</sup>

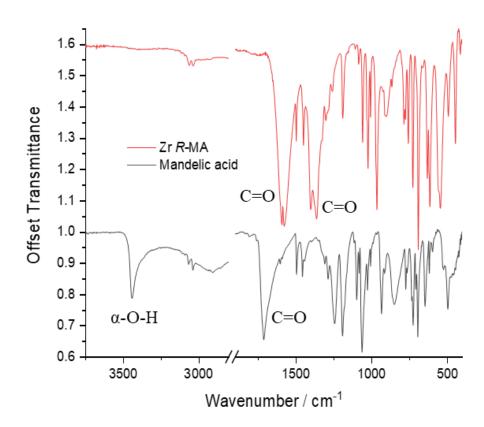


**Figure 6.9** FTIR spectra of zirconium mandelate made with (*R*)-mandelic acid (top, vertically offset) and free mandelic acid (bottom). Assignments of key bands are given. The differences between the two spectra indicate that coordination of mandelic acid to zirconium has taken place, as described in the main text. The x-axis has been truncated for presentation purposes.

EXAFS analysis of zirconium mandelate was used to probe the immediate local environment of the zirconium cations in the material. This technique detected only Zr-O correlations and no Zr-Zr correlations, as otherwise seen for the zirconium tetramer in zirconium oxychloride, i.e., each zirconium cation is surrounded by a shell of O atoms but with no other Zr atoms nearby (Fig. 6.10 and Table 6.1). In other words, the zirconium centres are individual and isolated. The  $k^2$ -weighted Zr K-edge EXAFS spectra were analysed over the k-range  $3-14 \text{ Å}^{-1}$ .

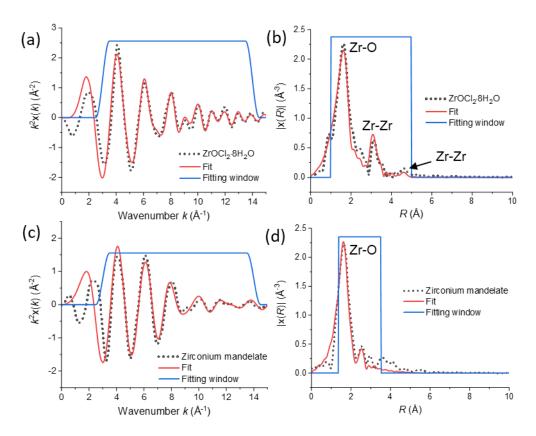


**Figure 6.40:** (a) Fit to Zr K-edge EXAFS data in *k*-space for zirconium oxychloride; (b) corresponding fit and data in *R*-space for zirconium oxychloride. (c) Fit to EXAFS data in *k*-space for zirconium mandelate; (d) corresponding fit and data in *R*-space for zirconium mandelate. The crystal structure of zirconium oxychloride is known to contain the zirconium tetramer; as such contributions are seen in the *R*-space plot for the Zr-Zr square-edge and the Zr-Zr diagonal correlations at ~ 3.2 Å & 4.6 Å (plot values), respectively. Such features are absent from the results for zirconium mandelate, suggestive of isolated zirconium centres. Atomic correlations for Zr-O and Zr-Zr are labelled. Note that the interatomic distances presented in the *R*-space plots are phase shifted from the true values by approximately 0.5 Å.

**Table 6.1:** Refined EXAFS parameters from the Zr K-edge data analysis in Figure 6.10. The atom label in the Shell column denotes a particular scattering path included in the overall fit (Zr to O/C).  $R_{\text{eff}}$  is the corresponding average interatomic distance as per the material's crystal structure; R is the refined distance adjusted during the fit. N,  $\sigma^2$ ,  $S_0^2$  &  $E_0$  represent coordination number, atomic position mean-squared disorder, amplitude reduction factor and threshold energy, respectively.

Zirconium oxychloride						Zirconium mandelate				
Shell	Reff / Å	N	$\sigma^2$ / $\mathring{\mathbf{A}}^2$	R / Å		Shell	Reff / Å	N	$\sigma^2$ / $\mathring{\mathbf{A}}^2$	R / Å
0	2.207	8	0.00985 ± 0.00149	2.177 ± 0.011		0	2.189	5	0.00305 ± 0.00107	2.135 ± 0.019
Zr	3.559	2	0.00494 ± 0.00087	3.560 ± 0.010		0	2.240	3	0.00177 ± 0.00151	2.267 ± 0.026
Zr	5.032	1	0.00796 ± 0.00707	5.010 ± 0.011		С	2.650	2	0.00380 ± 0.00964	2.726 ± 0.053
						С	3.014	2	0.00476 ± 0.00964	3.051 ± 0.076
$S_0^2 = 1.650 \pm 0.221, E_0 = -7.861 \pm 1.650 \text{ eV}$						$S_0^2 = 1.650 \pm 0.221, E_0 = -6.025 \pm 3.446 \text{ eV}$				

Imaging of the solid material revealed a needle-like morphology of individual crystallites, as can be seen in Figure 6.11.

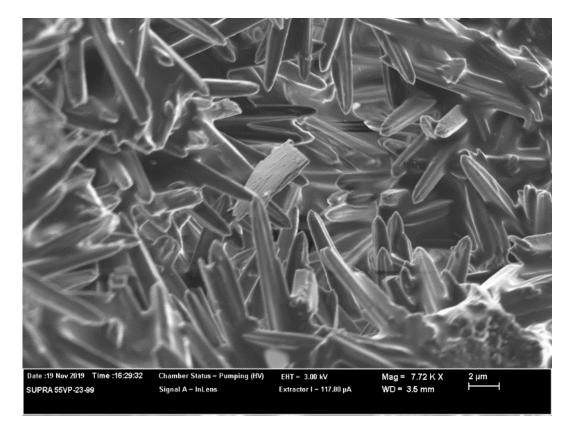


**Figure 6.51** A scanning electron microscopy image of solid zirconium mandelate, showing the rod or needle-like morphology of the individual crystals. Filled-in space between crystals (top right, for example) can be attributed to the build-up of carbon from the sample coating process.

A combination of both laboratory, and high-resolution synchrotron X-ray powder diffraction (Fig. 6.12 and Table 6.2) was used in the characteriation of zirconium mandelate. Use of the high-resolution technique specifically enabled the creation of an initial structural model, described below.

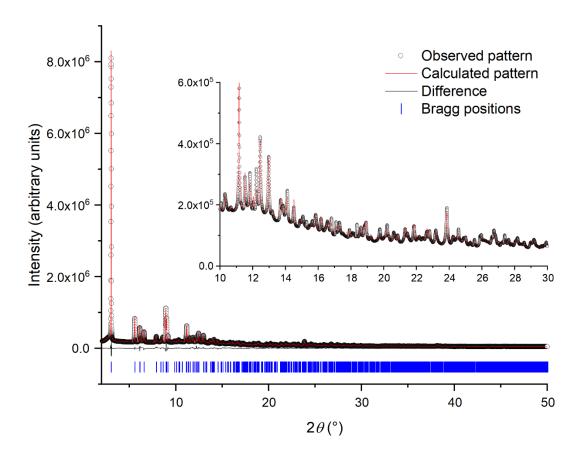


**Figure 6.62:** Final Rietveld fit to the synchrotron PXRD data. The wavelength of the synchrotron radiation was  $\lambda = 0.82445$  Å. The black open circles are the measured data, the red line the fit to the data and the black line the difference curve. The blue tick lines show the position of all allowed Bragg peaks within the angular range covered.

**Table 6.2:** Crystal structure, unit cell and experimental parameters from the processing of the PXRD data presented in Figure 6.12 for Zr(C<sub>6</sub>H<sub>5</sub>CH(OH)CO<sub>2</sub>H)<sub>4</sub>.

	$Zr(C_6H_5CH(OH)CO_2H)_4$
Crystal structure	Powder data
determined from	
CCDC	2004875
$M_{ m w}/{ m g~mol^{-1}}$	695.78
Crystal system	Monoclinic
Space group (no.)	<i>Pc</i> (7)
a/Å	17.0775(7)
$b/ m \AA$	5.63423(10)
$c/ ext{Å}$	16.9860(4)
$eta/ ext{Å}$	114.885(3)
$V/\text{Å}^3$	1482.62(8)
Z	2
$ ho_{calc}/{ m mg~m}^{-3}$	1.558
T/K	298
Radiation type	Synchrotron
λ/Å	0.82445
$2\theta$ range/°	2-50
$R_{ m p}/\%$	3.5
$R_{\rm wp}$ /%	4.9
$R_{ m B}/\%$	1.7
GoF	17

Solid-state NMR techniques were used to improve the initial structural model created following processing of high-resolution PXRD data. Successive improvements to the crystal structure were were guided by comparison of experimental spectra to those calculated from the model structure (Figs. 6.13, 6.14).<sup>60, 61</sup> Adjustments to the model were done to give the best possible match between the experimental spectra and gauge-including projector augmented wave (GIPAW)<sup>49</sup> calculated NMR spectra, and consistency with powder diffraction data.

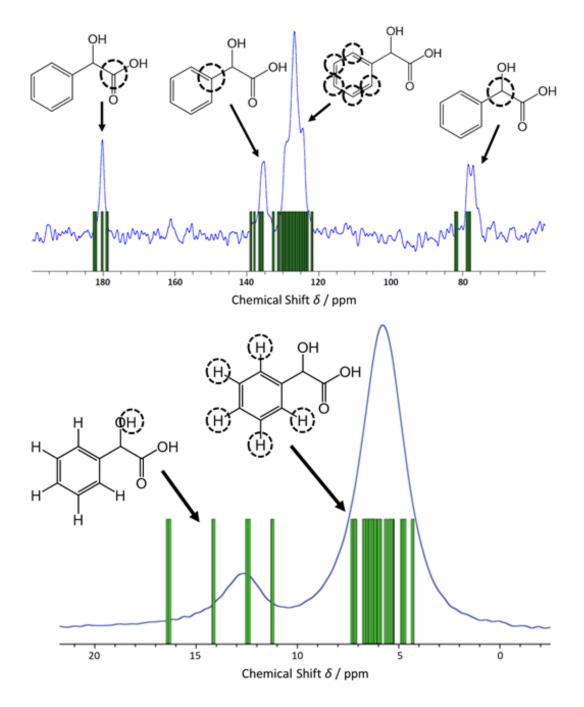


**Figure 6.73:** Solid-state NMR spectra ( $v_0(^1H) = 600 \text{ MHz}$ ) of zirconium mandelate with assignments. Top:  $^1H^{-13}C$  CP MAS ( $v_R = 12.5 \text{ kHz}$ , contact time = 1.5 ms, 16 co-added transients for a recycle delay of 60 s). Bottom:  $^1H$  one-pulse ( $v_R = 60 \text{ kHz}$ , 4 co-added transients for a recycle delay of 103 s). The experimental data (blue plots) are overlaid with GIPAW calculated chemical shifts (green bars). The noticeable discrepancies for the α-OH protons is attributed to the close proximity of these to the zirconium cation.

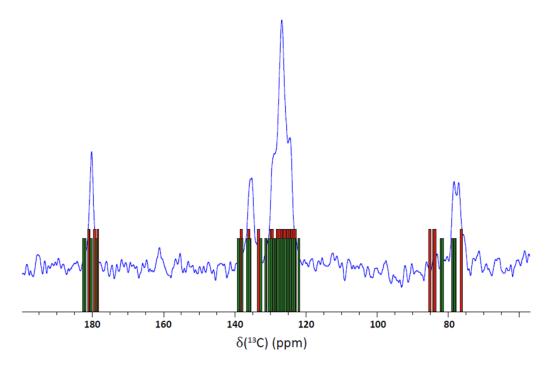


**Figure 6.84:** Solid-state  $^{1}$ H- $^{13}$ C CP MAS ( $v_{R} = 12.5$  kHz) NMR spectra ( $v_{0}(^{1}$ H) = 600 MHz) of zirconium mandelate recorded with a contact time of 1.5 ms, 16 co-added transients for a recycle delay of 60 s. The experimental data (blue plots) are overlaid with GIPAW calculated chemical shifts for the initial (red bars) and final (green bars) structural models.

GIPAW calculations were performed for each subsequent structural model and the resulting chemical shifts compared to the experimental solid-state NMR. The agreement between experiment and GIPAW calculation for organic molecules has an established discrepancy of 1% of the chemical shift range (~2 ppm for <sup>13</sup>C).<sup>62-65</sup> Initial structural solutions showed good agreement for all carbon environments except that of the hydroxyl carbon, for which the calculated <sup>13</sup>C chemical shifts for three of the mandelate models were more than 4 ppm higher (4.3 – 5.8 ppm) than the corresponding experimental resonances. It was also noted that overlap in the experimental resonances produced two peaks of equal height, suggesting that hydroxyl carbon resonances from two of the four mandelate molecules contributed to each, while the separation in GIPAW calculated chemical shifts would suggest a 3:1 ratio instead. This helped inform the generation of subsequent models, which were refined against the powder X-ray pattern until the ratio and calculated shift values from GIPAW calculation were in agreement with the experimental data.

#### **6.6.2** The Crystal Structure of Zirconium Mandelate

The structural model described here was that created from the combined use of powder X-ray diffraction and solid-state NMR as previously described. An initial model was generated from the Rietveld fit to the powder diffraction pattern and adjustments of (iterative improvements to) the positions of the atoms in the mandelate ligands was by comparison of calculated NMR shifts to those gathered experimentally – which was repeated until a good agreement was found. The number of ligands around each zirconium centre was confirmed by TGA; the EXAFS results previously described were consistent with the idea of isolated zirconium centres, which was taken into account.

Inspection of the structure of the complex shows the presence of isolated zirconium centres coordinated by two oxygen donor atoms from each of the four mandelate ligands (Fig. 6.15a). Each of the mandelate ligands is bonded via the oxygen of the alpha-hydroxy group and by one of the carboxylate oxygens. The second carboxylate oxygen is terminal. Looking closer, it can be seen that one of the two zirconium centres in the unit cell is coordinated by only (R)-mandelate, and the other by only (S)-mandelate ligands (Fig. 6.15b). Thus, racemisation of mandelic acid must take place in solution during the course of the reaction, as only (R)-mandelic acid (or (S)-) was used as a precursor, yet both stereochemical forms are present in the final product.

For this model, the four pairs of coordinating O atoms give rise to pairs of Zr-O distances of 2.173 & 2.146 Å, 2.195 & 2.236 Å, 2.182 & 2.190 Å and 2.203 & 2.238 Å, seemingly in line with the refined parameters from the EXAFS results above for zirconium mandelate. In fact, grouping and averaging these distances, in effect creating two O 'shells' like that done for the EXAFS data fitting, produces Zr-O distances of 2.225 Å and 2.177 Å. The former being the same as the corresponding EXAFS result, and the latter only ~0.05 Å different, suggestive of good agreement between the two techniques.

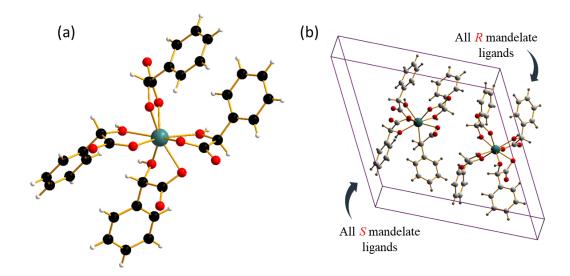


**Figure 6.15:** (a) View of the four mandelate ligands around a zirconium centre generated from crystal structure data. The zirconium cation is coloured turquoise, with oxygen, hydrogen, and carbon atoms in red, white, and black, respectively. (b) A single unit cell of zirconium mandelate containing two complexes, with the different stereochemical forms of the mandelate ligands on each of the zirconium centres indicated.

Mandelic acid is known in the literature to racemise readily in both acidic and basic solution, <sup>66</sup> and the occurance of this during synthesis of mandelate-containing materials to generate both stereochemical forms in the final product has been seen previously in mandelates of manganese, iron, cobalt, nickel and copper. <sup>56</sup> In these compounds, which have layered structures, each metal(II) cation is surrounded by six oxygen atoms, four of which arise from two mandelates that both coordinate via the alpha-OH oxygen and a carboxylate oxygen. The remaining two oxygen atoms arise from the coordination of a further two mandelate ligands (each via a carboxylate oxygen), both of which bridge to other metal centres (Fig. 6.16a). A number of other metal mandelates are known, including zinc and beryllium mandelate, <sup>67</sup> neodymium mandelate, <sup>68</sup> gadolinium, terbium, dysprosium and erbium mandelate, <sup>69</sup> europium mandelate<sup>70</sup> and rhodium mandelates. <sup>71</sup> Coordination through both the carboxylate and alpha-hydroxy groups is common amongst these, and the mandelate may also bridge two metal centres (e.g. Fig. 6.16b). A few structures are known for materials featuring

a combination of mandelate and other ligands, and these contain similar bonding motifs for mandelate, for example in complexes of Cu<sup>2+</sup> (Figs. 6.16c, 6.16d).<sup>72, 73</sup>

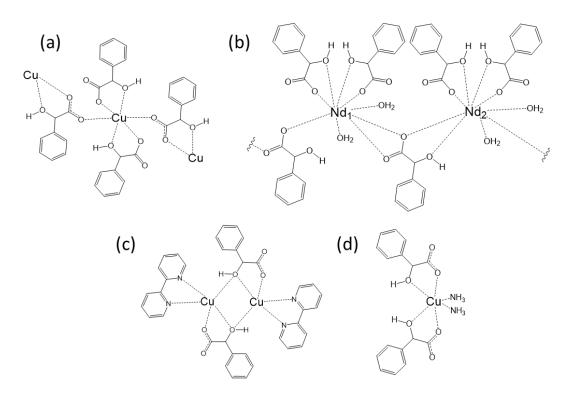


**Figure 6.96:** Depictions of examples of the coordination of mandelate in the solid state, from materials with known crystal structures. (a) The arrangement of mandelate ligands around Cu(II) as described by Beghidja *et al.*<sup>56</sup> (b) A schematic of the repeat unit of the layered structure of neodymium mandelate.<sup>68</sup> (c) The dinuclear Cu complex [Cu(bpy)(mandelate)]<sub>2</sub>·8H<sub>2</sub>O.<sup>73</sup> (d) The mononuclear Cu mandelate complex Cu(mandelate)<sub>2</sub>(NH<sub>3</sub>)<sub>2</sub>.<sup>72</sup>

# **6.7 Summary and Conclusions**

It has been demonstrated that with a strongly chelating ligand, specific choice of zirconium precursor and tuning of reaction conditions it is possible to overcome the issue of hydrolysis of zirconium in aqueous solution, which would otherwise ocurr so readily. As such, the possibility of the formation of zirconium oxy-clusters in the solution and consequently, solid, states is eliminated. It is this tendency to hydrolyse – leading to polymerisation, gelation or precipitation – that has left Zr(IV) complexes of organic ligands in aqueous media to be little studied.<sup>74</sup> An improved method of synthesis of zirconium mandelate has been developed. Through the combination of a number of characterisation methods including advanced techniques not readily available in a typical laboratory, the structure of the complex has been revealed for the first time. <sup>4</sup> The fact that the material features isolated zirconium centres makes it particularly noteworthy. The presence in the complex of both stereochemical forms of the ligand in question, despite limiting the reagents used to one of the two forms, further confirms long-held ideas about its racemisation in solution. Surveys of the available literature have revealed that complexes containing such isolated zirconium centres (specifically made from aqueous solution) are not often reported. Even with the use of excess acid, avoiding the formation of zirconium clusters is not always guaranteed.<sup>75</sup> Select examples include monomeric zirconium carbonate complexes detected via EXAFS in solution at specific concentrations.<sup>76, 77</sup> Occasionally, crystal structures are reported, such as those from the synthesis of potassium salts of zirconium malonate and of zirconium 2,6-dicarboxypicolinate (the latter also containing a nitrogen donor), which results in monomeric zirconium complexes separated by the additional cation.<sup>78</sup> Formation of mononuclear zirconium complexes as salts is relatively common; the zirconium complex of nitrilotriacetic acid is another known to exist as a potassium salt. <sup>79</sup> Also known is the structure of zirconium cupferrate, Zr(C<sub>6</sub>H<sub>5</sub>N<sub>2</sub>O<sub>2</sub>)<sub>4</sub>. <sup>80</sup> Here, each of the ligands bind to zirconium through oxygen forming a bidentate chelate in accordance with the structure and bonding of zirconium mandelate (Figs. 6.17a, 6.18b). The bonding in zirconium acetylacetonate, Zr(C<sub>5</sub>H<sub>7</sub>O<sub>2</sub>)<sub>4</sub>, is likewise (Fig. 6.17c).<sup>81</sup> The structure

of the tetrakisoxalatozirconate ion as found in the sodium salt Na<sub>4</sub>Zr(C<sub>2</sub>O<sub>4</sub>)<sub>4</sub>·3H<sub>2</sub>O is also known, <sup>82</sup> and also features ligand coordination in the same manner (Fig. 6.17d). The last examples of monomeric zirconium complexes that could be found involve oxydiacetate, ODA<sup>2-</sup>, which can act as a multidentate ligand with *three* oxygen donor atoms; from two carboxylate groups and an ether backbone. <sup>74, 83, 84</sup> One of these studies found that the number of ODA ligands that bind to zirconium depends on the pH – an idea already considered for zirconium mandelate <sup>27, 28</sup> – and proposed an equilibrium between zirconium tetramers and [Zr(H<sub>2</sub>O)<sub>8</sub>]<sup>4+</sup> species in solution, which provide the starting point for the formation of the metal-organic complex. <sup>74</sup> Otherwise, materials featuring isolated zirconium centres appear to be made only from non-aqueous solution. <sup>85-87</sup>

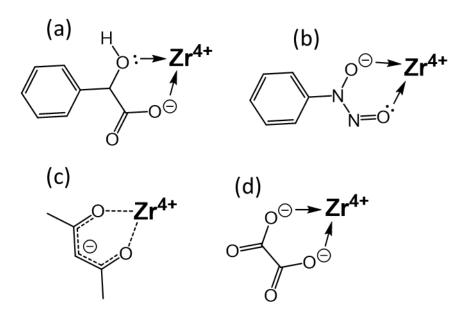


**Figure 6.17:** Depictions of individual ligand coordination to zirconium for the aforementioned complexes. (a) That for the main complex of interest, zirconium mandelate. (b), (c) and (d): the same for zirconium cupferrate, zirconium acetylacetonate and the tetrakisoxalatozirconate ion, respectively. All of the complexes in question have a total of four of the ligands drawn here.

This work has also provided an insight into the possible behaviour of mandelic acid when used in PZN solutions. It has been shown that the interaction of mandelic acid and zirconium in acidic conditions to form complexes happens readily enough that it would not be

unreasonable to assume that similar species may also arise in PZN solutions. These solutions are known from this project to be based upon the zirconium tetramer, and given the various bonding modes possible for mandelic acid, as seen in mandelate complexes of other metals (e.g. Fig. 6.16), it would also not be difficult to envisage that mandelate species might also bind to zirconium (tetramers) in a bridging fashion in LMT PZN solutions. It is known that benzilic acid, which features an additional phenyl group compared to mandelic acid, can do this. 88 There is also evidence to suggest that non-bridging chelation of carboxylates, 89 including mandelic acid, 90 to a single metal centre of a zirconium tetramer is possible. This could have the effect of 'capping' reactive zirconium centres of species in solution, both smaller minimally hydrolysed zirconium atoms and larger species that are the size of the zirconium tetramer and larger. The presence of mandelate ligands on solution zirconium species might also effect both the progress of hydrolysis in solution by steric bulk and by neutralising positive charges, and do similarly during coalescence of zirconium species during precipitation by base. This in particular may warrant further investigation. Overall, these results suggest there is still more to learn about the aqueous chemistry of zirconium and that with ligand design, yet more novel coordination complexes and networks may be possible.

# 6.8 Bibliography

- 1. D. A. Scapens, US Pat., Structured zirconium solutions, No. 10 501 332, 2019.
- D. A. Scapens, personal communication, LMT internal technical document on new manufacturing process.
- 3. C. A. Kumins, *Anal. Chem.*, 1947, **19**, 376-377.
- J. M. Crosland, E. K. Corlett, D. Scapens, N. Guillou, S. P. Brown and R. I. Walton, *Chem. Commun.*, 2020, 56, 10159-10162.
- 5. F. L. Winkler, *Repert. d. Pharm.*, 1831, **38**, 169-196.
- M. Motamedifar, A. Bazargani, M. R. Namazi and H. S. E. Sarai, World Appl. Sci.
   J., 2014, 31, 925-929.
- 7. N. E. Sakka and I. M. Gould, *Expert Rev. Clin. Pharmacol.*, 2016, **9**, 1047-1056.
- 8. R. M. Debowska, A. Kaszuba, I. Michalak, A. Dzwigalowska, C. Ciescinska, E. Jakimiuk, J. Zielinska and A. Kaszuba, *Przegl. Dermatol.*, 2015, **102**, 316-321.
- 9. D. E. Green, *Anal. Chem.*, 1948, **20**, 370-372.
- J. F. Flagg, H. A. Liebhafsky and E. H. Winslow, *J. Am. Chem. Soc.*, 1949, 71, 3630-3632.
- 11. W. W. Wendlandt, Anal. Chim. Acta, 1957, 16, 129-134.
- 12. W. M. Thornton and E. M. Hayden, Z. Anorg. Allg. Chem., 1914, **89**, 377-382.
- W. F. Hillebrand and C. E. F. Lundell, *Applied Inorganic Analysis*, John Wiley, New York, 1948.
- 14. J. J. Klingenberg and R. E. Oesper, *Anal. Chem.*, 1949, **21**, 1509-1511.
- 15. J. J. Klingenberg and R. A. Papucci, *Anal. Chem.*, 1952, **24**, 1861-1862.
- 16. R. B. Hahn, Anal. Chem., 1951, 23, 1259-1261.
- 17. M. R. Verma and S. D. Paul, *Nature*, 1954, **173**, 1237.
- 18. R. Belcher, A. Sykes and J. C. Tatlow, *Anal. Chim. Acta*, 1954, **10**, 34-47.
- R. S. Barbieri, V. R. Terra, A. M. Netto and J. C. Rocha, *Quim. Nova*, 1995, 18, 40-43.

- 20. A. A. Astanina and E. A. Ostroumov, *Zhur. Anal. Khim.*, 1951, **6**, 27-33.
- 21. A. A. Astanina and E. A. Ostroumov, *Chem. Abs.*, 1951, **45**, 6121.
- 22. E. C. Mills and S. E. Hermon, *Analyst*, 1953, **78**, 256.
- 23. G. Gavioli and E. Traldi, *Metall. Ital.*, 1950, **42**, 179-181.
- 24. R. B. Hahn, Anal. Chem., 1949, 21, 1579-1580.
- F. Feigl, Chemistry of Specific, Sensitive, and Selective Reactions, Academic Press Inc., New York, 1949.
- 26. R. B. Hahn and L. Weber, *J. Am. Chem. Soc.*, 1955, **77**, 4777-4779.
- 27. R. B. Hahn and E. S. Baginski, *Anal. Chim. Acta*, 1956, **14**, 45-47.
- 28. R. N. Kapoor and R. C. Mehrotra, *J. Am. Chem. Soc.*, 1958, **80**, 3569-3573.
- 29. E. M. Larsen and E. H. Homeier, *Inorg. Chem.*, 1972, **11**, 2687-2692.
- 30. A. S. Solovkin and S. V. Tsvetkova, *Russ. Chem. Rev.*, 1962, **31**, 655-669.
- 31. A. Clearfield and P. A. Vaughan, *Acta Cryst.*, 1956, **9**, 555-558.
- 32. G. M. Muha and P. A. Vaughan, J. Chem. Phys., 1960, 33, 194-199.
- J. H. Cavka, S. Jakobsen, U. Olsbye, N. Guillou, C. Lamberti, S. Bordiga and K. P. Lillerud, *J. Am. Chem. Soc.*, 2008, **130**, 13850-13851.
- C. Hennig, S. Weiss, W. Kraus, J. Kretzschmar and A. C. Sheinhost, *Inorg. Chem.*,
   2017, 56, 2473-2480.
- 35. C. Artner, M. Czakler and U. Schubert, *Inorg. Chim. Acta*, 2015, **432**, 208-212.
- 36. J. Singer and D. T. Cromer, *Acta Cryst.*, 1959, **12**, 719-723.
- 37. D. B. McWhan and G. Lundgren, *Inorg. Chem.*, 1966, **5**, 284-289.
- 38. P. Benard, M. Louer and D. Louer, *J. Solid State Chem.*, 1991, **94**, 27-35.
- V. Guillerm, F. Ragon, M. Dan-Hardi, T. Devic, M. Vishnuvarthan, B. Campo, A.
   Vimont, G. Clet, Q. Yang, G. Maurin, G. Ferey, A. Vittadini, S. Gross and C. Serre,
   Angew. Chem. Int. Ed., 2012, 51, 9267-9271.
- 40. Y. Bai, Y. Dou, L.-H. Xie, W. Rutledge, J.-R. Li and H.-C. Zhou, *Chem. Soc. Rev.*, 2016, **45**, 2327-2367.

- A. J. Dent, G. Cibin, S. Ramos, A. D. Smith, S. M. Scott, L. Varandas, M. R.
   Pearson, N. A. Krumpa, C. P. Jones and P. E. Robbins, *J. Phys.: Conf. Ser.*, 2009,
   190, 12039-12042.
- 42. B. Ravel and M. Newville, *J. Synchrotron Radiat.*, 2005, **12**, 537-541.
- 43. A. A. Coelho, J. Evans, I. Evans, A. Kern and S. Parsons, *Powder Diffr.*, 2011, **26**, 22-25.
- 44. A. Altomare, C. Cuocci, C. Giacovazzo, A. Moliterni, R. Rizzi, N. Corriero and A. Falcicchio, *J. Appl. Cryst.*, 2013, **46**, 1231-1235.
- 45. B. M. Fung, A. K. Khitrin and K. Ermolaev, *J. Magn. Reson.*, 2000, **142**, 97-101.
- 46. G. Metz, X. L. Wu and S. O. Smith, *J. Magn. Reson. Ser. A*, 1994, **110**, 219-227.
- S. J. Clark, M. D. Segall, C. J. Pickard, P. J. Hasnip, M. J. Probert, K. Refson and M. C. Payne, Z. Kristallogr., 2005, 220, 567-570.
- 48. J. P. Perdew, K. Burke and M. Ernzerhof, *Phys. Rev. Lett.*, 1996, **77**, 3865-3868.
- 49. C. J. Pickard and F. Mauri, *Phys. Rev. B*, 2001, **63**, 245101.
- 50. G. N. M. Reddy, D. S. Cook, D. Iuga, R. I. Walton, A. Marsh and S. P. Brown, *Solid State Nucl. Magn. Reson.*, 2015, **65**, 41-48.
- 51. R. K. Harris, P. Hodgkinson, C. J. Pickard, J. R. Yates and V.Zorin, *Magn. Reson. Chem.*, 2007, **45**, S174-S186.
- 52. A. Rabenau, Angew. Chem., 1985, **24**, 1026-1040.
- 53. D. R. Modeshia and R. I. Walton, *Chem. Soc. Rev.*, 2010, **39**, 4303-4325.
- 54. M. Shandilya, R. Rai and J. Singh, *Adv. Appl. Ceram.*, 2016, **115**, 354-376.
- 55. I. J. Bear and W. G. Mumme, *Acta Cryst.*, 1970, **26**, 1125-1131.
- A. Beghidja, S. Hallynck, R. Welter and P. Rabu, Eur. J. Inorg. Chem., 2005, 2005, 662-669.
- 57. H. M. Badawi and W. Forner, *Spectrochim. Acta A*, 2011, **78**, 1162-1167.
- 58. N. Nakamoto, *Infrared and Raman Spectra of Inorganic and Coordination Compounds*, John Wiley & Sons, New York, 4th edn., 1986.

- R. C. Silva, F. J. Caires, D. J. C. Gomes, T. A. D. Colman and M. Ionashiro, *J. Therm. Anal. Calorim.*, 2014, 117, 217-221.
- 60. P. Hodgkinson, *Prog. Nucl. Magn. Reson. Spectrosc.*, 2020, **118-119**, 10-53.
- 61. S. E. Ashbrook and D. McKay, *Chem. Commun.*, 2016, **52**, 7186-7204.
- D. V. Dudenko, P. A. Williams, C. E. Hughes, O. N. Antzutkin, S. P. Velaga, S. P.
   Brown and K. D. M. Harris, *J. Phys. Chem. C*, 2013, 117, 12258-12265.
- R. K. Harris, P. Y. Ghi, H. Puschmann, D. C. Apperley, U. J. Griesser, R. B.
   Hammond, C. Y. Ma, K. J. Roberts, G. J. Pearce, J. R. Yates and C. J. Pickard, Org.
   Proc. Res. Dev., 2005, 9, 902-910.
- J. R. Yates, S. E. Dobbins, C. J. Pickard, F. Mauri, P. Y. Ghi and R. K. Harris, *Phys. Chem. Chem. Phys.*, 2005, 7, 1402-1407.
- 65. A. L. Webber, L. Emsley, R. M. Claramunt and S. P. Brown, *J. Phys. Chem. A*, 2010, **114**, 10435-10442.
- 66. A. N. Campbell and A. J. R. Campbell, *J. Am. Chem. Soc.*, 1932, **54**, 4581-4585.
- 67. P. V. Khadikar, R. L. Ameria, M. G. Kekre and S. D. Chauhan, *J. Inorg. Nucl. Chem.*, 1973, **35**, 4301-4304.
- 68. M. Babij, P. Starynowicz and A. Mondry, *J. Mol. Struct.*, 2011, **1006**, 672-677.
- 69. M. Babij and A. Mondry, Opt. Mater, 2012, 34, 2061-2065.
- 70. M. Babij and A. Mondry, *J. Rare Earth*, 2011, **29**, 1188-1191.
- 71. F. Pruchnik, B. R. James and P. Kvintovics, *Can. J. CHem.*, 1986, **64**, 936-939.
- 72. H.-Q. Hao, W.-T. Liu, W. Tan, Z.-J. Lin and M.-L. Tong, *CrystEngComm*, 2009, **11**, 967-971.
- 73. S. Balboa, R. Carballo, A. Castineiras, J. M. Gonzalez-Perez and J. Niclos-Gutierrez, *Polyhedron*, 2008, **27**, 2921-2930.
- 74. W. Ma, H. v. Koningsveld, J. A. Peters and T. Maschmeyer, *Chem. Eur. J.*, 2001, **7**, 657-663.
- L. Pan, R. Heddy, J. Li, C. Zheng, X.-Y. Huang and X. Tang, *Inorg. Chem.*, 2008,
   47, 5537-5539.

- 76. F. Takasaki, K. Fujiwara, Y. Nakajima, T. Nishikawa, H. Masu, M. Imanari, Y. Hidaka and N. Ogawa, *Dalton Trans.*, 2015, **44**, 645-652.
- 77. F. Takasaki, K. Fujiwara, T. Kikuchi, T. Tanno, Y. Nakajima, Y. Toyoda and N. Ogawa, *Anal. Sci.*, 2017, **33**, 1007-1012.
- 78. G. R. Willey, T. J. Woodman, M. Fisher and M. G. B. Drew, *Transition Met. Chem.*, 1998, **23**, 467-471.
- J. L. Hoard, E. W. Silverton and J. V. Silverton, *J. Am. Chem. Soc.*, 1968, 90, 2300-2308.
- 80. W. Mark, Acta Chem. Scand., 1970, 24, 1398-1414.
- 81. J. V. Silverton and J. L. Hoard, *Inorg. Chem.*, 1963, **2**, 243-249.
- 82. G. L. Glen, J. V. Silverton and J. L. Hoard, *Inorg. Chem.*, 1963, **2**, 250-255.
- 83. R. Baggio, M. T. Garland, M. Perec and D. Vega, *Inorg. Chem.*, 1995, **34**, 1961-1963.
- 84. U. Thewalt and T. Guthner, *J. Organomet. Chem.*, 1989, **379**, 59-65.
- 85. R. C. Fay, Coord. Chem. Rev., 1986, 71, 113-138.
- 86. R. C. Fay, Coord. Chem. Rev., 1987, **80**, 131-156.
- 87. F. Guerard, Y.-S. Lee, R. Tripier, L. P. Szajek, J. R. Deschamps and M. W. Brechbiel, *Chem. Commun.*, 2013, **49**, 1002-1004.
- 88. M. H. Al-Hazmi, Y. Choi and A. W. Apblett, Sci. Adv. Mater., 2014, 6, 1438-1444.
- 89. J.-L. Tosan, B. Durand, M. Roubin, F. Chassagneux and F. Bertin, *J. Non-Cryst. Solids*, 1994, **168**, 23-32.
- 90. M. H. Al-Hazmi, Y. Choi and A. W. Apblett, *Adv. Phys. Chem.*, 2014, **2014**, 1-8.

# Chapter 7:

# **Conclusions and Further Work**

#### 7.1 Conclusions

Although there is a wealth of literature available regarding the aqueous solution chemistry of zirconium, it is predominantly focussed towards zirconium solutions containing chloride, perchlorate, or sulfate. There is relatively little on the other hand explicitly covering nitrate-based solutions of zirconium, especially of reports describing the use of modern characterisation techniques such as small-angle X-ray scattering, extended X-ray absorption fine structure, X-ray pair distribution function, and Raman and FTIR spectroscopies, as seen. It was expected that there is much more to learn about this specific type of acidic zirconium solution, which was the aim of the work described in this thesis.

The use of FTIR spectroscopy has been tested as a potential analysis method for investigating nitrate-based aqueous solutions of zirconium. Although spectra do show features that change with the composition of the solutions (the ratio of nitrate to zirconium, and mandelic acid level relative to zirconium), it is likely that this technique will only be of limited use to industry and the characterisation of these types of solutions in general; for a quick check to tell two solutions apart from one another for example. It was not seen that this technique could provide an insight into or a measure of the extent of zirconium hydrolysis in solution; nor did spectra show the presence of mandelic acid.

Raman spectroscopy, however, has been found to be much more informative. Raman spectra of nitrate-based aqueous solutions of zirconium display bands that are easily distinguished and assigned; the changes of which reflecting the changes taking place in solution arising due to increased hydrolysis of zirconium during or as a result of the heat treatment during synthesis. Spectra also vary accordingly with solution composition, and differences are seen between solutions based upon chloride and nitrate, in terms of the bands indicative of Zr-OH groups, as well as the presence or not of the respective anions. The most characteristic bands allow terminal and bridging OH groups to be distinguished and these

provide a fingerprint of growth of clusters in solution. Raman spectroscopy shows whether mandelic acid has been added solutions, unlike with infrared spectroscopy. Coordination of mandelate to zirconium in PZN solutions was not ruled out; on balance it is thought likely to take place given the strong affinity of mandelic acid towards zirconium. The growth and development of zirconium species in aqueous solution have been followed during synthesis in more detail than seen previously in the literature, and across a wider range of temperatures, showing the transformation from initial tetramer-like species to more hydrolysed, polymerised species, despite the complexity of fitting the multiple Zr-OH bands between 650 – 350 cm<sup>-1</sup>. Understanding of the behaviour of the nitrate anion in these solutions has also been furthered, and it is seen to increasingly coordinate to zirconium at higher temperatures. This technique in particular has been suggested as suitable for use in industry, to follow the changes in these types of solutions during synthesis, potentially giving real-time *in situ* information regarding the extent of zirconium hydrolysis.

Small-angle X-ray scattering has been used to determine the sizes of the zirconium particles in nitrate-based aqueous solutions of zirconium and has provided a complementary view of how solution particles change in response to solution composition, time, and temperature of heat treatment of solutions. *In situ* heating of aqueous zirconium solutions with SAXS measurements was not found to have been reported in the literature; this is the ideal form of measurement as the changes taking place in solution due to heating, and the measurements of, happen simultaneously. Otherwise, measurements are taken of samples *taken from* a heated solution for example, which may undergo further changes before measurement as the solutions quench to room temperature for instance. Results seen here suggest that for these solutions, modification of particle sizes of solution species is primarily due to the amount of nitrate or nitric acid used to make the solutions, with the presence of mandelic acid in solution having a much smaller effect; although the amount of mandelic acid used here, and in industry, is relatively low compared to the amount of zirconium in the solutions. Evidence has also been seen to suggest that in terms of the sizes of particles in these solutions, the solutions are stable with respect to aging over times of up to 45 days, which is

useful for industry as this will help to inform how long these solutions could be kept in storage without a change in solution properties. It has been seen that the largest particle sizes are achieved at the highest heat treatment temperatures, but that growth of particles is not necessarily continuous throughout the heat treatment process, and given enough time, will reach an upper limit. Thus, it could be possible to control particle sizes for a given solution composition just by choice of heat treatment temperature.

EXAFS measurements of nitrate-based aqueous solutions of zirconium have provided data which was found to be consistent with the idea that the solution species have structures like that of the zirconium tetramer, regardless of the exact solution composition or temperature of heat treatment. For solutions that have been subjected to high temperature heat treatment, there is likely to be connectivity of individual zirconium tetramers to build up larger structures, but EXAFS does not provide information about the longer interatomic correlations need to prove this.

X-ray PDF measurement of nitrate-based aqueous solutions of zirconium has also been reported, and preliminary results also suggest the presence of solution species with a structure based upon that of the zirconium tetramer. Zr-Zr correlations over longer distances seen in the data suggest that these species may grow to increasing lengths by the combination of multiple individual tetramers, forming buckled, ladder-like chains as opposed to sheets; as seen previously for chloride-base aqueous solutions of zirconium. Such data on nitrate-based solutions of zirconium specifically is as of yet unreported in the literature.

In addition to the work studying solutions of zirconium, an investigation into the intended solid reference material zirconium mandelate was successful. Despite being known of in the literature since the start of the last century, and used since then in gravimetric analyses of zirconium, characterisation of this material was limited. Knowledge regarding this metal mandelate has been furthered (a number of other metal mandelates are known of in the literature, and their structures reported); an optimised synthesis has been developed, its composition has been confirmed by TGA and its crystal structure reported for the first time, derived from a combination of powder X-ray diffraction and solid-state NMR. Despite the

strong affinity of mandelic acid for zirconium, it has not been seen clearly here what the overall effect of mandelic acid is in these aqueous zirconium solutions, particularly for the lower levels tested in this work. Changes in these solutions (increase of particle sizes and greater extent of hydrolysis for example) were predominantly due to heating to higher temperatures and changing the amount of nitrate relative to zirconium. Although this does not rule out this species still having an effect on final product properties of solids produced from these solutions, as mandelic acid may still have a role in the intermediary synthesis steps – precipitation and/or calcination, which have not been investigated here due to focus remaining on the zirconium solutions themselves.

Noteworthy outcomes of this project from the characterisation techniques just discussed are summarised in the schematic in Figure 7.1 below.

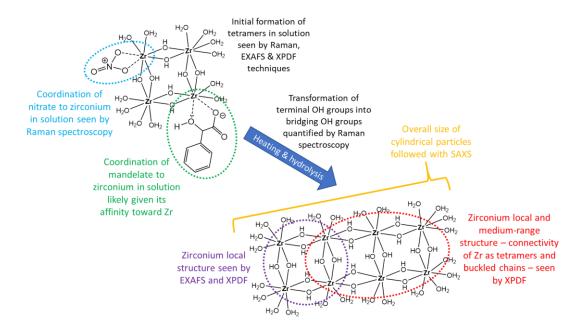


Figure 7.1 A cartoon schematic highlighting key outcomes of this project.

In addition to the techniques and results described above, a number of other characterisation methods were tested to see if they could provide any further useful information. Although these have not been reported in the thesis, it is worth describing them briefly here. Ultraviolet-visible spectroscopy was found to be unsuitable for these solutions as used in industry as the high concentration required extensive dilution of solutions to get the

absorption in range of conventional laboratory equipment. The solutions were also too highly acidic to be used with electrospray-ionisation mass spectrometry equipment, specifically the needles used to produce the fine droplets of solution required, and measurements of <sup>1</sup>H nuclear magnetic resonance (NMR) spectra, intended as a possible probe of the bridging and terminal hydroxy groups of solution zirconium species, provided poor quality data. Seeing the presence of the small amounts of mandelic acid present in these solutions via <sup>13</sup>C NMR was not always easy. Results from dynamic light scattering experiments were inconsistent, giving size distributions that varied noticeably between subsequent measurements of the same samples. It was thought at the time that the presence of a small number of very large zirconium species in solution had the effect of distorting the results.

#### 7.2 Further Work

The study of nitrate-based aqueous solutions of zirconium, and those including complexing agents such as mandelic acid, is still far from complete. Ultimately, further work is still needed regarding a full understanding of the effects of changing the properties of these solutions on the properties of solids, *e.g.* zirconia, made from these solutions. However, carrying out such work should be easier given the insights generated by this project, such as how suitable Raman spectroscopy is for following the development of solution species, especially as such measurements could be carried out *in situ* on industry (pilot) plants with fibre optic probes. Further study of gels made from zirconium solutions, and the formation of, would be useful as these could be considered as intermediates in the transformation from solutions to solids. They were investigated here based on the idea that the zirconium species in solution may be retained, following the process of drying from solution to gel. Indeed, simply characterising a greater range of solution compositions and those treated at higher or intermediate temperatures would be useful.

Characterisation *via* X-ray PDF has shown great promise here with the ease with which the structures of solution zirconium species can be identified. With a more in-depth

analysis of PDF data collected from a larger range of nitrate-based solutions, the effects of nitrate anions and mandelate could be seen more definitively. Total scattering measurements with *in situ* heating would be a suitable probe into the growth of solution zirconium species from the individual tetramers initially seen in solution into the tetramer chains that have been seen to arise due to heating.

## **Appendices**

# A.1 Quantities of Reagents used to make Aqueous Nitrate-Based Zirconium Solutions

**Table A.1.1** The quantities of reagents used to make the aqueous nitrate-based zirconium solutions described in this thesis. 'MA' = mandelic acid, 'DIW' = deionised water, 'ZBC' = zirconium basic carbonate.

Molar eq.	mol%	Mass of 30%	Mass of	Mass of	Mass of	Mass of DIW
$NO_3$	MA	HNO <sub>3</sub> (g)	DIW (g)	ZBC (g)	MA (g)	balance (g)
1	0	85.22697	42.61348	123.7624	0	114.4692
1.25	0	106.5337	53.26685	123.7624	0	82.50907
1.5	0	127.8404	63.92022	123.7624	0	50.54896
2	0	170.4539	31.85567	123.7624	0	40
1	0.5	85.22697	42.61348	123.7624	0.308696	114.1605
1.1:1	0.5	93.74966	46.87483	123.7624	0.308696	101.3765
1	1.5	85.22697	42.61348	123.7624	0.926087	113.5431
1.25	1.5	106.5337	53.26685	123.7624	0.926087	81.58298
1.5	1.5	127.8404	63.92022	123.7624	0.926087	49.62287
2	1.5	170.4539	30.92957	123.7624	0.926087	40
1	5	85.22697	42.61348	123.7624	3.086958	111.3822
1.5	5	127.8404	63.92022	123.7624	3.086958	47.462
2	5	170.4539	28.76877	123.7624	3.086958	40
1.5	10	127.8404	63.92022	123.7624	6.173917	44.37054
2	10	170.4539	25.68177	123.7624	6.173917	40

#### A.2 Fitting to Raman Spectra in Section 3.5.4.2

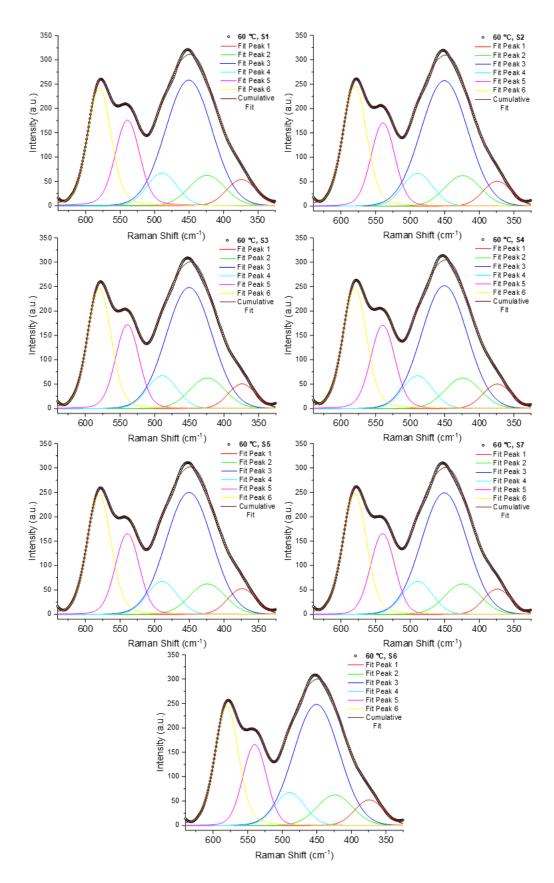


**Figure A.1** Zr-OH band fits from samples from a PZN synthesis reaching 60 °C.

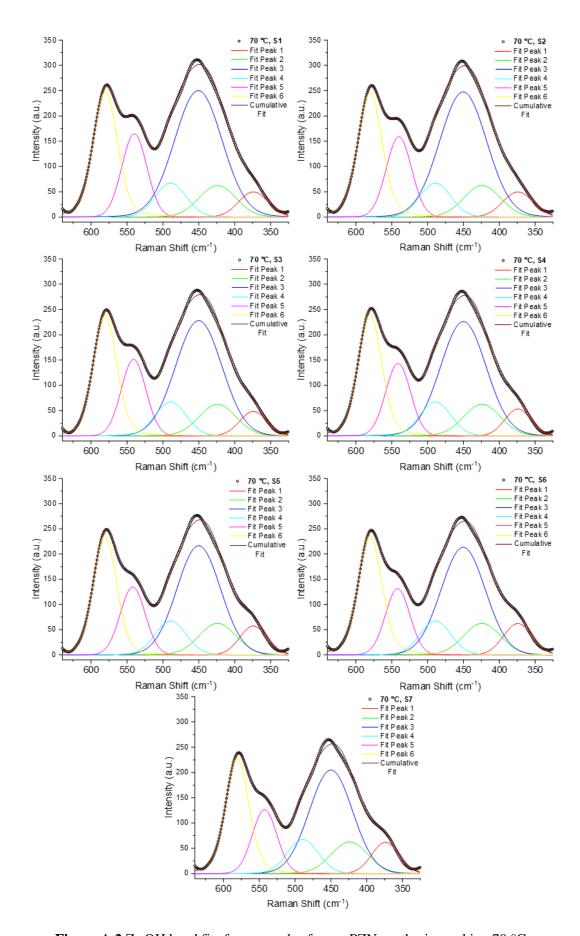
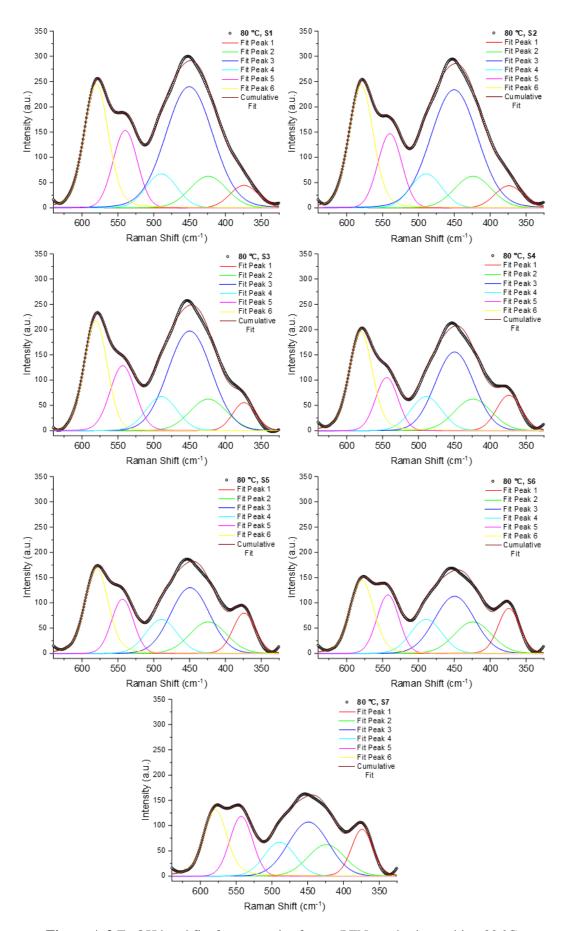


Figure A.2 Zr-OH band fits from samples from a PZN synthesis reaching 70 °C.



**Figure A.3** Zr-OH band fits from samples from a PZN synthesis reaching 80 °C.

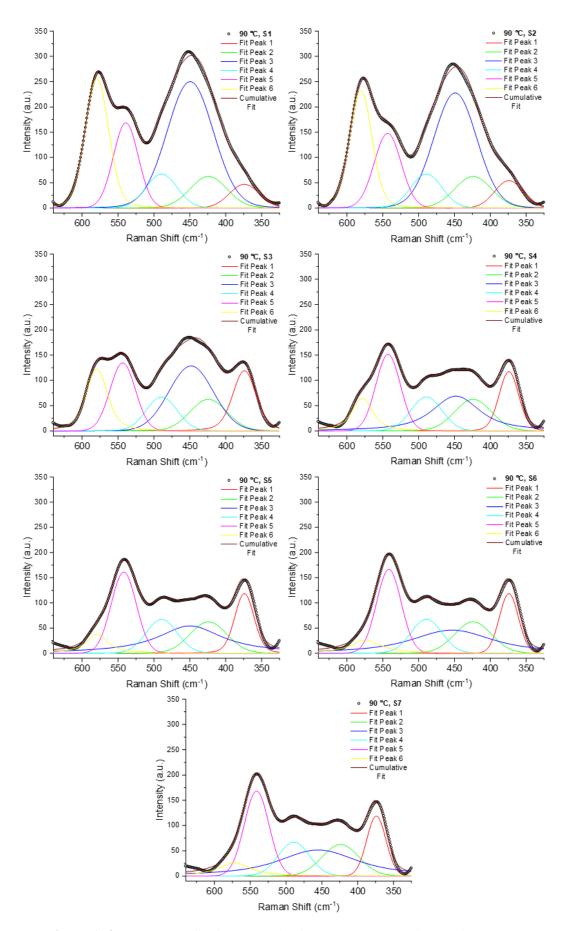
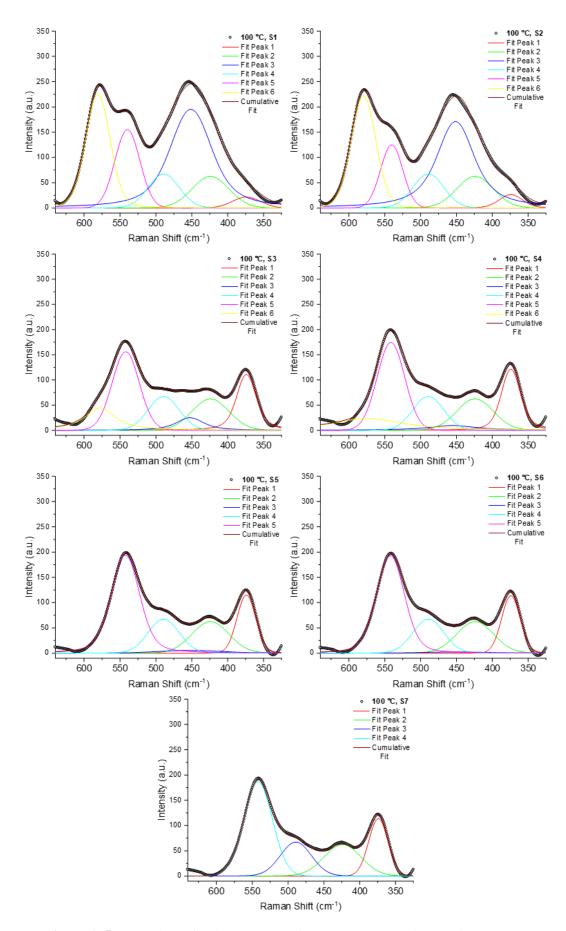


Figure A.4 Zr-OH band fits from samples from a PZN synthesis reaching 90 °C.



**Figure A.5** Zr-OH band fits from samples from a PZN synthesis reaching 100 °C.

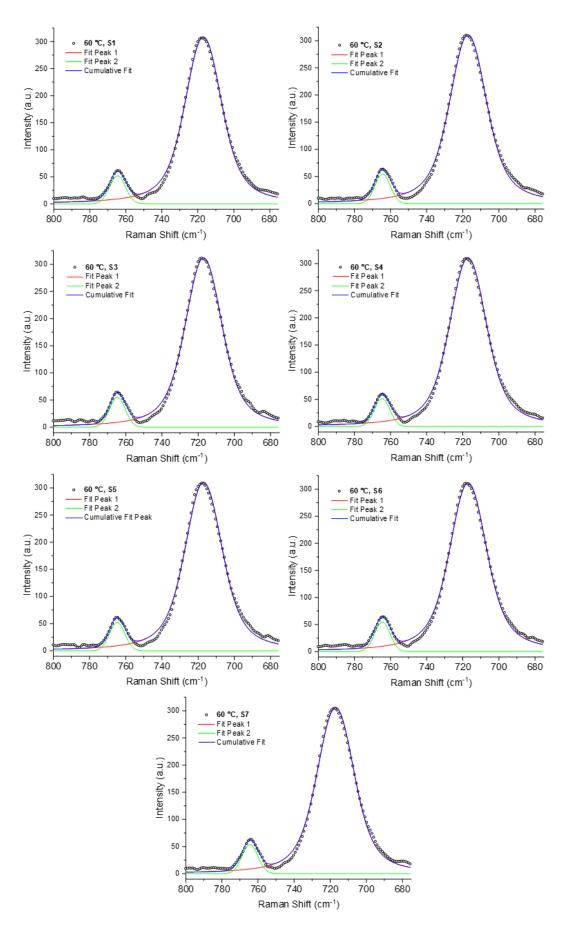


Figure A.6 Nitrate band fits from samples from a PZN synthesis reaching 60 °C.

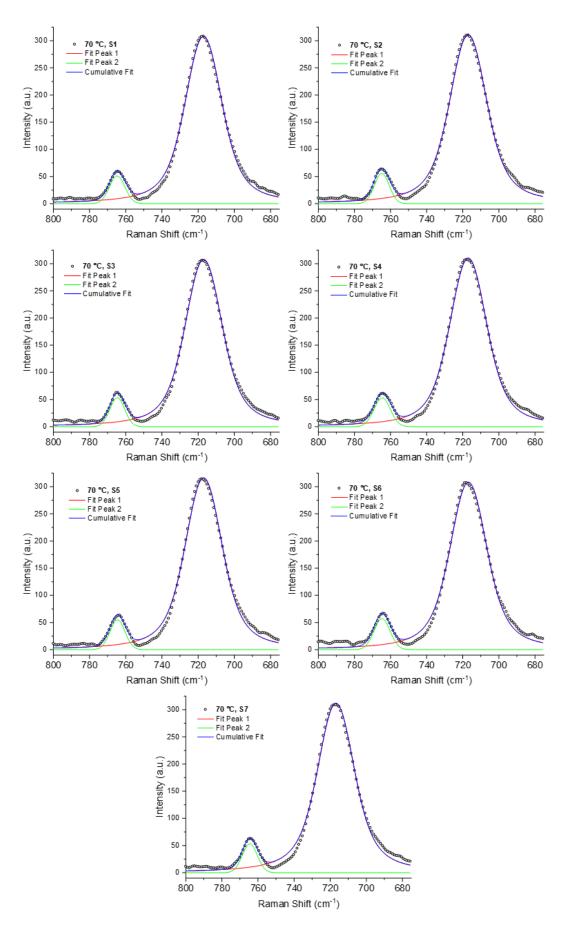


Figure A.7 Nitrate band fits from samples from a PZN synthesis reaching 70 °C.

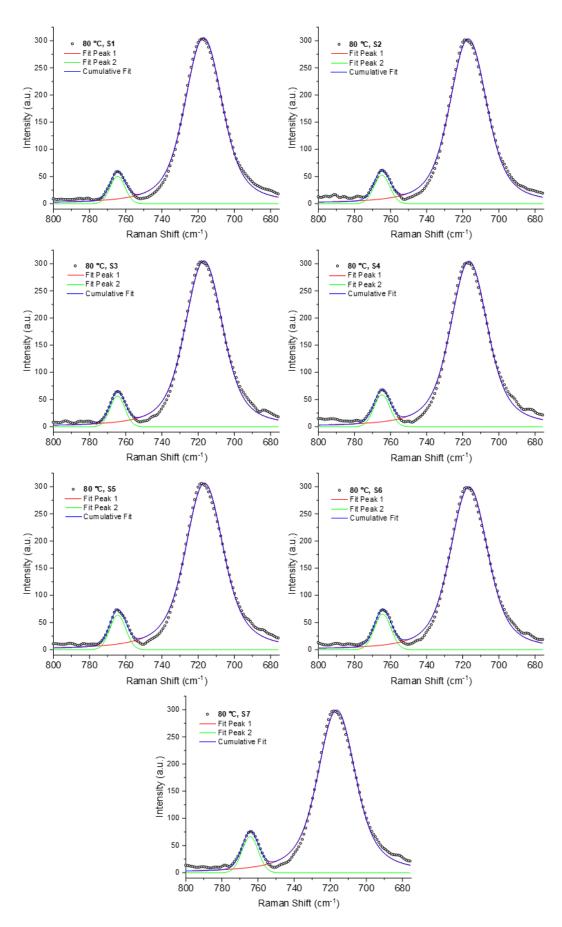


Figure A.8 Nitrate band fits from samples from a PZN synthesis reaching 80 °C.

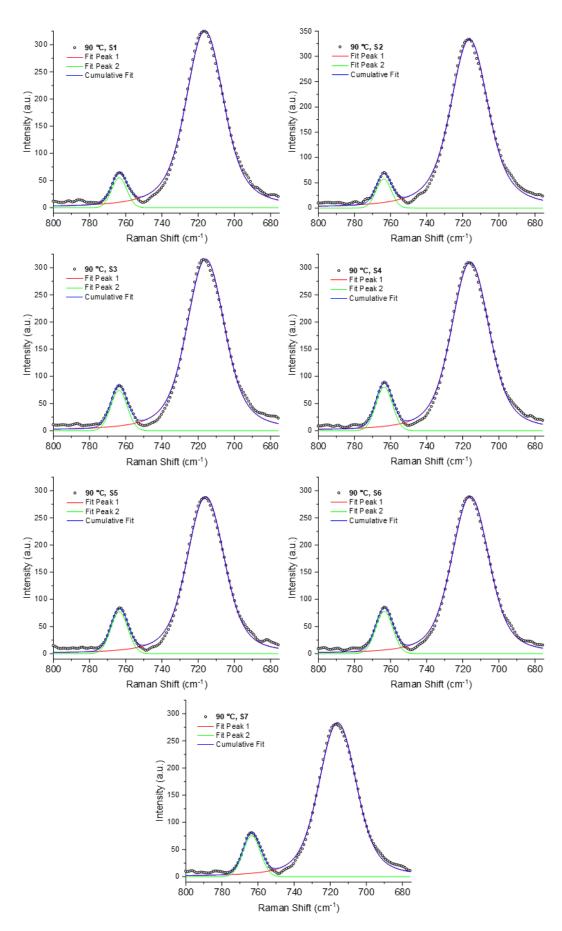


Figure A.9 Nitrate band fits from samples from a PZN synthesis reaching 90 °C.

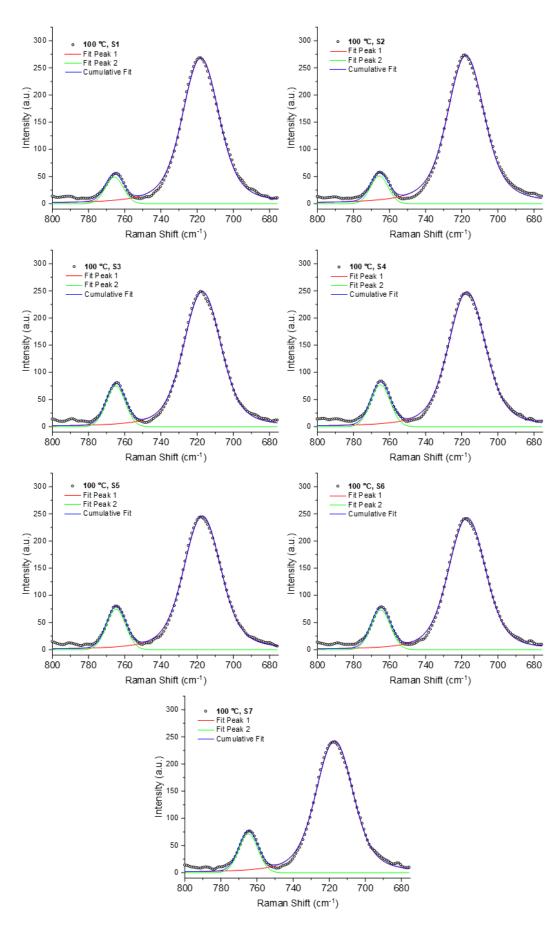
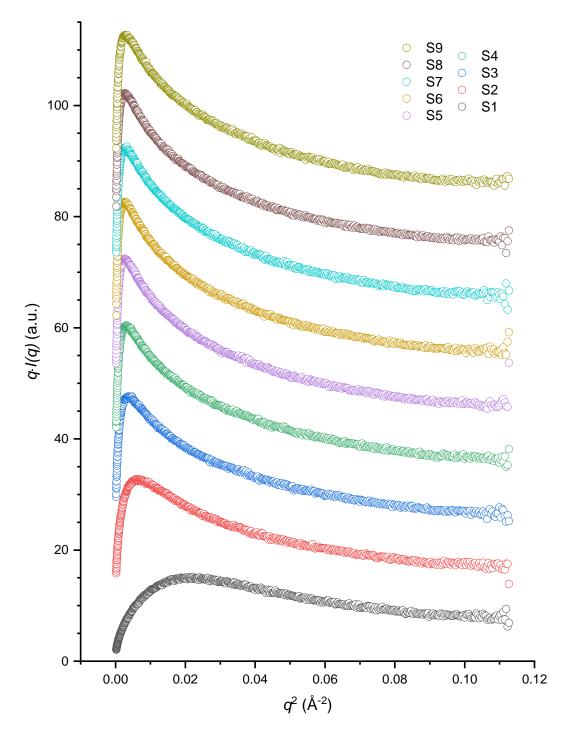
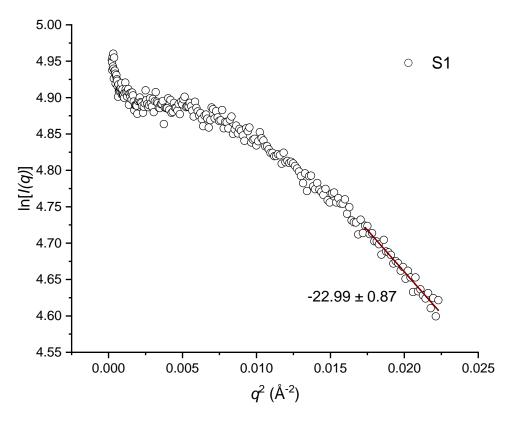


Figure A.10 Nitrate band fits from samples from a PZN synthesis reaching 100 °C.

### A.3 Plots from Determination of Particle Sizes in Section 4.5.2



**Figure A.11** GPA plots of scattering data for samples from the synthesis of a PZN solution composition 1:1 Zr:NO<sub>3</sub> and 1.5 mol% mandelic acid.



**Figure A.12** Linear fit to a Guinier plot for sample S1 from the synthesis of a PZN solution composition 1:1 Zr:NO<sub>3</sub> and 1.5 mol% mandelic acid. The linear fit slope is given.

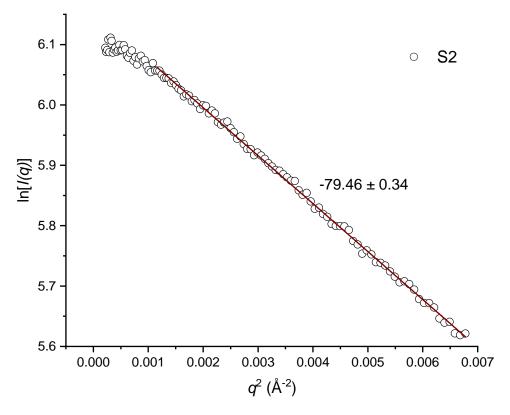


**Figure A.13** Linear fit to a Guinier plot for sample S2 from the synthesis of a PZN solution composition 1:1 Zr:NO<sub>3</sub> and 1.5 mol% mandelic acid. The linear fit slope is given.

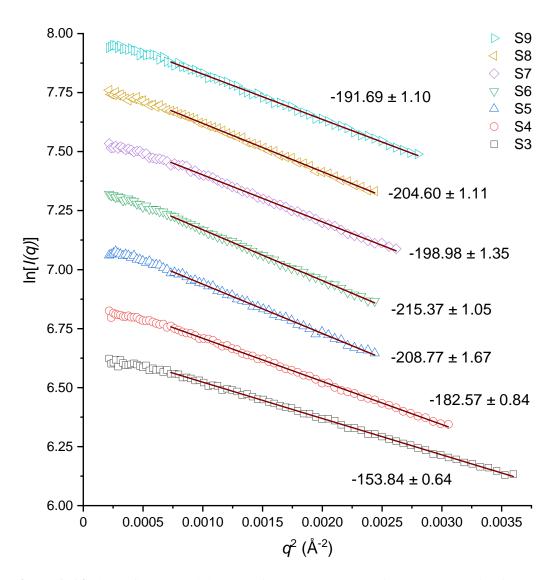


**Figure A.14** Linear fits to a Guinier plots for samples S2 – S9 from the synthesis of a PZN solution composition 1:1 Zr:NO<sub>3</sub> and 1.5 mol% mandelic acid. The linear fit slopes are given.

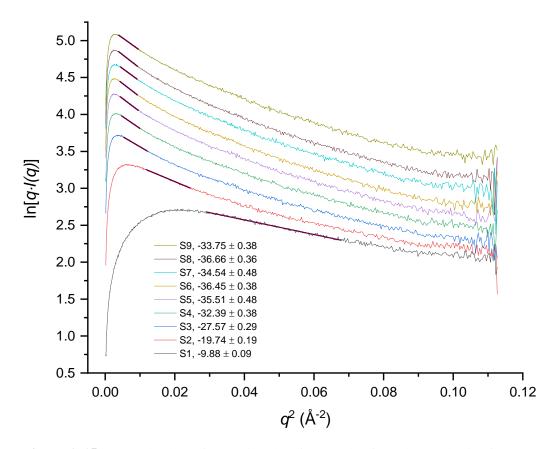


**Figure A.15** Longrods plots of scattering data for samples from the synthesis of a PZN solution composition 1:1 Zr:NO<sub>3</sub> and 1.5 mol% mandelic acid. The linear fit slopes are given in the legend.

### A.4 Plots from the Determination of Particle Sizes in Section 4.5.3

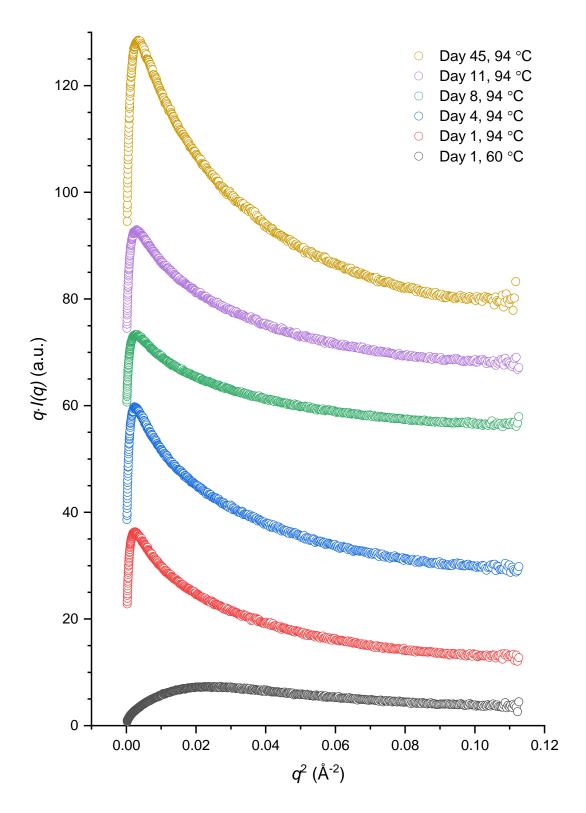


**Figure A.16** GPA plots of scattering data for aged samples from the synthesis of a PZN solution composition 1:1 Zr:NO<sub>3</sub> and 1.5 mol% mandelic acid

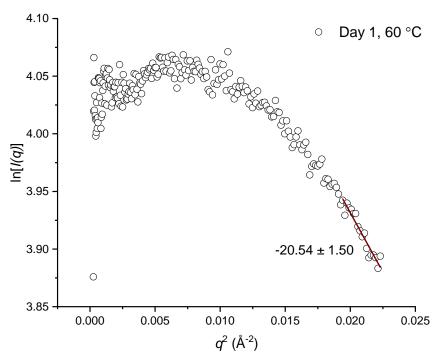


**Figure A.17** Linear fit to a Guinier plot for sample 'Day 1' from the synthesis of a PZN solution composition 1:1 Zr:NO<sub>3</sub> and 1.5 mol% mandelic acid. The linear fit slope is given.

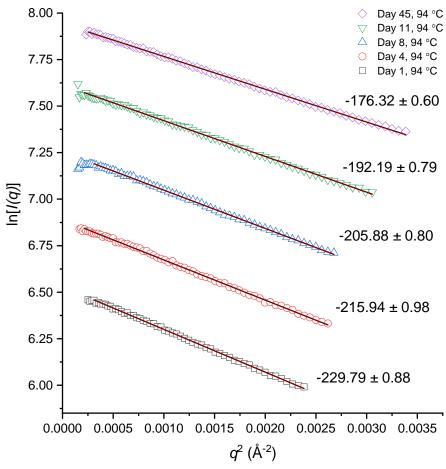


**Figure A.18** Linear fits to Guinier plots for samples from the synthesis of a PZN solution composition 1:1 Zr:NO<sub>3</sub> and 1.5 mol% mandelic acid. The linear fit slopes are given.

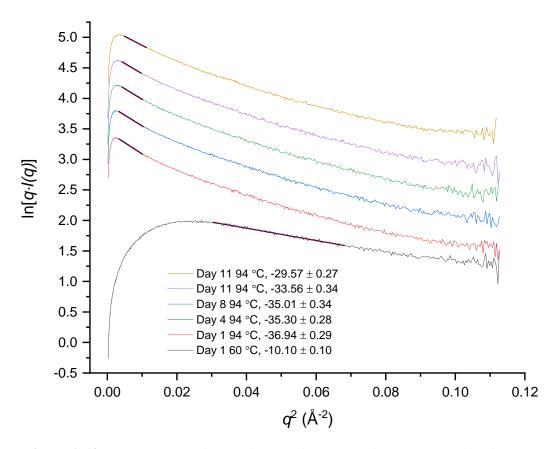


**Figure A.19** Longrods plots of scattering data for samples from the synthesis of a PZN solution composition 1:1 Zr:NO<sub>3</sub> and 1.5 mol% mandelic acid. The linear fit slopes are given in the legend.

#### A.5 Plots from the Determination of Particle Sizes in Section 4.5.4

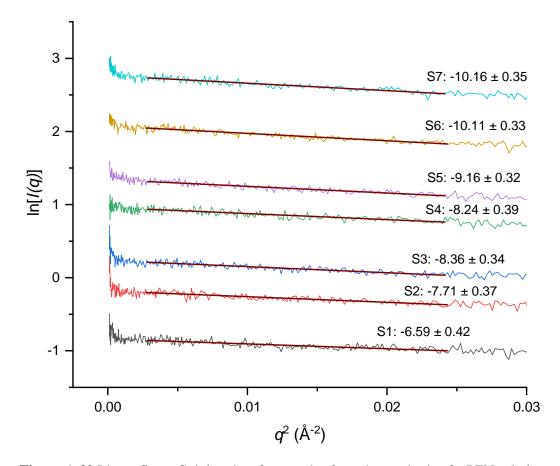


**Figure A.20** Linear fits to Guinier plots for samples from the synthesis of a PZN solution composition 2:1 Zr:NO<sub>3</sub> and 0 mol% mandelic acid, heated up to 60 °C. The linear fit slopes are given.

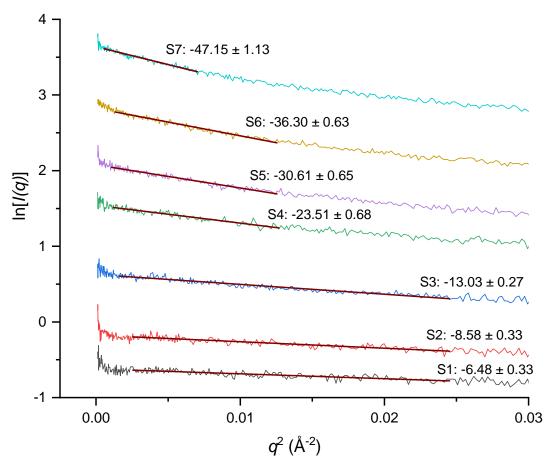


**Figure A.21** Linear fits to Guinier plots for samples from the synthesis of a PZN solution composition  $2:1 \text{ Zr:NO}_3$  and 0 mol% mandelic acid, heated up to  $70 \,^{\circ}\text{C}$ . The linear fit slopes are given.

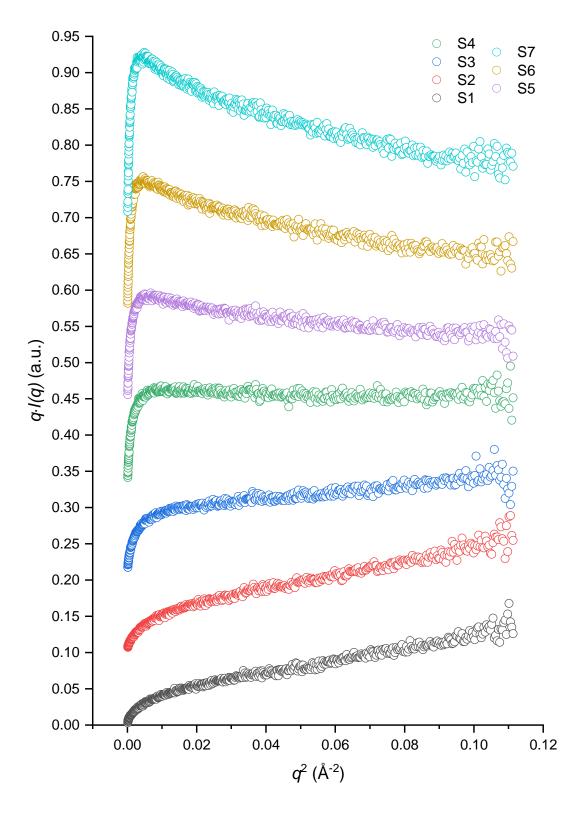


**Figure A.22** GPA plots of scattering data for samples from the synthesis of a PZN solution composition 2:1 Zr:NO<sub>3</sub> and 0 mol% mandelic acid, heated up to 80 °C.

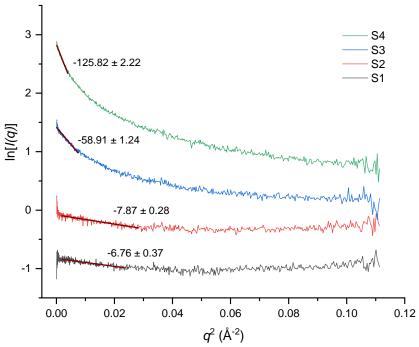


**Figure A.23** Linear fits to Guinier plots for samples S1 – S4 from the synthesis of a PZN solution composition 2:1 Zr:NO<sub>3</sub> and 0 mol% mandelic acid, heated up to 80 °C. The linear fit slopes are given.

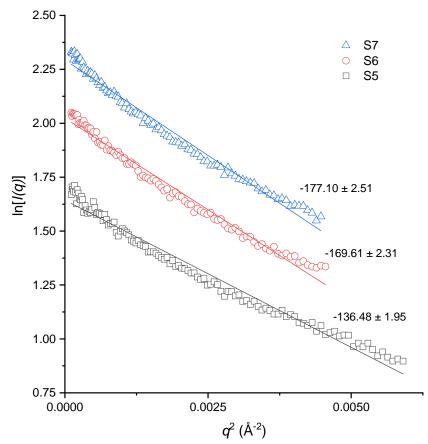


**Figure A.24** Linear fits to Guinier plots for samples S5-S7 from the synthesis of a PZN solution composition 2:1 Zr:NO<sub>3</sub> and 0 mol% mandelic acid, heated up to 80 °C. The linear fit slopes are given.

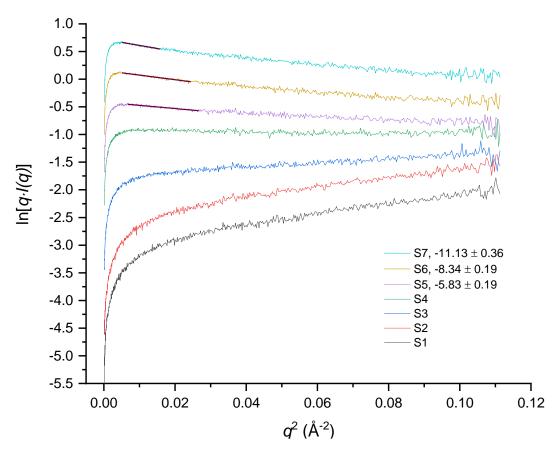


**Figure A.25** Linear fits to longrods plots for samples from the synthesis of a PZN solution composition 2:1 Zr:NO<sub>3</sub> and 0 mol% mandelic acid, heated up to 80 °C. The linear fit slopes are given where determined.

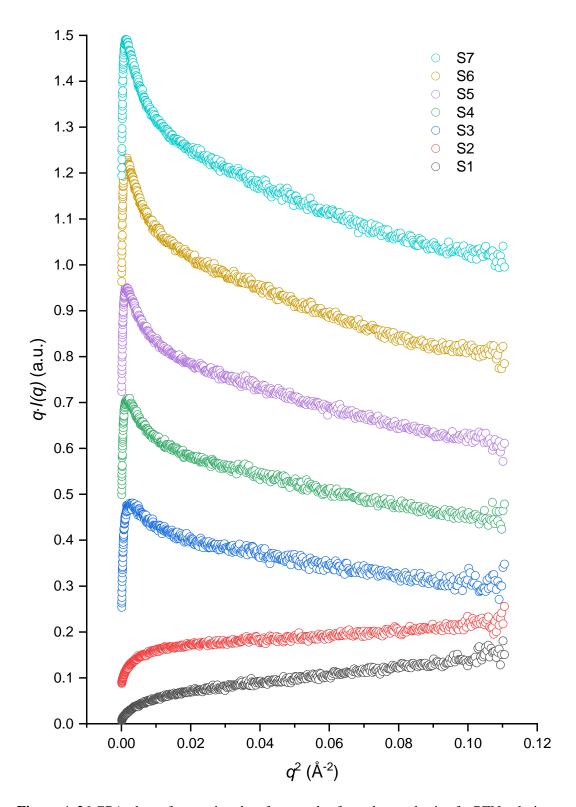


**Figure A.26** GPA plots of scattering data for samples from the synthesis of a PZN solution composition  $2:1 \text{ Zr:NO}_3$  and 0 mol% mandelic acid, heated up to  $90 \,^{\circ}\text{C}$ .

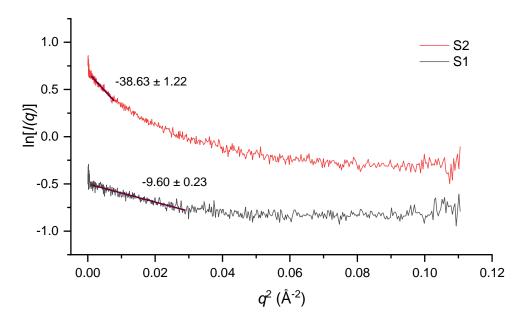


**Figure A.27** Linear fits to Guinier plots for samples S1 − S2 from the synthesis of a PZN solution composition 2:1 Zr:NO<sub>3</sub> and 0 mol% mandelic acid, heated up to 90 °C. The linear fit slopes are given.

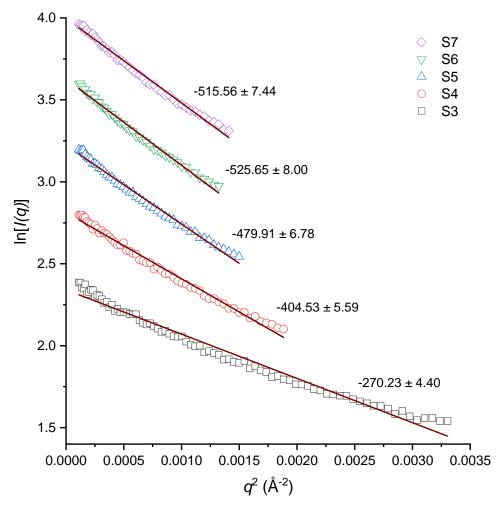


**Figure A.28** Linear fits to Guinier plots for samples S3 – S7 from the synthesis of a PZN solution composition 2:1 Zr:NO<sub>3</sub> and 0 mol% mandelic acid, heated up to 90 °C. The linear fit slopes are given.

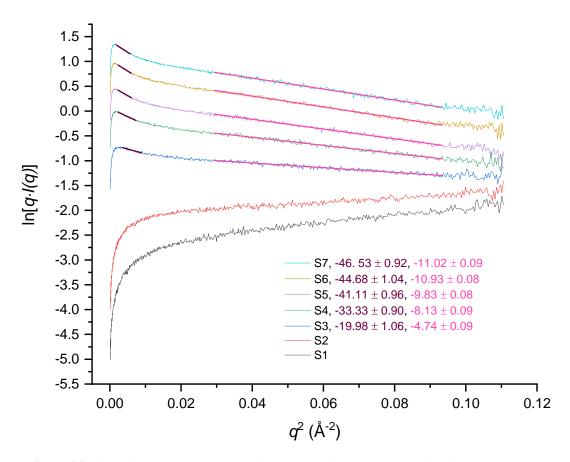


**Figure 29** Linear fits to longrods plots for samples from the synthesis of a PZN solution composition  $2:1 \text{ Zr:NO}_3$  and 0 mol% mandelic acid, heated up to  $90 \,^{\circ}\text{C}$ . The linear fit slopes are given where determined.

# A.6 Refined Parameters from Zr K-Edge EXAFS Analysis of Samples in Section 5.4

**Table A.2** Refined EXAFS parameters from the Zr K-edge data analysis for a PZN solution of **1:1** Zr:NO<sub>3</sub> and 0 mol% mandelic acid, heated *in situ*. The atom label in the Shell column denotes a particular scattering path included in the fit.  $R_{\rm eff}$  is the average interatomic distance as per the crystal structure; R is the refined distance adjusted during the fit. N,  $\sigma^2$ ,  $S_0^2$  &  $E_0$  represent coordination number, atomic position mean-squared disorder, amplitude reduction factor and threshold energy, respectively.

	Heated at 60 °C					Heated up to 94 °C					
Shell	Reff / Å	N	$\sigma^2$ / $\mathring{\mathbf{A}}^2$	R / Å		Shell	Reff / Å	N	$\sigma^2$ / $\mathring{\mathbf{A}}^2$	R / Å	
0	2.124	3	0.00525 ± 0.04096	2.198 ± 0.450		0	2.124	3	0.00679 ± 0.01256	2.111 ± 0.082	
0	2.210	3	0.00588 ± 0.03523	2.136 ± 0.494		0	2.210	3	0.00424 ± 0.00928	2.193 ± 0.074	
0	2.326	2	0.00382 ± 0.00984	2.323 ± 0.078		0	2.326	2	0.00321 ± 0.00534	2.328 ± 0.030	
Zr	3.559	3	0.00742 ± 0.00103	3.601 ± 0.011		Zr	3.559	3	0.00796 ± 0.00123	3.585 ± 0.012	
Zr	5.032	2	0.01209 ± 0.00542	5.095 ± 0.054		Zr	5.032	2	0.01188 ± 0.00645	5.053 ± 0.063	
$S_0^2 =$	$S_0^2 = 2.221 \pm 0.372, E_0 = -6.890 \pm 1.938 \text{ eV}$					$S_0^2 = 2.762 \pm 0.549, E_0 = -7.381 \pm 2.115 \text{ eV}$					

**Table A.3** Refined EXAFS parameters from the Zr K-edge data analysis for a PZN solution of **1:1 Zr:NO<sub>3</sub> and 1.5 mol% mandelic acid**, heated *in situ*. An explanation of column designations may be found in the caption for Table A.2.

Heated at 60 °C						Heated up to 94 °C					
Shell	Reff / Å	N	$\sigma^2$ / $\mathring{\mathbf{A}}^2$	R / Å		Shell	Reff / Å	N	$\sigma^2$ / $\mathring{\mathbf{A}}^2$	R / Å	
0	2.124	3	0.00709 ± 0.02622	2.136 ± 0.240		0	2.124	3	0.00489 ± 0.00564	2.087 ± 0.029	
0	2.210	3	0.00453 ± 0.01061	2.188 ± 0.217		0	2.210	3	0.00106 ± 0.00375	2.187 ± 0.025	
0	2.326	2	0.00319 ± 0.00622	2.323 ± 0.043		0	2.326	2	0.00051 ± 0.00313	2.322 ± 0.022	
Zr	3.559	3	0.00747 ± 0.00114	3.599 ± 0.011		Zr	3.559	3	0.00731 ± 0.00126	3.580 ± 0.013	
Zr	5.032	2	0.01471 ± 0.00542	5.047 ± 0.010		Zr	5.032	2	0.01188 ± 0.00672	5.036 ± 0.066	
$S_0^2 =$	$S_0^2 = 2.443 \pm 0.476, E_0 = -7.085 \pm 1.901 \text{ eV}$					$S_0^2 = 2.216 \pm 0.441, E_0 = -8.023 \pm 2.240 \text{ eV}$					

**Table A.4** Refined EXAFS parameters from the Zr K-edge data analysis for dried gels from PZN solutions. An explanation of column designations may be found in the caption for Table A.2.

1	1:1 Zr:NO <sub>3</sub> , 0 mol% mandelic acid					1:1 Zr:NO <sub>3</sub> , 1.5 mol% mandelic acid					
Shell	Reff / Å	N	$\sigma^2$ / $\mathring{\mathbf{A}}^2$	R / Å		Shell	Reff / Å	N	$\sigma^2$ / Å <sup>2</sup>	R / Å	
0	2.124	3	0.04656 ± 0.01848	2.023 ± 0.092		0	2.124	3	0.04956 ± 0.02276	2.029 ± 0.111	
0	2.210	3	0.00625 ± 0.00150	2.137 ± 0.011		0	2.210	3	0.00632 ± 0.00159	2.138 ± 0.011	
0	2.326	2	0.00609 ± 0.00215	2.289 ± 0.017		0	2.326	2	0.00625 ± 0.00230	2.292 ± 0.018	
Zr	3.559	3	0.00716 ± 0.00087	3.562 ± 0.008		Zr	3.559	3	0.00735 ± 0.00094	3.563 ± 0.009	
Zr	5.032	2	0.01209 ± 0.00417	5.022 ± 0.041		Zr	5.032	2	0.01223 ± 0.00449	5.025 ± 0.044	
$S_0^2 =$	$S_0^2 = 2.599 \pm 0.433, E_0 = -7.871 \pm 1.644 \text{ eV}$					$S_0^2 = 2.779 \pm 0.450, E_0 = -8.692 \pm 1.784 \text{ eV}$					

**Table A.5** Refined EXAFS parameters from the Zr K-edge data analysis for dried gels from PZN solutions. An explanation of column designations may be found in the caption for Table A.2.

	1:1 Zr:Cl, 0 mol% mandelic acid									
Shell	Reff / Å	N	$\sigma^2$ / Å <sup>2</sup>	R / Å						
0	2.124	3	0.00488 ± 0.01596	2.127 ± 0.210						
0	2.210	3	0.00529 ± 0.03646	2.212 ± 0.153						
0	2.326	2	0.00399 ± 0.01190	2.338 ± 0.091						
Zr	3.559	3	0.00846 ± 0.00138	3.591 ± 0.014						
Zr	5.032	2	0.01343 ± 0.00933	5.090 ± 0.086						
$S_0^2 =$	$S_0^2 = 1.782 \pm 0.384, E_0 = -5.373 \pm 2.161 \text{ eV}$									

**Table A.6** Refined EXAFS parameters from the Zr K-edge data analysis for as-made commercial aqueous zirconium solutions. An explanation of column designations may be found in the caption for Table A.2.

Z	Zirconium oxynitrate 'ZON' solution					Zirconium oxychloride 'ZOC' solution					
Shell	Reff / Å	N	$\sigma^2$ / $\mathring{\mathbf{A}}^2$	R / Å		Shell	Reff / Å	N	$\sigma^2$ / $\mathring{\mathbf{A}}^2$	R / Å	
0	2.124	3	0.00171 ± 0.00322	2.122 ± 0.092		0	2.124	3	0.00161 ± 0.00420	2.118 ± 0.111	
0	2.210	3	0.00077 ± 0.00477	2.236 ± 0.011		0	2.210	3	0.00060 ± 0.00642	2.226 ± 0.011	
0	2.326	2	0.00224 ± 0.00215	2.325 ± 0.017		0	2.326	2	0.00166 ± 0.00736	2.337 ± 0.018	
Zr	3.559	3	0.00713 ± 0.00087	3.590 ± 0.008		Zr	3.559	3	0.00735 ± 0.00123	3.593 ± 0.009	
Zr	5.032	2	0.01093 ± 0.00417	5.053 ± 0.041		Zr	5.032	2	0.01288 ± 0.01008	5.055 ± 0.044	
$S_0^2 =$	$S_0^2 = 3.556 \pm 0.637, E_0 = -6.069 \pm 2.024 \text{ eV}$					$S_0^2 = 3.294 \pm 0.616, E_0 = -7.043 \pm 2.116 \text{ eV}$					